Syntheses and Photophysical Studies of Two-Dimensional Hybrid Organic-Inorganic Semiconductors

by

Watcharaphol Paritmongkol

Master of Chemistry
University of Oxford, 2015

SUBMITTED TO THE DEPARTMENT OF CHEMISTRY IN PARTIAL FULFILLMENT OF THE REQUIREMENT FOR THE DEGREE OF

DOCTOR OF PHILOSOPHY IN CHEMISTRY
AT THE
MASSACHUSETTS INSTITUTE OF TECHNOLOGY

September 2021

Signature of Author: _____

Department of Chemistry
August 11, 2021

Certified by: _____

William A. Tisdale
MacVicar Faculty Fellow, Associate Professor
Thesis Supervisor

Accepted by: _____

Adam Willard
Associate Professor
Graduate Officer

This doctoral thesis has been examined by a committee of the
Department of Chemistry as follows:

Professor Moungi G. Bawendi _____

Thesis Committee Chair

Lester Wolfe Professor of Chemistry

Professor William A. Tisdale _____

Thesis Supervisor

MacVicar Faculty Fellow, Associate Professor of Chemical Engineering

Professor Gabriela S. Schlau-Cohen _____

Member, Thesis Committee

Associate Professor of Chemistry

Syntheses and Photophysical Studies of Two-Dimensional Hybrid Organic-Inorganic Semiconductors

by

Watcharaphol Paritmongkol

Submitted to the Department of Chemistry on August 11, 2021
in Partial Fulfillment of the Requirements for the Degree of
Doctor of Philosophy in Chemistry

Abstract

This thesis focuses on the studies of two families of two-dimensional (2D) hybrid organic-inorganic semiconductors with exciting properties for optoelectronic applications. The first family is 2D lead halide perovskites (LHPs), which have received immense interest due to their solution processability and interesting luminescent properties. However, their uses in energy harvesting and light-emitting applications are limited by the difficulty in their synthesis, the knowledge of their structural-property relationships, and the understanding of their exciton physics. In this thesis, we first present cooling-induced crystallization to produce phase-pure 2D LHPs with controllable chemical compositions. Using single-crystal X-ray diffraction, we refined their crystal structures across temperatures and observed two phase transitions corresponding to structural changes in organic and inorganic sub-lattices. The structural information across these phase transitions was then used to explain temperature-dependent optical properties and address the debate over the origins of their broadband emission. We observed two broadband emission features and distinguished defect-associated from self-trapped exciton (STE) emission by the difference in their temperature-dependent behaviors. Moreover, we found that the temperature dependence of STE emission is strongly correlated with exciton-phonon coupling strength and structural distortion, suggesting a possible tuning of this property by compositional engineering.

The second material is silver phenylselenolate (AgSePh), an emerging 2D metal organic chalcogenolate (MOC) material with blue luminescence, in-plane anisotropy, large exciton binding energy, non-toxic and earth-abundant elemental composition, and a scalable synthetic method. Despite these desirable characteristics for modern electronics, its fundamental studies and device integration are limited by its crystal size and quality produced by current synthetic methods. In this thesis, we report two synthetic advances to produce AgSePh thin films with controllable grain size from <200 nm to >5 μm and microcrystals with increased crystal size from ~2 μm to >1mm. Systematic optical and electrical characterizations through photoluminescence spectroscopy and electrical conductivity suggest higher crystalline qualities with lower defect densities in these samples. Using ^{77}Se nuclear magnetic resonance spectroscopy and monitoring reaction kinetics, we provide mechanistic insights that enable the development of generalizable single-crystal growth. Overall, we expect these reported synthetic methods to facilitate the studies on this exciting material and its family.

Thesis Supervisor: William A. Tisdale
Title: MacVicar Faculty Fellow, Associate Professor of Chemical Engineering

Acknowledgements

Before the personal acknowledgments, I would like to start by thanking the Department of Energy for the financial support on two-dimensional lead halide perovskite (2D LHP) projects presented in this thesis. I also would like to thank the Department of Defense, who believed in our ideas and provided funding on metal organochalcogenide (MOC) research.

Next, I would like to express my profound gratitude to my thesis advisor, Prof. William Tisdale, for his mentorship, support, and guidance throughout my PhD. His advising style gave me the freedom to explore, execute, and lead the research topics of my interests without bound. Although finding an interesting research idea from scratch gave me a hard time in my early years, the experience developed me into a capable scientist and led me to pioneer MOC research, which had become a main research direction in the Tisdale lab. Furthermore, Will's emphasis on science communication was another valuable part of my PhD training and taught me to present clearly and concisely in written work and oral presentations. Moreover, I appreciate his leadership to create a collaborative and inclusive group culture and his attention to the physical and emotional well-being of every group member. Additionally, I am in debt to his career advice and endless support in writing me recommendation letters for countless programs I applied to. Without his help, I would not be able to participate in the 70th Lindau Nobel Laureate Meeting or be nominated by MIT to apply for the Schmidt Science Postdoctoral Fellowship. Thank you so much for believing in me.

Moreover, I would like to extend my gratitude to my thesis committee members, Prof. Moungi Bawendi and Prof. Gabriela Schlau-Cohen, for their sincere comments, advice, and guidance on scientific research and career development. I will never forget your teaching and will always remember to follow my interest, passion, and motivation throughout my scientific career.

My work would not have been possible without help from many members of the Tisdale lab. I began the 2D LHP research because of the seminal work by Mark Weidman, Michael Seitz, and Dan Congreve. Seung Kyun (SK) Ha was my lab partner who struggled through the pain of perovskite's instability and accompanied me from the start to the end of my PhD. With a question of his, Nabeel Dahod sparked my idea on single crystal growth of 2D LHPs which led to multiple collaboration works and published papers between the two of us. I would not have come this far without that question, and it was a great pleasure to work with him. Yunan Gao, Aaron Goodman, Matthew Ashner, and Kris Williams were Tisdale lab's optics gurus who taught me laser-lab skills and helped me start my spectroscopy experiments. Wenbi Shcherbakov-Wu was my laser-lab companion who accompanied me through various problems in the laser lab and was always there when I needed. She was also a superb electron micrograph photographer and an excellent lab safety officer. I am really thankful for her help and service. Eric Powers helped me with all transient absorption spectroscopy work presented in this thesis. His enthusiasm in science, thoughtful questions, organized presentations, and eagerness to help were good examples for every fellow lab member. Woo Seok Lee played a key role in the electrical characterization of MOCs and deserved recognition as a co-first author of the paper based on the work described in Chapter 4. Tomoaki Sakurada was another vital member of the MOC team, and his organic chemistry skills were crucial for the new discoveries in this new research playground. I thank Woo Seok and Tomoaki for

allowing me to lead the team and bringing in new ideas and techniques to push forward this uncharted MOC research boundary. I also acknowledge the help of Ruomeng Wan on organic synthesis and diffuse reflectance spectroscopy, Nannan Mao on microabsorption spectroscopy, Raman spectroscopy, and atomic force microscopy, and Alexia Stollmann on temperature-dependent powder x-ray diffraction. Barbara Balkwill was a fantastic group admin who was always happy to help and cared for every group member. Additionally, I would like to extend my appreciation to other Tisdale lab members and alumni – Jolene Mork, Rachel Gilmore, Elizabeth Lee, Katie Mauck, Katie Shulenberger, Dahin Kim, Sam Winslow, Narumi Wong, Abby Taussig, Makhsud Saidaminov, Robert Keitel, Leo Spiegel, Deepankur Thureja, and Alex Hernandez – and talented undergraduate students – Janny Cai, Veerapatr Yotamornsunthorn, Blair Williams, Thomas Sun, and Annlin Su – for being a part of my memorable PhD journey. The interactions with all of them have shaped me into who I have become.

During my PhD, I also had the privilege to work with many great scientists outside of the Tisdale lab. I thank three crystallography experts – Dr. Shao-Liang Zheng, Dr. Charles Settens, and Dr. Peter Müller – for their help with X-ray techniques and structural refinement on various projects throughout my time at MIT. Prof. Dan Congreve and Prof. Mahesh Gangishetty provided me with useful scientific discussion and help with silver film growth. I also thank them for their invaluable career advice, which I will take to the next stages of my career. I was also fortunate to take part in the collaboration work with Prof. Paulina Plochocka and Dr. Mateusz Dyksik. The data from their magneto-absorption spectroscopy technique were stunning and shed light on the question Will and I had long been curious about.

The challenges throughout my PhD journey would not be bearable without the moral support from multiple friends I met during my time at MIT and before. I thank my Thai MIT PhD seniors – Nopphon Weeranoppanant, Yanin Sukjai, Aniwat Tiralap, and Paphonwit Chaiwatanodom – for the thought-provoking discussion over Friday-night dinners. I am also thankful to Nicha Apichitsopa and Boonsom Uranukul for the weekly lunch gathering at Stata Center and Koch Institute. Furthermore, my gratitude is extended to Ajarn Sasinee Ung-kanont, Tanatorn Khotavivattana, Anupong Tangpeerachaikul, and Jesada Temaismithi, who had supported me during the good and bad times since before I came to MIT. Additionally, my appreciation would not be complete without thanking every member of the Thai Student at MIT and other Thai students in Boston and Cambridge areas.

The PhD journey would be much more difficult without the strong academic background I acquired from previous institutions and the strong passion for science that these institutions instilled in my heart. I am grateful to Mahidol Wittayanusorn School and Thailand's Chemistry Olympiad Selection Camp for providing me with excellent science education and made me decided to pursue my undergraduate degree in chemistry. I thank the University of Oxford for broadening my world and providing me with a firm chemistry foundation. I am deeply grateful to all teachers, professors, and friends I interacted with at these places.

Last but not least, I am in debt to mom, dad, and Aim. They have provided me with unwavering support and unconditional love. Thank you for listening to all of my good and bad stories and for keeping me company over the up and down moments. I cannot imagine the world without them, and I love them from the bottom of my heart.

Contents

List of Figures

List of Tables

Chapter 1 Introduction

Semiconductors have become an integral part of our society as they are the main components of electronic devices and play significant roles in solar energy conversion and lighting. Due to the growing complexity of modern problems, novel semiconductors with exotic properties and new applications are needed to meet the world's challenges.

For the last decade, two-dimensional (2D) semiconductors with a-few-monolayer thicknesses have emerged as promising electronic materials for a variety of emerging applications due to strong light-matter and charge-charge interactions in these systems.[1–5] A prominent sub-family of 2D semiconductors is the transition metal dichalcogenides (TMDs), which contain stacks of 2D inorganic sheets directly interacting through van der Waals interaction and exhibit a layer-dependent tunable bandgap.[1,6,7] Due to quantum confinement and reduced dielectric screening, TMD monolayers exhibit strong exciton binding energy on the order of hundreds of meV,[8–10] leading to a stable exciton at room temperature and fascinating many-particle phenomena.[11,12] However, the strong electronic coupling to TMDs' surroundings makes their properties sensitive to substrates and environments,[13,14] adding extra preparation steps, such as layer transfer[15] and encapsulation,[16,17] for fundamental studies and practical applications. Despite the progress and promise of TMDs, new 2D semiconductors are sought that can overcome the limitations of these existing materials and open up new electronic and photophysical phenomena.

The core of this thesis is in the discovery and understanding of novel semiconductors whose properties can surpass those of the existing materials. Specifically, this thesis focuses on two families of novel 2D hybrid organic-inorganic semiconductors: 2D lead halide perovskites (LHPs)

and 2D metal organic chalcogenolates (MOCs). In contrast to TMDs, 2D LHPs and 2D MOCs contain organic moieties that passivate the surface and decouple the electronic interaction between inorganic layers.[2] Hence, 2D LHPs are insensitive to substrates, and strong excitonic properties can be realized in structures containing multiple 2D sheets and single crystals.[2,18–21] Moreover, due to their hybrid nature, they can be synthesized at low temperatures, providing a more sustainable solution compared to conventional semiconductors.

The following chapters describe my PhD research on the syntheses and photophysical studies of 2D LHPs and 2D MOCs. In Chapter 2, background knowledge on the structures, properties, and syntheses of these materials will be given. Chapter 3 will present an advance in the synthesis of phase-pure 2D LHPs and the understanding of their structural trends across varying chemical composition and sample temperature. Chapter 4 will focus on addressing the debate over the origin of broadband emission in 2D LHPs. Chapters 5 and 6, will be centered on silver phenylselenolate (AgSePh), a member of the 2D MOC family, and two chemical strategies to produce AgSePh thin films and microcrystals with improved size and quality. Optical, electrical, and mechanistic studies on AgSePh thin films and microcrystals will also be reported in these chapters. After that, this thesis will end with a summary and outlook in Chapter 7.

Chapter 2 Background

2.1 2D Lead Halide Perovskites

Layered 2D LHPs have emerged as an alternative to their bulk or three-dimensional (3D) counterparts because of their improved stability,[22,23] rich structural flexibility,[24,25] and greater tunability of optical properties.[24,26] Because of the ease of their syntheses and excellent properties, 2D LHPs have been investigated for various optoelectronic applications, such as solar cells,[22,23,27–31] light-emitting diodes,[32–35] and photodetectors.[36–39] To better understand 2D LHPs, a brief introduction to 3D LHPs is required.

2.1.1 Lead Halide Perovskites

Perovskite refers to the mineral $CaTiO_3$ and any structure adopting the same ABX_3 structural framework.[40] In the case of LHPs, the B-site is occupied by Pb^{2+} ion and the X-site contains a halide anion (Cl^-, Br^- or I^-) (Figure 2-1). These two ions form BX_6 octahedra which situates at the corners of the unit cell, leaving a space at the center for the A-site ion. The major role of this A-site ion is to balance the charge and support the extended octahedra structure.[40,41] Due to the spatial constraint, the size of A-site ion is limited by the Goldschmidt's tolerance factor described by[42]

$$t = \frac{1}{\sqrt{2}}\left(\frac{R_A + R_X}{R_B + R_X}\right), \tag{2-1}$$

where R_A, R_B, and R_X are the ionic radii for the corresponding ions. For 3D perovskites, t is restricted between 0.8 and 1.0, and this leaves three common A-site ions for 3D LHPs: methylammonium (MA^+), formamidinium (FA^+) and cesium (Cs^+).

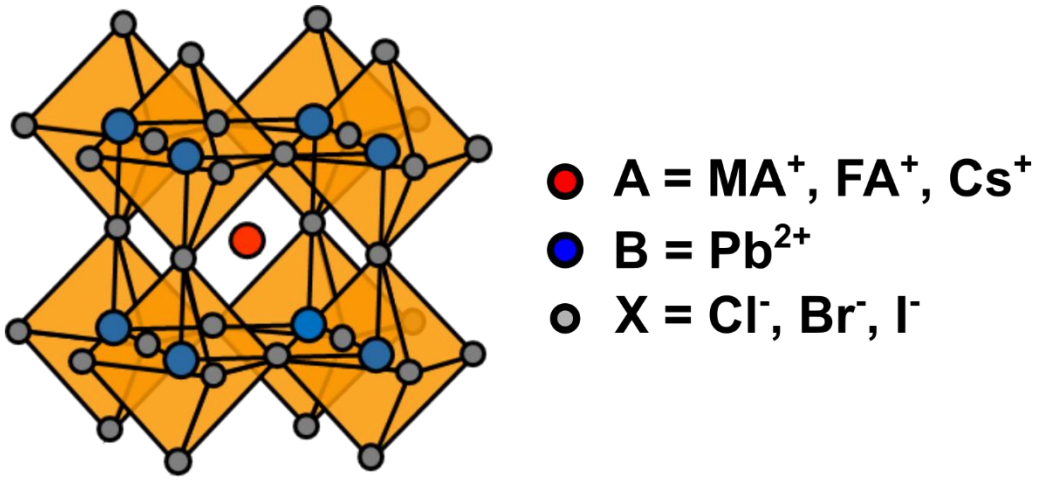

Figure 2-1. ABX_3 perovskite structure where A is a small cation (i.e., methylammonium $\{MA^+\}$, formamidinium $\{FA^+\}$, or cesium $\{Cs^+\}$), B is a divalent cation of lead (Pb^{2+}), and X is a halide anion (Cl^-, Br^-, I^-).

The first synthesis and characterization of LHPs date back to the study by Weber in 1978.[43] However, the interest in this material faded away before being sparked again in 2009 after the Miyasaka group at the University of Tokyo discovered that this solution processable material can be used in dye-sensitized solar cells.[44] Since then, there has been a surge in research on perovskites and the solar-conversion efficiency of perovskite photovoltaics has been improved to 22%,[44–47] rivalling the 26% efficiency of silicon photovoltaics. This remarkable efficiency is achieved owing to appealing properties of LHPS such as high absorption coefficients,[41,48] defect tolerance,[49,50] long carrier diffusion lengths[51–53] and long carrier lifetimes.[52–54]

However, long-term stability of 3D LHPs is a major hurdle that prevents the widespread use of 3D LHP electronics. Because of their ionic lattices, 3D LHPs are unstable in ambient moisture.[55] An approach to improve the stability of LHPs is incorporation of large A-site ions with long hydrophobic chains, thereby leading to the formation of a new type of perovskites.

2.1.2 Structures and Properties of 2D Lead Halide Perovskites

2D LHPs form when a larger A-site ion than that predicted by the Goldschmidt's tolerance factor is used. The structures of 2D LHPs consist of 2D inorganic slabs of ABX_3 perovskite unit cells separated by large monovalent cations (Figure 2-2a). Their general formula is $L_2[ABX_3]_{n-1}BX_4$ or $L_2A_{n-1}B_nX_{3n+1}$, where L is a large monovalent cation, A is a small cation (i.e., methylammonium {MA^+}, formamidinium {FA^+}, or cesium {Cs^+}), B is a divalent cation of lead (Pb^{2+}), X is a halide anion (Cl^-, Br^-, or I^-), and *n* determines the inorganic quantum-well thickness defined by the number of corner-sharing BX_6 octahedral layers. Because L is usually a large organic molecule with an amine functional group in its protonated form, L acts as an electronically insulating organic spacer, and 2D LHPs form natural quantum-well structures.

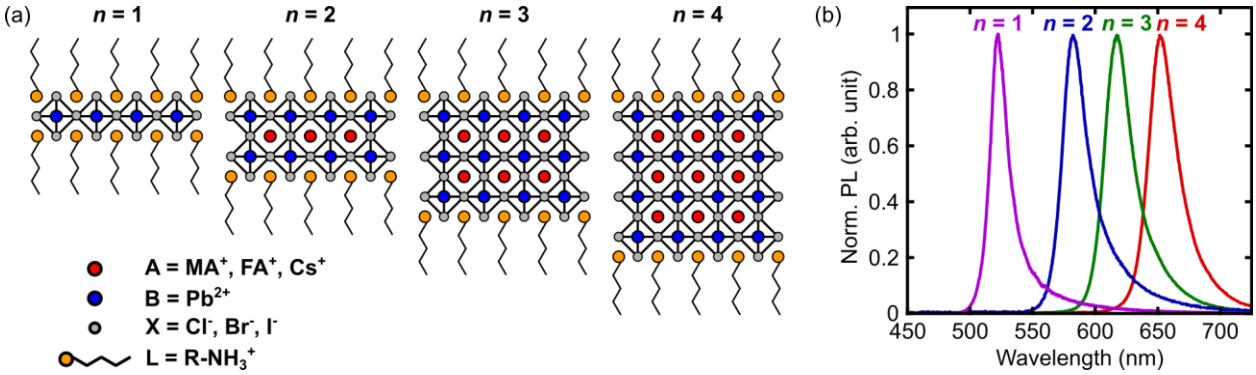

Figure 2-2. (a) Structures of 2D LHPs with varying quantum-well thickness (*n*). (b) Photoluminescence spectra of 2D LHPs with varying *n*.

Because of the spatial confinement and the low dielectric screening of organic spacers, 2D LHPs have high exciton binding energies (>400 meV for single-layered 2D LHPs).[18,56] Moreover, both optical and electronic properties of 2D LHPs can be tuned by varying the identities of each constituent ion (L, A, B, and X) as well as *n*.[24,26] For example, the photoluminescence emission of 2D LHPs blue-shifts in steps as *n* decreases due to the quantum confinement along the stacking direction (Figure 2-2b). Additionally, exciton binding energies and photoluminescence quantum yields can be influenced by the choices of organic spacers. Other properties of 2D LHPs include

strong anisotropy,[57,58] narrow and broadband light emission,[59] large Rashba splitting,[60–62] ferroelectricity,[61,63] ferromagnetism[64,65] and nonlinear effects.[66–68]

2.1.3 Syntheses of 2D Lead Halide Perovskites

Another attractive property of 2D LHPs is in the ease of their synthesis and solution processability which allow the production of optoelectronic devices at low temperature (<200 °C) and low cost. A variety of methods can be used to prepare 2D LHPs.[24,40,59,69–73] Polycrystalline thin films of 2D LHPs can be made by spin-casting a mixture of PbX_2, AX, and LX dissolved in dimethylformamide and/or dimethylsulfoxide onto a spinning substrate. The same mixture can also be added dropwise to a nonpolar solvent, such as toluene, to produce 2D nanoplatelets via ligand-assisted reprecipitation.[26,56,74] Colloidal solutions of 2D nanoplatelets can be prepared by a modified hot-injection method,[75,76] similar to the approach used to synthesize halide perovskite quantum dots.[77] In addition, 2D sheets of LHPs can be grown directly on a substrate by solvent evaporation[78] as well as chemical vapor deposition.[79,80] Inverse temperature crystallization,[81] which employs the retrograde solubility of perovskite reagents, was successfully used to make high-quality single crystals of 3D LHPs. However, the reagents of 2D LHPs do not show retrograde solubility, and the method is not feasible to grow 2D LHP single crystals[82] because of the difference in surface–solvent interaction. Antisolvent vapor-assisted growth has also been a successful approach for growing 3D LHPs[52] as well as $n = 1$ 2D LHPs,[83] but successful application of this method to the preparation of $n \geq 2$ 2D LHPs has not been reported. Another method to synthesize of 2D LHPs with quantum-well thicknesses of $n \leq 3$ was reported using controlled ratios of solvent and antisolvent.[84] However, the method that has demonstrated the greatest versatility so far is cooling-induced crystallization, which has been shown to produce pure single crystals of 2D MA lead iodide perovskites with precise thickness control of up to $n = 5$.[85–87] Recently, this limit

has been extended further to $n = 7$,[88] and has been applied to a variety of organic spacers.[29,37,85,89,90] In this method, perovskite ions are dissolved in hot aqueous hydrohalic acid, and the solution is then allowed to cool slowly to induce crystallization.

2.2 2D Metal Organic Chalcogenolates

Metal organic chalcogenolates (MOCs) of coinage metals[91] are non-toxic covalently bound hybrid organic-inorganic materials and have been studied for various applications in medicine,[92–94] nanomaterials synthesis,[95] light emission,[96–102] and sensors.[103,104] They adopt $[M(ER)]_n$ chemical formula, where M = Cu(I), Ag(I), Au(I); E = S, Se, Te; and R is an organic hydrocarbon.[91] Depending on various factors, such as size, steric hindrance, and metallophilic interaction, MOCs exist as zero-, one-, and two-dimensional (0D, 1D, 2D) materials.[91,105] 0D MOCs are oligomers and have properties of molecular complexes. On the other hand, 1D and 2D MOCs exist as coordination polymers and exhibit semiconducting properties. This thesis will focus on silver phenylselenolate (AgSePh),[97,106–112] a 2D MOC with interesting optical and excitonic properties.

2.2.1 Structure and Properties of Silver Phenylselenolate

AgSePh is a 2D hybrid organic-inorganic semiconductor with a narrow blue luminescence centered at 467 nm[97] suitable for blue light-emitting applications. AgSePh adopts a lamellar structure consisting of layers of Ag atoms arranged in a distorted hexagonal pattern and connected through μ_4-SePh ligands situating above and below the layer plane (Figure 2-3).[113] Due to this structure, AgSePh shows in-plane anisotropy,[111] high exciton binding energy (~400 meV),[109,111] and picosecond PL lifetime.[109] Moreover, unlike 2D LHPs, the soft acid-soft base interaction between Ag and Se atoms makes Ag-Se bonds covalent.[91,105] This covalent interaction not only leads to AgSePh being stable in both polar and non-polar solvents,[91,105] but also allows a unique

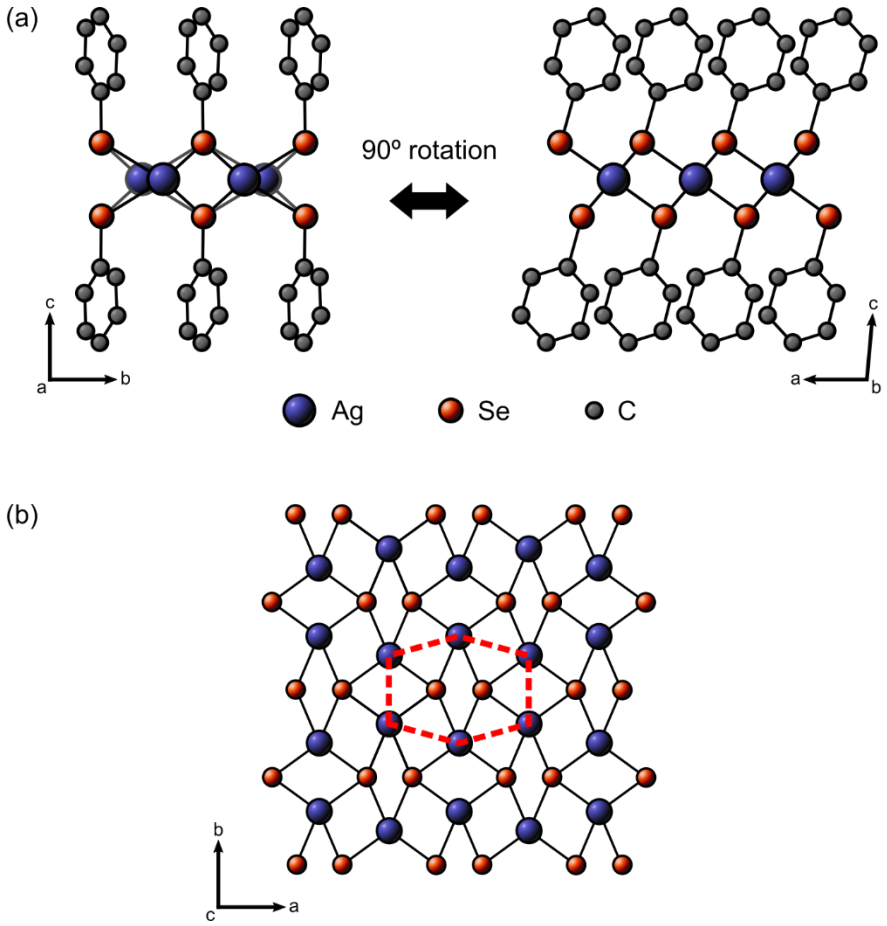

Figure 2-3. Crystal structures of AgSePh (a) along crystallographic a and b axes, and (b) along crystallographic c axis showing in-plane anisotropy and the difference in Ag-Ag distances.

electronic band gap tuning by organic functionalization.[114] Furthermore, AgSePh can be synthesized by a scalable method[106] that is compatible with modern microelectronics. With these interesting optical properties, chemical stability, non-toxic and earth-abundant elemental composition, and a scalable synthetic method, AgSePh deserves an investigation as a potential next-generation semiconducting material.

2.2.2 Syntheses of Silver Phenylselenolate

The syntheses of AgSePh reported so far can be categorized into three methods: single-crystal growth,[113] solution-phase synthesis,[97,107,108] and vapor-phase synthesis.[106,110] The single-crystal growth was the method used in the first discovery of AgSePh and can be performed by dissolving

silver chloride (AgCl) and triphenylphosphine (PPh_3) in dry tetrahydrofuran (THF) overnight. Then, a freshly prepared solution of lithium phenylselenolate (PhSeLi) is added at 0 °C before the reaction mixture is allowed to warm to room temperature and layered with diethyl ether. After a few days, crystalline AgSePh forms via slow diffusion of diethyl ether.

For the solution-phase synthesis, two protocols have been reported.[108,115] Both protocols employ silver nitrate ($AgNO_3$) as a starting material but differ in the source of organoselenium and solvent used. For the first protocol,[97] diphenyl diselenide (Ph_2Se_2) is dissolved in toluene and layered on top of an aqueous solution of $AgNO_3$, resulting in a biphasic reaction that slowly produces AgSePh microcrystals with the average size of 2 μm over a few days. Larger AgSePh microcrystals with a size of 5 μm can also be obtained within an hour by performing the reaction at 180 °C in a hydrothermal reactor.[107] On the other hand, the second protocol uses selenophenol (PhSeH), which can be dissolved along with $AgNO_3$ in a polar solvent mixture of water/ethanol.[108] While both protocols yield AgSePh microcrystals, larger microcrystals are still needed for investigation of their properties and incorporation in modern electronics.

The vapor-phase synthesis is by far the most attractive synthesis method of AgSePh as it allows a scalable production of AgSePh thin films for flexible electronics.[106,110,112] In this method, a silver film is transformed into a bright yellow film of AgSePh by interacting with Ph_2Se_2 vapor in a sealed container.[106] Alternatively, a silver oxide film and PhSeH vapor can be used to give the same result.[110]

Chapter 3 Synthetic Variation and Structural Trends in Layered Two-Dimensional Alkylammonium Lead Halide Perovskites

The basis of this chapter has been published as:

W. Paritmongkol, N.S. Dahod, A. Stollmann, N. Mao, C. Settens, S.-L. Zheng, W.A. Tisdale "Synthetic Variation and Structural Trends in Layered Two-Dimensional Alkylammonium Lead Halide Perovskites" ***Chem. Mater.*** 31, 5592-5607 (2019).

3.1 Introduction

Electronic and optical properties of perovskites are determined by their structure.[24,40,59,60,116] While the structural evolution of 3D LHPs and single-layered (n = 1) 2D LHPs with the absence of small A-site cations has been extensively investigated and shows interesting temperature-dependent transformations,[117–122] little is known about $n \geq 2$ 2D LHPs. This understanding has been hampered, in part, by the difficulty of synthesizing phase-pure variants of $n \geq 2$ 2D LHP single crystals.[59]

Herein, we report successful cooling-induced crystallization and structural evolution of $(C_4H_9NH_3)_2(MA)Pb_2I_7$, $(C_4H_9NH_3)_2(MA)_2Pb_3I_{10}$, $(C_4H_9NH_3)_2(MA)_3Pb_4I_{13}$, $(C_5H_{11}NH_3)_2(MA)Pb_2I_7$, $(C_6H_{13}NH_3)_2(MA)Pb_2I_7$, and $(C_4H_9NH_3)_2(FA)Pb_2I_7$. Henceforth, these chemical formulae will be abbreviated as n = 2 BA-MAPbI, n = 3 BA-MAPbI, n = 4 BA-MAPbI, n = 2 PA-MAPbI, n = 2 HA-MAPbI, and n = 2 BA-FAPbI, respectively. Here, BA, PA, and HA stand for butylammonium, pentylammonium, and hexylammonium, respectively. Optical absorption (Abs), photoluminescence (PL), and X-ray diffraction further confirm their chemical

compositions and structures. Moreover, we discuss factors that influence the phase purity of 2D LHP crystals and provide guidance for achieving 2D LHP crystals of desired composition.

Furthermore, structural dependence of 2D LHPs on quantum-well thicknesses, organic-spacer lengths, and A-site cations are discussed. We found that (i) there is a general trend of lower crystal symmetry as the temperature is reduced; (ii) PbI_6 octahedra on a surface (i.e., proximal to the organic-spacer layer) have higher distortion and tilting angles than their middle-layer counterparts; (iii) there is an alternation of axial Pb–I bond lengths, with terminal bonds being the shortest; (iv) there is a cohesive trend in the change of Pb–(μ-I)–Pb bond angles as the crystal symmetry is lowered; and (v) there are increases in the extents of interdigitation and corrugation tilts of organic-spacer molecules as 2D LHPs adopt their lower-temperature structures. Increasing the length of the organic-spacer molecule affects the number of phase transitions of $n = 2$ samples and the tilting angles of PbI_6 octahedra, while replacing the A-site cation from MA to FA has little effect on the structures–except in the tilting angles of the PbI_6 octahedra. In addition, structural distortion is used to explain PL peak shifts across phase transitions.

Finally, we conclude by further modification of the cooling-induced crystallization to prepare bromine-based 2D LHPs. Successful syntheses of $n = 1$ BA-PbBr, $n = 2$ BA-MAPbBr, and $n = 3$ BA-MAPbBr are reported, along with their Abs and PL spectra and powder X-ray diffraction (PXRD) patterns.

3.2 Syntheses of Iodide 2D LHPs

Iodide 2D LHPs were synthesized using a modified procedure based on the cooling-induced crystallization method[37,85,86] (Figure 3-1a). Detailed tables specifying reagent quantities and conditions used to synthesize each 2D LHP composition can be found in Table 3-1. Additional

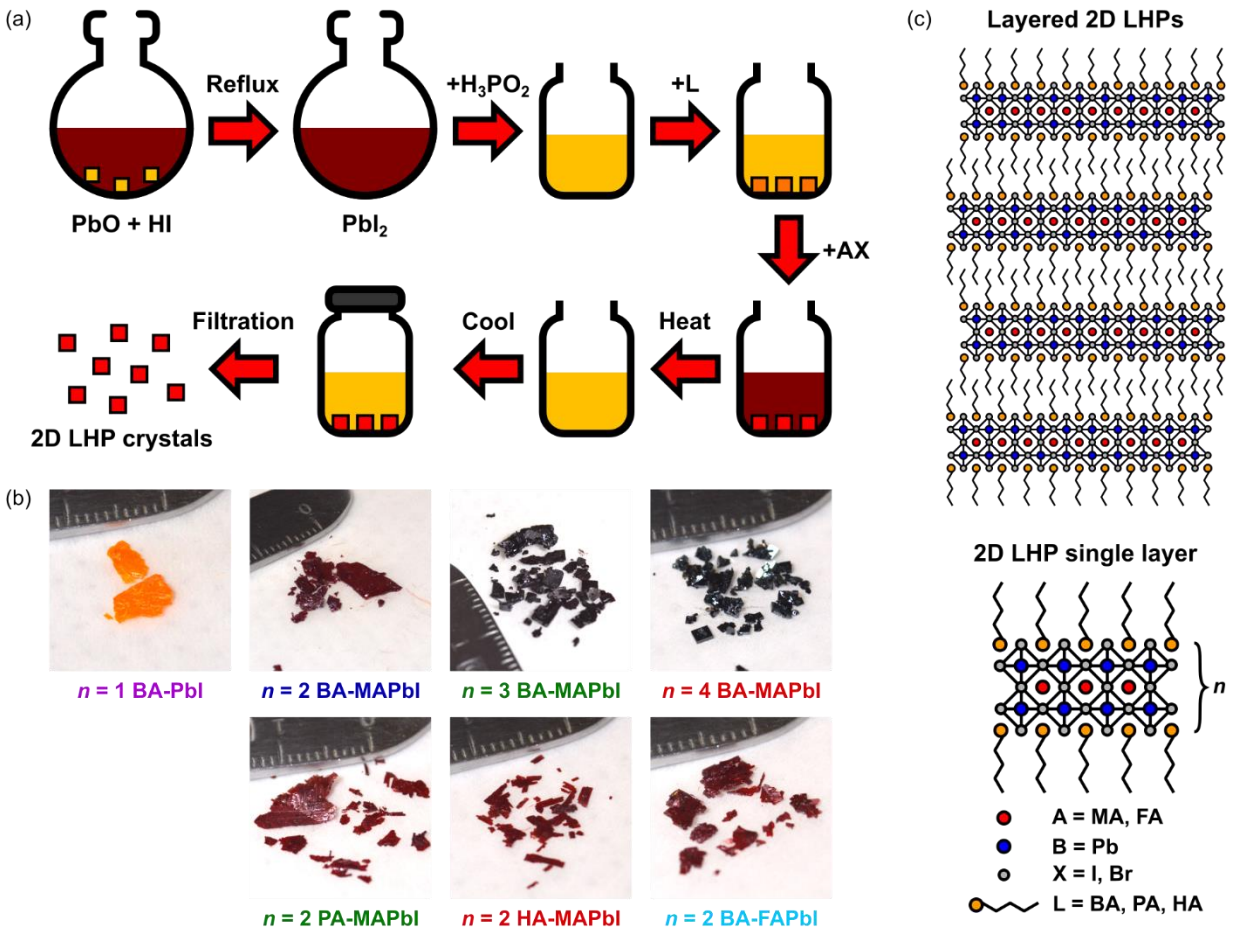

Figure 3-1. (a) Schematic describing cooling-induced crystallization of 2D lead halide perovskites (LHPs). (b) Photographs of 2D LHP crystals. The spacing between minor ticks on the ruler is 1 mm. (c) Schematic illustrations showing the structures of layered 2D LHPs and a 2D LHP single layer. MA = methylammonium; FA = formamidinium; BA = butylammonium; PA = pentylammonium; HA = hexylammonium.

procedural details are included in Session 3.9. Briefly, a large volume of lead (II) iodide (PbI_2) solution was prepared by the reaction of lead (II) oxide (PbO) and 55% hydrogen iodide (HI) solution under reflux. A small volume of PbI_2 solution was then transferred into a vial, and hypophosphorus acid (H_3PO_2) was added to reduce any residual iodine (I_2) back to HI. After a few seconds, the solution turned bright yellow. Next, the long chain organic cation (L) was added, forming an orange precipitate of n = 1 L-PbI. To make thicker members of the iodide 2D LHP family (n > 1), a solution of the A-site cation iodide (AI) salt was prepared in a separate vial by

Table 3-1. Reagent quantities used for iodide 2D LHP syntheses.

	n **= 1 BA-PbI**	***n*** **= 2 BA-MAPbI**	***n*** **= 3 BA-MAPbI**	***n*** **= 4 BA-MAPbI**	***n*** **= 2 PA-MAPbI**	***n*** **= 2 HA-MAPbI**	***n*** **= 2 BA-FAPbI**
PbO mass (g)	0.558	0.558	0.558	0.558	0.558	0.279	0.558
Number of moles of PbO (mmol)	2.5	2.5	2.5	2.5	2.5	1.25	2.5
HI volume to make PbI_2 solution (mL)	3	3	3	3	3	1.5	3
H_3PO_2 volume (µL)	425	425	425	425	425	213	425
AI mass (g)	-	0.1987	0.2650	0.2981	0.1987	0.1739	0.2150
Number of moles of AI (mmol)	-	1.25	1.67	1.875	1.25	1.09	1.25
AI% w.r.t. stoichiometric amount	-	100	100	100	100	175	100
HI volume to make AI solution (mL)	-	0.75	0.75	0.75	0.75	1	0.75
L volume (µL)	247	161	107	49	174	83	161
Number of moles of L (mmol)	2.5	1.625	0.997	0.5	1.5	0.625	1.625
L% w.r.t. stoichiometric amount	50	65	65	40	60	50	65
Additional volume of HI added to the combined solution	5	0	0	0	0.25	0	0.75
Total volume of HI used (mL)	8	3.75	3.75	3.75	4	2.5	4.5

dissolving the salt into HI. This AI solution was subsequently added into the solution containing the orange precipitate. This combined solution was then heated until clear, and slowly cooled to produce crystals of iodide 2D LHPs. The crystals were then collected by suction filtration and dried under reduced pressure. Photographs of crystals obtained by this method are shown in Figure 3-1b.

We found that controlling relative quantities of reagents was the key to obtaining pure crystals. Deviating from the optimal concentrations in the starting solutions resulted in crystals containing impurities of thicker (e.g., $n + 1$) and/or thinner (e.g., $n - 1$) iodide 2D LHPs. Because of the differences in solubilities among different reagents, each solidifies at a different rate and at a different temperature during cooling. Consequently, the optimal starting concentrations are not simply the stoichiometric amounts found from the chemical formulae of iodide 2D LHPs; to obtain pure crystals of the desired iodide 2D LHPs, the precipitation rates of precursors must be balanced, which can be achieved by adjusting concentrations.

The overall effect of changing long chain organic-spacer concentrations can be predicted from the chemical formulae of iodide 2D LHPs. As we go from $n = 1$ iodide 2D LHP to bulk LHP, the L:Pb ratio decreases from 2:1 to 0:1. This decrease suggests that the higher concentration of long-chain organic cation favors the formation of thinner (lower-n) iodide 2D LHPs, which was indeed observed experimentally (Figure 3-2a). The long-chain organic spacer is the least soluble component of the reaction mixture and is the first to precipitate as the solution is cooled. When a stoichiometric amount of long-chain organic spacer was used, a complete crystallization of orange $n = 1$ iodide 2D LHP or thinner (i.e. $n - 1$) iodide 2D LHPs was observed. Consequently, the

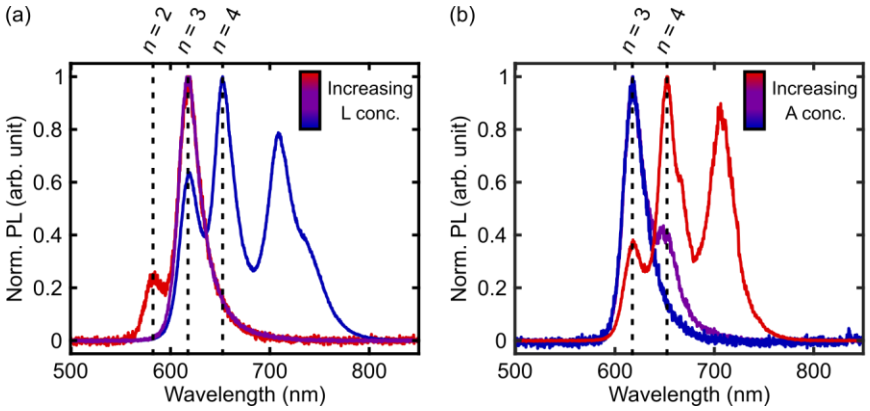

Figure 3-2. (a) Photoluminescence spectra showing the effect of organic spacer (L) concentration. In this experiment, we attempted to synthesize pure n = 3 BA-MAPbI. If the L concentration is too low, photoluminescence peaks due to n = 4 BA-MAPbI and higher members appear. On the other hand, if the L concentration is too high, photoluminescence peak due to n = 2 BA-MAPbI is observed. (b) Photoluminescence spectra showing the effect of A-site cation concentration. In this experiment, we attempted to synthesize pure n = 3 BA-MAPbI. If the A-site cation concentration is too high, photoluminescence peaks due to n = 4 BA-MAPbI and higher members appear.

amount of long chain organic spacer used in our synthesis was always kept below that predicted from stoichiometry (Table 3-1).

Because the solubility of the long-chain organic spacer in HI decreases with increasing alkylammonium chain length, decreasing concentrations are needed as the chain length increases. The percentages of long-chain organic spacers used with respect to their stoichiometric amounts for making *n* = 2 BA-MAPbI, *n* = 2 PA-MAPbI, and *n* = 2 HA-MAPbI decreased from 65 to 60 to 50%, respectively (Table 3-1). The trend in solubility also affects the crystal shape. As HA is the least soluble among the three organic spacers, it precipitated out fastest during cooling–resulting in thinner, smaller crystals. On the other hand, large crystals with lateral sizes of up to 5 mm of *n* = 2 BA-MAPbI and *n* = 2 PA-MAPbI (Figure 3-1b) could be obtained easily with this method. These crystals were large enough that lamellar structure is evident in macroscale morphology. This observation agrees with the reflections along the (*h*00) planes in X-ray diffraction data as reported previously[37,82] and shown again in this work.

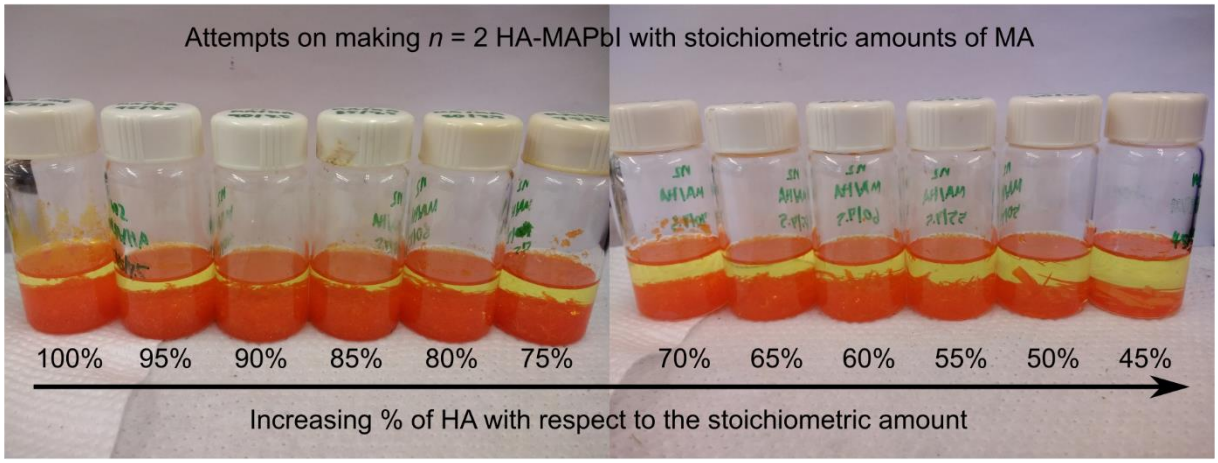

Figure 3-3. Crystals of n = 1 HA-PbI obtained as the main products from the syntheses of n = 2 HA-MAPbI with 100% of MA stoichiometric amounts. Regardless of the amounts of HA used, only the orange crystals of n = 1 HA-PbI were yielded.

Thicker (higher-n) 2D LHPs can be obtained by decreasing the concentration of the long-chain organic spacer in the reaction mixture. The optimal percentage of long-chain organic spacer with respect to the stoichiometrically required amount shows a downward trend (Table 3-1) because of higher solubility of the A-site cation and lower solubility of long-chain organic spacer. We found that fixing the percentage of long-chain organic spacer while changing n results in thinner (e.g. $n - 1$) impurities.

The effect of changing A-site cation concentration can be similarly understood. We observed that increasing the concentration of the A-site cation favors the formation of thicker (higher-n) iodide 2D LHPs (Figure 3-2b). In most of our syntheses, stoichiometric amounts of A-site cations were used. However, because of the low solubility of HA, a more saturated solution of MA – more MA in the starting mixture – was needed to match the precipitation rate of HA. As a result, 175% of MA stoichiometric amount was needed to form phase-pure n = 2 HA-MAPbI. When a stoichiometric amount of MA was used, orange crystals of n = 1 iodide 2D LHP were observed to be the main products, regardless of the initial concentration of HA (Figure 3-3).

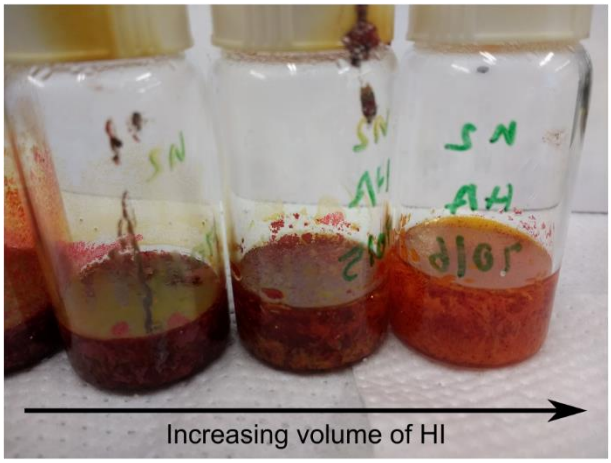

Figure 3-4. Picture of crystals in solutions showing the effect of HI volume to the synthesis products. When a small volume of HI is used, a crowded solution of n = 2 HA-MAPbI (cherry red crystals) is obtained. As the volume of HI increases, the solution is less crowded but the main products become orange crystal of n = 1 HA-PbI.

Adjusting the total volume of HI also affected the quality of the final crystallization product. We found that a small volume of HI often resulted in mixed-phase iodide 2D LHPs and crowded solutions with small crystals, whereas increasing HI volume promoted the formation of larger crystals. However, when too much HI was added, the A-site cation did not precipitate out of solution, resulting in the formation of n = 1 iodide 2D LHP crystals (Figure 3-4). We also found that greater HI volume (per gram of PbO) was needed for the weakly-soluble longer-chain organic spacers. When tuning n, HI volume was kept the same to minimize the number of changing parameters (Table 3-1).

When the A-site cation was changed from MA to FA or Cs, additional difficulties emerged. In the case of the FA cation, the precipitation rate was found to be faster, and the resulting crystal sizes tended to be smaller. To grow larger crystals of high-purity n = 2 BA-FAPbI, the volume of HI was increased relative to the amounts of other reagents. Attempts to synthesize n > 2 BA-FAPbI were unsuccessful; formation of n = 2 BA-FAPbI was always observed, regardless of how the

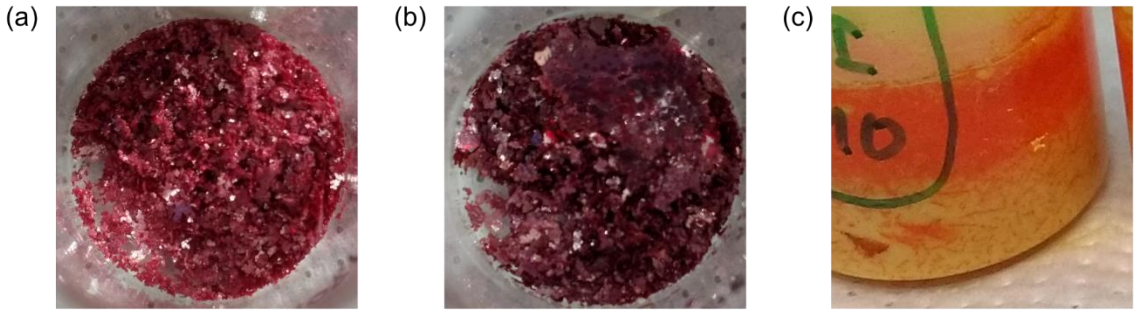

Figure 3-5. (a-b) Ruby-red crystals of n = 2 BA-FAPbI formed as the main products of the attempted syntheses of n = 3 BA-FAPbI (a) and n = 4 BA-FAPbI (b). (c) White solid of CsI and orange crystals of n = 1 BA-PbI were yielded from the attempted synthesis of n = 2 BA-CsPbI.

synthesis conditions were varied (Figure 3-5a and 3-5b). This observation suggests that n = 2 BA-FAPbI might be the most thermodynamically stable product among the iodide 2D LHPs with FA cations.[24] Similar observations have been reported in the case of n = 5 BA-MAPbI, which undergoes disproportionation to form n = 3 BA-MAPbI and bulk $MAPbI_3$.[86] Finally, we note that attempts to synthesize iodide 2D LHPs with Cs cation were unsuccessful because of the poor solubility of CsI in HI. These attempts resulted in a mixture of white CsI solid and orange n = 1 BA-PbI 2D LHP (Figure 3-5c).

In general, we observed some seasonal variation in the synthesis product. During high-humidity seasons, needlelike crystals with yellow color emerged as a by-product (Figure 3-6). Because of the shape and color of this byproduct, it may be a water complex such as $MAPbI_3 \cdot H_2O$[123,124] or $(MA)_4PbI_6 \cdot H_2O$.[124–127] Comparison of its PXRD pattern to known structures of candidate compounds in the Cambridge Crystallographic Data Center are shown in Figure 3-7. The formation of these unknown crystals could be avoided by slightly increasing the AX fraction by approximately 5%.

Figure 3-6. Picture of n = 2 BA-MAPbI crystals with yellow, needlelike crystal byproducts.

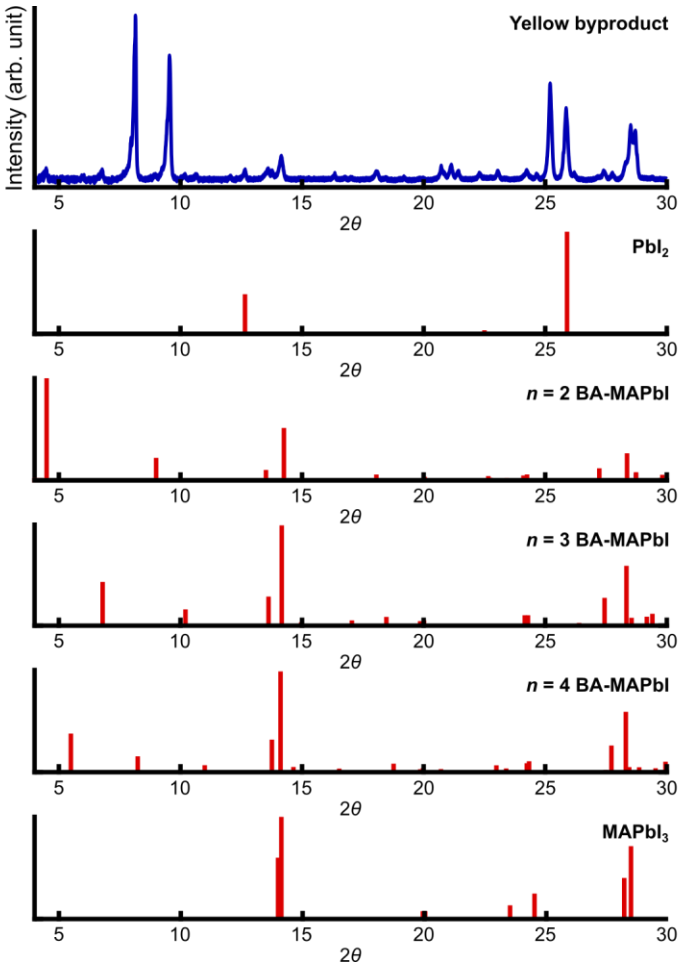

Figure 3-7. Powder X-ray diffractogram of the yellow, needlelike crystal byproduct, and simulated X-ray diffraction patterns of PbI_2, n = 2 BA-MAPbI, n = 3 BA-MAPbI, n = 4 BA-MAPbI, and $MAPbI_3$.

3.3 Stability of Iodide 2D LHP Crystals and Exfoliated Flakes

All of the iodide 2D LHP crystals synthesized by this method were stable to storage inside a N_2 glovebox for more than 1 year (Figure 3-8). Additionally, the large crystals shown in Figure 3-1b could be mechanically exfoliated to form thin 2D LHP flakes (Figure 3-9; see Section 3.9). However, when the crystals were exfoliated and kept under ambient conditions, newly generated surfaces underwent a transition after ~3 days to form a yellow solid (Figure 3-10). We hypothesize that because the interaction between the long-chain organic spacer and the lead halide octahedra has a hydrogen-bonding character,[128] the long-chain organic spacer can be easily stripped off

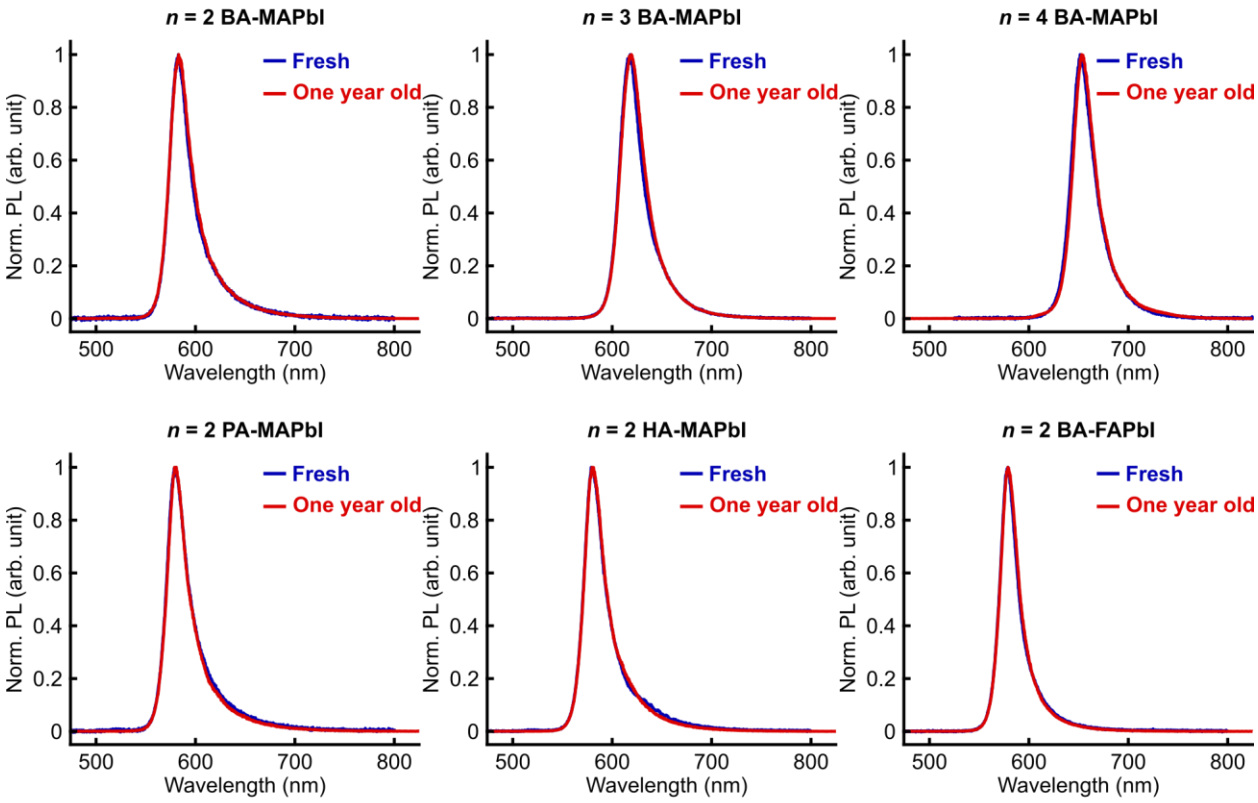

Figure 3-8. Effect of storage in N_2 glovebox: photoluminescence spectra of fresh and one-year-old samples of n = 2 BA-MAPbI, n = 3 BA-MAPbI, n = 4 BA-MAPbI, n = 2 PA-MAPbI, n = 2 HA-MAPbI, and n = 2 BA-FAPbI. The one-year-old samples were stored in a N_2 glovebox with <10 ppm O_2 and <1 ppm H_2O.

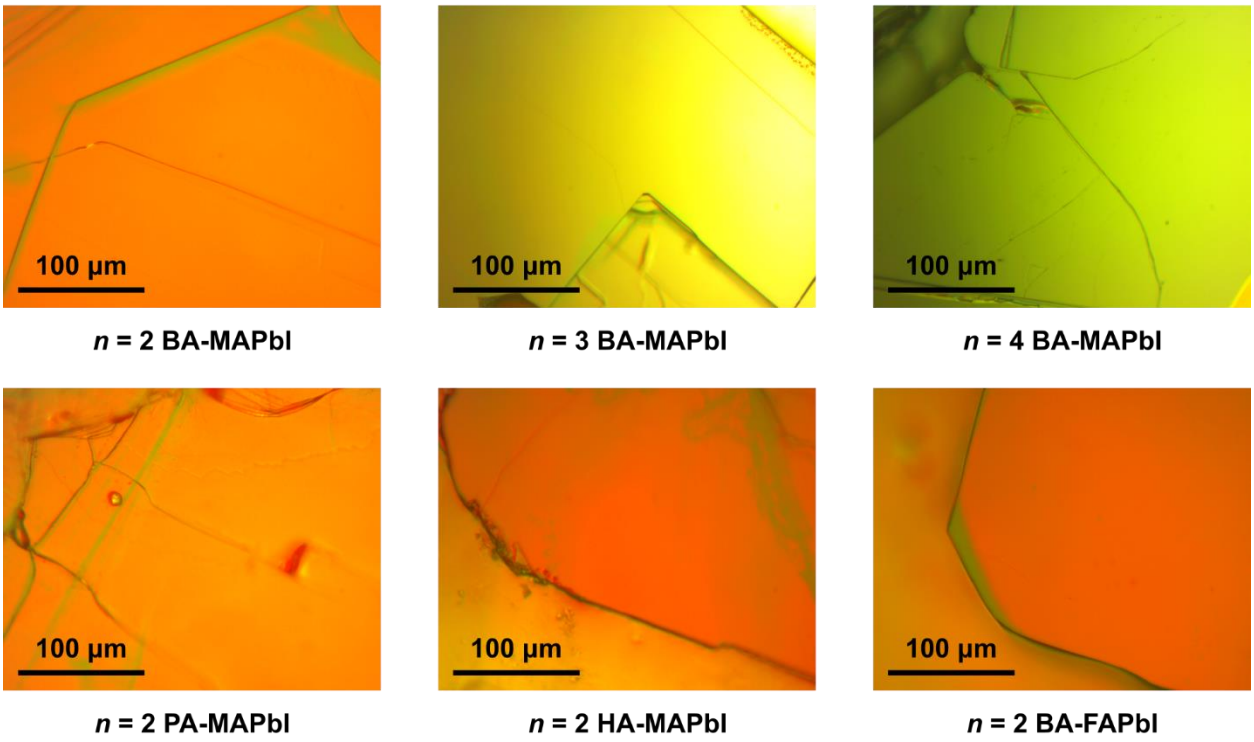

Figure 3-9. Bright-filed micrographs of exfoliated flakes of 2D LHPs

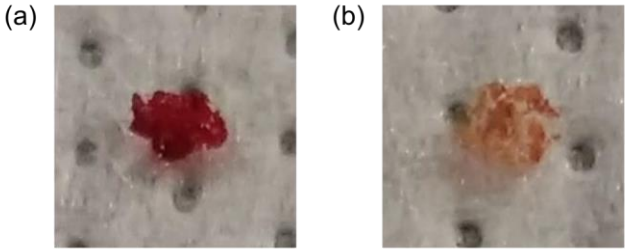

Figure 3-10. (a) Newly exfoliated flake of *n* = 2 HA-MAPbI. (b) The same exfoliated flake after storing under ambient conditions for 3 days.

during exfoliation. The newly exposed surface is unprotected and susceptible to attack from H_2O and O_2 in the air to form PbI_2. This hypothesis was tested by storing exfoliated crystals either in inert atmosphere or in oil. No apparent color change was observed under either condition (in the case of oil, the experiment was performed for 1 week). These observations suggest that the stability of exfoliated 2D LHP flakes could be further improved through encapsulation by a polymer layer[129,130] or another 2D material, such as hexagonal boron nitride.[16,129,131–133]

3.4 Optical Characterization of Iodide 2D LHP Crystals

Room-temperature Abs and PL spectra of exfoliated iodide 2D LHPs are shown in Figure 3-11. All variants exhibit a single sharp excitonic absorption resonance 100–500 meV below the

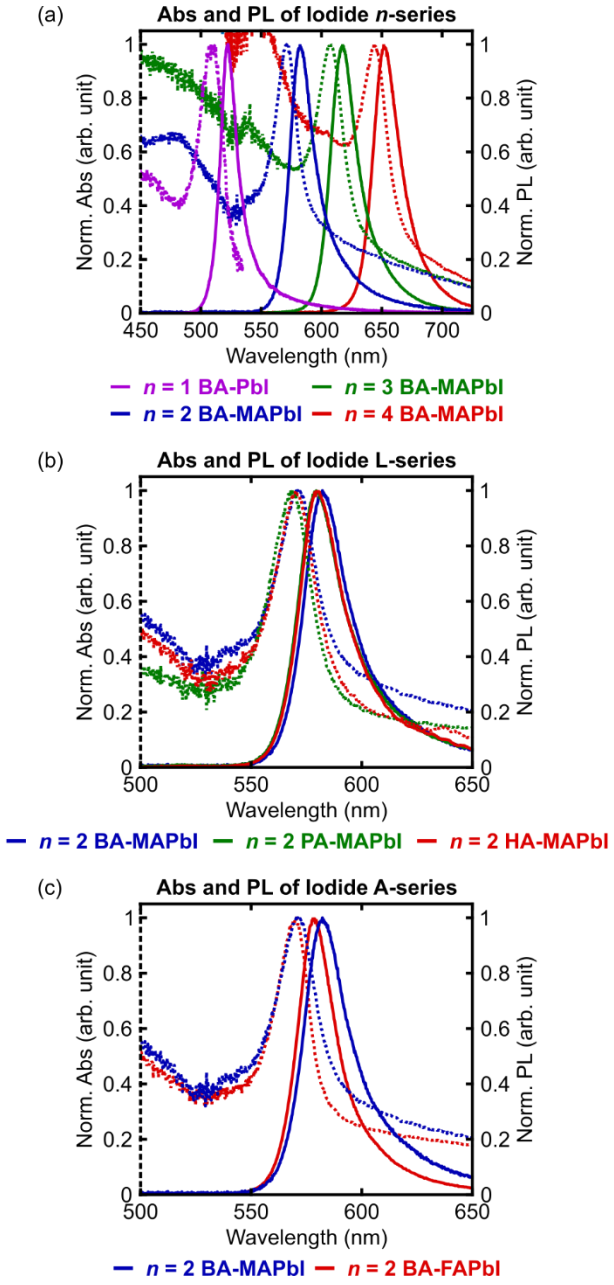

Figure 3-11. Abs (dotted) and PL (solid) spectra of exfoliated 2D LHP flakes at room temperature. Comparisons are shown for (a) $n = 1$ BA-PbI, $n = 2$ BA-MAPbI, $n = 3$ BA-MAPbI, and $n = 4$ BA-MAPbI; (b) $n = 2$ BA-MAPbI, $n = 2$ PA-MAPbI, and $n = 2$ HA-MAPbI; and (c) $n = 2$ BA-MAPbI and $n = 2$ BA-FAPbI.

Table 3-2. Summary of absorption (Abs) peak wavelengths, photoluminescence (PL) peak wavelengths, PL full width at half-maxima (FWHM), and Stokes shifts of iodide and bromide 2D LHP crystals.

Sample	Abs peak wavelength (nm)	PL peak wavelength (nm)	PL fwhm (nm)	Stokes shift (nm)
n = 1 BA-PbI	508±1	522±1	17±2	14±2
n = 2 BA-MAPbI	571±1	582±1	25±2	11±2
n = 3 BA-MAPbI	607±1	617±1	27±2	10±2
n = 4 BA-MAPbI	643±1	652±1	27±2	9±2
n = 2 PA-MAPbI	569±1	579±1	25±2	10±2
n = 2 HA-MAPbI	570±1	580±1	25±2	10±2
n = 2 BA-FAPbI	570±1	578±1	21±2	8±2
n = 1 BA-PbBr	406±1	418±1	17±2	12±2
n = 2 BA-MAPbBr	436±1	445±1	17±2	9±2
n = 3 BA-MAPbBr	456±1	466±1	16±2	10±2

continuum band and Stokes-shifted emission close in energy to the 1s excitonic absorption feature. 2D alkylammonium LHPs exhibit large exciton binding energies (470 meV for *n* = 1 butylammonium lead iodide) because of spatial confinement of electrons and holes within the 2D inorganic lattice and low dielectric screening from the long-chain organic-spacer layer.[18] Increasing *n* red-shifts the excitonic resonance in both Abs and PL spectra (Figure 3-11a). These shifts are the result of two partially offsetting factors: quantum confinement, which widens the electronic band gap as *n* decreases, and dielectric confinement, which leads to an increase in exciton binding energy as *n* decreases–thereby reducing the magnitude of the overall blue shift. The *n* = 2–4 samples show similar PL full width at half-maximum (FWHM) of 25–27 nm, as well as similar Stokes shifts of ~10 nm (Table 3-2). In contrast, the *n* = 1 sample shows a narrower PL FWHM of 17 ± 2 nm.

For the *n* = 2 iodide samples, Abs and PL spectra were largely unaffected when the organic-spacer length increased from four to six carbons (Figure 3-11b). All samples showed Abs peaks

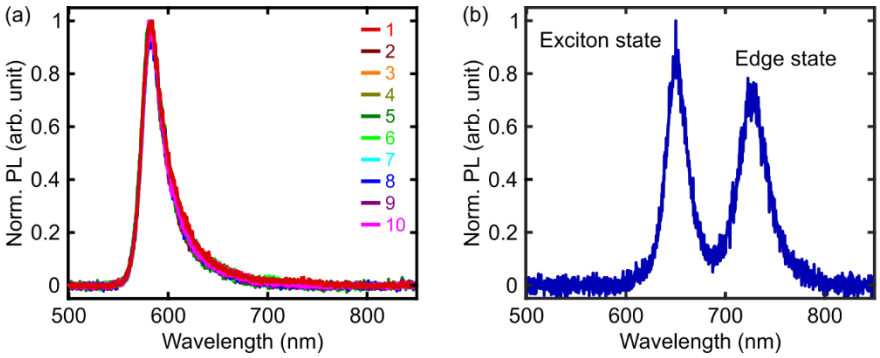

Figure 3-12. (a) Photoluminescence spectra obtained at different locations on a high-purity sample of n = 2 BA-MAPbI. All spectra show single emission peaks without impurity emission from iodide 2D LHPs with other quantum-well thicknesses. (b) A photoluminescence spectrum of n = 4 BA-MAPbI showing emission due to an exciton and an edge state.

centered near ~570 nm, PL peaks centered near ~580 nm, PL fwhm of ~25 nm, and Stokes shift of ~10 nm (Table 3-2). However, when the A-site cation was changed from MA to FA (Figure 3-11c), the PL FWHM decreased from 25 ± 2 nm to 21 ± 2 nm.

The observation of single Abs and PL peaks in each sample also indicates the high purity of these samples. Occasionally, when checking PL from multiple locations under a microscope, regions exhibiting PL from thicker (e.g., n + 1) or thinner (e.g., n − 1) iodide 2D LHPs could be observed. These observations were rare in high-purity samples (Figure 3-12a), and phase impurity was not detected by PXRD (Section 3.5). However, red-shifted emission attributed to edge states[130,134] (Figure 3-12b) could be observed under air exposure, in agreement with the report from Dou et al.[130]

3.5 Structural Insights from PXRD

Initial structural characterization was performed using PXRD on finely ground crystals (Figures 3-13a, 3-13b, and 3-13c). All samples showed (111) peaks near 14° 2θ angle and characteristic stacking peaks of 2D layered materials, which manifest as periodic (h00) diffraction peaks in the PXRD pattern.[85] Below the (111) peak, we observe either two, three, four, or five of

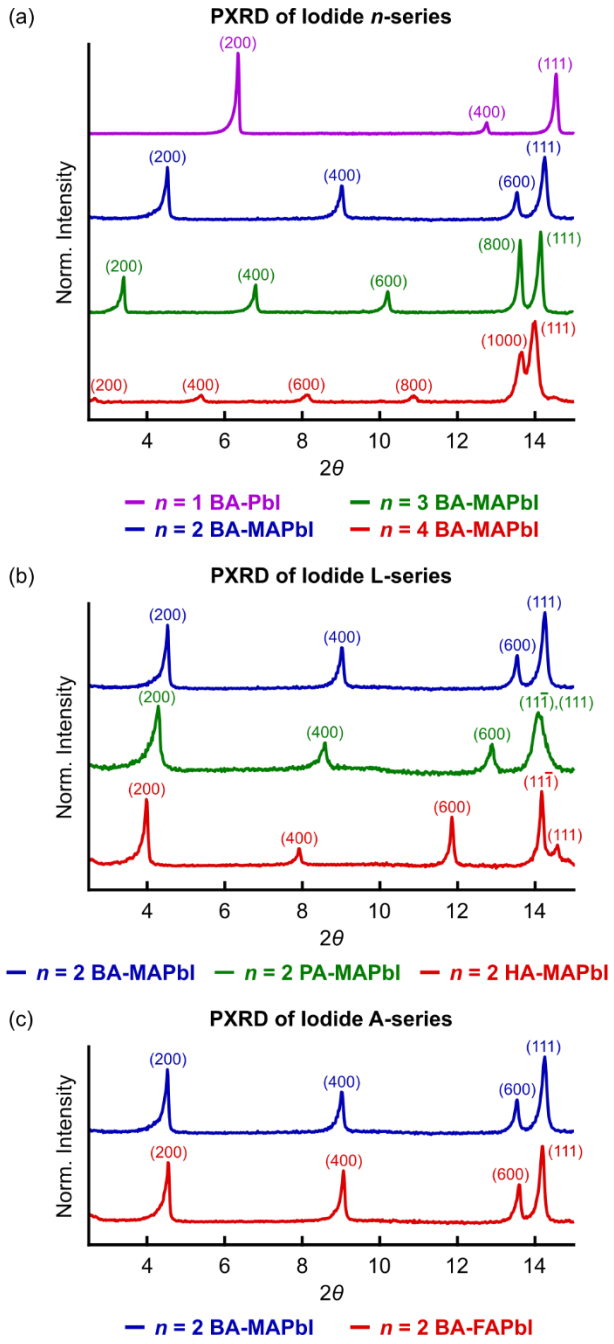

Figure 3-13. Powder X-ray diffractograms of (a) iodide *n*-series, (b) iodide L-series, and (c) iodide A-series. All peaks are labeled with their corresponding diffraction planes. Evenly spaced (*h*00) peaks correspond to the periodicity in the stacking direction.

the evenly spaced (*h*00) reflections for samples with BA organic spacer and n = 1, 2, 3, and 4, respectively (Figure 3-13a).[85] The increasing number of reflections in this region indicates a larger unit cell parameter along the stacking direction, and this number can be used to confirm the value

of *n* and the purity of the samples. When the organic spacer is lengthened from four to five and six carbons, the evenly spaced reflections shift to lower 2θ angles (Figure 3-13b), reflecting the larger spacing distances in samples with longer alkylammonium chains. On the other hand, the substitution of A-site cation from MA to FA does not induce a significant change in the PXRD patterns as shown in Figure 3-13c.

Using the positions of (*h*00) reflections, the stacking period of each iodide 2D LHP can be calculated. The stacking periods of *n* = 1 BA-PbI, *n* = 2 BA-MAPbI, *n* = 3 BA-MAPbI, and *n* = 4 BA-MAPbI were deduced to be 1.39, 1.96, 2.60, and 3.22 nm, respectively. This incremental increase of ~0.6 nm corresponds to the thickness of an additional PbI_6 octahedral layer as *n* increases.[37,85] Using the same approach, stacking periods of *n* = 2 PA-MAPbI and *n* = 2 HA-MAPbI were found to be 2.07 and 2.25 nm, larger than that of *n* = 2 BA-MAPbI by 0.11 and 0.29 nm, respectively. This non-stepwise increase as the alkylammonium chain length increases is due to the different extents of interdigitation in the organic-spacer layers as the organic-spacer length is changed, as determined by single-crystal X-ray diffraction (SCXRD – see Section 3.6). When changing the A-site cation from MA to FA, the stacking period remained constant at 1.96 nm. This is not surprising, as MA and FA have similar ionic radii of 2.70 and 2.79 Å, respectively.[135]

In addition to the shifts in the stacking peaks, changing sample identities can lead to a similar effect on the position of the (111) peak. As the period of the (111) planes is influenced by the unit cell parameter in the stacking direction, increasing *n* results in the (111) peaks move to lower 2θ angles (Figure 3-13a). When the organic-spacer molecule is changed from BA to PA and HA, the (111) peak starts to split into two peaks of (111) and (11$\bar{1}$) reflections (Figure 3-13b). This split arises from the fact that *n* = 2 BA-MAPbI, *n* = 2 PA-MAPbI, and *n* = 2 HA-MAPbI have different crystal symmetries: *n* = 2 BA-MAPbI adopts orthorhombic *Cmcm*, but *n* = 2 PA-MAPbI and *n* =

2 HA-MAPbI adopt monoclinic *C*2/*c* at room temperature. Similar to the effect on the stacking peaks, replacing MA by FA has a marginal effect on the (111) peak position (Figure 3-13c).

Temperature-dependent PXRD below room temperature was then performed to find the phase transitions of the samples. The data (Figures 3-14 – 3-20) show that (i) n = 2 BA-MAPbI, n = 3 BA-MAPbI, and n = 4 BA-MAPbI have two phase transitions below room temperature; (ii) n = 2 BA-FAPbI has one phase transition below room temperature; and (iii) n = 2 PA-MAPbI and n = 2 HA-MAPbI have no phase transition below room temperature. The higher-temperature phase transitions of n = 2 BA-MAPbI, n = 3 BA-MAPbI, and n = 4 BA-MAPbI fall between 280 and 290 K, and the phase transition of n = 2 BA-FAPbI happens at a slightly lower-temperature range between 266 and 280 K. Recent work from our group[136] described these phase transitions as partial melting transitions of the organic spacer layers, similar to what has been observed in n = 1 2D LHPs.[137] Using differential scanning calorimetry (DSC), we assigned the phase-transition temperatures to be 283 K for n = 2 BA-MAPbI, 282 K for n = 3 BA-MAPbI, 283 K for n = 4 BA-MAPbI, and 268 K for n = 2 BA-FAPbI. We also showed that n = 2 PA-MAPbI and n = 2 HA-MAPbI exhibit analogous phase transitions at 351 and 369 K, respectively. These phase-transition temperatures agree with recently published data from Kanatzidis and co-workers.[88,90] On the other hand, the temperatures of the lower-temperature phase transitions of n = 2 BA-MAPbI, n = 3 BA-MAPbI, and n = 4 BA-MAPbI have a decreasing trend with ~186–196 K for n = 2 BA-MAPbI, ~156–176 K for n = 3 BA-MAPbI and ~136–146 K for n = 4 BA-MAPbI. Recent work by Kanatzidis and co-workers[90] has suggested that this lower-temperature phase transition corresponds to a structural change to a triclinic structure and its behavior is similar to the transition from β-phase to γ-phase in bulk $MAPbI_3$.

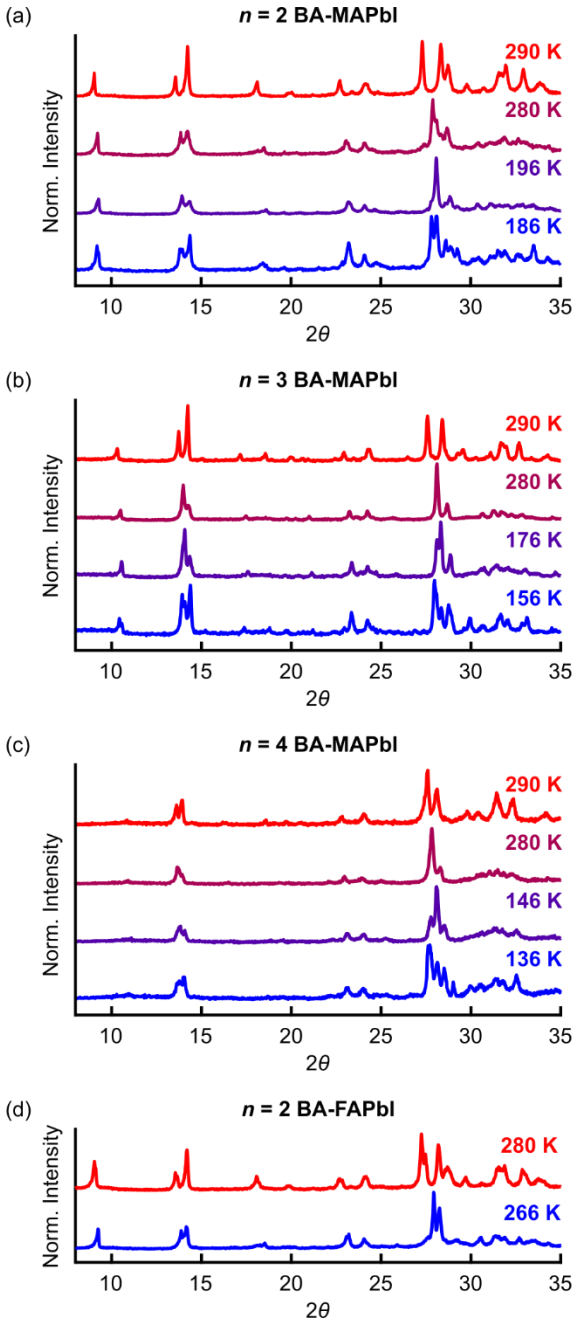

Figure 3-14. Selected temperature-dependent powder X-ray diffractograms showing the phase transitions in (a) $n = 2$ BA-MAPbI, (b) $n = 3$ BA-MAPbI, (c) $n = 4$ BA-MAPbI, and (d) $n = 2$ BA-FAPbI.

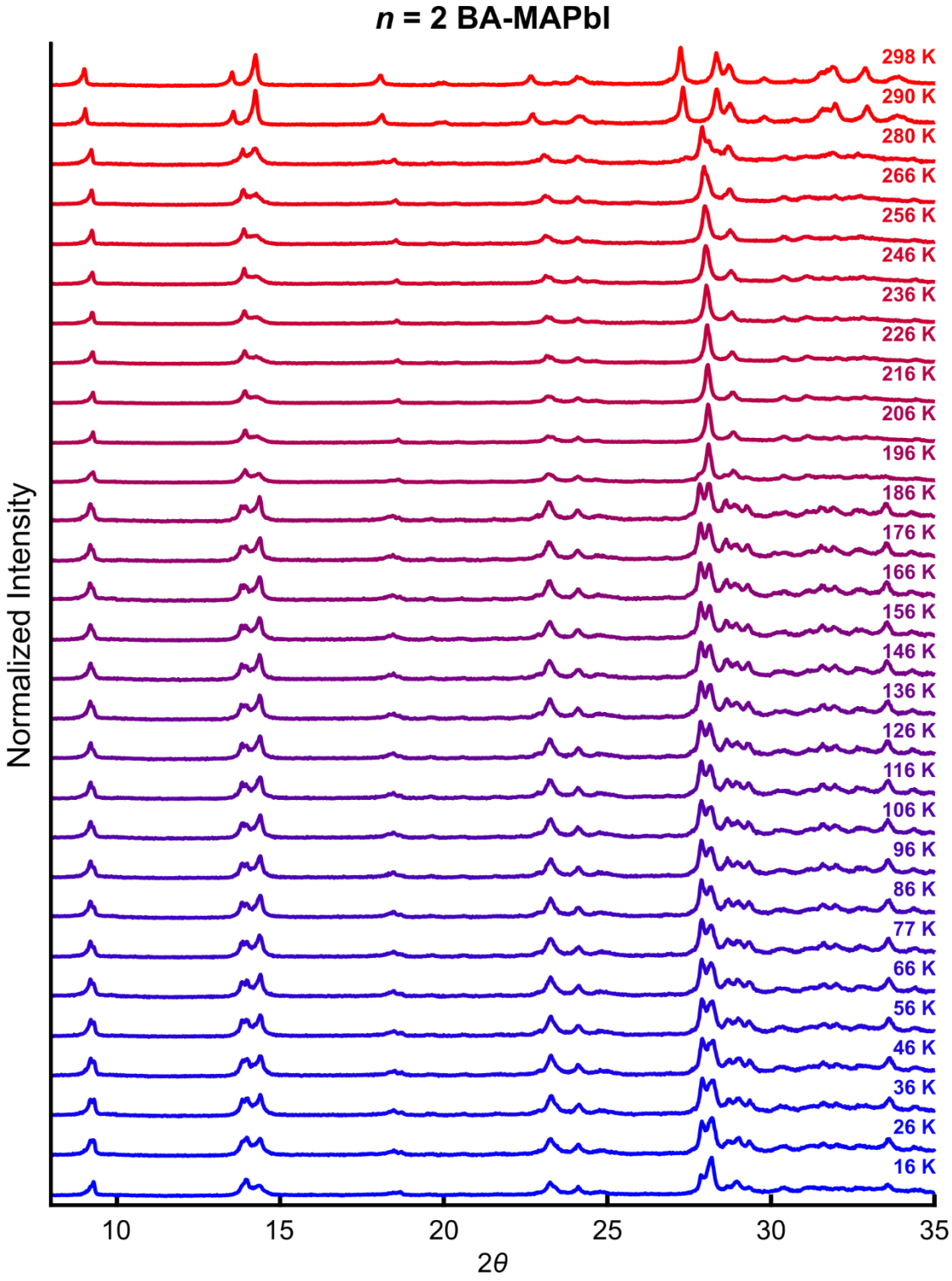

Figure 3-15. Temperature-dependent powder X-ray diffractograms of *n* = 2 BA-MAPbI between 16 K and 298 K.

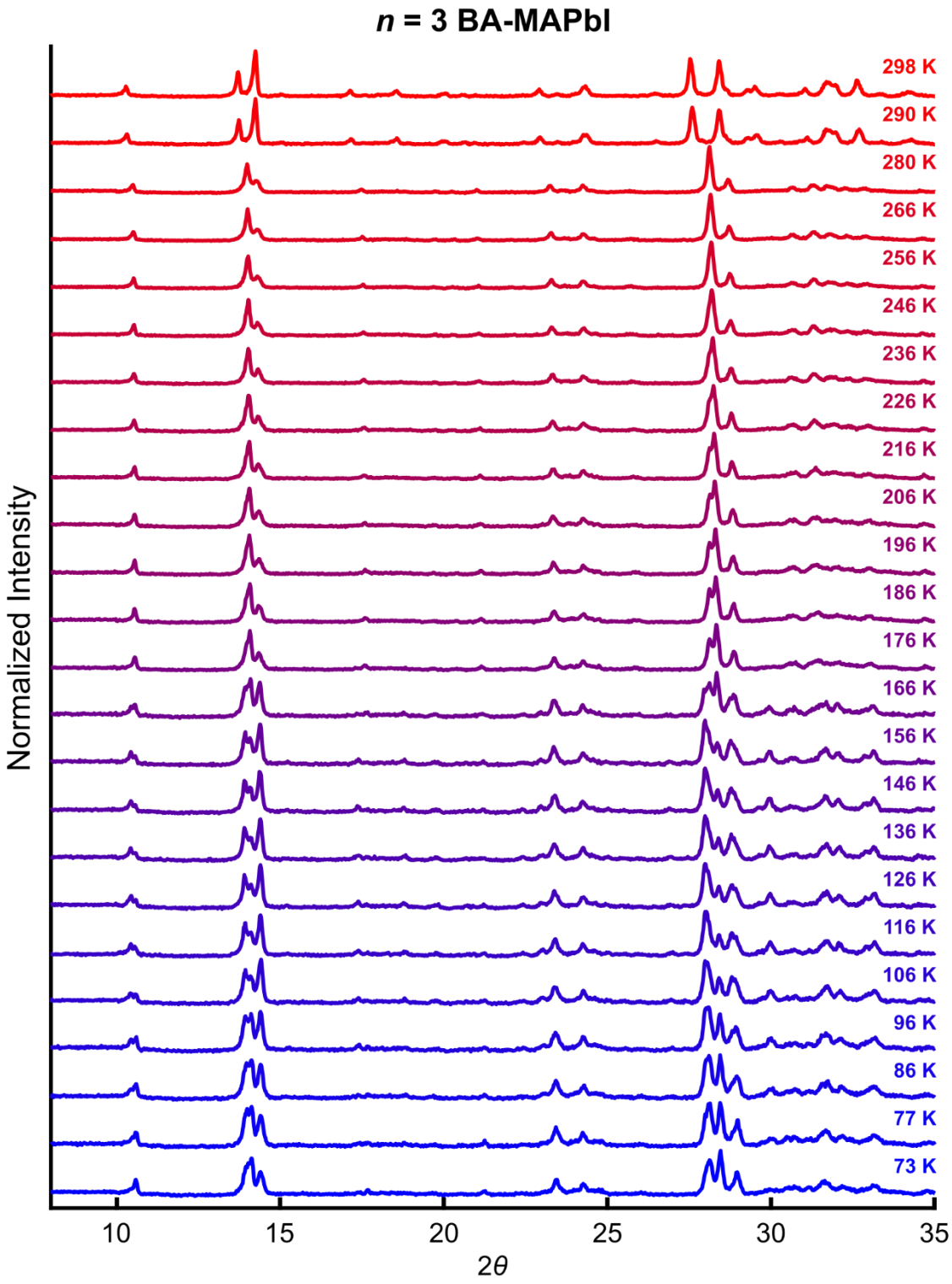

Figure 3-16. Temperature-dependent powder X-ray diffractograms of n = 3 BA-MAPbI between 73 K and 298 K.

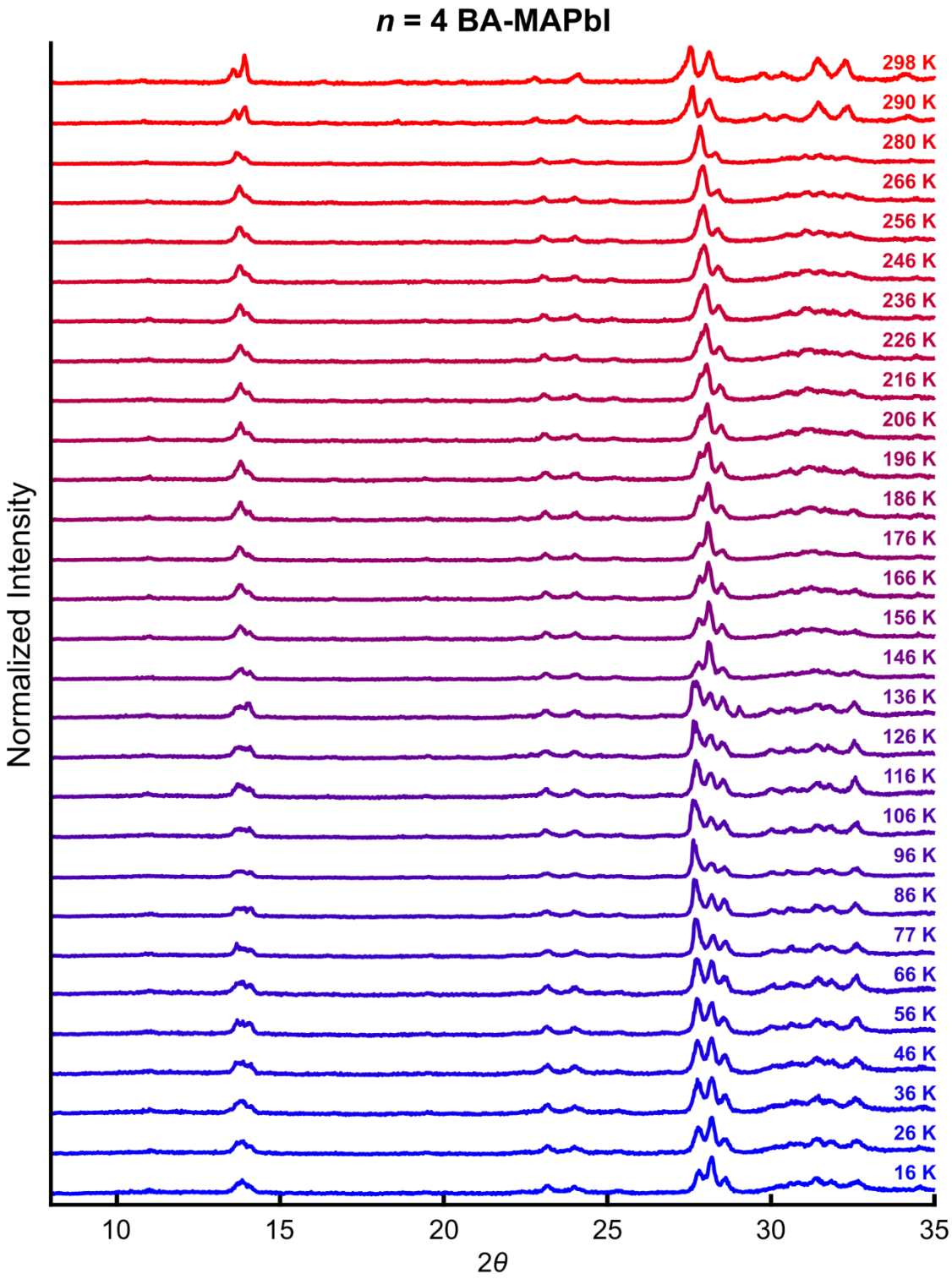

Figure 3-17. Temperature-dependent powder X-ray diffractograms of n = 4 BA-MAPbI between 16 K and 298 K.

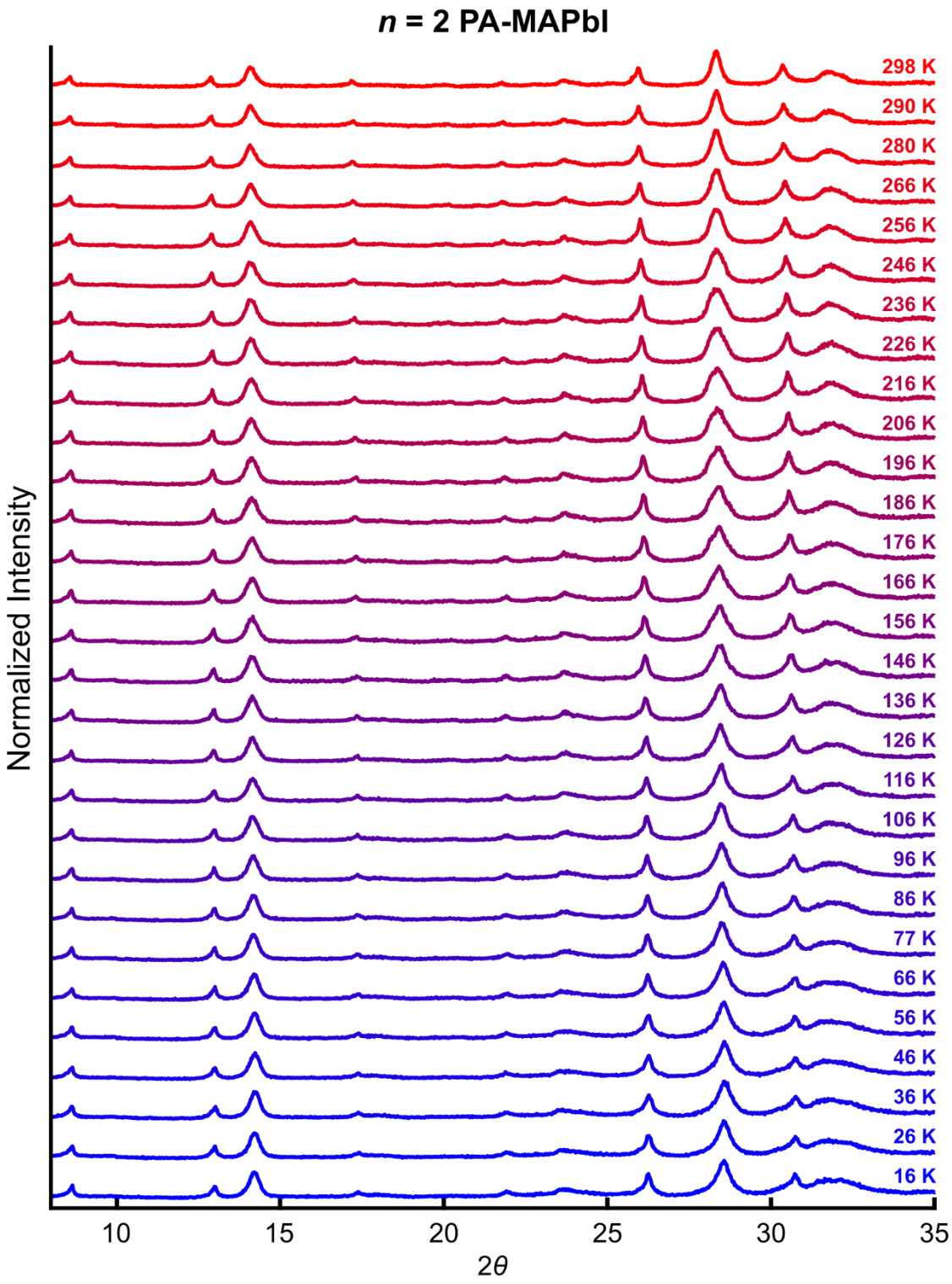

Figure 3-18. Temperature-dependent powder X-ray diffractograms of n = 2 PA-MAPbI between 16 K and 298 K.

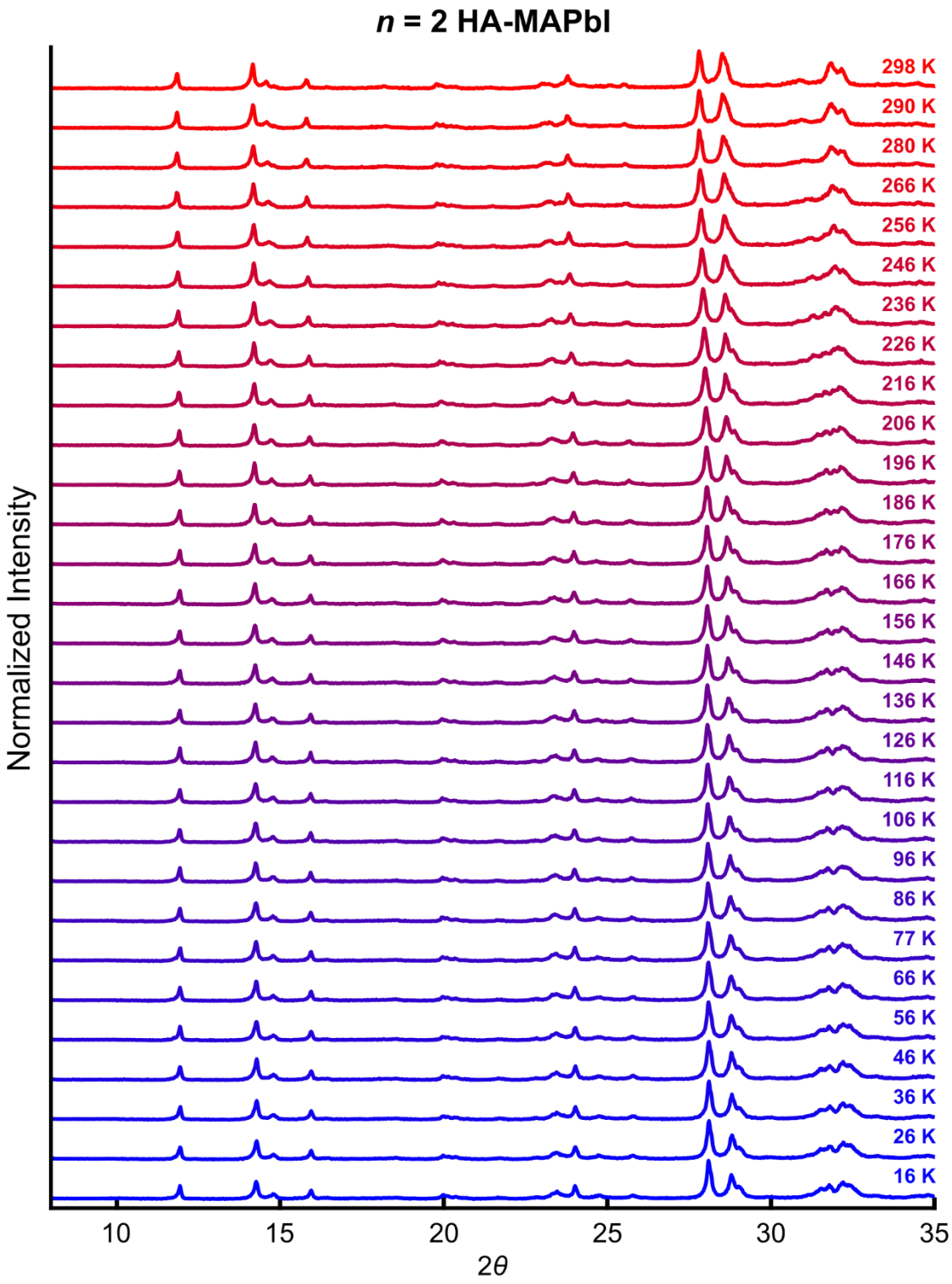

Figure 3-19. Temperature-dependent powder X-ray diffractograms of n = 2 PA-MAPbI between 16 K and 298 K.

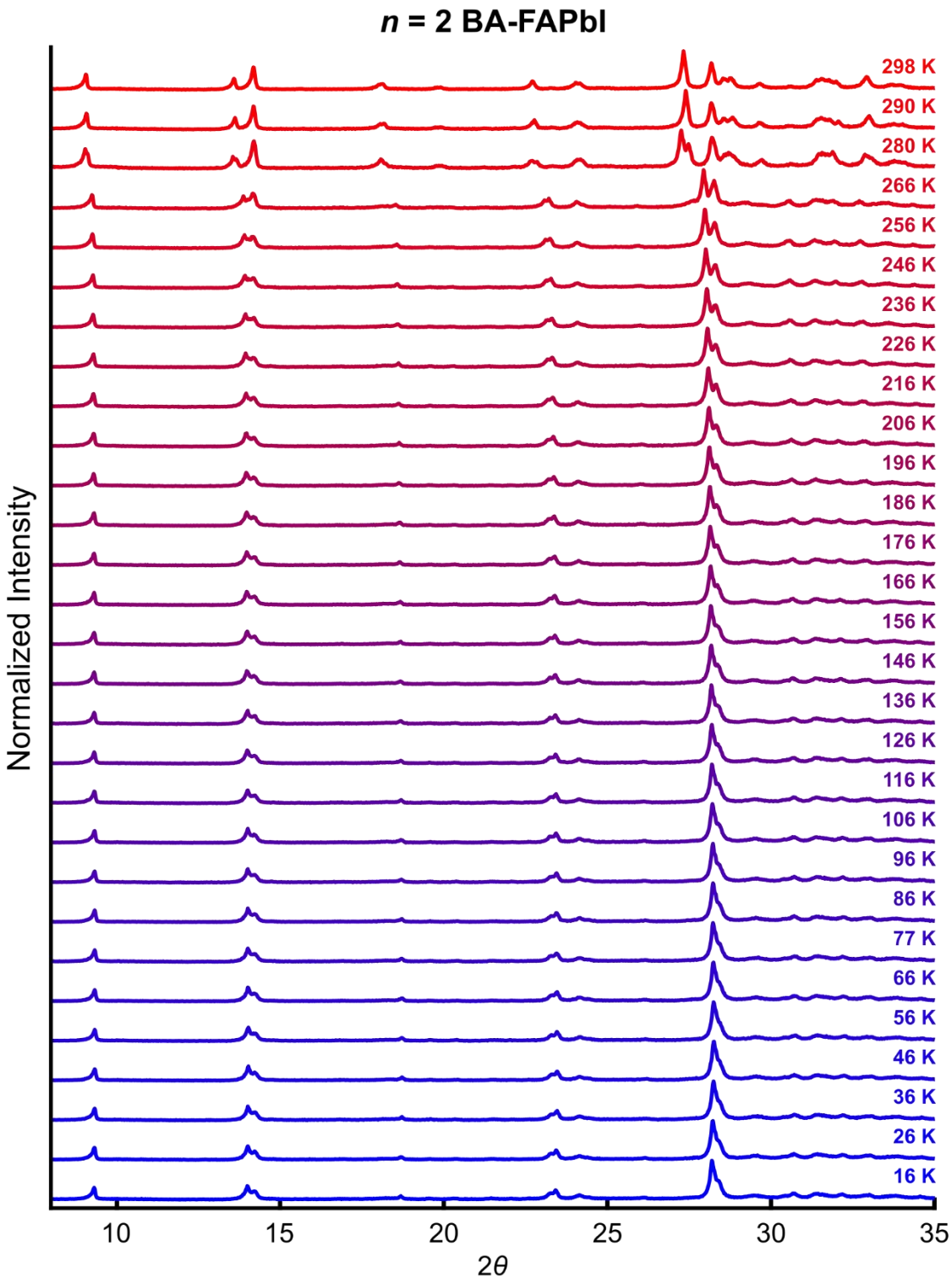

Figure 3-20. Temperature-dependent powder X-ray diffractograms of n = 2 BA-FAPbI between 16 K and 298 K.

3.6 Analysis of Iodide 2D LHP Crystal Structures

Crystal structures of all iodide 2D LHP samples were acquired by performing SCXRD on single crystals obtained directly from their mother liquors. Using the phase-transition temperatures identified by powder XRD and DSC discussed in Section 3.5, we collected the crystal structures by mounting crystals at 300 K. Then, the temperature was raised, if needed, to a temperature above the highest phase-transition temperature before the temperature was lowered to below a phase transition. We were able to observe the structural transformation at and above room temperature in all samples. However, we did not observe the phase transitions at ~136–196 K of n = 2 BA-MAPbI, n = 3 BA-MAPbI, and n = 4 BA-MAPbI by SCXRD even when the temperature was lowered to 100 K. Useful crystal models could not be obtained because of poor crystal qualities at lower temperature caused by the phase changes and possible X-ray damages. The space groups and phase transitions of all iodide 2D LHP samples are summarized in Figure 3-21.

When refining crystal structures, we note that there is a space group choice dilemma between a centrosymmetric and noncentrosymmetric space group. For example, *Cmcm* and *Ama*2 space groups have the same systematic absence of reflections. However, we decided to present the centrosymmetric space group over the noncentrosymmetric space group in this work because the E-value statistics and the combined figure of merit values suggest the centrosymmetric space group. Moreover, we found that there is no significant improvement in the final refinement model for the noncentrosymmetric space group with a ~50% inversion twinning. In addition, when it is unclear between a centrosymmetric and noncentrosymmetric space group, the centrosymmetric space group is usually recommended.[136] Choosing the centrosymmetric space group may lead to a refinement with a disorder model, which suggests that the crystal consists of two or multiple

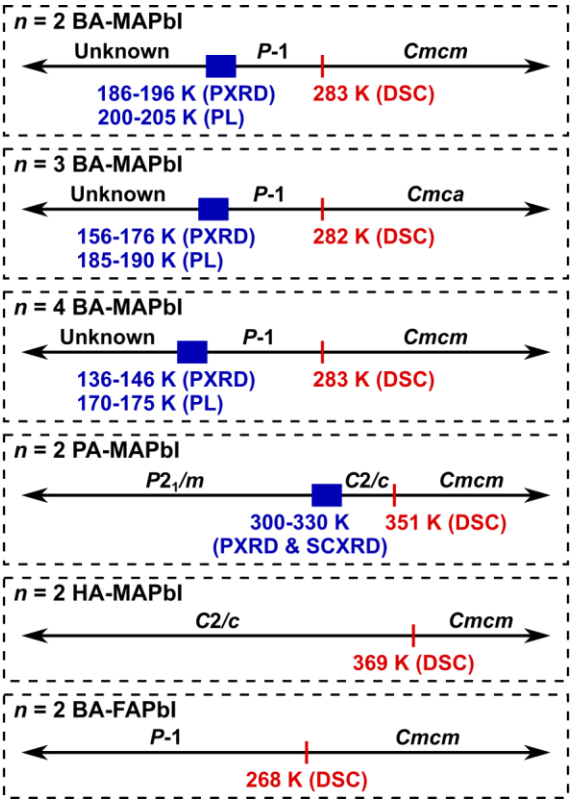

Figure 3-21. Summary of space groups and phase transitions identified by temperature-dependent PXRD, temperature-dependent PL, DSC, and SCXRD.

undistinguished structures.[136] Nevertheless, the noncentrosymmetric space group is still possible if the presence of a polar space group is confirmed by other techniques.

All of the refined crystal structures show that every iodide 2D LHP sample consists of stacks of inorganic slabs separated by bilayers of organic molecular spacers. In the inorganic sublattice, PbI_6 octahedra share their corners in both lateral and stacking directions, and the number of PbI_6 octahedra layers increase with *n*. The inorganic sublattice shows distortion with respect to the perfect cubic unit cell of the iodide 3D LHP, and adjacent PbI_6 octahedra have out-of-phase out-of-plane tilting with respect to each other. In all samples, adjacent inorganic slabs are staggered, and all samples are categorized as members of Ruddlesden–Popper perovskites.[24,85]

3.6.1 Structural Comparison of Iodide 2D LHP Crystals with Different n

At 300 K, n = 2, 3, and 4 BA-MAPbI crystallizes in orthorhombic space groups *Cmcm*, *Cmca*, and *Cmcm*, respectively (Table 3-3 and 3-22). For n = 2 BA-MAPbI, all PbI_6 octahedra are equivalent and can be related by symmetry operations. When the quantum-well thickness increases to n = 3 and 4, two distinct types of PbI_6 octahedra emerge: surface PbI_6 octahedra, which are adjacent to the organic-spacer layer, and middle-layer PbI_6 octahedra, which are surrounded on all sides by other PbI_6 octahedra. Using this terminology, all PbI_6 octahedra in n = 2 iodide 2D LHPs can be treated as surface PbI_6 octahedra. The surface and the middle-layer PbI_6 octahedra differ by their out-of-plane tilting angles. The out-of-plane tilting angles of the Pb–I bonds on the surfaces are between 9.5° and 10°, and for the nonsurface Pb–I bonds, these numbers decrease to ~6°–7° in n = 2 and 4 samples, and 0° in n = 3 sample (Figure 3-23). Although the middle layer of n = 3 BA-MAPbI does not have any out-of-plane tilting, it still shows distortion in the form of in-plane, out-of-phase rotation between adjacent PbI_6 octahedra. The difference in out-of-plane tilting angles in the surface PbI_6 octahedra and the middle-layer PbI_6 octahedra reflects the difference in the interaction between the PbI_6 octahedral framework with the smaller MA cation and the larger organic-spacer cations.

In addition to the out-of-plane tilting, the degree of distortion can be quantified by bond length distortion[138–141] and bond angle variance.[138,142] The bond length distortion (Δd) of an octahedron is defined as

$$\Delta d = \left(\frac{1}{6}\right)\sum\left[\frac{d_n - d}{d}\right]^2 \tag{3-1}$$

Table 3-3. Crystal data and structure refinement for n = 2 BA-MAPbI, n = 3 BA-MAPbI, and n = 4 BA-MAPbI

	n = 2 BA-MAPbI		n = 3 BA-MAPbI		n = 4 BA-MAPbI	
Chemical formula	$C_9H_{30}I_7N_3Pb_2$		$C_{10}H_{36}I_{10}N_4Pb_3$		$C_{11}H_{42}I_{13}N_5Pb_4$	
M_r	1483.04		2103.00		2722.95	
Temperature (K)	300	250	300	250	300	250
Crystal system	Orthorhombic	Triclinic	Orthorhombic	Triclinic	Orthorhombic	Triclinic
Space group	*Cmcm*	*P*-1	*Cmca*	*P*-1	*Cmcm*	*P*-1
a (Å)	39.277 (4),	8.7432 (10)	51.963 (8)	8.7799 (13)	64.305 (5)	8.8047 (11)
b (Å)	8.9317 (8)	9.0448 (10)	8.9349 (13)	9.0236 (14)	8.9327 (6)	8.9991 (12)
c (Å)	8.8533 (8)	19.669 (2)	8.8648 (13)	25.436 (4)	8.8835 (6)	31.917 (4)
α (°)	90	102.905 (3)	90	90.030 (3)	90	97.912 (2)
β (°)	90	95.093 (3)	90	95.685 (3)	90	93.216 (2)
γ (°)	90	91.393 (3)	90	91.316 (3)	90	91.222 (2)
V (Å^3)	3105.9 (5)	1508.6 (3)	4115.8 (10)	2004.8 (5)	5102.9 (6)	2499.9 (6)
Z	4	2	4	2	4	2
μ (mm^{-1})	17.79	18.31	19.75	20.27	21.04	21.47
Crystal size (mm)	0.10 × 0.06 × 0.02	0.10 × 0.06 × 0.02	0.18 × 0.09 × 0.06	0.18 × 0.09 × 0.06	0.12 × 0.08 × 0.02	0.12 × 0.08 × 0.02
No. of measured reflections	24804	25836	27562	28054	34882	34039
No. of independent reflections	1506	5344	1859	7091	2459	8853
No. of observed [$I > 2\sigma(I)$] reflections	1100	4101	1428	5876	1677	6378
R_{int}	0.053	0.052	0.045	0.042	0.049	0.044
$(\sin\theta/\lambda)_{max}$ (Å^{-1})	0.596	0.597	0.597	0.597	0.597	0.596
$R[F^2 > 2\sigma(F^2)]$, $wR(F^2)$, S	0.039, 0.101, 1.07	0.057, 0.138, 1.08	0.042, 0.115, 1.09	0.056, 0.136, 1.09	0.041, 0.109, 1.05	0.062, 0.166, 1.07
No. of reflections	1506	5344	1859	7091	2459	8853
No. of parameters	92	222	109	276	133	355
No. of restraints	71	126	68	124	84	113
$\Delta\rho_{max}$, $\Delta\rho_{min}$ (e Å^{-3})	1.32, -0.93	2.18, -1.56	0.62, -2.00	2.21, -4.06	1.11, -1.98	2.57, -3.98

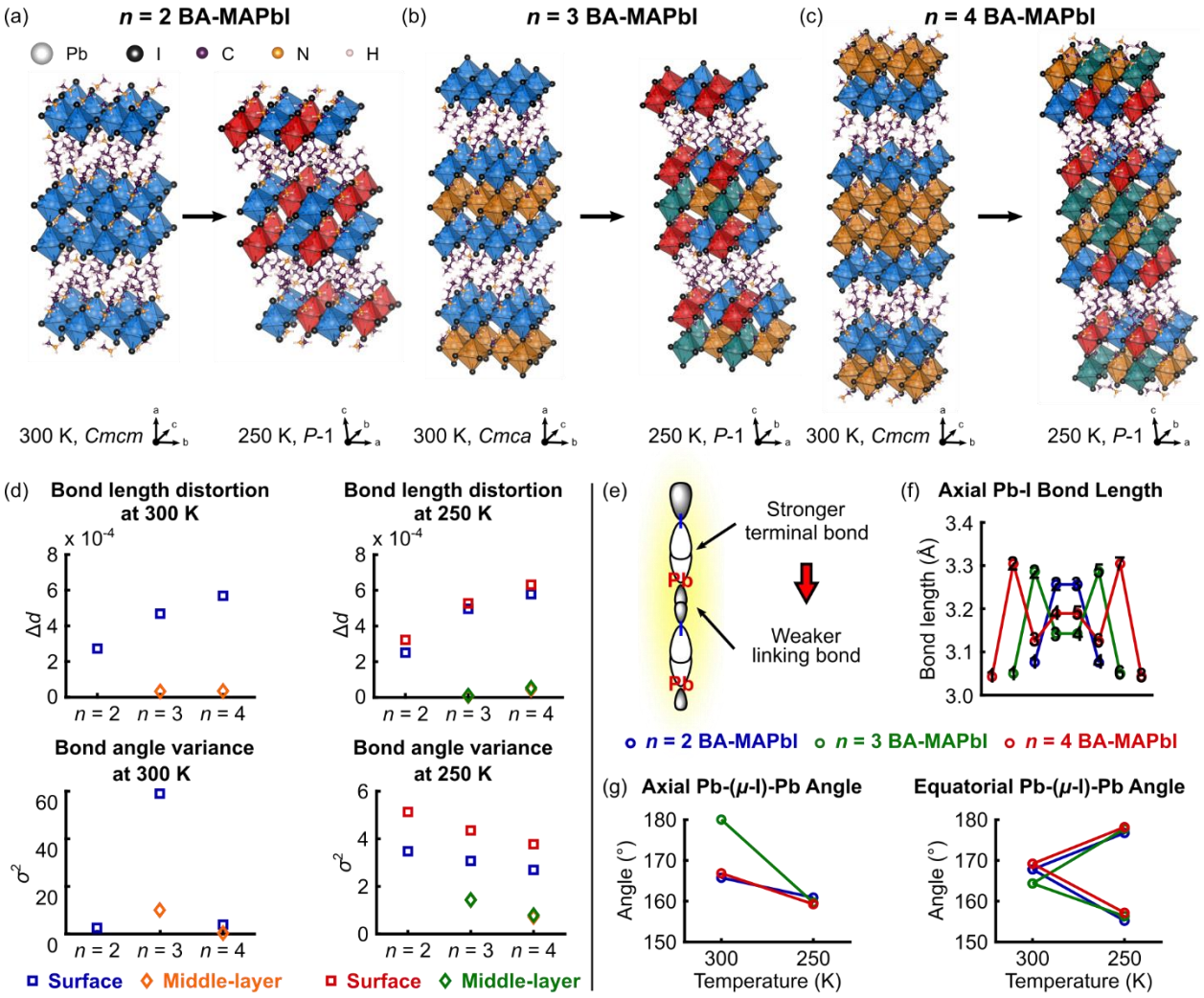

Figure 3-22. *Analysis of crystal structures for n = 2, 3, and 4 BA-MAPbI.* (a) Structural phase transition of n = 2 BA-MAPbI from orthorhombic *Cmcm* at 300 K to triclinic *P*-1 at 250 K. (b) Structural phase transition of n = 3 BA-MAPbI from orthorhombic *Cmca* at 300 K to triclinic *P*-1 at 250 K. (c) Structural phase transition of n = 4 BA-MAPbI from orthorhombic *Cmcm* at 300 K to triclinic *P*-1 at 250 K. Structurally similar PbI_6 octahedra are labeled by blue, orange, red, and green colors. (Disorder is omitted in all illustrations for clarity.) (d) Bond length distortion ($\boldsymbol{\Delta d}$, top) and bond angle variance ($\boldsymbol{\sigma^2}$, bottom) of each type of PbI_6 octahedra of n = 2, 3, and 4 BA-MAPbI at 300 K (left) and 250 K (right). (e) Schematic diagram showing the orbital overlap of a terminal Pb–I bond and a linking Pb–I bond. (f) Plot of axial Pb–I bond length starting from the top to the bottom of the inorganic quantum wells of n = 2 BA-MAPbI (blue), n = 3 BA-MAPbI (green), and n = 4 BA-MAPbI (red). The number on the plot indicates the order of the bond starting from the top of the inorganic quantum wells. (g) Evolution of Pb–(μ-I)–Pb angle in axial (left) and equatorial (right) directions of n = 2 BA-MAPbI (blue), n = 3 BA-MAPbI (green), and n = 4 BA-MAPbI (red).

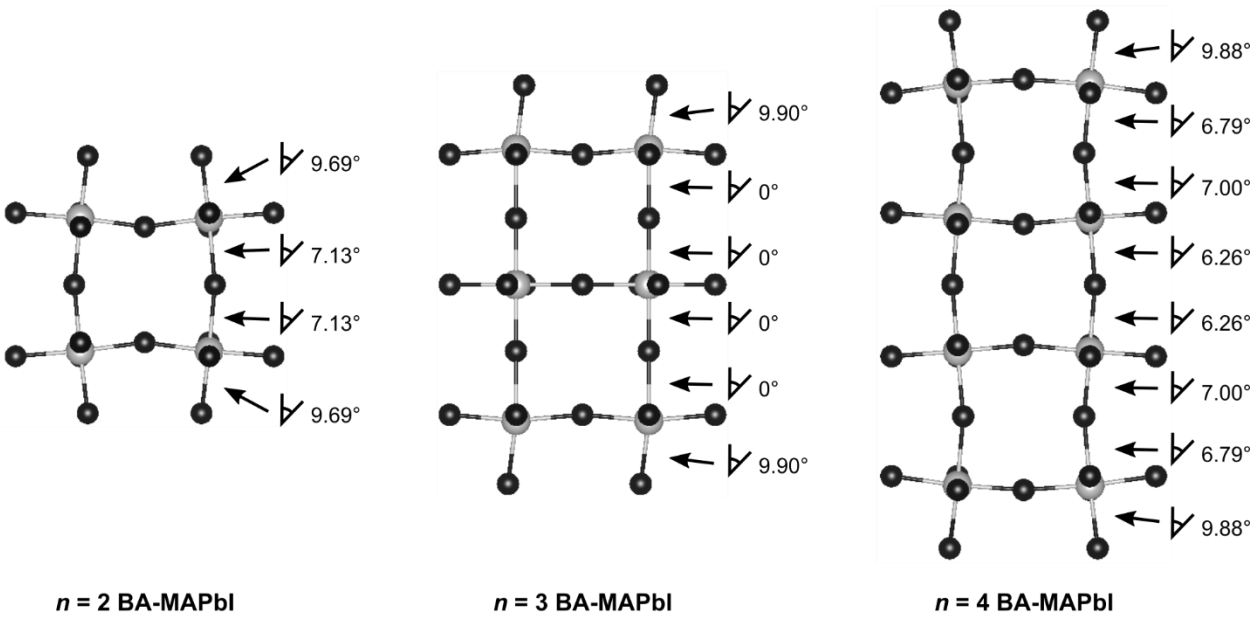

Figure 3-23. Illustrations of *n* = 2 BA-MAPbI, *n* = 3 BA-MAPbI, and *n* = 4 BA-MAPbI showing out-of-plane tilting angles of axial Pb-I bonds. The angles are measured with respect to the stacking direction.

where d_n is the individual Pb–I bond distance, and d is the mean Pb–I bond distance. Additionally, the bond angle variance (σ^2) of an octahedron can be calculated by

$$\sigma^2 \sum_{i=1}^{12} \frac{(\theta_i - 90)^2}{11} \tag{3-2}$$

where θ_i is the individual I–Pb–I angle. Nonzero values of these two parameters indicate distortion from a perfect octahedron, which is characterized by six equal bond lengths and 90° bond angles. Across *n* = 2, 3, and 4 BA-MAPbI, both Δd and σ^2 are larger for surface octahedra than in middle-layer octahedra (3-22d left panel), in agreement with the extent of out-of-plane tilting discussed above.

A closer inspection of the bond lengths across samples with different *n* also sheds light on how the bonding orbitals of Pb and I interact. In iodide 2D LHPs, Pb–I bonds can be classified as terminal-axial (T-Ax) Pb–I bonds, linking-axial (L-Ax) Pb–I bonds, and linking-equatorial (L-Eq)

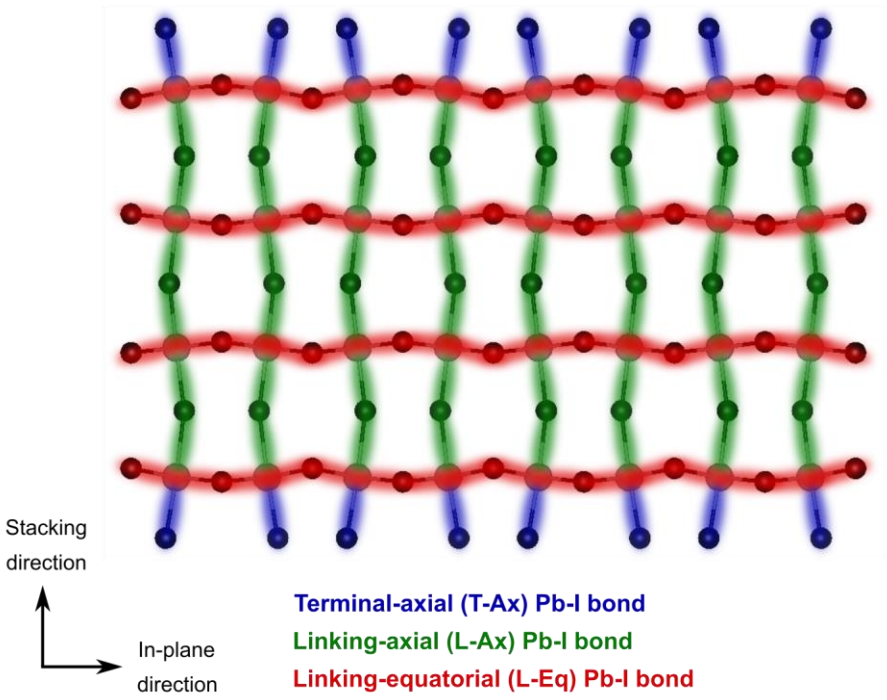

Figure 3-24. Illustration of an inorganic slab highlighting the three types of Pb-I bonds: terminal-axial (T-Ax), linking-axial (L-Ax), and linking-equatorial (L-Eq) bonds.

Pb–I bonds (Figure 3-24), where axial and equatorial directions are defined as out-of-plane and in-plane directions, respectively. A general trend observed across all iodide 2D LHP samples is that the T-Ax Pb–I bond is always the shortest bond among the three types. This can be explained by noting that the orbitals of a terminal I atom are only interacting with the orbitals from one Pb atom, whereas those of a linking I atom are shared with the orbitals from two Pb atoms (3-22e). Hence, orbital overlap is greatest in the T-Ax Pb–I bond, and this bond is the shortest and strongest. Going from the top to the bottom of the inorganic slab, the axial Pb–I bond lengths exhibit a zigzag pattern with a reflection plane at the middle of the inorganic slab (3-22f). This behavior can be explained by noting that the two Ax I atoms in each PbI_6 octahedron are interacting with the same orbitals of the Pb atom (3-22e). Thus, stronger orbital overlap in one Ax Pb–I bond will make the orbital overlap of the other Ax Pb–I bond weaker, resulting in two Ax Pb–I bonds with different bond lengths. This effect is called the trans effect and is commonly found in transition-metal

complexes.[143] This alternation of bond length is not unique to 2D LHPs and has been previously observed in both cubic and tetragonal phases of $MAPbI_3$.[144] The Pb–I bond lengths in cubic and tetragonal $MAPbI_3$ alternate between 3.21 and 3.10 Å for the former and between 3.20 and 3.13 Å for the latter. These Pb–I bond lengths are also similar to the Pb–I bond lengths of 3.19 and 3.12 Å found in the middle-layer PbI_6 octahedra. However, an exception of bond-length alternation was observed in the middle-layer PbI_6 octahedra of n = 3 BA-MAPbI, which has equal Ax Pb–I bond lengths due to symmetry. On the other hand, L-Eq Pb–I bond lengths have a small variation and are 3.16 ± 0.02 Å long, which is similar to those found in cubic and tetragonal $MAPbI_3$.[144]

When n = 2, 3, and 4 BA-MAPbI are cooled to 250 K, the 2D LHPs retain their staggered geometry but undergo phase transitions to a lower symmetry space group of triclinic P-1 (Figures 3-22a, 3-22b, and 3-22c). As a result, both surface PbI_6 octahedra and middle-layer PbI_6 octahedra bifurcate into two families, each with different distortions yet similar magnitudes (Figure 3-22d right panel). The phase transformation is accompanied by a significant change in the Pb–(μ-I)–Pb bond angles (3-22g): (i) the Pb–(μ-I)–Pb bond angles in axial direction reduce to ~160°, leading to significant increases in out-of-plane tilting across the three samples; and (ii) the Pb–(μ-I)–Pb bond angles in equatorial direction with initial values of ~164°–172° separate into two groups with lower bond angles of ~153°–160° and higher bond angles of ~175°–180°. This alteration in bond angles suggests a higher degree of distortion with respect to the ideal perovskite structure with all Pb–(μ-I)–Pb bond angles being 180°. In addition, the middle-layer PbI_6 octahedra of n = 3 BA-MAPbI in this phase shows an out-of-plane tilting, unlike in the higher-temperature phase.

3.6.2 Structural Comparison of Iodide 2D LHP Crystals with Different Organic-Spacer Lengths

Previous reports on n = 1 iodide 2D LHP have shown that the number of phase-transition and transition temperatures are dependent on the length of organic spacer.[120–122] In this study, we observed that n = 2 BA-MAPbI, n = 2 PA-MAPbI, and n = 2 HA-MAPbI exhibited one, two, and one phase transitions between 100 and 300 K, 100 and 363 K, and 100 and 385 K, respectively (Table 3-4 and Figures 3-22a, 3-25a, and 3-25b). The highest-temperature phases of these three samples all share the same orthorhombic *Cmcm* space group. As the temperature decreases, structural distortions lower the crystal symmetry in all three materials. When cooled, the crystal symmetry of n = 2 BA-MAPbI is lowered to triclinic *P*-1, and those of n = 2 PA-MAPbI and HA-MAPbI are lowered to monoclinic *C*2/*c*, with an additional lowering of symmetry to $P2_1/m$ in the case of n = 2 PA-MAPbI.

The structures of n = 2 BA-MAPbI, n = 2 PA-MAPbI, and n = 2 HA-MAPbI in orthorhombic *Cmcm* space group share many similarities. First, in each structure, all PbI_6 octahedra are equivalent. Adjacent octahedra have out-of-phase out-of-plane tilting, and larger tilting angles are observed in the T-Ax Pb–I bonds compared to the L-Ax Pb–I bonds. The latter reflects the larger space required to accommodate an organic-spacer molecule compared to a MA cation. A closer inspection of these tilting angles show that there are decreasing trends in both angles as the organic spacer is increased (Figure 3-25d), and these changes are accompanied by increasing Pb–(μ-I)–Pb angles closer to 180° (Figure 3-25e). An explanation for these behaviors can be given by noting that iodide 2D LHPs consist of interconnected inorganic slabs and organic-spacer layers. In the organic-spacer layer, there is an interaction between organic-spacer molecules from different slabs,

Table 3-4. Crystal data and structure refinement for *n* = 2 PA-MAPbI, *n* = 2 HA-MAPbI, and *n* = 2 BA-FAPbI

	n = 2 PA-MAPbI			*n* = 2 HA-MAPbI		*n* = 2 BA-FAPbI	
Chemical formula	$C_{11}H_{34}I_7N_3Pb_2$			$C_{13}H_{38}I_7N_3Pb_2$		$C_9H_{29}I_7N_4Pb_2$	
M_r	1511.09			1539.14		1496.04	
Temperature (K)	363	330	250	385	300	300	230
Crystal system	Orthorhombic	Monoclinic	Monoclinic	Orthorhombic	Monoclinic	Orthorhombic	Triclinic
Space group	*Cmcm*	*C*2/*c*	$P2_1/m$	*Cmcm*	*C*2/*c*	*Cmcm*	*P*-1
a (Å)	42.539 (10)	41.588 (14)	8.8283 (8),	46.859 (6)	45.481 (13)	39.204 (5)	8.858 (2)
b (Å)	8.993 (2)	9.000 (3)	41.044 (4)	8.9403 (12)	8.929 (2)	8.9490 (12)	9.137 (2)
c (Å)	8.902 (2)	8.901 (3)	8.9886 (8)	8.9064 (12)	8.816 (2)	8.9431 (11)	38.382 (9)
α (°)	90	90	90	90	90	90	90.140 (3)
β (°)	90	95.269 (6)	90.8995 (14)	90	98.159 (5)	90	90.154 (4)
γ (°)	90	90	90	90	90	90	90.009 (3)
V (Å^3)	3405.5 (13)	3317.5 (19)	3256.6 (5)	3731.2 (9)	3544.0 (17)	3137.6 (7)	3106.5 (12)
Z	4	4	4	4	4	4	4
μ (mm^{-1})	16.22	16.65	16.97	14.81	15.59	17.61	17.78
Crystal size (mm)	0.14 × 0.12 × 0.06	0.14 × 0.12 × 0.06	0.14 × 0.12 × 0.06	0.12 × 0.10 × 0.04	0.12 × 0.10 × 0.04	0.12 × 0.08 × 0.04	0.12 × 0.08 × 0.04
No. of measured reflections	29137	24756	56672	25310	27856	22442	24070
No. of independent reflections	1640	2949	5860	1794	3169	1526	10698
No. of observed [$I > 2\sigma(I)$] reflections	1298	2347	4179	841	2702	1009	6276
R_{int}	0.029	0.053	0.048	0.052	0.061	0.067	0.051
$(\sin\theta/\lambda)_{max}$ (Å^{-1})	0.596	0.596	0.596	0.595	0.601	0.598	0.597
$R[F^2 > 2\sigma(F^2)]$, $wR(F^2)$, *S*	0.026, 0.070, 1.08	0.058, 0.158, 1.11	0.054, 0.143, 1.07	0.050, 0.196, 1.05	0.097, 0.265, 1.08	0.056, 0.118, 1.06	0.100, 0.269, 1.05
No. of reflections	1640	2949	5860	1794	3169	1526	10698
No. of parameters	99	134	262	119	133	103	443
No. of restraints	48	49	124	72	69	61	283
$\Delta\rho_{max}$, $\Delta\rho_{min}$ (e Å^{-3})	1.08, -0.72	2.24, -2.66	2.38, -1.80	1.01, -0.92	3.96, -2.62	2.01, -1.64	3.43, -4.31

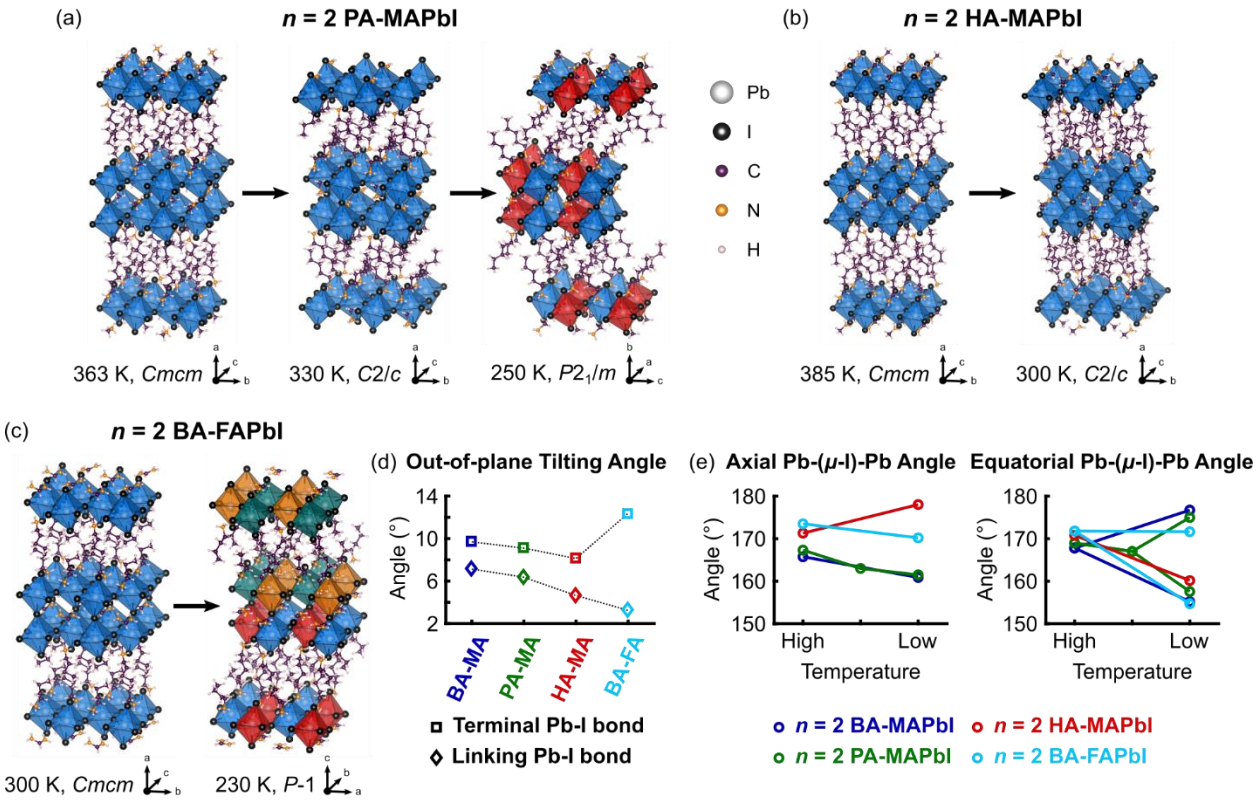

Figure 3-25. *Analysis of crystal structures for n = 2 iodide 2D LHP with changing organic-spacer cation (L) or A-site cation.* (a) Structural phase transition of $n = 2$ PA-MAPbI from orthorhombic *Cmcm* at 363 K to monoclinic *C*2/*c* at 330 K and monoclinic $P2_1/m$ at 250 K. (b) Structural phase transition of $n = 2$ HA-MAPbI from orthorhombic *Cmcm* at 385 K to monoclinic *C*2/*c* at 300 K. (c) Structural phase transition of $n = 2$ BA-FAPbI from orthorhombic *Cmcm* at 300 K to triclinic *P*-1 at 230 K. (Disorder is omitted in all illustrations for clarity.) (d) Graph showing the out-of-plane tilting angle of terminal and linking Pb–I bonds in $n = 2$ BA-MAPbI (blue), $n = 2$ PA-MAPbI (green), $n = 2$ HA-MAPbI (red), and $n = 2$ BA-FAPbI (cyan). (e) Evolution of Pb–(μ-I)–Pb angle in axial (left) and equatorial (right) directions of $n = 2$ BA-MAPbI (blue), $n = 2$ PA-MAPbI (green), $n = 2$ HA-MAPbI (red), and $n = 2$ BA-FAPbI (cyan).

resulting in a stress in the layer. This stress can be transmitted to the inorganic slab through the carbon chain of the organic-spacer molecule, resulting in the distortion of the PbI_6 octahedra. As the organic-spacer length increases, the stress is more absorbed by the longer carbon chain, and less is transmitted to the PbI_6 octahedra. As a result, the PbI_6 octahedra have a smaller degree of distortion in the sample with longer organic-spacer length.

Unlike n = 2 BA-MAPbI and n = 2 HA-MAPbI, n = 2 PA-MAPbI exhibits two phase transitions over the temperature range investigated (Figure 3-25a). At 330 K, n = 2 PA-MAPbI adopts a monoclinic $C2/c$ structure with all PbI_6 octahedra being equivalent. Compared to the higher-temperature orthorhombic phase, the inorganic sublattice in the monoclinic phase maintains a similar structure with out-of-phase out-of-plane tilting but with slightly lower Pb–(μ-I)–Pb bond angles (Figure 3-25e). However, a significant difference is observed in the organic-spacer layer with an increase in the corrugation tilt (defined as the angle between the organic-spacer chain and the normal vector of the inorganic slab) from 26.7° to 40.6°. When the temperature is further reduced to 250 K, the crystal symmetry is lowered to $P2_1/m$. In this phase, two types of PbI_6 octahedra with different distortion are observed, similar to the P-1 phase of n = 2 BA-MAPbI at 250 K. Nevertheless, the two types of PbI_6 octahedra in n = 2 PA-MAPbI alternate only along the lateral direction, unlike those in n = 2 BA-MAPbI, which alternate in both vertical and lateral directions. In this phase, the Pb–(μ-I)–Pb bond angles in the axial direction decrease further, but the Pb–(μ-I)–Pb bond angles in the equatorial direction are separated into two groups with lower bond angles of less than 160° and higher bond angles of more than 173°, similar to the transformation discussed above in the case of n = 2, 3 and 4 BA-MAPbI. Although significant transformation is observed in the inorganic sublattice, the change in the organic-spacer layer is negligible, with a small increase of corrugation tilt by less than 1°. As a result, the phase transition from the orthorhombic *Cmcm* phase to monoclinic $C2/c$ phase of n = 2 PA-MAPbI is primarily defined by a transition in the organic-spacer layer, and the phase transition from the monoclinic $C2/c$ phase to the $P2_1/m$ phase is primarily defined by a transition in the inorganic sublattice.

For n = 2 HA-MAPbI, only one transition–from the orthorhombic *Cmcm* to the monoclinic $C2/c$–is observed (Figure 3-25b). This transition is similar to that of n = 2 PA-MAPbI from the

orthorhombic *Cmcm* to the monoclinic *C*2/*c*: equivalence of PbI_6 octahedra is maintained, Pb–(μ-I)–Pb bond angles in the equatorial direction decrease, and the corrugation tilts of the organic spacers increase. However, unlike other iodide 2D LHPs discussed so far, which have smaller Pb–(μ-I)–Pb bond angles in the axial direction at lower temperature, n = 2 HA-MAPbI has a higher value of this bond angle of 178°, very close to the ideal geometry of 180° (Figure 3-22e). In addition, there is a significant in-plane rotation of the PbI_6 octahedra in the monoclinic *C*2/*c* phase, unlike any other phases of n = 2 iodide 2D LHPs discussed so far.

3.6.3 Structural Comparison of Iodide 2D LHP Crystals with Different A-site Cations

Unlike n = 1 iodide 2D LHPs, iodide 2D LHPs with n = 2 and above include an A-site cation. In this study, we investigated the effect of replacing the A-site cation from MA to FA. At 300 K, both n = 2 BA-MAPbI and n = 2 BA-FAPbI adopt the same orthorhombic *Cmcm* phase and have similar appearance (Figures 3-22a and 3-25c). Nevertheless, all Pb–(μ-I) –Pb bond angles of n = 2 BA-FAPbI are significantly higher and closer to 180° (Figure 3-25e). The out-of-plane tilting of the T-Ax and the L-Ax Pb–I bonds in n = 2 BA-FAPbI also increase and decrease to the values of 12° and 3.3°, respectively (Figure 3-22d). It is surprising that MA and FA cations with slightly different sizes (MA = 2.70 Å and FA = 2.79 Å)[135] lead to such dramatic differences in the crystal structures. Although MA and FA cations are dynamically disordered, they have preferred orientations with slightly lower potential energies because of the directional hydrogen bonding between the hydrogens on the polar head groups and I in the PbI_6 extended structure. These hydrogen bonds can dislocate the I and tilt the PbI_6 octahedra. Because MA and FA cations have different charge distributions and different hydrogen bonding characters, we believe that these may be the cause of such dramatic difference in the crystal structures.

The low-temperature phase of n = 2 BA-FAPbI is similar to that of n = 2 BA-MAPbI. At 230 K, n = 2 BA-FAPbI crystallizes in triclinic P-1 phase with lower symmetry compared to the orthorhombic $Cmcm$ at 300 K (Figure 3-25c). In the triclinic P-1 phase, n = 2 BA-FAPbI has four types of PbI_6 octahedra with different distortion. Although Pb–(μ-I)–Pb bond angles in the axial direction of n = 2 BA-FAPbI in triclinic P-1 phase are still higher than those of n = 2 BA-MAPbI with equivalent structure (Figure 3-25e), the average Pb–(μ-I)–Pb bond angle in the equatorial direction of n = 2 BA-FAPbI is lower at 163.2°, compared to 165.7° for n = 2 BA-MAPbI. For the organic-spacer layers, similar corrugation tilting within a few degrees is observed.

3.6.4 Near-Room-Temperature Structural Transformations in the Organic-Spacer Layer

Similarities were observed across all iodide 2D LHPs in their transformation from orthorhombic to lower-symmetry phases as the sample is cooled (Figure 3-26). In all samples, the high-temperature phase shows interdigitation of the organic cation spacers; the extent of interdigitation increases when a sample is cooled below its phase-transition temperature. Furthermore, all transitions (except the second transition of n = 2 PA-MAPbI between monoclinic $C2/c$ and monoclinic $P2_1/m$) are accompanied by significant changes in the corrugation tilt angle of the organic-spacer molecules. Using thermodynamic data from DSC, we previously described these transitions as partial melting/freezing transitions of the organic sublattice,[136] which has also been observed in n = 1 2D LHPs.[137]

3.6.5 Structure-Dependent Optical Properties

To understand the structure–property relationship of 2D LHPs, we collected temperature-dependent photoluminescence (PL) spectra (Figure 3-27). In agreement with our temperature-dependent PXRD experiments, n = 2 BA-MAPbI, n = 3 BA-MAPbI, and n = 4 BA-MAPbI showed

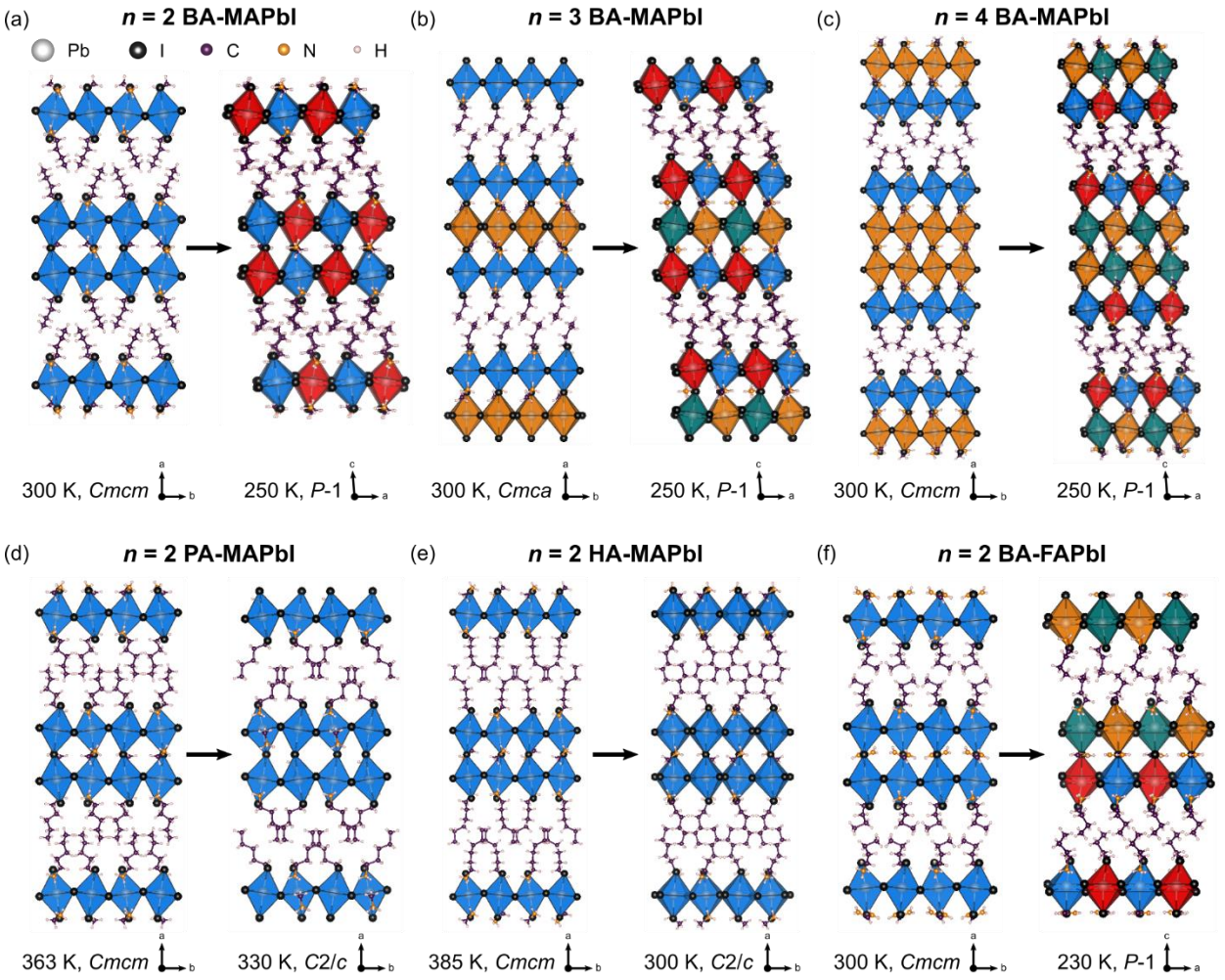

Figure 3-26. Structural phase transitions viewed from the side to highlight the transitions of the organic-spacer layers in (a) n = 2 BA-MAPbI, (b) n = 3 BA-MAPbI, (c) n = 4 BA-MAPbI, (d) n = 2 BA-FAPbI, (e) n = 2 PA-MAPbI, and (f) n = 2 HA-MAPbI. (Disorder is omitted in all illustrations for clarity.)

two sudden shifts of the PL spectrum, whereas n = 2 BA-FAPbI showed only one shift within the investigated temperature range. The first peak shift of n = 2 BA-MAPbI, n = 3 BA-MAPbI, and n = 4 BA-MAPbI all occurred between 280 K and 285 K (Figure 3-28a). On the other hand, their second peak shifts were observed at decreasing temperatures as n increased: 200-205 K for n = 2 BA-MAPbI, 185-190 K for n = 3 BA-MAPbI, and 170-175 K for n = 4 BA-MAPbI (Figure 3-28b). For n = 2 BA-FAPbI, the only peak shift was detected between 265 K and 270 K (Figure 3-28a).

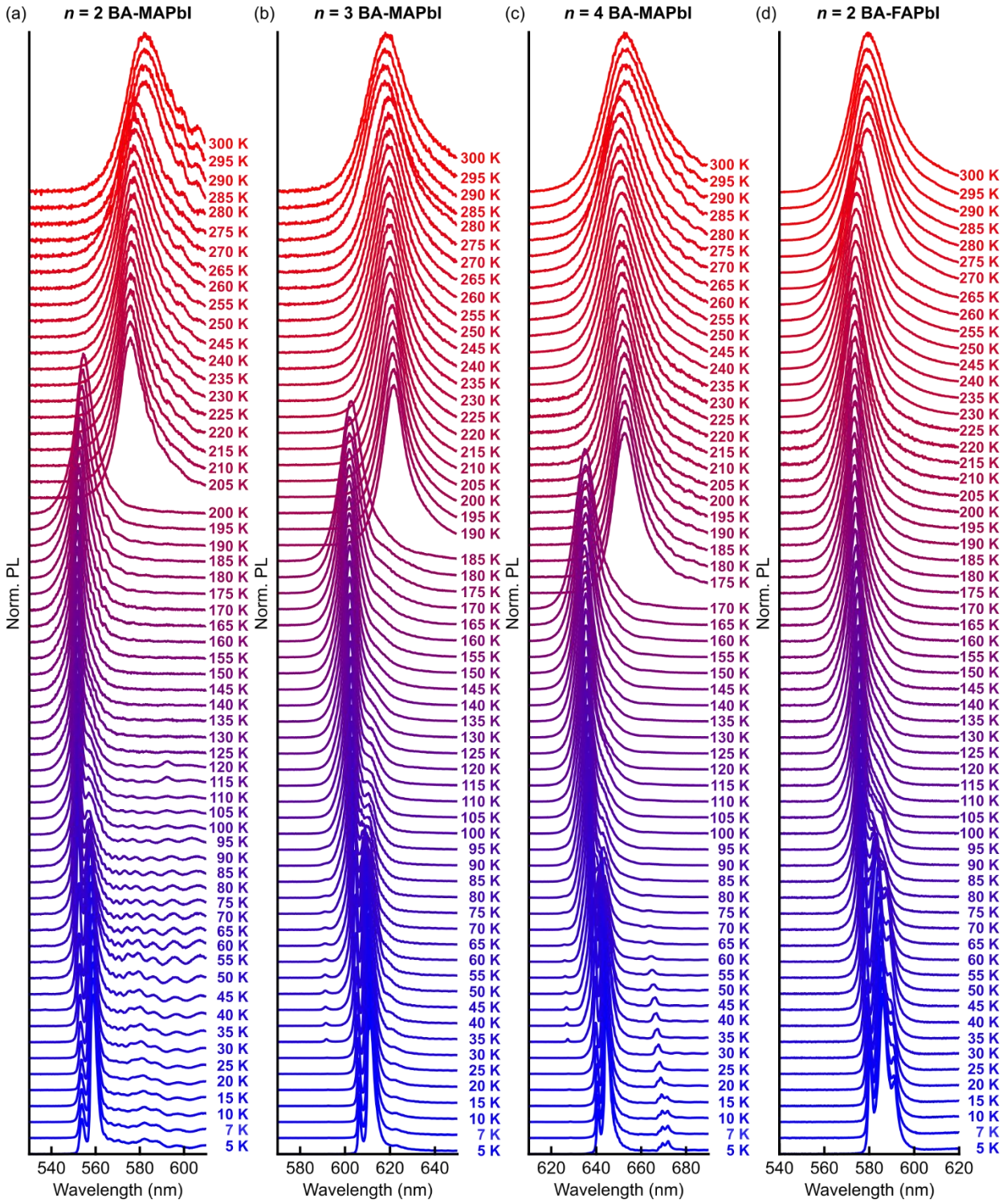

Figure 3-27. Temperature-dependent photoluminescence spectra of (a) *n* = 2 BA-MAPbI, (b) *n* = 2 BA-MAPbI, (c) *n* = 2 BA-MAPbI, and (d) *n* = 2 BA-MAPbI between 5 K and 300 K.

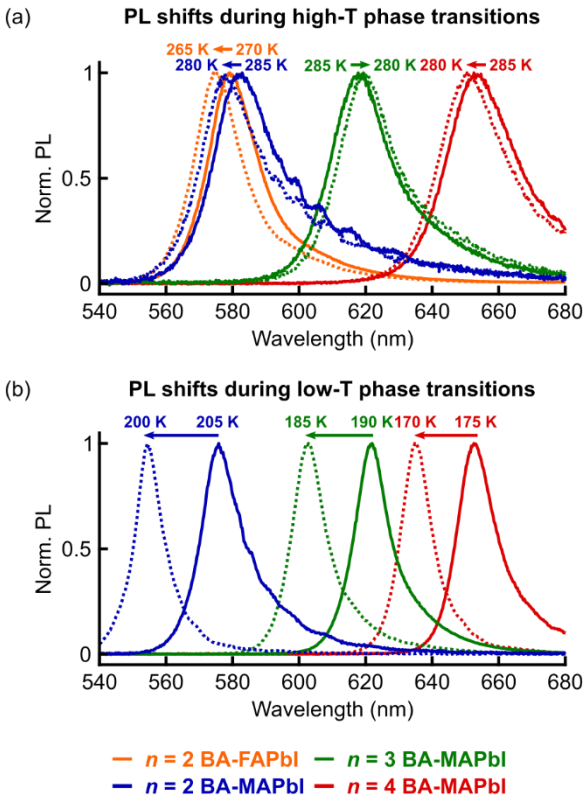

Figure 3-28. PL spectra of n = 2 BA-MAPbI (blue), n = 3 BA-MAPbI (green), n = 4 BA-MAPbI (red), and n = 2 BA-FAPbI (orange) above and below (a) higher-temperature phase transitions and (b) lower-temperature phase transitions.

As shown in Figure 3-28a, when n = 2 BA-MAPbI, n = 4 BA-MAPbI, and n = 2 BA-FAPbI are cooled to undergo the near-room-temperature transitions, their peaks blue-shift. In contrast, the peak of n = 3 BA-MAPbI red-shifts even though all of these transitions correspond to the melting/freezing transitions in the organic subphases. These observations can be explained by the effect of distortion on the electronic band structure of 2D LHPs.

The electronic band structure of 2D LHPs has been calculated by various groups.[145–149] It has been shown that the valence band maximum (VBM) of 2D LHPs is formed by the antibonding interaction between Pb s orbitals and I p_x and p_y orbitals, and the conduction band minimum (CBM) arises from the weakly antibonding interaction between Pb p_x and p_y orbitals and I s orbitals. For

2D LHPs, a narrow band of Pb p_z orbitals situates significantly above the CBM. For 3D LHPs, the Pb p_z orbitals interact with I s orbitals, and together with Pb p_x and p_y orbitals form triply degenerate bands at the CBM.[150] Similar to the Pb p_z orbitals of 2D LHPs, the electronic bands of A-site cations and organic spacers are well above and below the CBM and the VBM, respectively. However, the A-site cations and organic spacers can indirectly influence the band gaps of 2D LHPs by inducing structural distortion.

There are two main types of structural distortion that influence the band gaps of 2D LHPs.[148,149] The first is octahedral tilting characterized by Pb–(μ-I)–Pb bond angles. Smaller Pb–(μ-I)–Pb bond angles or higher angular distortion compared to the perfect 180° Pb–(μ-I)–Pb bond angle cause a weaker interaction between Pb s orbitals and I p_x and p_y orbitals in the VBM. The smaller angles also lead to a lower symmetry of lattice, resulting in a mixing of I p and s orbitals and an increase in the antibonding interaction in the CBM. As a result, when Pb–(μ-I)–Pb bond angles become smaller, the band gap energies of 2D LHPs increase. The other important factor is equatorial Pb–I bond lengths. Shorter equatorial Pb–I bond lengths lead to an increase in the antibonding interaction in the VBM, but the CBM is less affected because of its weak antibonding character. Consequently, the band gap energies of 2D LHPs decrease as Pb–I bond lengths become shorter.

The equatorial Pb–(μ-I)–Pb bond angles and the equatorial Pb–I bond lengths of n = 2 BA-MAPbI, n = 3 BA-MAPbI, n = 4 BA-MAPbI, and n = 2 FA-MAPbI are summarized in Table 3-5. As the samples are cooled to undergo the phase transitions, the equatorial Pb–(μ-I)–Pb bond angles decrease, and the equatorial Pb–I bond lengths increase, resulting in increases in the band gap energies. However, there is an exception in the case of the middle-layer PbI_6 octahedra of n = 3 BA-MAPbI whose average equatorial Pb–(μ-I)–Pb bond angle increases significantly while the average equatorial Pb–I bond length remains almost constant. Calculations have shown that the

Table 3-5. Average equatorial Pb–(μ-I)–Pb bond angles and Pb–I bond lengths of *n* = 2 BA-MAPbI, *n* = 3 BA-MAPbI, *n* = 4 BA-MAPbI, and *n* = 2 FA-MAPbI with standard deviations in parentheses

	n = 2 BA-MAPbI		*n* = 3 BA-MAPbI		*n* = 4 BA-MAPbI		*n* = 2 BA-FAPbI	
Temperature (K)	300	250	300	250	300	250	300	230
Average Pb–(μ-I)$_{eq}$–Pb of surface PbI_6 octahedra (Å)	167.81 (5)	165.97 (3)	168.4 (1)	166.50 (3)	168.10 (4)	166.97 (3)	171.82 (7)	163.2 (7)
Average Pb–(μ-I)$_{eq}$–Pb of middle-layer PbI_6 octahedra (Å)	-	-	163.09 (17)	168.11 (4)	170.28 (4)	168.37 (4)	-	-
Average Pb–I_{eq} lengths of surface PbI_6 octahedra (°)	3.1629 (3)	3.1827 (5)	3.164 (2)	3.1831 (5)	3.1685 (3)	3.1819 (6)	3.1724 (5)	3.225 (30)
Average Pb–I_{eq} lengths of middle-layer PbI_6 octahedra (°)	-	-	3.1810 (15)	3.1794 (7)	3.1609 (3)	3.1782 (6)	-	-

lowest-energy exciton density is localized in the middle-layer octahedra, rather than near their surface counterparts.[18] Hence, we hypothesize that the changes in the bond lengths and bond angles of the middle-layer PbI_6 octahedra have a higher influence on the band gap energy and explain why the PL peak of *n* = 3 BA-MAPbI red-shifts as the sample is cooled to undergo the melting/freezing transition.

The effect of distortion on the electronic structure of 2D LHPs can also shed light on the structural transformation of the lower-temperature phase transitions of *n* = 2 BA-MAPbI, *n* = 3 BA-MAPbI, and *n* = 4 BA-MAPbI. Although these transitions were not observed by SCXRD, the shifts in PL peaks to higher energies (Figure 3-28b) suggest that these transitions involve decreases in the equatorial Pb–(μ-I)–Pb bond angles or longer equatorial Pb–I bond lengths or a combination of both.

3.7 Synthesis of Bromide 2D LHP Crystals

The cooling-induced crystallization method we described for the synthesis of iodide 2D LHPs could be modified to prepare bromide 2D LHPs, as well. As explained in Session 3.9, first, a large volume of lead (II) bromide ($PbBr_2$) solution was prepared by reacting PbO with HBr solution under reflux. A small volume of this solution was then transferred into a small vial. Without the addition of H_3PO_2, a small volume of BA was added and white precipitate of n = 1 BA-PbBr formed. In a separate vial, a solution of the A-site cation bromide salt was prepared by dissolving the salt in HBr. This solution was subsequently added to the solution containing white precipitate to form a combined solution. This combined solution was heated until clear and then slowly cooled to produce crystals of bromide 2D LHPs. Finally, these crystals were collected by suction filtration and dried under reduced pressure. Examples of crystals obtained by this method are shown in Figure 3-29a.

When synthesizing bromide 2D LHPs, we found that the effects of each synthesis parameter on the purity of the product described earlier for iodide 2D LHPs also applied to the case of bromide 2D LHPs. However, bromide 2D LHPs exhibited faster precipitation rates, which resulted in the formation of smaller crystals. To grow larger bromide 2D LHPs, it was necessary to lower the concentration of each reagent by adding additional volume of HBr to the final solution.

Occasionally, we observed inhomogeneous orange colorings on bromide 2D LHPs during suction filtration and drying (Figure 3-30). These orange colorings were easily noticed in the cases of white n = 1 BA-PbBr and yellow n = 2 BA-MAPbBr. Further investigation showed that the PL spectra obtained from orange regions were identical to the clear regions. As no MA cation was involved in the synthesis of n = 1 BA-PbBr, the orange coloring cannot be due to higher members

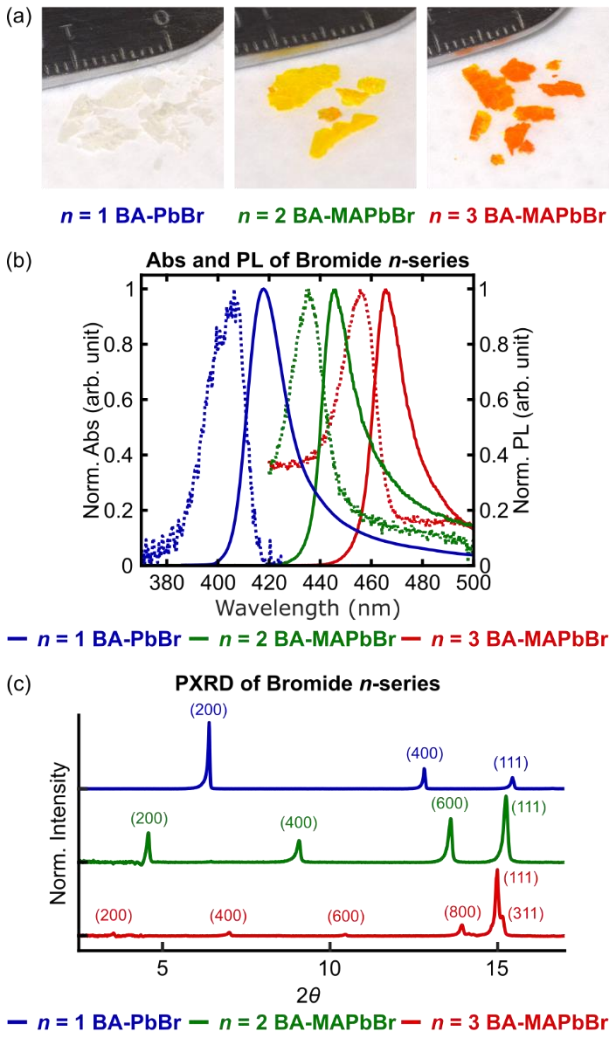

Figure 3-29. *Bromide 2D LHPs.* (a) Photographs of 2D LHP crystals: n = 1 BA-PbBr (left), n = 2 BA-MAPbBr (middle), and n = 3 BA-MAPbBr (right). The spacing between minor ticks on the ruler is 1 mm. (b) Abs (dotted) and PL (solid) spectra of n = 1 BA-PbBr (blue), n = 2 BA-MAPbBr (green), and n = 3 BA-MAPbBr (red). (c) Powder X-ray diffractograms of n = 1 BA-PbBr (blue), n = 2 BA-MAPbBr (green), and n = 3 BA-MAPbBr (red). All peaks are labeled with their corresponding diffraction planes by analogy to the iodide series.

of bromide 2D LHPs. One possible cause is the presence of molecular Br_2 intercalated in the organic-spacer layer, similar to the previously reported intercalation of I_2 in 2D LHPs.[151]

Figure 3-29b shows the Abs and the PL spectra of exfoliated n = 1, 2, and 3 bromide 2D LHPs with BA organic spacer. Only the absorption of the 1s excitonic resonance was captured in these experiments because of poor signal-to-noise ratio at wavelengths shorter than ~420 nm in our

Figure 3-30. Orange coloring on white crystals of n = 1 BA-PbBr. Because the synthesis of n = 1 BA-PbBr does not involve MA cation, these orange colorings are not believed to be due to the formation of bulk $MAPbBr_3$ or higher members of bromide 2D LHPs.

measurements. The presence of a single PL peak corresponding to the measured absorption resonance confirmed the high phase purity of these 2D LHP crystals.

The PXRD patterns of bromide 2D LHPs (Figure 3-29c) show the same features as those observed in their iodide counterparts.[39] Because of the smaller size of bromine compared to iodine, the inorganic slabs of bromide 2D LHPs are thinner, and all peaks shift to higher 2θ. The (111) peaks appear at ~15° 2θ, while the number of evenly spaced (h00) peaks below the (111) peak is still n + 1. The calculated stacking periods corresponding to these Bragg peaks for n = 1 BA-PbBr, n = 2 BA-MAPbBr, and n = 3 BA-MAPbBr are 1.38, 1.95, and 2.52 nm, respectively.

3.8 Conclusions

We have reported cooling-induced crystallization of high-quality 2D LHP crystals of n = 2 BA-MAPbI, n = 3 BA-MAPbI, n = 4 BA-MAPbI, n = 2 PA-MAPbI, n = 2 HA-MAPbI, and n = 2 BA-FAPbI, as well as crystal structures for these compounds at multiple temperatures. We also observed structural distortion and correlated it with PL peak shifts across phase transitions. Moreover, the synthetic approach is generalizable to the bromide 2D LHP system, and high-quality

crystals of n = 1 BA-PbBr, n = 2 BA-MAPbBr, and n = 3 BA-MAPbBr were demonstrated. Overall, this work illuminates broader structural trends in 2D alkylammonium LHPs, and their effects on optical properties. The structural insights reported in this work will provide a foundation for understanding thermal, electronic, and optical properties of 2D LHPs.

3.9 Methods

Synthesis of Iodide 2D LHPs. Crystals of iodide 2D LHPs were synthesized using a modified procedure based on a cooling-induced crystallization method, as reported before.[37,85,86] For the synthesis of iodide 2D LHPs, a large volume of lead (II) iodide (PbI_2) was prepared by dissolving lead (II) oxide (PbO, 99.9+% (trace metal basis) <10 μm, powder, Acros Organics) in 55% hydrogen iodide (HI) solution (contains no stabilizer, ACS reagent, 55%, MilliporeSigma) under reflux for 15 min. A small volume of this solution was then transferred into a small vial and mixed with hypophosphorous acid (H_3PO_2). After the mixed solution turned bright yellow, a small volume of long-chain organic spacer (L = butylamine {BA}, pentylamine {PA}, or hexylamine {HA}) was added in an ice bath, and an orange precipitate of n = 1 L-PbI was formed. To synthesize a higher member of iodide 2D LHPs, a solution of the A-site cation iodide salt (AI = MAI or FAI) was prepared in a separate vial by dissolving the salt in HI. This AI solution was subsequently added into the solution containing the orange precipitate to form a combined solution. Additional volume of HI may be added before the final solution was heated on a hotplate set at 130 °C for 4 min or until clear. Crystals of iodide 2D LHPs were then grown by storing the clear solution in a thermos filled with hot sand at 110 °C. After a day, the crystals were isolated by suction filtration and dried under reduced pressure for at least 12 h. The quantities of reagents used for making iodide 2D LHPs can be found in Table 3-1.

Synthesis of Bromide 2D LHPs. To synthesize bromide 2D LHPs, lead (II) bromide ($PbBr_2$) was prepared by dissolving PbO (99.9+% (trace metal basis) <10 µm, powder, Acros Organics) in hydrogen bromide (HBr) solution (ACS reagent, 48%, MilliporeSigma) under reflux for 15 min. A small volume of this solution was then transferred into a small vial. Without any addition of H_3PO_2, a small volume of BA was added in an ice bath and a white precipitate of n = 1 BA-PbBr was formed. In a separate vial, a solution of the A-site cation bromide salt (ABr = MABr) was prepared by dissolving the salt in HBr. This ABr solution was subsequently added into the solution containing the white precipitate to form a combined solution. Additional volume of HBr was added before the final solution was heated on a hotplate set at 130 °C for 4 min or until clear. Crystals of bromide 2D LHPs were then grown by storing the clear solution in a thermos filled with hot sand at 110 °C. After a day, the crystals were isolated by suction filtration and dried under reduced pressure for at least 12 h. The quantities of reagents used for making bromide 2D LHPs can be found in Table 3-6.

Table 3-6. Reagent quantities used for bromide 2D LHP syntheses.

	***n* = 1 BA-PbBr**	***n* = 2 BA-MAPbBr**	***n* = 3 BA-MAPbBr**
PbO mass (g)	0.558	0.279	0.279
Number of moles of PbO (mmol)	2.5	1.25	1.25
HBr volume to make $PbBr_2$ solution (mL)	3	1.5	1.5
ABr mass (g)	-	0.0700	0.0933
Number of moles of ABr (mmol)	-	0.625	0.833
ABr% w.r.t. stoichiometric amount	-	100	100
HBr volume to make ABr solution (mL)	-	0.4	0.4
L volume (µL)	247	74	37
Number of moles of L (mmol)	2.5	0.75	0.375
L% w.r.t. stoichiometric amount	50	60	45
Additional volume of HBr added to the combined solution	5	0.5	0.5
Total volume of HBr used (mL)	8	2.4	2.4

Mechanical Exfoliation. Exfoliated flakes of 2D LHPs were prepared by tapes. A crystal of 2D LHPs was mounted on a piece of single-sided adhesive tape (Ultron Systems, 1007R-6.0). The two ends of the tape were then folded together and separated to exfoliate the crystal. This step was repeated 5–10 times before the tape was gently pressed on a substrate. After the tape was removed from the substrate, thin flakes of 2D LHPs were transferred onto the substrate.

Absorption Measurement. Transparent flakes of 2D LHPs were mechanically exfoliated onto a fused quartz substrate for Abs measurements. The Abs spectra were obtained using a transmission mode on a home-built microabsorption setup. An incident white light beam (Thorlabs, SLS201L) was focused onto the sample through an inverted lens (10×, NA = 0.25). The transmitted light was collected by a 100× lens (NA = 0.90) and analyzed by a Raman spectrometer (T64000, HORIBA) with 150 g/mm grating. The absorbance (A) of a 2D LHP sample was calculated by $A = -\log_{10}(I/I_0)$, where I and I_0 are the transmitted light intensities on the 2D LHP flake and the nearby quartz substrate.

Photoluminescence. Steady-state PL measurements were performed on an inverted microscope (Nikon, Ti-U Eclipse) in air or vacuum. The samples were excited by focusing the output of a 405 nm pulsed laser diode (Picoquant, LDHDC-405M, 2.5 MHz repetition rate) by an objective lens (Nikon, CFI S Plan Fluor ELWD, 40×, 0.6 NA) to <1 μm spot. The PL was collected in the epi configuration and passed through a dichroic mirror and a long-pass filter. Then, it was directed into a spectrograph (SP-2500, Princeton Instruments) mounted with a cooled charge-coupled detector (Princeton Instruments, Pixis). Laser power was kept below ~125 nW throughout the measurements. For the measurement on n = 1 BA-PbBr, the excitation source was replaced by a 375 nm LED (Thorlabs, M375F2). PL measurements under vacuum were achieved by mounting 2D LHP crystals in a microscopy cryostat (Janis Research, ST-500), and the sample was cooled

by flowing liquid helium through a cold finger attached to the base of the sample. PL spectra measured under air and vacuum were identical.

Powder X-ray Diffraction. PXRD data were collected using a PANalytical X'Pert Pro MPD X-ray diffractometer (Cu Kα radiation, λ = 1.54184 Å) with high-speed Bragg–Brentano optics. A 0.04 rad soller slit, a 1° anti-scatter slit, a 10 mm mask, and a programmable divergence slit with an illuminated length of 6 mm were used in the incident beam path. The diffracted beam optics included a 0.04 rad soller slit, a Ni filter and an automatic receiving slit. The detector was an ultrafast X'Celerator RTMS detector. The angular step in 2θ was 0.04°. For temperature-dependent measurements, an Oxford Cryosystems PheniX cooler and an Anton Paar HTK-1200N heating stage were used. All temperature-dependent measurements were taken during heating, and the reversibility was checked by comparing room-temperature data at the beginning and the end of the experiment. At each temperature, the temperature was stabilized for ~15 min during the data collection.

Single-Crystal X-ray Crystallography. A crystal was mounted on a diffractometer at 300 K. The temperature was raised/lowered down to measurement temperatures at a rate of 5 K/h before the data sets were collected. The intensities of the reflections were collected by means of a Bruker APEX II CCD diffractometer (Mo Kα radiation, λ = 0.71073 Å) equipped with an Oxford Cryosystems nitrogen flow apparatus. The collection method involved 0.5° scans in ω at 28° in 2θ. Data integration down to 0.84 Å resolution was carried out using SAINT V8.37A (Bruker diffractometer, 2016) with reflection spot size optimization. Abs corrections were made with the program SADABS (Bruker diffractometer, 2016). The structure was solved by the intrinsic phasing methods and refined by least-squares methods F^2 using SHELXT-2014[152] and SHELXL-

2014[153] with the OLEX 2 interface.[154] Non-hydrogen atoms were refined anisotropically, and hydrogen atoms were allowed to ride on the respective atoms. Further details on refinement can be found in the CIF files available on the database of The Cambridge Crystallographic Data Center (CCDC 1880158-1880170). Visualization of crystallographic data was performed by using VESTA.[155]

Chapter 4 Two Origins of Broadband Emission in Multilayered 2D Lead Iodide Perovskites

The basis of this chapter has been published as:

W. Paritmongkol, E.R. Powers, N.S. Dahod, W.A. Tisdale "Two Origins of Broadband Emission in Multilayered 2D Lead Iodide Perovskites" ***J. Phys. Chem. Lett.*** 11, 8565-8572 (2020).

4.1 Introduction

Two-dimensional lead halide perovskites (2D LHPs) have been shown to exhibit broadband emission covering the entire visible spectrum, suggesting their use as a single-source white-light phosphor.[3,138,139,156–160] Since the first demonstration of 2D LHPs with broadband emission in 2014,[159] broadband emission has also been found in other types of halide perovskites including zero-dimensional,[161] lead-free,[162–167] and double perovskites.[168,169]

Two mechanisms have been proposed to account for the broadband emission in halide perovskites: defect-associated emission, and emission from self-trapped excitons (STEs).[59,170] Defect-associated emission[171–174] arises from excitons trapped by a finite number of semipermanent crystal defects, whereas STEs[160,175–180] are excitons trapped by the lattice distortion induced by the excitons themselves. Both mechanisms rely on the same assumption that when an exciton is trapped, the excited-state energy is strongly red-shifted compared to the ground state and broadband emission arises from transitions between multiple vibronic bands.[181]

Although it is generally believed that STEs are the main cause of broadband emissions in chloride and bromide 2D LHPs, there is still a debate on the origin of broadband emission in the

iodide counterpart.[59,170,174,178] Defect-associated emission by iodide interstitials[171,173] and surface defects,[172] as well as STEs facilitated by tin doping have been proposed.[178,182] Furthermore, most studies so far have been conducted on single-layered 2D LHPs and systematic studies on multilayered 2D LHPs with different chemical constituents are still lacking.[59,170] Such systematic composition-dependent studies can be helpful in elucidating the underlying photophysics regardless of the identity of the halide anions and may guide design strategies for the rational engineering of broadband emission.

To address this debate and expand the body of data on multilayered 2D LHPs, we used temperature-dependent photoluminescence (PL) spectroscopy and transient absorption (TA) spectroscopy to investigate the broadband emission in six iodide 2D LHPs with varying quantum-well thicknesses (n), A-site cations, and organic spacers: $(C_4H_9NH_3)_2(CH_3NH_3)Pb_2I_7$, $(C_4H_9NH_3)_2(CH_3NH_3)_2Pb_3I_{10}$, $(C_4H_9NH_3)_2(CH_3NH_3)_3Pb_4I_{13}$, $(C_4H_9NH_3)_2(NH_2CHNH_2)Pb_2I_7$, $(C_6H_{13}NH_3)_2(CH_3NH_3)Pb_2I_7$, and $(C_6H_5CH_2CH_2NH_3)_2(CH_3NH_3)Pb_2I_7$. For convenience, these chemical formulas will be abbreviated as n = 2 BA-MAPbI, n = 3 BA-MAPbI, n = 4 BA-MAPbI, n = 2 BA-FAPbI, n = 2 HA-MAPbI, and n = 2 PEA-MAPbI, respectively. The crystals of these 2D LHPs were synthesized by a cooling-induced crystallization method (see Session 4.7), and their purities were confirmed by PL spectroscopy (Figure 4-1). Crystal structures of some of these compounds were reported in an earlier work (Chapter 3).[183]

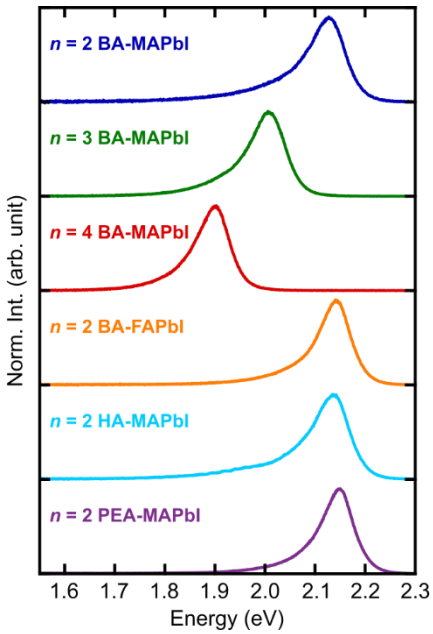

Figure 4-1. Room-temperature photoluminescence spectra of n = 2 BA-MAPbI (blue), n = 3 BA-MAPbI (green), n = 4 BA-MAPbI (red), n = 2 BA-FAPbI (orange), n = 2 HA-MAPbI (cyan), and n = 2 PEA-MAPbI (purple). All samples show single emission peaks, implying that they do not contain impurities due to lower-n and higher-n 2D LHPs.

4.2 Temperature-Dependent Photoluminescence of Iodide 2D LHPs

Figure 4-2 shows intensity-normalized PL spectra from exfoliated 2D LHP crystals as a function of sample temperature from 5 K up to 300 K. PL line width broadening was observed across all samples as temperature increased. All samples showed a single excitonic emission peak near room temperature, which split into two or more peaks at temperatures below ~70 K. Moreover, continuous temperature-dependent shifts in peak positions were observed in all samples, with some abrupt jumps in peak position marked by structural phase transitions.[88,90,136,183] In addition, broad PL emission between ~1.2 and ~1.7 eV was observed at low temperature in all samples but was more prominent in n = 2 samples.

The discontinuities in peak positions observed in Figure 4-2 are the results of structural phase transitions.[88,90,136,183] In our previous publication,[136] we showed that the transitions near room

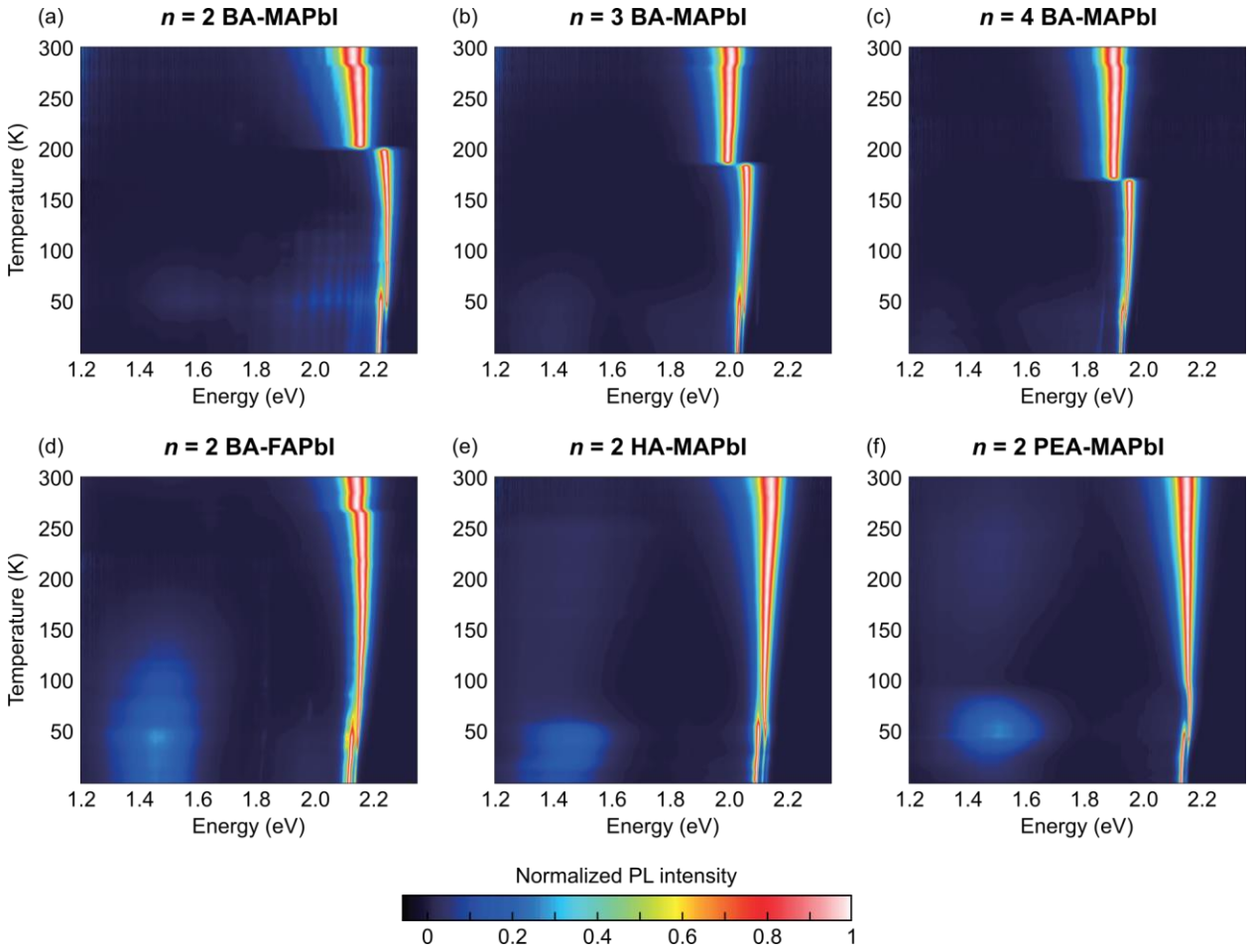

Figure 4-2. Temperature-dependent photoluminescence (PL) spectra of n = 2 BA-MAPbI, n = 3 BA-MAPbI, n = 4 BA-MAPbI, n = 2 BA-FAPbI, n = 2 HA-MAPbI, and n = 2 PEA-MAPbI. The PL spectra were recorded at 5, 7, 10, and up to 300 K with 5-K steps. Each spectrum has been normalized with respect to its maximum-intensity feature following careful wavelength-dependent sensitivity calibration and proper wavelength-to-photon-energy conversion. MA = methylammonium; BA = butylammonium; FA = formamidinium; HA = hexylammonium; PEA = phenylethylammonium.

temperature at 280-285 K for n = 2-4 BA-MAPbI, and at 265-270 K for n = 2 BA-FAPbI correspond to the melting/freezing transition in the organic spacer layers. On the other hand, the low-temperature transitions at 170-205 K for n = 2-4 BA-MAPbI are believed to be similar to the tetragonal-to-orthorhombic phase transition in bulk $MAPbI_3$.[90] No discontinuity in the peak position was observed for n = 2 HA-MAPbI in agreement with our previously reported differential scanning calorimetry and temperature-dependent powder X-ray diffraction studies.[136,183] Similarly,

because n = 2 PEA-MAPbI showed no discontinuity in the peak position, we conclude that n = 2 PEA-MAPbI underwent no phase transition between 5 and 300 K.

4.3 Broadband Emission in Iodide 2D LHPs

An interesting feature observed across all of the investigated 2D LHPs is the broad emission at low temperature. Specifically, for n = 2-4 BA-MAPbI, two broad emission (BE) features were observed in each sample: the first (labeled "BE1") appeared directly below the free-exciton (FE)

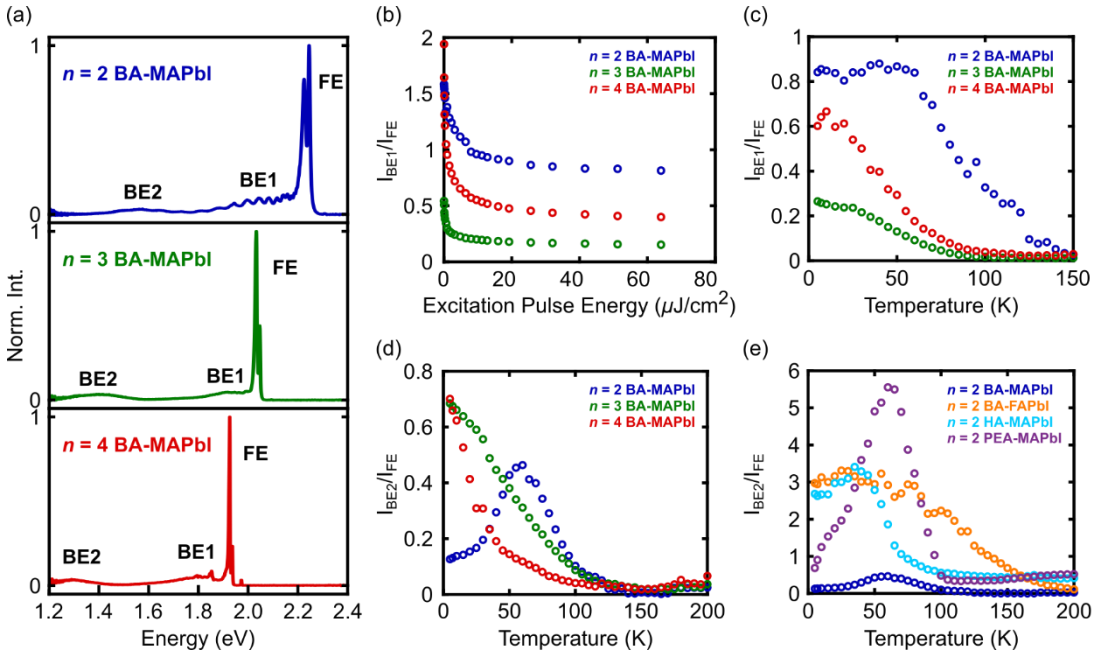

Figure 4-3. *Analysis of PL intensities.* (a) PL spectra of n = 2 BA-MAPbI at 60 K (blue), n = 3 BA-MAPbI at 5 K (green), and n = 4 BA-MAPbI at 5 K (red), showing the emission due to free exciton (FE) and two broad emission features (BE1 and BE2). (b) Power dependence of the relative emission intensities between BE1 and FE of n = 2-4 BA-MAPbI at 5 K. (c) Temperature dependence of the relative emission intensities between BE1 and FE of n = 2-4 BA-MAPbI. (d) Temperature dependence of the relative emission intensities between BE2 and FE of n = 2-4 BA-MAPbI. (e) Temperature dependence of the relative emission intensities between BE2 and FE of n = 2 BA-MAPbI (blue), n = 2 BA-FAPbI (orange), n = 2 HA-MAPbI (cyan), and n = 2 PEA-MAPbI (purple). All temperature-dependent studies were performed with laser excitation pulse energy of ~8 μJ/cm^2.

emission and the other (labeled "BE2") was observed in the ~1.2-1.7 eV range (Figure 4-3a). As *n* increased, the centers of these broad emission features shifted to lower energies in concert with the shift in FE emission energy.

To elucidate the underlying mechanisms of BE1 and BE2, we analyzed their integrated PL intensity ratios with respect to the integrated intensity of FE emission (I_{BE1}/I_{FE} and I_{BE2}/I_{FE}) (Figures 4-3b, 4-3c, 4-3d, and 4-3e). In the case of defect-associated emission, the number of crystal defects is presumed to be finite so that these states can become saturated at high laser excitation powers.[171–173,184] Moreover, it is expected that the activation barrier between free-exciton and defect electronic states is one-way; that is, free excitons will become trapped without having to cross a significant energy barrier whereas trapped excitons require energy to become free (Figure 4-4). This behavior gives rise to an increasing ratio of defect-associated emission to free-exciton emission at low temperature.

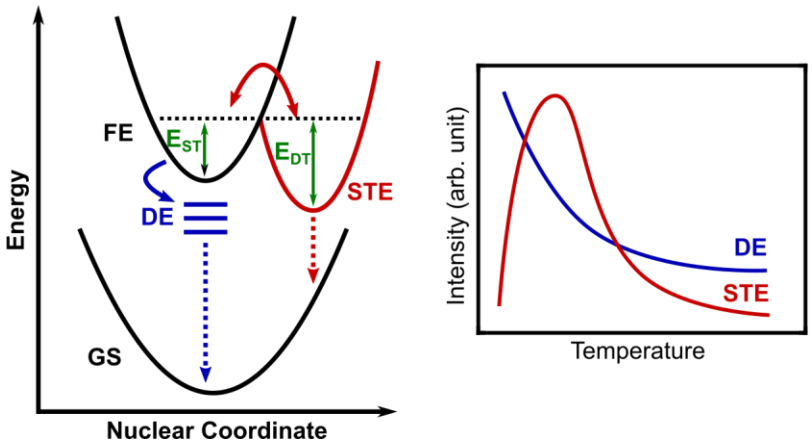

Figure 4-4. Diagram showing the energy levels of free exciton (FE), self-trapped exciton (STE), defect (DE) and ground state (GS). FE can readily be trapped by defect states without crossing an energy barrier whereas thermal energy is required to release excitons from DE states. Hence, defect-associated emission is expected to monotonically increase at low temperature. On the other hand, energy barriers of self-trapping (EST) and detrapping (EDT) need to be overcome to transition between FE and STE. Since the STE state is lower in energy compared to the free state, EDT is higher than EST, resulting in a characteristic rise-and-decay intensity of emission from STE.

For n = 2-4 BA-MAPbI, I_{BE1}/I_{FE} decreased monotonically with increasing laser excitation power and showed evidence of saturation at high laser excitation powers (Figure 4-3b). The same ratio also increased monotonically as the temperature was lowered (Figure 4-3c), suggesting emission from defect-bound exciton to be the cause of BE1. This excitonic nature is confirmed by the linear behavior of power-dependent PL emission intensity (Figure 4-5). In addition, we found that BE1 was suppressed in n = 2 BA-FAPbI, n = 2 HA-MAPbI, and n = 2 PEA-MAPbI (Figures 4-2 and 4-6), implying that the defect formation can be controlled by A-site cations and organic spacers.

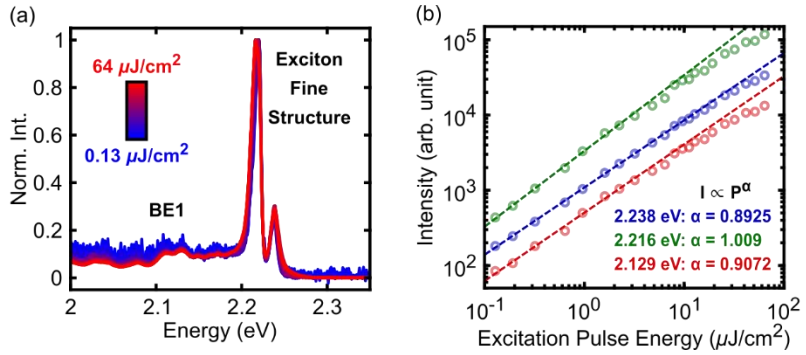

Figure 4-5. *Power-dependent PL spectroscopy of n = 2 BA-MAPbI at 5 K.* (a) Normalized PL spectra with laser excitation pulse energy ranging from 0.13 μJ/cm^2 to 64 μJ/cm^2. (b) Power-dependent PL emission intensities at 2.238 eV (blue), 2.216 eV (green), and 2.129 eV (red) with fits to $\boldsymbol{I \propto P^{\alpha}}$. The fits at low excitation pulse energy give $\boldsymbol{\alpha}$ values at three selected wavelengths close to 1, suggesting that both BE1 and exciton fine structure are excitonic in nature. The deviation from the linear trend at high laser excitation pulse energy is due to multi-exciton interaction.

On the other hand, STEs are caused by light-driven exciton-lattice interactions that could occur within any unit cell of an otherwise pristine crystal lattice.[59,158,169,176,181] In the STE model,[176,181] excitons move between FE states and STE states by crossing a potential energy barrier (Figure 4-4) associated with the energy required to deform the crystal atoms from their equilibrium positions. Because the STE state is lower in energy compared to the free state, the activation energy of detrapping is higher than the activation energy of trapping. This difference in activation energies

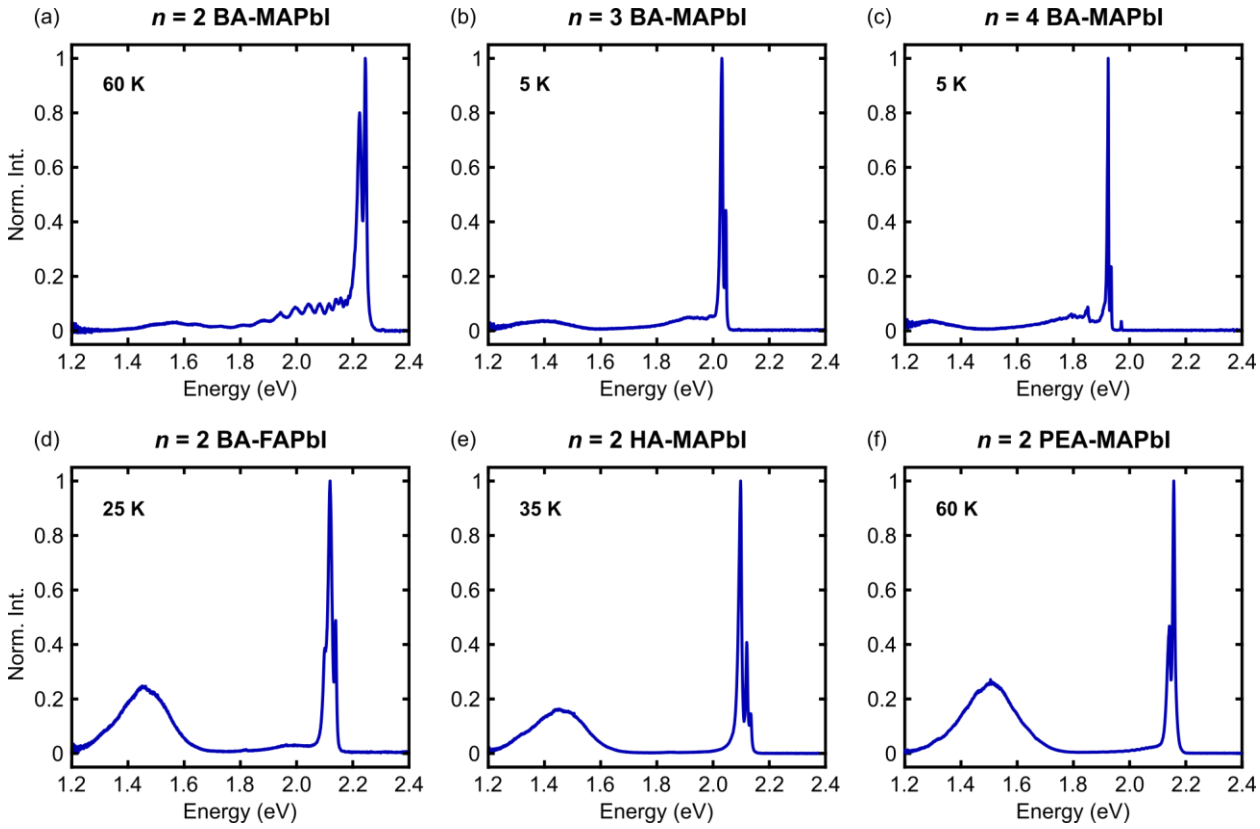

Figure 4-6. Photoluminescence spectra of $n = 2$-4 BA-MAPbI, $n = 2$ BA-FAPbI, $n = 2$ HA-MAPbI, and $n = 2$ PEA-MAPbI at temperatures with the highest self-trapped exciton emission.

thus leads to a nonmonotonic variation of the I_{STE}/I_{FE} ratio with changing sample temperature. At high temperature, delocalization of the FE is entropically favored. As the sample temperature is reduced, Boltzmann statistics eventually favors localization of an STE leading to a higher I_{STE}/I_{FE} ratio. However, as temperature is reduced even further, there is insufficient thermal energy available to overcome the activation energy for self-localization and the I_{STE}/I_{FE} ratio decreases. This characteristic rise-and-decay behavior was observed in I_{BE2}/I_{FE} as a function of temperature in some samples (Figure 4-3d,e), signifying that STEs are the cause of BE2.

4.4 Confirming the Two Origins of Broadband Emission

To further support the assignment of BE2 to an STE, we performed PL spectroscopy with below-gap excitation. Because of the highly nonequilibrium lattice configuration, an STE cannot

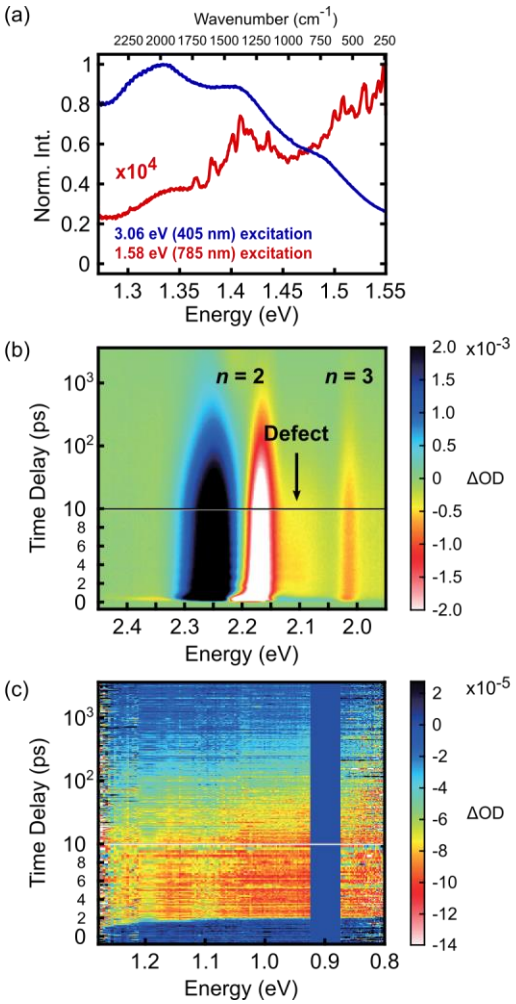

Figure 4-7. *Sub-gap excitation and transient absorption.* (a) PL spectra obtained from resonant (blue) and below-gap excitations (red) at 80 K of n = 2 PEA-MAPbI. (b) Visible and (c) NIR TA spectra of n = 2 BA-MAPbI at 80 K. Data near 0.9 eV in panel c were omitted because of strong scattering from the pump laser (λ = 450 nm) at 3λ. Similar spectra of other investigated samples can be found in Figures 4-10 and **Error! Reference source not found.**.

be directly excited from the ground state by below-gap light.[174] 4-7a shows the comparison between the PL spectra obtained by resonant (3.06 eV, 405 nm) and below-gap (1.58 eV, 785 nm) excitation in n = 2 PEA-MAPbI at T = 80 K. The shape of the spectrum under 1.58 eV excitation is markedly different from that observed with 3.06 eV excitation. Moreover, the spectrum at 1.58 eV excitation could be observed only at excitation intensities above ~10^4-10^5 W/cm^2 (Figure 4-8), which is ~10^3-10^4 times greater than the laser intensities required for resonant excitation. Consequently, we assign the 1.58 eV spectrum to nonresonant Raman scattering. This assignment

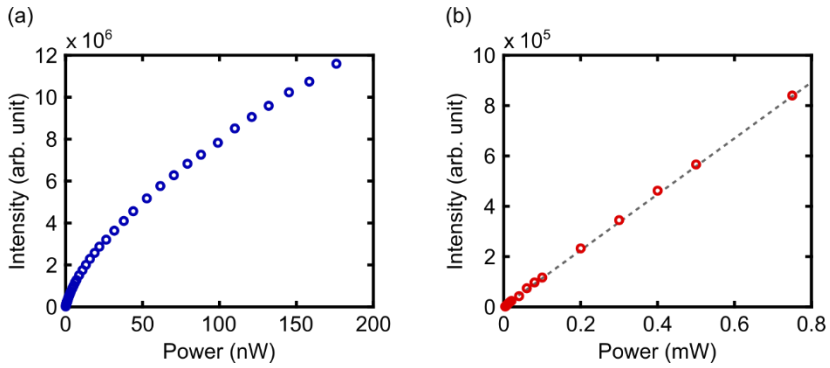

Figure 4-8. Comparison between resonant (3.06 eV, 405 nm) and below-gap excitations (1.58 eV, 785 nm). Power-dependent photoluminescence intensities of (a) resonant excitation and (b) below-gap excitation.

is further confirmed by a linear power dependence of the below-gap spectrum (Figure 4-8), which also rules out two-photon absorption as the origin of photoluminescence observed under below-gap excitation conditions. These observations strongly suggest that BE2 does *not* arise from the radiative transition of a deep trap state down to the ground state as suggested by Kahmann *et al.*[174]

Transient absorption (TA) spectroscopy has been used to probe the presence of both mid-gap structural defects and STEs by observing either a ground state bleach signal from the saturation of mid-gap defect states[172] or induced absorption corresponding to excitation of STEs to higher-lying excited states.[176] To confirm our assignment of BE1 and BE2, we performed TA measurements in both the visible and near-infrared (NIR) spectral regions. The samples used for TA were slightly different from those used for PL studies; to obtain semi-transparent thin films, the native crystals were sonicated in toluene and then drop cast onto a glass substrate (see Experimental section).

Figures 4-7b and 4-9 show the TA spectra of n = 2-4 BA-MAPbI in the visible region at 80 K. In each sample, there were four identifiable spectral features: three bleach signals and one induced absorption signal. For n = 2 BA-MAPbI, the highest-energy bleach signal at ~2.17 eV (Figure 4-7b) was accompanied by an induced absorption signal, and together appear at the excitonic transition, corresponding to ground-state bleach and band gap renormalization of the band-edge excitonic

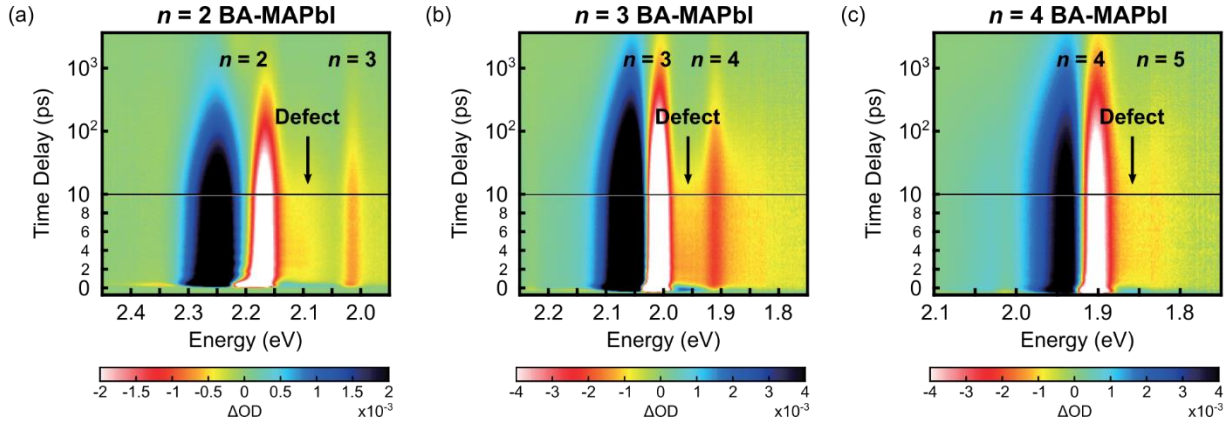

Figure 4-9. Transient absorption spectra in the visible region at 80 K of (a) n = 2 BA-MAPbI, (b) n = 3 BA-MAPbI, and (c) n = 4 BA-MAPbI. Labels indicate the signals due to the corresponding species and defects.

state. The second bleach feature, at ~2.10 eV, appeared directly below the first bleach signal and resembles a similar TA spectral feature previously assigned to surface trap states by Wu *et al.*[172] This TA spectral feature is also at the same energy as the BE1 emission feature, reinforcing its assignment to structural defects.

The final bleach feature in the visible TA spectrum of the n = 2 BA-MAPbI thin films (Figure 4-7b), observed at ~2.02 eV, is weaker than the primary excitonic transition and close in energy to the expected location of an n = 3 excitonic transition. We assign this to an n+1 impurity generated during the preparation of thin-film samples. Sonication of pure n = 2 crystals likely resulted in the generation of underpassivated surfaces and subsequent aggregation to form thicker-layer 2D LHPs.[26,183,185] We note that the starting crystals were pure as all of their photoluminescence spectra showed single emission peaks (Figures 4-1 and 4-2). For n = 3-4 BA-MAPbI (Figures 4-9b and 4-9c), similar analyses were performed to reach the same conclusions.

We also performed transient absorption in the NIR spectral window (λ = 950 – 1550 nm / 0.8 – 1.3 eV) to look for potential induced absorption signals associated with excitation of STEs to higher-lying states.[176] Interestingly, NIR TA spectroscopy did not reveal an induced absorption feature but rather a very weak (2 orders of magnitude weaker than the band-edge exciton transition),

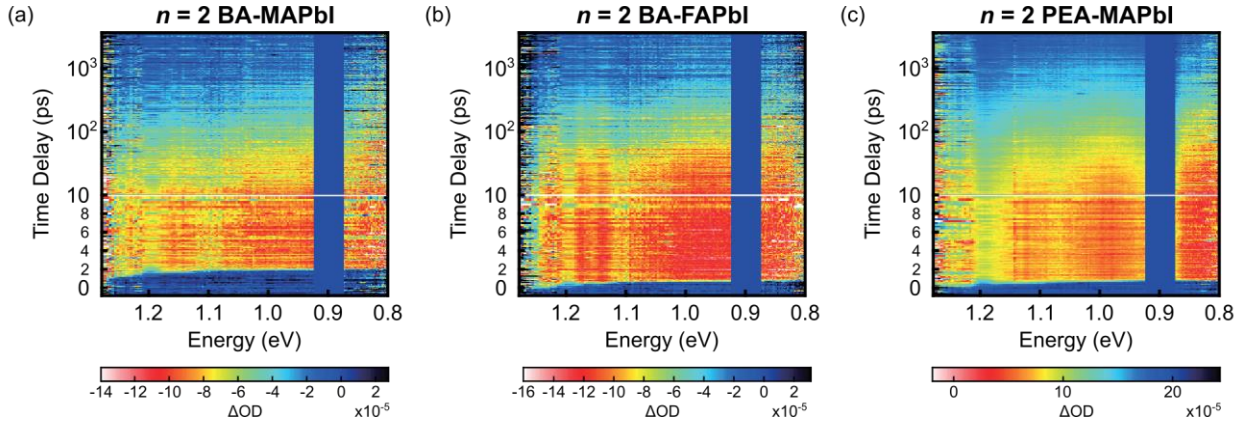

Figure 4-10. Transient absorption spectra in the NIR region at 80 K of (a) n = 2 BA-MAPbI, (b) n = 2 BA-FAPbI, and (c) n = 2 PEA-MAPbI. The region around 0.9 eV was omitted due to the scattering from pump laser.

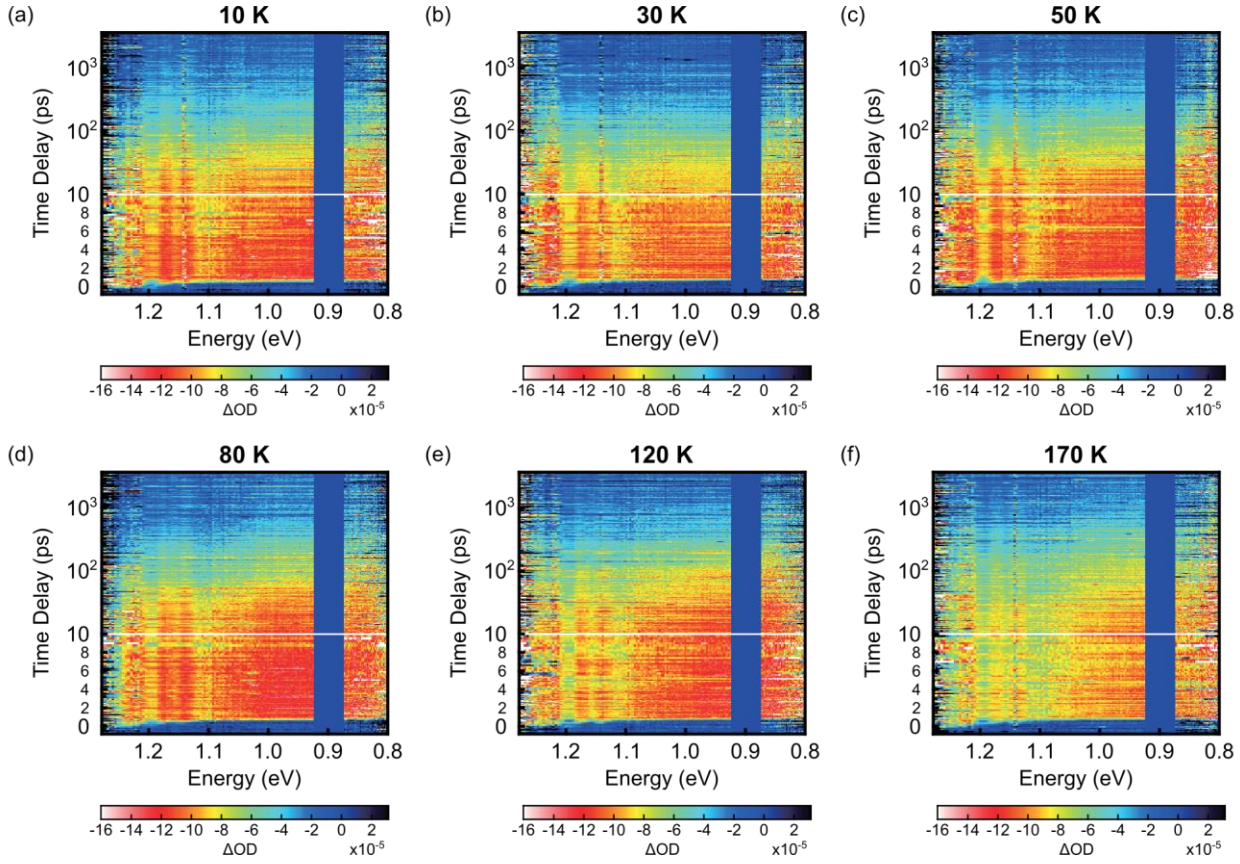

Figure 4-11. Transient absorption spectra in the NIR region at (a) 10 K, (b) 30 K, (c) 50 K, (d) 80 K, (e) 120 K, and (f) 170 K of n = 2 BA-FAPbI. The region around 0.9 eV was omitted due to the scattering from pump laser (λ = 450 nm) at 3λ.

unstructured increased transmission signal across all $n = 2$ samples regardless of the A-site cation or organic spacer cation (Figures 4-7c and 4-10). The lack of an induced absorption signal in the presence of STEs could be explained by forbidden transitions to higher-lying electronic states or the occurrence of such transitions outside our spectral observation window. Because the weak, unstructured signal appeared similarly across samples and over a broad temperature range from 10 to 170 K (Figure 4-11) – but were absent in a blank substrate – we assign the signal to pump-induced changes in refractive index.[186] We note that we were unable to assess stimulated emission from the STE because of limitations of the instrument detection window.

4.5 Trends in Self-Trapped Exciton Emission

Comparison of the I_{BE2}/I_{FE} of iodide 2D LHPs with varying quantum-well thicknesses and across different $n = 2$ 2D LHPs (Figures 4-3d and 4-3e) also showed interesting trends. As n increases, the I_{BE2}/I_{FE} maxima decreases in magnitude and shifts to lower temperatures. Replacing either the A-site cation or the organic spacer of $n = 2$ BA-MAPbI also resulted in a marked increase in the broadband emission intensity.

As the formation of STEs is driven by the strong interaction between FEs and phonons,[170,177,187] we attempted to extract exciton-phonon coupling strengths from the temperature-dependent PL line widths of FE emission peaks. The temperature-dependent line widths were analyzed by fitting the FE line shape to a convolution of Lorentzian and Gaussian functions to account for homogeneous and inhomogeneous broadening, respectively.[188] To extract the homogeneous contribution due to exciton-phonon interactions, we fitted the spectra at 5 K and kept the Gaussian (inhomogeneous) component constant at all higher temperatures. The temperature-dependent Lorentzian component then contains useful information about exciton-phonon coupling. Note that at low temperature, the PL emission peak of each sample splits into multiple peaks (Figure 4-12).

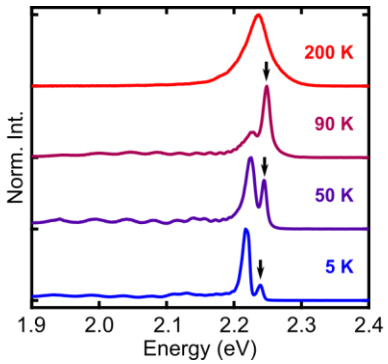

Figure 4-12. Selected photoluminescence spectra of $n = 2$ BA-MAPbI at 5 K, 50 K, 90 K and 200 K, showing multiple excitonic peaks at low temperature which were fitted by a multiple-peak model. Arrows indicate the main excitonic peak whose line width broadening is used for subsequent line width broadening analysis.

To analyze line width broadening at low temperature, we performed the fitting with a multiple-peak model and focused on the high energy peak because it becomes the dominant feature at higher temperatures.

Figures 4-13a and 4-14 show the temperature-dependent homogeneous PL line width broadening of all six samples under investigation. While some discontinuation from either phase transitions or changes in the number of fitting peaks can be seen, we found that the half width at half-maximum of the homogeneous PL line width (Γ_{homo}) was best described by a combination of a temperature-independent PL line width Γ_0 and a contribution from a single high-energy phonon mode:[188–192]

$$\Gamma_{homo}(T) = \Gamma_0 + \frac{\Gamma_{ph}}{\left[\exp\left(\frac{E_{ph}}{k_B T}\right) - 1\right]}. \quad (4\text{-}1)$$

Here, Γ_{ph} is an exciton-phonon coupling strength, E_{ph} the energy of the vibrational mode responsible for PL line width broadening, and k_B the Boltzmann constant. The extracted values of Γ_{ph} and E_{ph} (Figure 4-13b and Table 4-1) decrease with increasing n. E_{ph} was near ~12 meV and Γ_{ph} was near ~20 meV for all $n = 2$ samples (Table 4-1) except $n = 2$ BA-MAPbI; the

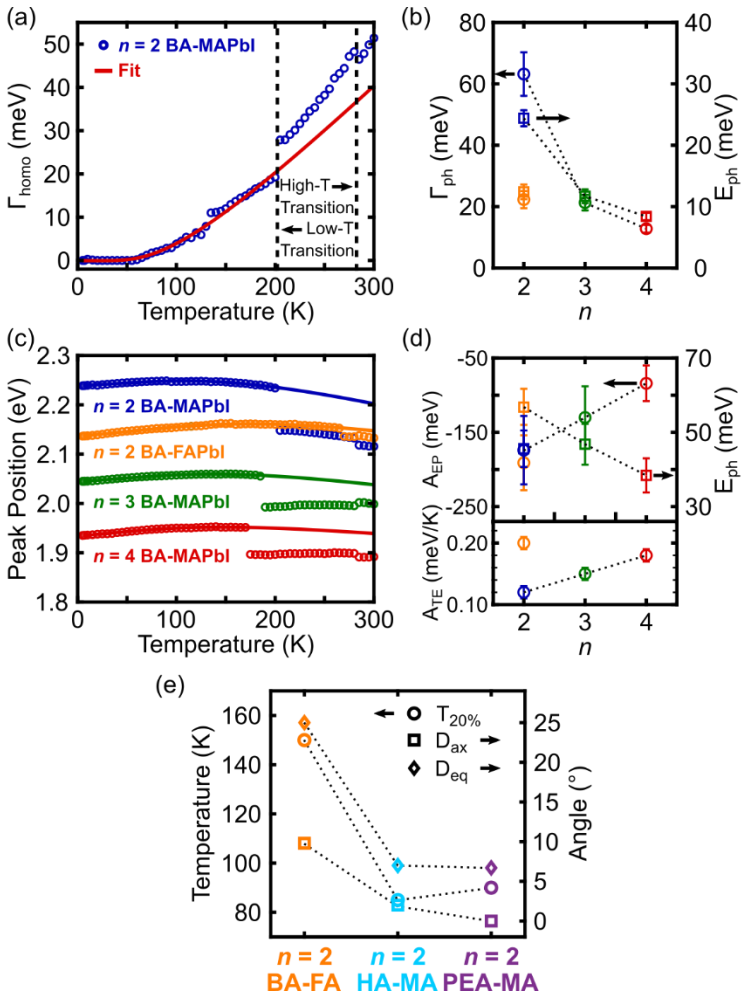

Figure 4-13. Correlation of STE emission to exciton-phonon coupling and structural deformation. (a) Homogeneous line width broadening of n = 2 BA-MAPbI. The solid line is the fit to Equation 4-1. The homogeneous line width broadening of other investigated 2D LHPs can be found in Figure 4-14. (b) Extracted $\boldsymbol{\Gamma_{ph}}$ and $\boldsymbol{E_{ph}}$ values of n = 2-4 BA-MAPbI and n = 2 BA-FAPbI, showing the decreasing trends of the two parameters with respect to layer thickness, n. The extracted values of other investigated samples can be found in Table 4-1. (c) Temperature-dependent photoluminescence peak positions of n = 2-4 BA-MAPbI and n = 2 BA-FAPbI. The solid lines are the fits of the peak positions of the lowest-temperature phases to Equation 4-2. (d) Extracted $\boldsymbol{A_{EP}}$, $\boldsymbol{A_{TE}}$, and $\boldsymbol{E_{ph}}$ values of n = 2-4 BA-MAPbI and n = 2 BA-FAPbI. $\boldsymbol{A_{EP}}$ and $\boldsymbol{E_{ph}}$ have higher magnitudes in thinner (lower-n) samples whereas the trend in $\boldsymbol{A_{TE}}$ is the opposite. The extracted values of other investigated samples can be found in Table 4-2. (e) Correlation between temperatures with significant STE emission and structural distortions across n = 2 iodide 2D LHPs. $T_{20\%}$ is the highest temperature where I_{BE2}/I_{FE} is above 20% of the maximum I_{BE2}/I_{FE}. D_{ax} and D_{eq} are the distortion of Pb-(μ-I)$_{ax}$-Pb angle and the maximum distortion of out-of-plane Pb-(μ-I)$_{eq}$-Pb angle away from 180°, respectively. Structural data were obtained from crystallographic information reported in refs 32 and 52.

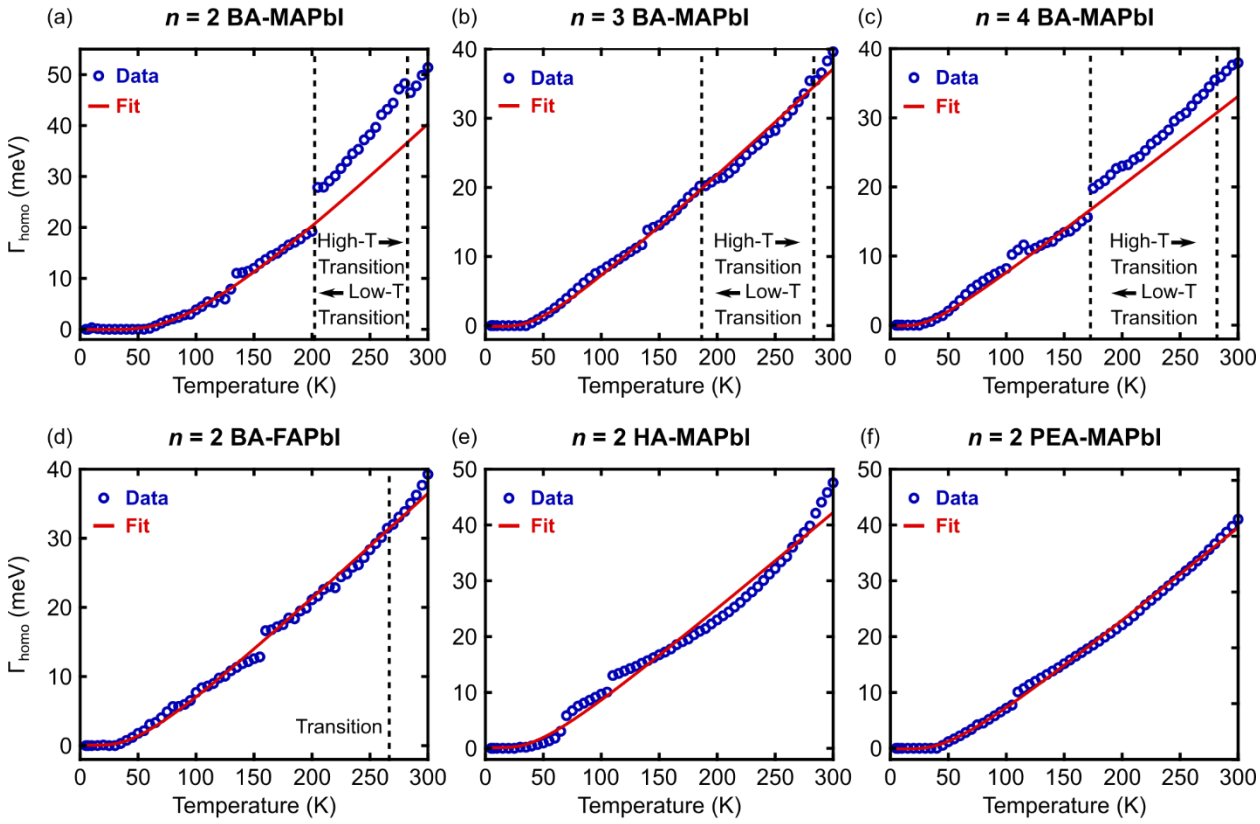

Figure 4-14. Homogeneous line width broadening of n = 2-4 BA-MAPbI, n = 2 BA-FAPbI, n = 2 HA-MAPbI, and n = 2 PEA-MAPbI, and their corresponding fits with contribution from high-energy phonons.

Table 4-1. Summary of extracted $\boldsymbol{\Gamma_{ph}}$ and $\boldsymbol{E_{ph}}$ values of n = 2-4 BA-MAPbI, n = 2 BA-FAPbI, n = 2 HA-MAPbI, and n = 2 PEA-MAPbI.

Sample	Γ_{ph} (meV)	E_{ph} (meV)
n = 2 BA-MAPbI	63.2 ± 7.1	24.4 ± 1.3
n = 3 BA-MAPbI	21.3 ± 2.5	11.7 ± 1.1
n = 4 BA-MAPbI	12.8 ± 1.3	8.4 ± 0.6
n = 2 BA-FAPbI	22.3 ± 2.8	12.4 ± 1.2
n = 2 HA-MAPbI	23.0 ± 7.9	11.3 ± 3.2
n = 2 PEA-MAPbI	25.5 ± 2.5	12.8 ± 1.0

higher Γ_{ph} and E_{ph} values extracted from the n = 2 BA-MAPbI data may be an artifact arising from the nearby presence of intense broadband emission directly below the narrow peaks at low

temperatures. However, the decreasing trends in Γ_{ph} and E_{ph} with increasing n is clear if the comparison is performed on other n = 2 samples.

Similar trends in exciton-phonon coupling strength and energy of the dominant phonon mode can also be obtained through analysis of the temperature-dependent FE peak position. Using a quasi-harmonic approximation, the temperature-dependent band gap, $E_g(T)$, can be described by[193–196]

$$E_g(T) = E_0 + A_{TE}T + A_{EP}\left(\frac{2}{\exp\left(\frac{E_{ph}}{k_B T}\right)-1}+1\right). \quad (4\text{-}2)$$

Here, E_0 is the unrenormalized band gap, and A_{TE} and A_{EP} determine the strengths of thermal expansion and exciton-phonon coupling, respectively. E_{ph} is the energy of the vibrational mode responsible for the temperature-dependent trend, while k_B is the Boltzmann constant. Assuming that the exciton binding energy is independent of temperature, temperature-dependent band gaps can thus be represented by shifts in excitonic PL peaks. Figure 4-13c shows the temperature-dependence of PL peak positions of n = 2-4 BA-MAPbI and n = 2 BA-FAPbI, and their corresponding fits with Equation 4-2 on the lowest-temperature phases. The extracted values of A_{EP} and E_{ph} (Figure 4-13d and Table 4-2) decrease with increasing n, agreeing with the decreasing trends of Γ_{ph} and E_{ph} from the line width broadening analysis. Furthermore, A_{TE}

Table 4-2. Summary of extracted $\boldsymbol{E_0}$, $\boldsymbol{A_{TE}}$, $\boldsymbol{A_{EP}}$, and $\boldsymbol{E_{ph}}$ values of n = 2-4 BA-MAPbI and n = 2 FA-MAPbI.

Sample	E_0 (eV)	A_{TE} (meV/K)	A_{EP} (meV)	E_{ph} (meV)
n = 2 BA-MAPbI	2.41 ± 0.05	0.12 ± 0.01	-174 ± 46	45.6 ± 4.9
n = 3 BA-MAPbI	2.17 ± 0.05	0.15 ± 0.01	-130 ± 42	46.8 ± 5.5
n = 4 BA-MAPbI	2.02 ± 0.02	0.18 ± 0.01	-84 ± 24	38.4 ± 4.6
n = 2 BA-FAPbI	2.33 ± 0.04	0.20 ± 0.01	-191 ± 37	56.8 ± 4.8

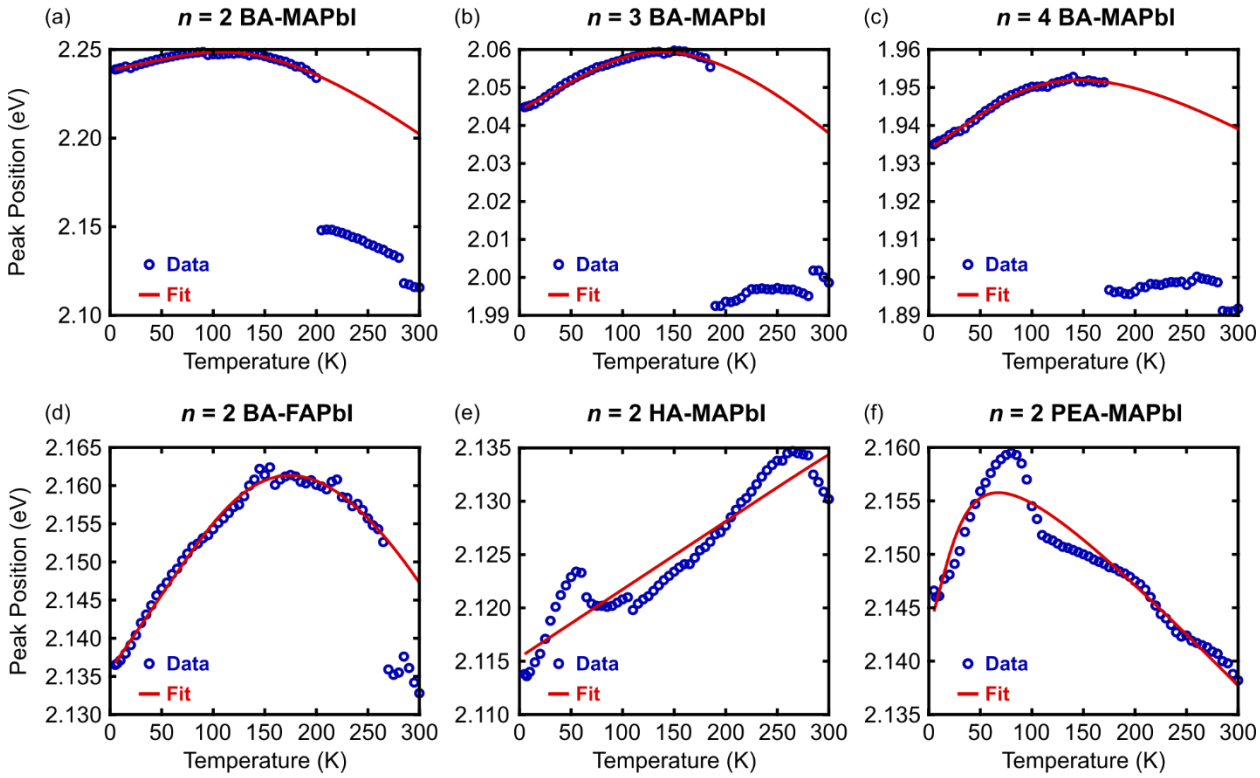

Figure 4-15. Temperature-dependent photoluminescence peak positions of *n* = 2-4 BA-MAPbI, *n* = 2 BA-FAPbI, *n* = 2 HA-MAPbI, and *n* = 2 PEA-MAPbI, and their corresponding fits.

(Figure 4-13d and Table 4-2) shows an opposite trend with higher values with increasing *n*, which may be related to the larger volume per perovskite layer in higher-*n* 2D LHPs.

Both the temperature-dependent line width analysis and the temperature-dependent peak position analysis indicate that exciton-phonon coupling strength and energy of the dominant phonon mode decrease with increasing *n*. In our experiments, stronger electron-phonon coupling was correlated with stronger STE emission in *n* = 2-4 BA-MAPbI. Theoretical calculations have shown that for 2D materials, increasing exciton-phonon coupling can change STEs from being metastable states with low-energy barriers to being stable states with high-energy barriers.[187] As a result, the I_{BE2}/I_{FE} maxima have increasing magnitudes and shift to higher temperatures as *n* decreases. Following this trend, this finding explains why broadband white-light emission in 2D LHPs is largely observed in 2D LHPs with *n* = 1.[138,156–160]

Unlike the analysis of temperature-dependent line width broadening, the results of temperature-dependent peak positions suggest that replacing the A-site cation or the organic spacer cation while keeping the same *n* can influence the nature of exciton-phonon coupling (Figures 4.13d and 4-15, and Table S3). Because exciton-phonon coupling alone fails to describe the change in STE emission as a function of A-site cation and organic spacer across $n = 2$ samples (Figure 4-3e), we consider other explanations. In particular, exciton self-trapping is thought to occur more readily in 2D perovskite materials whose ground-state lattice configurations exhibit significant structural distortion.[138,139,160,177,197,198] Several correlations between STE emission and structural distortion parameters – such as octahedral elongation,[138,197] octahedral angle variance,[138,197] and out-of-plane distortion of Pb-(μ-Br)-Pb angles[160] – have been proposed. To explain the trend across $n = 2$ samples, we focused our attention on the temperature at which STE emission starts to become a significant contribution to the overall emission intensity – quantified by the parameter $T_{20\%}$, or the highest temperature where I_{BE2}/I_{FE} is above 20% of the maximum I_{BE2}/I_{FE}. We found that $T_{20\%}$ can be correlated with two Pb-(μ-I)-Pb distortion parameters: D_{ax} or the distortion of Pb-$(\mu\text{-I})_{ax}$-Pb angle away from 180° and D_{eq} or the maximum distortion of out-of-plane Pb-$(\mu\text{-I})_{eq}$-Pb angle away from 180° (Figure 4-13e). A recent calculation has suggested that STE is more favorable in perovskites with low electronic dimensionalities because they have flatter electronic bands, leading to heavy electrons and holes that can localize to form STEs with lower entropic penalty.[177] As the dispersion of electronic bands in multilayered 2D LHPs is influenced by both the bonding within and between layers of lead iodide octahedral, we found that emission from STEs is more prominent in $n = 2$ BA-FAPbI whose D_{ax} and D_{eq} are higher compared to those of other $n = 2$ samples (Figure 4-13e). Unfortunately, we could not extend this correlation of $T_{20\%}$ with D_{ax} and

D_{eq} to n = 2-4 BA-MAPbI because of the lack of crystallographic data on the low temperature phases that exhibit STE emission.[183,199]

Although the sample size is limited, another interesting idea emerging from the results presented in Figure 4-13e is that STE emissions and structural distortion are significantly affected by changing A-site cations from MA to FA, but they are less sensitive to the identities of organic spacers. This observation is strikingly different from the behaviors of n = 1 2D LHPs where organic spacers have been found to play a major role in excitonic emissions, STE emissions and structural distortion.[59,145,170] This dissimilarity might be explained by noting that unlike n = 1 2D LHPs, multilayered 2D LHPs contain A-site cations which support the Pb-I octahedral framework and make them less sensitive to steric strain imposed by the organic spacers nearby. As a result, structural distortion induced by A-site cations is the main component in tuning STE emission in multilayered perovskites.

Overall, the temperature-dependent trends in emission intensity, exciton-phonon coupling strength, and their correlation with structural distortions of the native perovskite lattice suggest STEs to be the primary cause of BE2. Moreover, sub-gap photoexcitation experiments (Figure 4-7a) rule out the possibility of permanent or quasi-permanent trap states as the origin of BE2. Nonetheless, it remains possible that the STE emission we observe is not purely intrinsic. As evidenced by the existence of the shallow emission feature BE1, structural defects are clearly present in these samples. The formation of STEs may be facilitated by the presence of existing structural defects within the lattice, so-called “extrinsic STEs”. We observe variation in the intensity of BE2 across samples (Figure 4-16), lending some support to the extrinsic STE hypothesis. The identity of these defects may be iodine interstitials, Sn doping, or light-induced defects as suggested by others.[59,173,178,182]

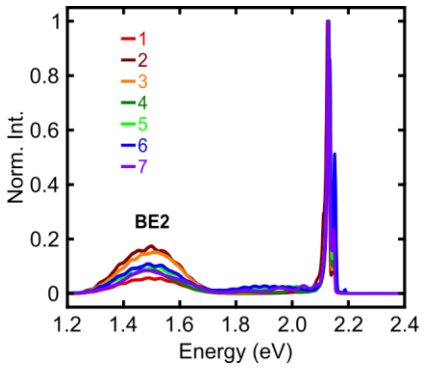

Figure 4-16. Location-dependent photoluminescence spectra at seven different areas of $n = 2$ PEA-MAPbI at 5 K.

4.6 Conclusions

In conclusion, we have shown by PL spectroscopy and TA spectroscopy that broadband emission in iodide 2D LHPs can arise from both defect-associated emission and STE emission. While the broadband emission from defect-associated emission appeared directly below the band-edge exciton emission, the STE emission was observed deep in the band gap in the near-infrared region. Moreover, we found that the relative intensity of STE emission to FE emission decreases in higher-*n* 2D LHPs in agreement with increasing exciton-phonon couplings obtained from analyses of temperature-dependent photoluminescence line widths and peak positions. Structural analysis also suggested that multilayered perovskites with higher structural distortions exhibit stable STE at higher temperatures, and structural distortion can be controlled by changing A-site cations. The trends across different LHP compositions observed in this work suggest strategies to enhance or suppress broadband emission through chemical constituents in multilayered 2D LHPs. For example, mixing A-site cations may be a way forward to engineer structural distortion to increase or decrease broadband emission in multi-layered 2D LHPs.

4.7 Methods

Synthesis of 2D LHP crystals. Crystals of 2D LHPs were prepared by the previously reported cooling induced crystallization.[183] A solution of lead(II) iodide (PbI_2) was prepared by dissolving lead(II) oxide (PbO, 99.9+%, (trace metal basis) <10 microns, powder, ACROS Organic) in 55% hydrogen iodide solution (HI, contains no stabilizer, ACS reagent, 55%, MilliporeSigma). Then, hypophosphorus acid (H_3PO_2) and a small volume of organic spacer (L) were then added, forming an orange precipitate of L_2PbI_4 in a bright yellow solution. In a separate vial, an iodide salt or methylammonium (MA) or formamidinium (FA) was dissolved in aqueous HI, before it was combined with the solution containing the orange precipitate. This mixed solution was then heated to 130 °C until it becomes clear. After that, it was allowed to cool to room temperature inside a thermos filled with hot sand at 110 °C to induce crystallization. Crystals were then collected by suction filtration and then dried under reduced pressure for at least 12 hours. The quantities of reagents used can be found in Table 4-3.

Sample preparation for temperature-dependent photoluminescence. To achieve a good thermal equilibrium during the temperature-dependent study, the crystals of 2D LHPs were exfoliated by tapes (3M) to be 5-30 μm thick as measured by profilometry (Bruker DXT Stylus Profilometer). Then, the exfoliated samples on tapes were directly attached onto the base of a microscopy cryostat (Janis Research, ST-500).

Temperature-dependent photoluminescence. Steady-state photoluminescence was performed by using a 405 nm diode laser (Picoquant, LDHDC-405M) at 2.5 MHz repetition rate as an excitation source on an inverted microscope (Nikon, Ti-U Eclipse). The excitation laser was focused to <1 μm spot by a 40x objective lens (Nikon, CFI S Plan Fluor ELWD), and the photoluminescence was detected by a spectrograph (SP-2500, Princeton Instruments) equipped

Table 4-3. Reagent quantities used for iodide 2D LHP syntheses.

	***n* = 2 BA-MAPbI**	***n* = 3 BA-MAPbI**	***n* = 4 BA-MAPbI**	***n* = 2 BA-FAPbI**	***n* = 2 HA-MAPbI**	***n* = 2 PEA-MAPbI**
PbO mass (g)	0.558	0.558	0.558	0.558	0.279	0.279
Number of moles of PbO (mmol)	2.5	2.5	2.5	2.5	1.25	1.25
HI volume to make PbI_2 solution (mL)	3	3	3	3	1.5	1.5
H_3PO_2 volume (µL)	425	425	425	425	213	213
AI mass (g)	0.1987	0.2650	0.2981	0.2150	0.1739	0.1739
Number of moles of AI (mmol)	1.25	1.67	1.875	1.25	1.09	1.09
AI% w.r.t. stoichiometric amount	100	100	100	100	175	175
HI volume to make AI solution (mL)	0.75	0.75	0.75	0.75	1	1
L volume (µL)	161	107	49	161	83	55
Number of moles of L (mmol)	1.625	0.997	0.5	1.625	0.625	0.4375
L% w.r.t. stoichiometric amount	65	65	40	65	50	35
Additional volume of HI added to the combined solution	0	0	0	0.75	0	0
Total volume of HI used (mL)	3.75	3.75	3.75	4.5	2.5	2.5

with a cooled charge-coupled detector (Princeton Instruments, Pixis). Sample cooling was achieved by flowing liquid helium through a cold finger attached to the base of the cryostat. All PL spectra shown were corrected for wavelength-dependent sensitivity and were converted from wavelength scale to energy scale by Jacobian transformation.[200] The excitation pulse energy was kept at ~8 µJ/cm^2 throughout unless otherwise stated.

Photoluminescence by below-gap excitation. The PL spectrum by below-gap excitation was obtained by using the same microscope and spectrograph as used for 405 nm excitation, but with a 785 nm narrow-band CW laser (Ondax) equipped with cleanup filters (Ondax) to remove undesirable amplified spontaneous emission

Sample preparation for transient absorption spectroscopy. The samples for transient absorption spectroscopy were prepared by sonicating ~5 mg of 2D LHP crystals in 5 mL of toluene followed by drop casting on a glass substrate.

Transient absorption spectroscopy. Transient absorption spectroscopy was performed using a Yb regenerative amplifier (Spectra-Physics Spirit) with 1040 nm output and 200 kHz repetition rate. Pump laser pulses centered at 450 nm were generated by directing a portion of 1040 nm light into a two-stage noncollinear optical parametric amplifier followed by a β-barium borate second harmonic generation stage (Spectra-Physics Spirit-NOPA). The pump laser pulses were compressed to ~50 fs full width at half maximum (FWHM) via a fused silica prism compressor, sent through a mechanical delay stage (Newport), and modulated at 5 kHz by a mechanical chopper (Thorlabs). Pump fluence was adjusted to ~1.0-1.2mW using neutral density filters. Visible probe laser pulses were generated by focusing a second portion of 1040 nm output on a 4 mm YAG window with a 50mm focal length lens. IR probe laser pulses were generated by focusing the second portion of 1040 nm output on a 6 mm YAG window with a 75mm focal length lens. Pump and probe laser pulses were then overlapped on film samples mounted in a tower cryostat (Janis Research, ST-100) with a spot diameter of ~160μm FWHM using a 200mm focal length concave mirror, and then the transmitted probe laser pulses were detected by either a visible or IR fiber-coupled spectrometer mounted with a high-speed CMOS camera (Ultrafast Systems). All data presented are the average of at least 10 scans to ensure dynamics did not change with laser exposure. The visible TA data were corrected for chirp in the probe pulse using a cross correlation between the pump and probe pulses in fused silica. Further, the average of 9 time points before time zero was background subtracted from each spectrum to remove the effects of spontaneous photoluminescence.

Chapter 5 Morphological Control of 2D Hybrid Organic-Inorganic Semiconductor AgSePh

The basis of this chapter has been prepared for a submission as:

W. Paritmongkol‡, W.S. Lee‡, W. Shcherbakov-Wu, S.K. Ha, T. Sakurada, S.J. Oh, W.A. Tisdale "Morphological Control of 2D Hybrid Organic-Inorganic Semiconductor AgSePh"

(‡ indicates equal contribution)

5.1 Introduction

Metal organic chalcogenolates (MOCs) of coinage metals are non-toxic covalently bound hybrid organic-inorganic materials with $[M(ER)]_n$ chemical formula, where M = Cu(I), Ag(I), Au(I); E = S, Se, Te; and R is an organic hydrocarbon.[91] Recently, silver phenylselenolate (AgSePh), a 2D member of the broader class of MOC coordination polymers, has gained a renewed interest as a novel class of hybrid organic-inorganic 2D semiconductors.[97,106–112] While AgSePh was discovered and its structure first refined almost 20 years ago,[113] its semiconducting properties were not realized until 2018.[97,106] Recent studies[97,106–112] have demonstrated many promising properties of AgSePh such as strong exciton binding energy,[109,111] chemical robustness,[97,107] non-toxic elemental composition,[97] in-plane anisotropy,[111] and low-cost and scalable synthetic methods.[106,110] Moreover, the covalent interaction between organic and inorganic layers potentially opens a new door to control the properties of 2D semiconductors through organic functionalization as shown in the thiolate analogues of AgSePh.[114]

Despite recent progress in the synthesis and characterization of AgSePh, the development of a synthetic approach capable of controlling the material morphology – as well as an understanding of the effect of crystal quality on the resulting optical and electrical properties – is needed. For anisotropic semiconductors, in particular, morphology control is essential for their deployment in electronic and optoelectronic devices. For example, perpendicular alignment of 1D or 2D materials to a substrate is favorable for thin-film solar cell applications where an efficient charge extraction is achieved via top and bottom electrodes.[23,201] In contrast, parallel alignment is required in lateral light-emitting devices, photodetectors, and field-effect transistors for maximizing light coupling as well as charge transport efficiencies between lateral electrodes.[202–204] Moreover, large crystals with improved crystalline quality are needed to realize high-performing electronic and optoelectronic devices by enhancing both inter- and intra-crystal charge transports.[205–209]

In this work, we report a simple chemical strategy for controlling crystal size and orientation as well as simultaneously improving crystalline quality in AgSePh films. The method, which is based on the vapor tarnishing approach first reported by Hohman & co-workers in 2018,[106] relies on introduction of a solvent vapor to assist the chemical transformation reaction between a metallic silver (Ag) film and diphenyl diselenide (Ph_2Se_2) vapor. In this study, 28 solvent vapors with different polarities, boiling points and functional groups were tested, showing a wide range of crystal sizes from <200 nm to >1 μm, and demonstrating varying crystal orientations between parallel and perpendicular to substrates. Chemicals such as dimethyl sulfoxide (DMSO) and propylamine ($PrNH_2$) – which are known to form complexes with Ag^+ ions in solution – yielded the largest crystal sizes (>5 μm) with completely parallel crystal orientation on the substrate. Systematic optical and optoelectronic characterizations were conducted on representative AgSePh films prepared with water (H_2O), DMSO, and $PrNH_2$. While they all showed similar optical

properties in terms of absorption and emission spectra, photoluminescence (PL) lifetime, and PL quantum yield (QY), AgSePh films prepared with DMSO showed a higher photoconductivity (by one order of magnitude) with the lowest dark conductivity and no ionic migration, suggesting the improvement of both crystal morphology and crystalline quality with fewer defects. The existence of persistent defect-derived mid-gap states was confirmed by sub-gap excitation photo-response in optoelectronic measurements and mid-gap emission in low-temperature PL spectroscopy, indicating that further improvement is still possible. Our findings introduce a new strategy for controlling AgSePh crystal morphology, provide insight into the chemical transformation reaction of metallic silver and the electronic properties of resulting AgSePh films, and enable electronic and optoelectronic devices based on MOCs.

5.2 Preparation of AgSePh Films

AgSePh crystallizes in the form of a 2D semiconductor consisting of stacks of 2D sheets bound together by interlayer van der Waals interactions (Figure 5-1a).[97,113] Each 2D sheet consists of a layer of Ag^+ ions arranged in a distorted hexagonal pattern and sandwiched between two layers of phenylselenolate anions ($PhSe^-$), with mostly covalent character to the Ag-Se bond. AgSePh films can be prepared by a vapor-phase chemical transformation method (Figure 5-1b).[106] In this method, an Ag film is deposited on an inert substrate (e.g., glass, silicon wafers, etc.) by thermal evaporation then placed inside a sealed pressure vessel containing Ph_2Se_2 powder. After heating the vessel to 80-180 °C for a few days, the film is transformed into a brightly luminescent homogeneous film of AgSePh. The time it takes for the reaction to complete depends largely on original Ag film thicknesses and the reaction temperatures. Increasing Ag film thickness will require a longer reaction time, whereas increasing the temperature will speed up the reaction. For

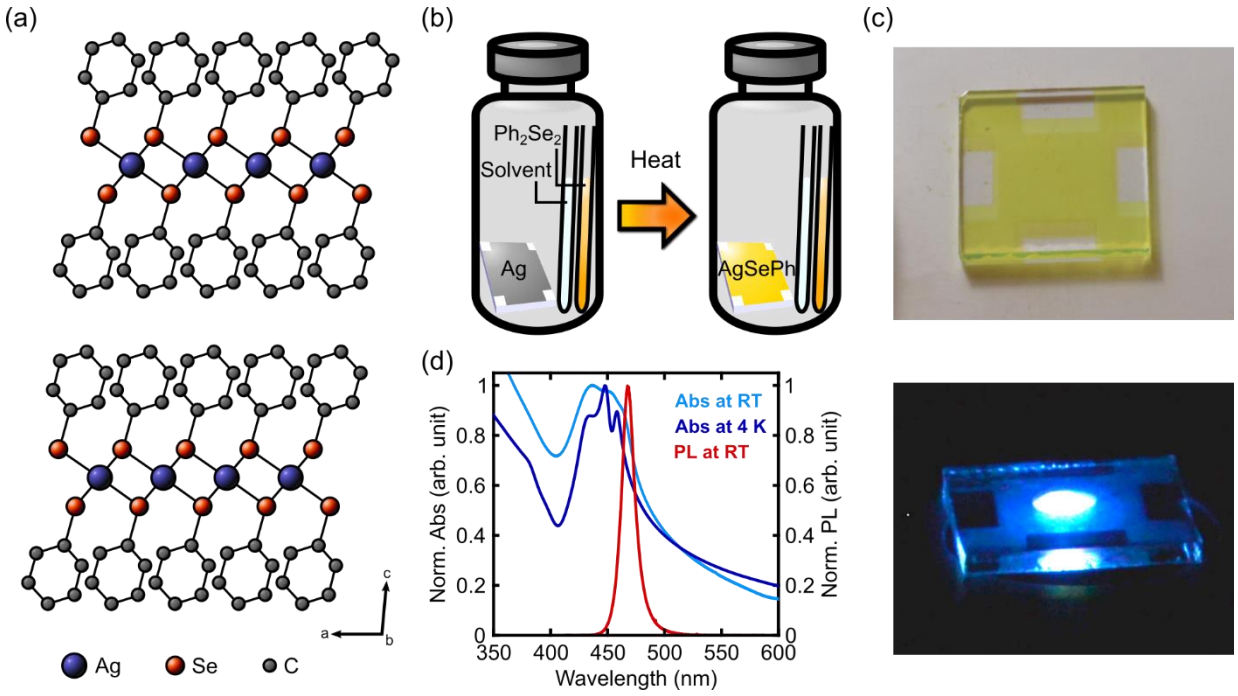

Figure 5-1. (a) The layered 2D structure of silver phenylselenolate (AgSePh) generated from crystallographic information reported in ref. [113]. (b) A schematic of a chemical transformation reaction performed by heating a silver (Ag) film in a sealed container containing diphenyl diselenide (Ph_2Se_2) in the presence of a solvent. (c) Images of AgSePh films under ambient light (top) and 405 nm laser excitation (bottom). (d) Optical properties of AgSePh: absorption spectrum at room temperature (cyan), absorption spectrum at 4 K (blue), and photoluminescence spectrum (red).

example, it takes 2 days at 120 °C for 15 nm thick silver films, 3 days at 100 °C for 15 nm thick silver films, and 6 days at 100 °C for 50 nm thick silver films for the reaction to go to completion.

An example image of a yellow AgSePh film prepared at 100 °C from a 15 nm thick silver film is shown in Figure 1c top. Under photo-excitation by a 405 nm laser diode, the film emitted blue light (Figure 5-1c bottom) centered around 467 nm and with a narrow full-width-at-half-maximum of 14 nm (Figure 5-1d). The absorption spectrum of the AgSePh film showed two resolved excitonic peaks centered at 436 and 453 nm. When the temperature was reduced to 4 K to minimize linewidth broadening from phonons, another resolvable peak emerged at 458 nm, and the previous two peaks shifted to 435 and 448 nm. These observations suggest that there are multiple stable excitonic states in AgSePh, possibly originating from the in-plane anisotropy.[111]

5.3 Solvent-Vapor Induced Morphological Changes in AgSePh Films

Figure 5-2 shows scanning electron microscopy (SEM) images of AgSePh films prepared by the chemical transformation method. In Figure 5-2a, the SEM image shows the typical morphology of an AgSePh film grown in the absence of any solvent vapor, with grain sizes of ~200 nm aligned mostly perpendicular to the glass substrate. Although this alignment may be more favorable for thin-film solar cell devices requiring efficient charge extraction perpendicular to substrates' and electrodes' surfaces,[23,201] the parallel orientation of AgSePh crystals is needed in other device applications. In agreement with the earlier work of Trang *et al.*,[106] we found that introducing water in the reaction vial (Figure 5-2b) can improve the morphology, suggesting that further improvement could be made with other solvents.

To further investigate the influence of solvent vapors on film morphology, we tested solvents with different properties based on polarity, boiling point, and functional group. In general, we found that the addition of solvent vapor led to an increase in crystal sizes but did not necessarily change the crystal orientation. For example, introducing non-polar alkanes – hexane, heptane, octane, and decane – increased the crystal sizes to ~500 nm while retaining mostly perpendicular crystal orientation (Figure 5-2c). Similar results but slightly thicker crystals were observed in polar aprotic solvents, such as diethyl ether (DEE), dichloromethane (DCM), chloroform, methyl acetate (MeOAc), and acetone (Figure 5-2d). On the other hand, the addition of polar protic alcohols – methanol (MeOH), ethanol (EtOH), butanol (BuOH), pentanol (PnOH), and hexanol (HexOH) – improved the crystal size to almost a micron and also oriented crystals parallel to the substrate surface (Figure 5-2e). Interestingly, solvent boiling point did not seem to be a major factor as no significant change across the alkane and the alcohol series with different carbon chain lengths was observed.

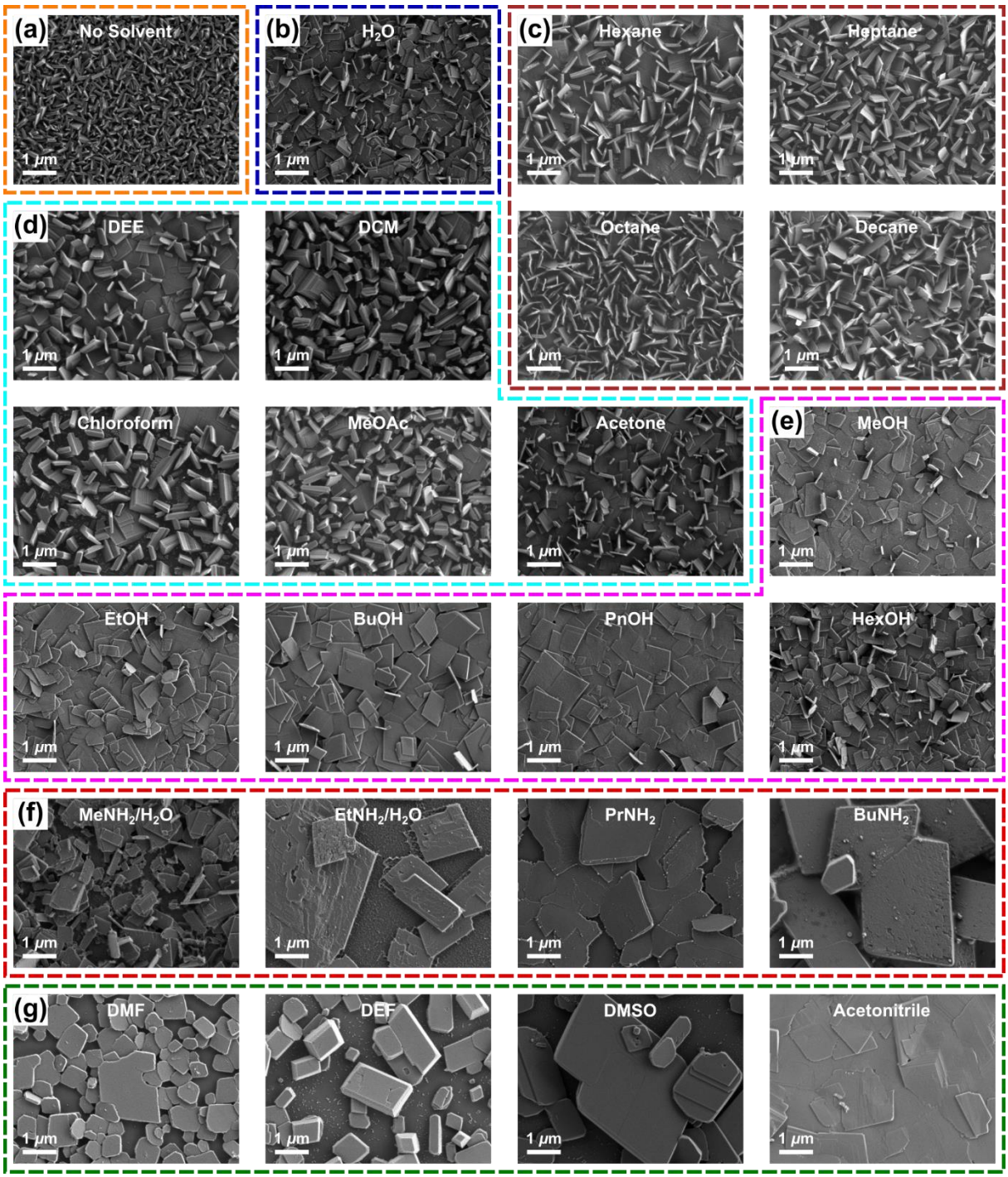

Figure 5-2. *Solvent vapor-induced morphology engineering of AgSePh films.* Scanning electron micrographs of AgSePh films prepared with (a) no extra solvent added, (b) water, (c) non-polar alkanes, (d) polar aprotic solvents, (e) polar protic alcohols, (f) amines, and (g) coordinating solvents. H_2O = water, DEE = diethyl ether, DCM = dichloromethane, MeOAc = methyl acetate, MeOH = methanol, EtOH = ethanol, BuOH = butanol, PnOH = pentanol, HexOH = hexanol, $MeNH_2$ = methylamine, $EtNH_2$ = ethylamine, $PrNH_2$ = propylamine, $BuNH_2$ = butylamine, DMF = dimethylformamide, DEF = diethylformamide, and DMSO = dimethyl sulfoxide.

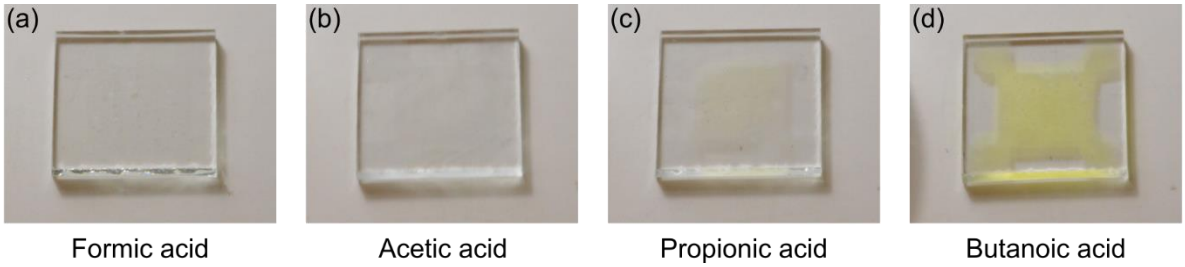

Figure 5-3. Images of resulting AgSePh films prepared with (a) formic acid, (b) acetic acid, (c) propionic acid, and (d) butanoic acid.

Solvents containing functional groups commonly found on nanomaterial surfaces – such as carboxylic acids and amines – were found to have a more dramatic effect than the alkanes or the alcohols. Although MOCs are known to be insoluble in most solvents,[91] introducing vapors of carboxylic acids – formic acid, acetic acid, propionic acid, and butanoic acid – to the reaction caused some film corrosion and film detachment from substrate surfaces (Figure 5-3). We noticed that corrosion tended to happen more with lower boiling-point carboxylic acids and may arise from the repeated condensation and evaporation during the chemical transformation reaction. On the other hand, the addition of amines – aqueous methylamine ($MeNH_2/H_2O$), aqueous ethylamine ($EtNH_2/H_2O$), propylamine ($PrNH_2$), and butylamine ($BuNH_2$) – resulted in a dramatic improvement in crystal size to more than a few micrometers (Figure 5-2f).

Finally, coordinating solvents such as dimethyl formamide (DMF), diethyl formamide (DEF), dimethyl sulfoxide (DMSO), and acetonitrile (Figure 5-2g) also led to dramatic improvements in crystal size and orientation. Individual crystals prepared with amines or coordinating solvents were large enough to be seen using an optical microscope (Figure 5-4).

Changes in preferred crystal orientation could be observed *via* X-ray diffraction. Figure 5-5a illustrates the X-ray diffraction patterns of four selected samples: AgSePh films synthesized with no additional solvent vapor, and AgSePh films synthesized with vapors of H_2O, DMSO, and $PrNH_2$. In general, all sample showed evenly spaced (00*h*) diffraction peaks below 20° 2θ angle

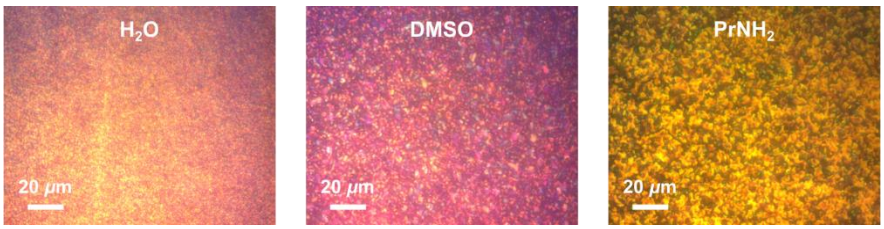

Figure 5-4. Optical images of AgSePh films prepared in the presence of H_2O (left), DMSO (middle), and $PrNH_2$ (right) vapors. For the last two samples, the crystals were large enough to be resolvable under an optical microscope.

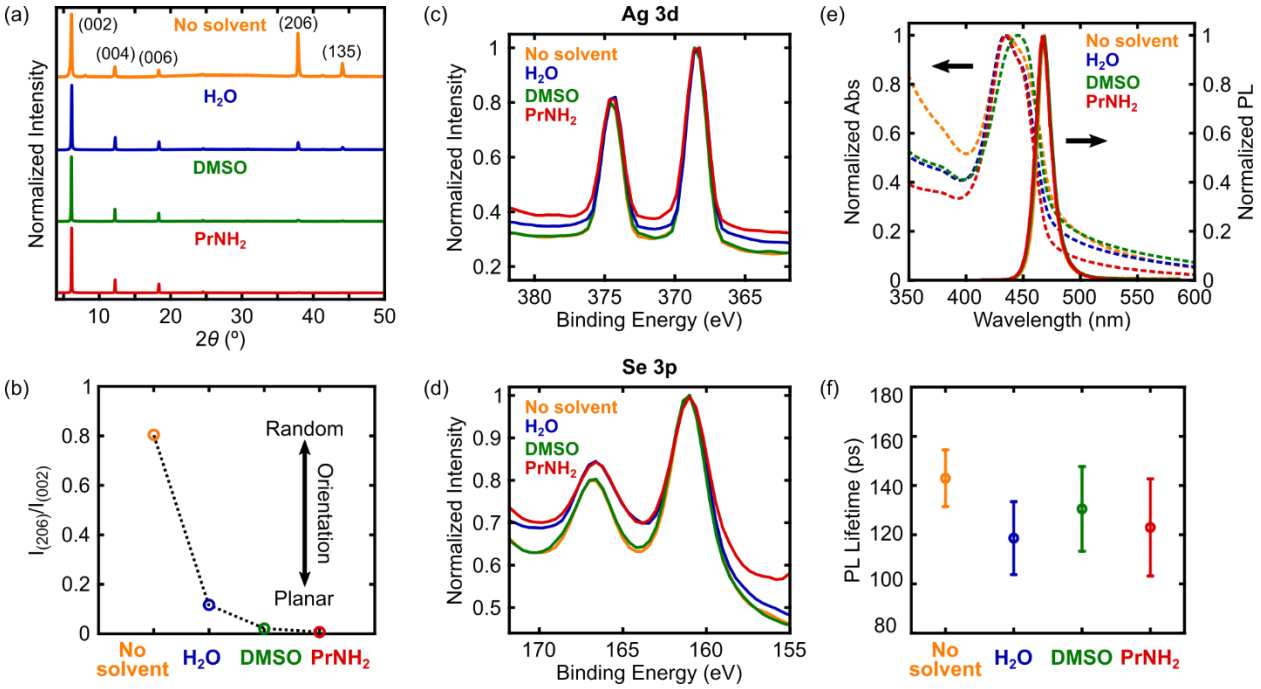

Figure 5-5. *Characterization of solvent vapor-induced AgSePh films.* (a) X-ray diffractograms of AgSePh films prepared in the absence of solvent vapor (orange), and in the presence of water (H_2O, blue), dimethyl sulfoxide (DMSO, green), and propylamine ($PrNH_2$, red). All peaks are labeled with their corresponding diffraction planes. (b) Intensity ratio between the (206) peak and the (002) peak, reflecting the change in preferred orientation of AgSePh films. (c, d) X-ray photoemission spectra of AgSePh films in Ag 3d and Se 3p regions. (e) Absorption (dotted) and photoluminescence (solid) spectra of representative AgSePh films. (f) Photoluminescence lifetimes of representative AgSePh films.

corresponding to the stacking of layered materials with a period of ~1.4 nm. Above 35° 2θ angle, two diffraction peaks corresponding to (206) and (135) peaks were observed. Because the diffraction planes of (206) and (135) peaks have some components along the plane of AgSePh

whereas those of (00*h*) peaks solely originate from the direction perpendicular to the 2D plane, the intensity ratio between (206) and (002) peaks ($I_{(206)}/I_{(002)}$) can be used to gauge the degree of preferred crystal orientation. Figure 5-5b shows the decreasing ratio of $I_{(206)}/I_{(002)}$ when solvent vapors were introduced. In the case of AgSePh films prepared with DMSO or $PrNH_2$, the $I_{(206)}/I_{(002)}$ ratio is nearly zero, suggesting near-complete parallel orientation of AgSePh crystals on the substrate surface. However, small amounts of $I_{(206)}/I_{(002)}$ were still detected and arose mainly because of the tilts caused by the overlap of neighboring crystals, as shown in Figures 5-2f and 5-2g.

While the addition of solvent vapors could lead to a morphological change, we found that it did not alter the resulting films' chemistry. Figures 5-5c and 5-5d show X-ray photoemission spectra of selected AgSePh films prepared with no additional solvent vapor and with H_2O, DMSO, and $PrNH_2$ vapors. In all samples, the spectra contain two peaks in the Ag 3d region and two peaks in the Se 3p region. The peaks at 374.4, 368.4, 166.6, and 161.0 eV correspond to Ag $3d_{3/2}$, Ag $3d_{5/2}$, Se $3p_{1/2}$, and Se $3p_{3/2}$, respectively. As the peak locations in X-ray photoemission spectroscopy are sensitive to the chemical state and local bonding environment, the fact that the X-ray photoemission peaks appear at the same positions regardless of the samples suggests that the presence or absence of solvent vapor does not affect the product's identity. The elemental analysis from X-ray photoemission spectroscopy also gave the Ag:Se ratio of 1:0.9, agreeing within experimental error to the AgSePh chemical formula.

The addition of solvent vapors did not lead to a significant change in the optical properties, either. The PL spectra of AgSePh films prepared with and without solvent vapors all appeared at ~467 nm (Figures 5-5e and 5-6), and the absorption spectra (Figure 5-5e) showed two closely separated peaks at 436 and 453 nm with a slight variation in their intensity ratio. Because these

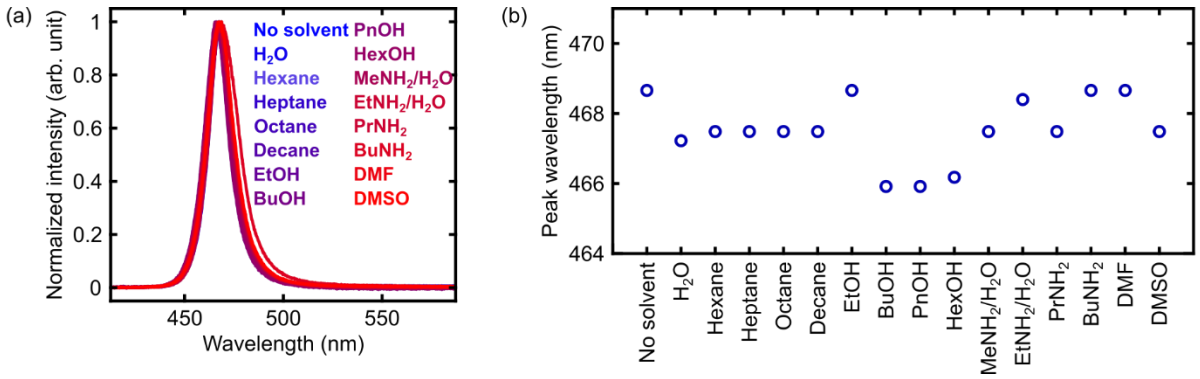

Figure 5-6. Optical properties of AgSePh films prepared with and without added solvents. (a) Normalized photoluminescence spectra. (b) Photoluminescence peak wavelengths. Regardless of added solvents, both graphs show identical photoluminescence properties within experimental error.

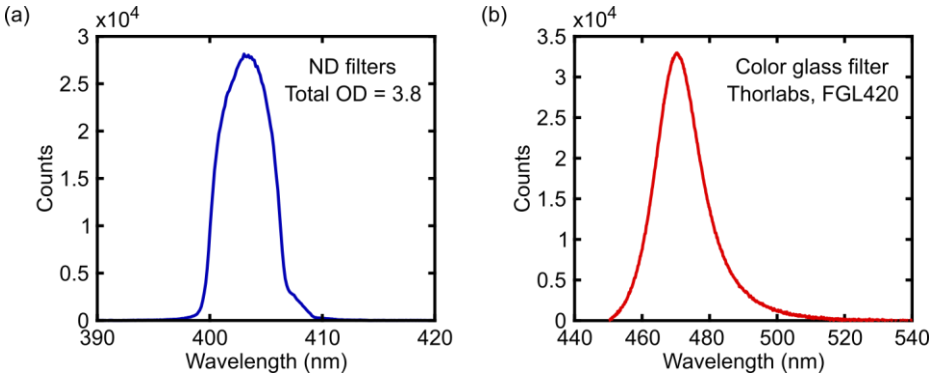

Figure 5-7. The differences of spectra in (a) the excitation and (b) the emission regions of a typical photoluminescence quantum yield experiment on AgSePh films. The ratio of integrated emission and emission signals after the correction from ND and color glass filters gives a photoluminescence quantum yield of ~0.05%.

two absorption peaks have orthogonal polarization,[111] the change in their intensity ratio may reflect the altered film morphology caused by the solvent vapors. Moreover, PL QYs of these films were measured to be ~0.05% using an absolute method based on an integrating sphere (Figure 5-7).[210]

Time-resolved PL spectroscopy was employed to understand the dynamics of the PL emission. We found that the time-resolved PL traces of the selected AgSePh films prepared with no additional solvent vapor and with H_2O, DMSO, and $PrNH_2$ vapors (Figure 5-8) were best fitted by a convolution of instrument response function and a single exponential decay function. The

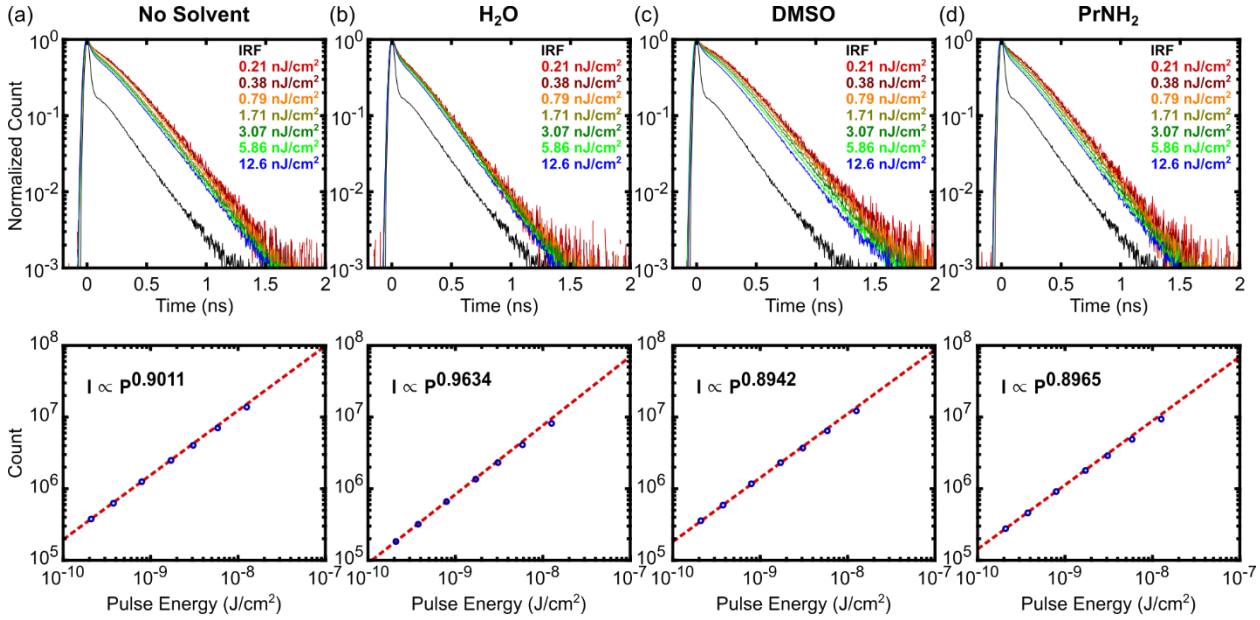

Figure 5-8. (Top) Time-resolved photoluminescence traces as a function of laser fluence of AgSePh films prepared with (a) no solvent vapor and with vapors of (b) H_2O, (c) DMSO, and (d) $PrNH_2$. IRF denotes the instrument response function of the measurement. (Bottom) Plots of integrated time-resolved photoluminescence count as a function of laser fluence. The fits to $\boldsymbol{I \propto P^{\alpha}}$ give $\boldsymbol{\alpha}$ values close to 1, suggesting that the photoluminescence emission is excitonic in nature.

extracted PL lifetimes (Figure 5-5f) range between 100 ps and 150 ps. Time-resolved PL spectroscopy was also performed as a function of laser fluence (Figure 5-8). The fits of integrated time-resolved photoluminescence counts to the functional form $I \propto P^{\alpha}$ yield α values close to 1, confirming the excitonic character of AgSePh.

5.4 Insight on the Solvent-Vapor Induced Morphological Change in AgSePh Films

In general, solvent effects are usually parameterized by the dielectric constant and the dipole moment.[211] However, we found that large AgSePh crystals could be formed by both amines and coordinating solvents (DMF, DEF, DMSO, and acetonitrile) whose dielectric constants and dipole moments varied widely (Figure 5-9). Hence, these two parameters are not sufficient to explain the increase in the crystal size. Nevertheless, amines and coordinating solvents have one thing in

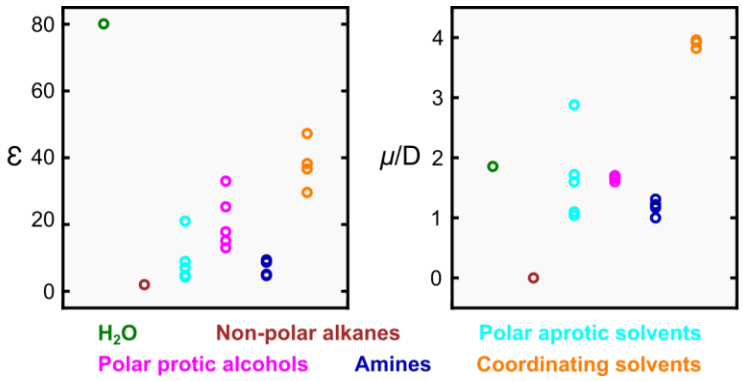

Figure 5-9. Plots of dielectric constant (left) and dipole moment (right) of H_2O (green), non-polar alkanes (brown), polar aprotic solvents (cyan), polar protic alcohols (magenta), amines (blue), and coordinating solvents (orange).

common: they are known to form complexes with Ag^+ ions.[212–215] (An example of this is a readily formed silver-ammonia complex in the Tollens' reagent commonly used in organic chemistry to test the presence of an aldehyde functional group.) This finding suggests that an intermediate of the chemical transformation reaction is an Ag^+ ion, and that the chemical transformation reaction must undergo a multi-step reaction including the oxidation of Ag to Ag^+ as well as the complex formation of Ag^+ with suitable solvent molecules:

$$Ag \xrightarrow{Oxidation} Ag^+ \xrightarrow[Formation]{Complex} Ag^+ - Solvent \longrightarrow AgSePh.$$

The complexes between Ag^+ ions and solvent molecules may lead to increased crystal size of AgSePh by altering the reactivity of Ag^+ ions or their diffusion rate. Additionally, Ag^+ ion complex formation may have a pre-alignment effect, facilitating the growth of AgSePh crystals. For example, $[H_3N\text{-}Ag\text{-}NH_3]^+$, a complex formed between Ag^+ ions and ammonia, adopts a linear structure with Ag-Ag bond distances in the range of 2.9-3.1 Å,[212] similar to the Ag-Ag bond distances in AgSePh of 2.91 and 3.03 Å.[113]

To investigate the effect of solvent vapors on the growth of AgSePh further, we performed an *ex-situ* SEM study on AgSePh films prepared in the presence of H_2O, DMSO, and $PrNH_2$ vapors after 6, 24, and 72 hours of reaction time at 100 ºC (Figure 5-10). In contrast to the sample prepared

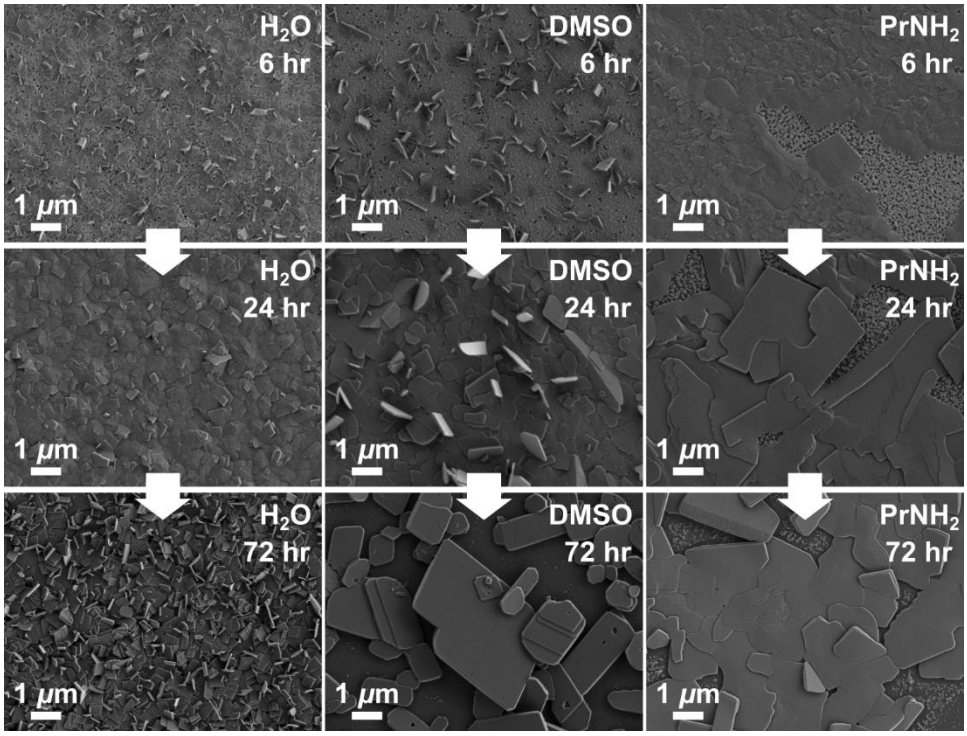

Figure 5-10. Observing the growth of solvent vapor induced AgSePh films. SEM micrographs of AgSePh films prepared in H_2O (left), DMSO (middle), and $PrNH_2$ (right) vapors with reactions times of 6, 24, and 72 hours.

in the presence of H_2O vapor whose average crystal size stopped changing after 24 hr, AgSePh crystals prepared in the presence of DMSO vapor continued to grow until the reaction was completed, reaching lateral dimensions as large as 5 μm. AgSePh films grown in the presence of $PrNH_2$ vapor exhibited qualitatively different growth. Instead of the individual crystallites observed after 6 hours of growth in the presence of H_2O or DMSO, the $PrNH_2$ vapor led to smoother, more continuous AgSePh films.

5.5 Optoelectronic Properties of AgSePh Films

Morphology and crystal size directly affect electrical and optoelectronic device properties because they determine the effective current path length and the charge transport efficiency. All other properties being equal, AgSePh films with larger crystals aligned parallel to substrates are expected to show higher conductivity and photoconductivity in lateral device architectures because

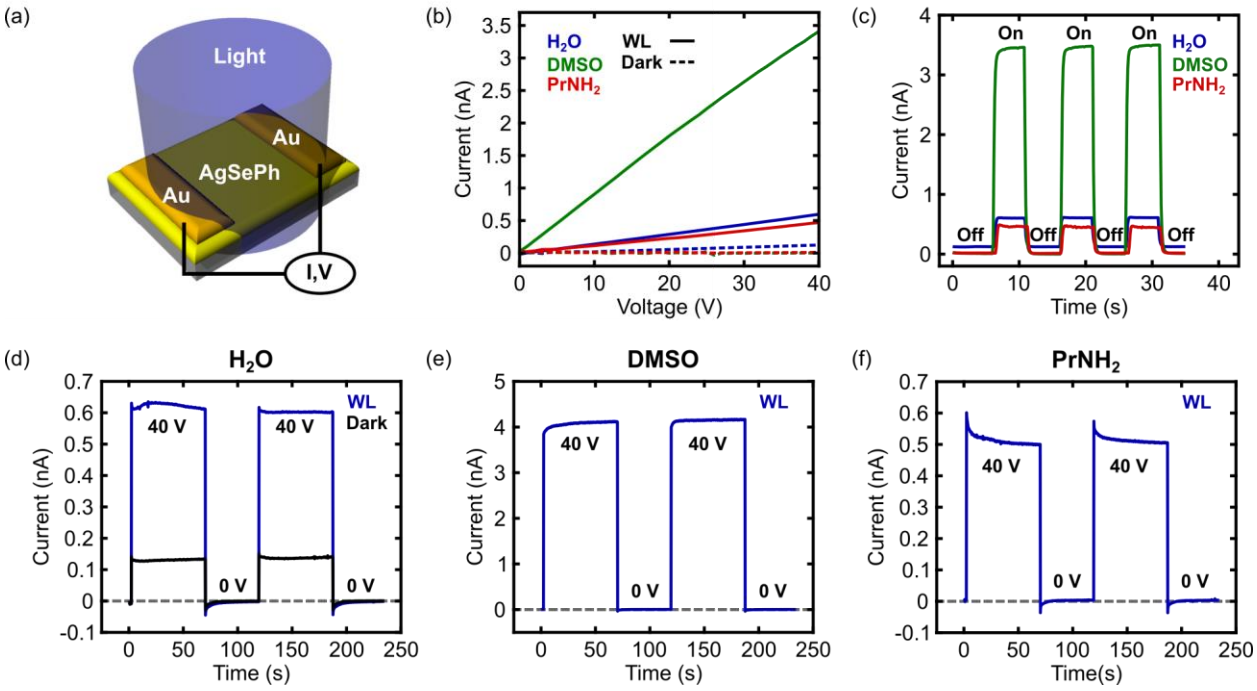

Figure 5-11. *Comparison of electrical and optoelectronic properties of representative AgSePh films.* (a) A schematic of the lateral photodetector architecture. (b) Current versus voltage curves of AgSePh films prepared with H_2O (blue), DMSO (green), and $PrNH_2$ (red) vapors under dark (dashed line) and white light (solid line) conditions. (c) White light on/off cycle tests of AgSePh films prepared with H_2O (blue), DMSO (green), and $PrNH_2$ (red). (d-f) Current versus time curves of AgSePh films prepared with (d) H_2O, (e) DMSO, and (f) $PrNH_2$ upon applied pulsed voltages of 40 V and 0 V under dark (black solid line) and white light (blue solid line) conditions.

fewer grain boundaries must be traversed before charges reach an electrode. To investigate the effects of solvent and morphology on the optoelectronic properties of AgSePh films, we fabricated photoconductive detectors using representative AgSePh films prepared in H_2O, DMSO, and $PrNH_2$ vapors (Figures 5-11a and 5-12, and Methods). Figure 5-11b shows the representative photodetectors' current versus voltage curves under dark and white light conditions. Surprisingly, the AgSePh film prepared in H_2O vapor, which had the smallest average crystal size, showed the highest dark conductivity of 4.6×10^{-7} S/m. On the other hand, the dark conductivity of the AgSePh films prepared in DMSO and $PrNH_2$ vapors, which had micron crystal sizes, was below our instrument limit of 3.7×10^{-9} S/m. Upon white light illumination (Figure 5-13, 4.17 mW/cm^2), AgSePh films prepared in H_2O, DMSO and $PrNH_2$ vapors showed photoconductivities of 1.7 x

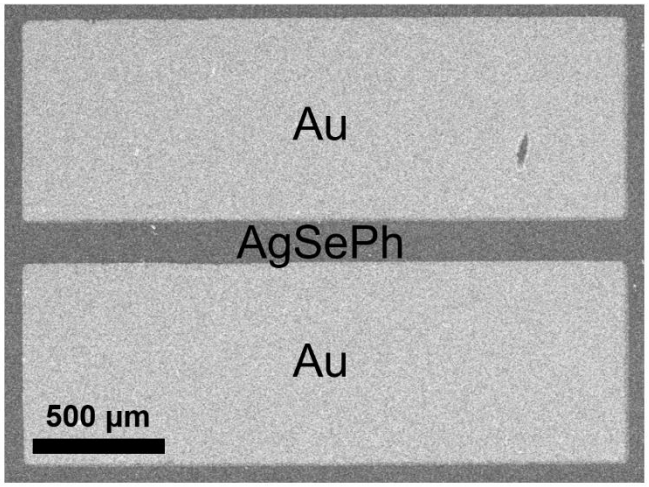

Figure 5-12. Scanning electron micrograph of a photodetector.

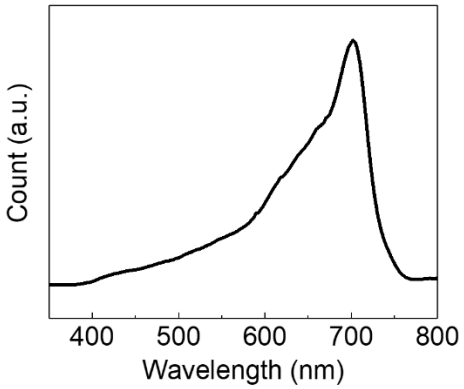

Figure 5-13. Emission spectrum of a white light illuminator (MI-150, Edmund Optics).

10^{-6}, 1.3 x 10^{-5}, and 1.7 x 10^{-6} S/m with stable and reproducible on/off ratios of 5.0, 3.5 x 10^{2}, 4.7 x 10^{1}, respectively (Figures 5-11b and 5-11c).

The dark conductivity, σ, and photoconductivity, $\Delta\sigma$, of a semiconductor can be determined by[216]

$$\sigma = \mu_e e n + \mu_h e p\,, \tag{5-1}$$

and

$$\Delta\sigma = \mu_e e \Delta n + \mu_h e \Delta p = \left(\mu_e + \mu_h\right) e \tau G\,, \tag{5-2}$$

where μ_e is the electron mobility, e is the electric charge, n is the electron density under dark condition, μ_h is the hole mobility, h is the hole density under dark condition, Δn is the photo-generated electron density, Δp is the photo-generated hole density, τ is the carrier lifetime, and G is the carrier photo-generation rate. G can be defined by

$$G = \phi(\lambda)\left[1 - R(\lambda)\right]\left[1 - e^{-\alpha(\lambda)t}\right], \tag{5-3}$$

where ϕ is the incident photon flux, λ is the wavelength of the incident photon, R is the fraction of photons that are reflected, α is the absorption coefficient, t is the thickness of absorbing material, respectively.

Considering that the AgSePh films prepared in H_2O, DMSO and $PrNH_2$ vapors had the same thickness (Figures 5-14 and 5-15), were illuminated by the same photon flux, and showed similar absorption features (Figure 5-5e) and PL lifetimes (Figure 5-5f), the origin of higher photoconductivity of the AgSePh film prepared in DMSO is most likely attributed to higher carrier mobility. This higher carrier mobility in the film prepared in DMSO also suggests that the cause of higher dark conductivity (by two orders of magnitude) in the AgSePh film prepared in H_2O was due to a higher dark carrier density, which may arise from a larger density of defects, as previously observed in TMDs[217,218] and 2D LHPs.[205] These defects may arise from Ag and Se vacancies/interstitials that act as donors or acceptors, providing additional free carriers to the system and also acting as scattering sites that lower the free carrier mobility. Indeed, the higher photoconductivity by almost one order of magnitude and non-measurable dark conductivity in the AgSePh film prepared in DMSO vapor indicate higher crystalline quality and lower defect densities, resembling an ideal intrinsic semiconductor. Overall, these conductivity and photoconductivity measurements indicate that solvent vapor-assisted growth influences not only

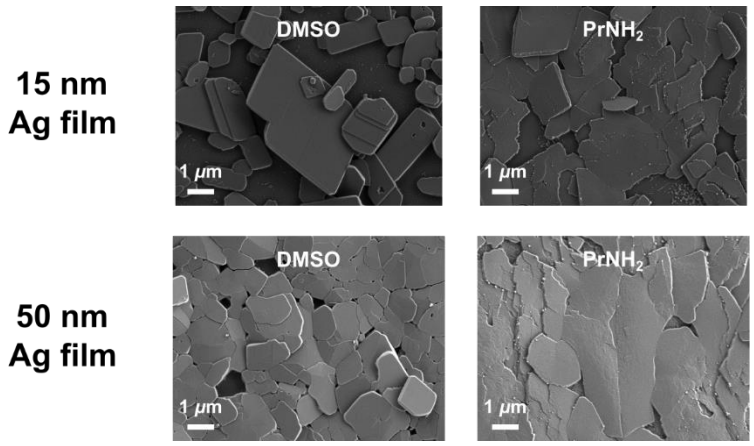

Figure 5-14. Scanning electron micrographs showing the morphology of AgSePh films prepared from original Ag films with thicknesses of 15 nm and 50 nm. The AgSePh films prepared from 50 nm-thick Ag films showed more complete surface coverage and were more suitable for electrical measurements.

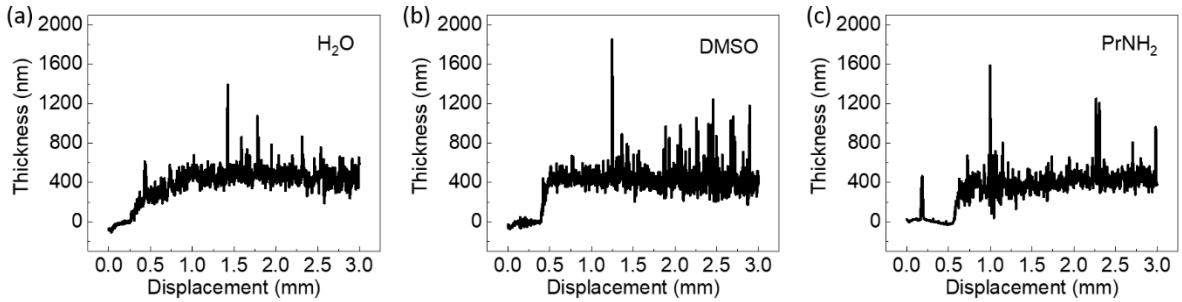

Figure 5-15. Thickness profiles of AgSePh films prepared with (a) H_2O, (b) DMSO, and (c) $PrNH_2$ from 50 nm-thick Ag films on glass substrates. The thickness profiles were measured using a Dektak 150 Profilometer.

the crystal morphology and orientation, but also the crystalline quality of AgSePh.

Electronic and optoelectronic devices such as field-effect transistors and solar cells can suffer from hysteresis and instability arising from ion migration.[219–222] To study potential ion migrations such as Ag or Se vacancies in AgSePh films, we monitored current as a function of time by applying pulsed voltages of 40 V repeatedly under dark and white light conditions (Figures 5-11d, 5-11e, and 5-11f). For AgSePh films prepared in H_2O and $PrNH_2$ vapors, their photocurrents increased instantly upon applied voltage before slowly decreasing to a constant value (Figures

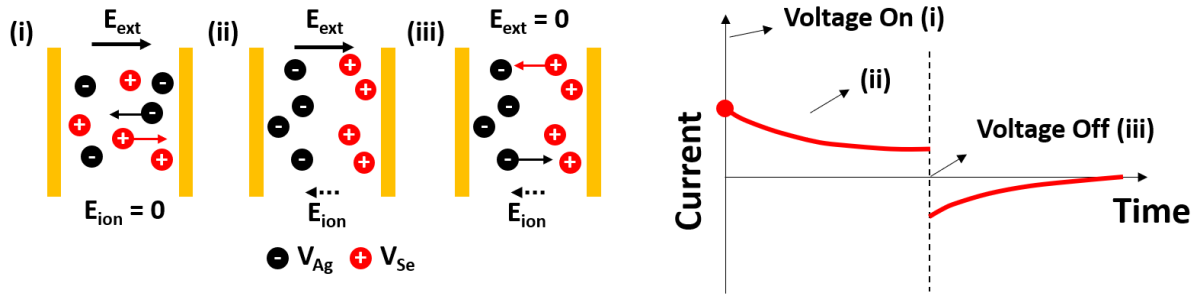

Figure 5-16. Schematics showing the dynamics of ion migration depending on external voltage and its resulting current change. V_{Ag} and V_{Se} represent Ag vacancy and Se vacancy, respectively. E_{ext} and E_{ion} represent external electric potential and ion-induced electric potential, respectively.

5-11d, 5-11e, and 5-11f). When the applied voltage was removed, a negative current was immediately observed before decaying to zero. The transient current decay upon applied voltage and the immediate change of current direction followed by a slow decay to zero after removing the applied voltage suggest the existence of an ion-induced electric potential caused by ion migration (Figure 5-16). Similar behaviors were also observed under dark for AgSePh films prepared in H_2O vapor (Figure 5-11d). In contrast, the AgSePh film prepared with DMSO did not show such sign of ion migration, further reinforcing its higher crystalline quality than AgSePh films prepared in H_2O and $PrNH_2$ vapors.

To further investigate optoelectronic properties of AgSePh films, wavelength-dependent photocurrent measurement and response time analysis was conducted on AgSePh films prepared with DMSO (Figure 5-17). Figures 5-17a and 5-17b show current versus voltage curves and light on/off cycle tests under 405 nm (1.66 mW/cm^2), 525 nm (0.37 mW/cm^2), and 660 nm (0.83 mW/cm^2) light illumination, respectively. Interestingly, AgSePh prepared with DMSO shows considerable photoresponses to sub-gap excitation at 525 nm and 625 nm, possibly indicating a persistent presence of mid-gap carriers. Moreover, the device showed a fast response with a rise time of less than 7.5 ms and a fall time of ~15.1 ms (Figure 5-17c). Similar results of

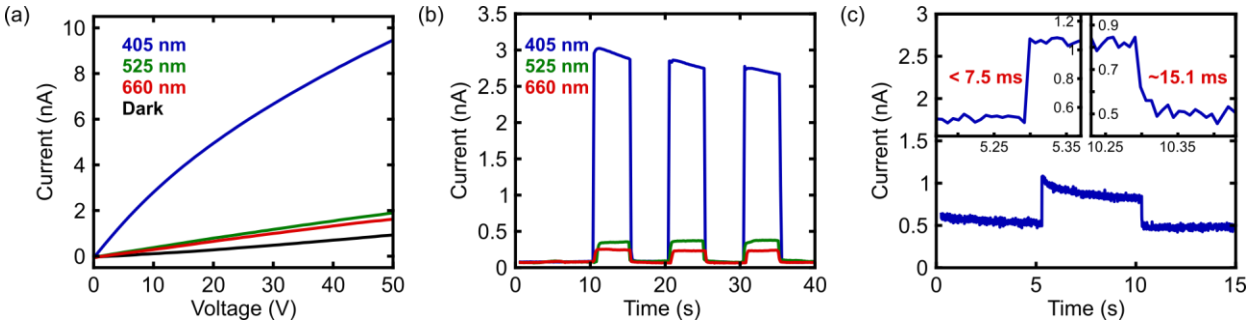

Figure 5-17. *Detailed optoelectronic characterization of AgSePh prepared with DMSO.* (a) Current versus voltage curves and (b) on/off cycle tests of AgSePh films prepared with DMSO under periodic illumination of 405 nm (blue, 1.66 mW/cm^2), 525 nm (green, 0.37 mW/cm^2), and 660 nm (red, 0.83 mW/cm^2) light. (c) Response time analysis of AgSePh films prepared with DMSO under 405 nm light illumination.

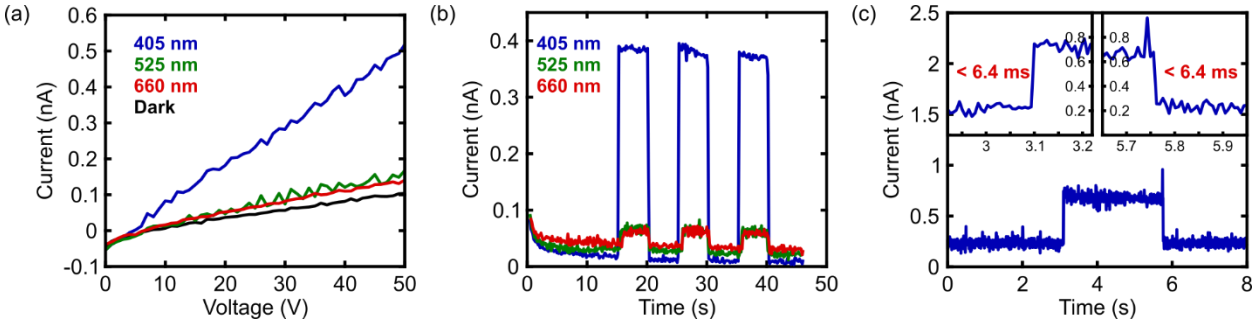

Figure 5-18. *Detailed optoelectronic characterization of AgSePh prepared with PrNH$_2$.* (a) Current versus voltage curves and (b) on/off cycle tests of AgSePh films prepared with PrNH$_2$ (green) under periodic illumination of 405 nm (blue, 1.66 mW/cm^2), 525 nm (green, 0.37 mW/cm^2), and 660 nm (red, 0.83 mW/cm^2) light. (c) Response time analysis of AgSePh films prepared with PrNH$_2$ under 405 nm light illumination.

photoresponses to sub-gap excitation and fast rise and fall times were also observed in the AgSePh films prepared with PrNH$_2$ (Figure 5-18).

5.6 Temperature-Dependent Photoluminescence

We performed temperature-dependent PL spectroscopy from 5 K to 300 K (Figure 5-19) on AgSePh films prepared on single-crystal quartz substrates. In general, we observed a blue shift in the excitonic PL peak position and a narrowing of the excitonic PL linewidth at low

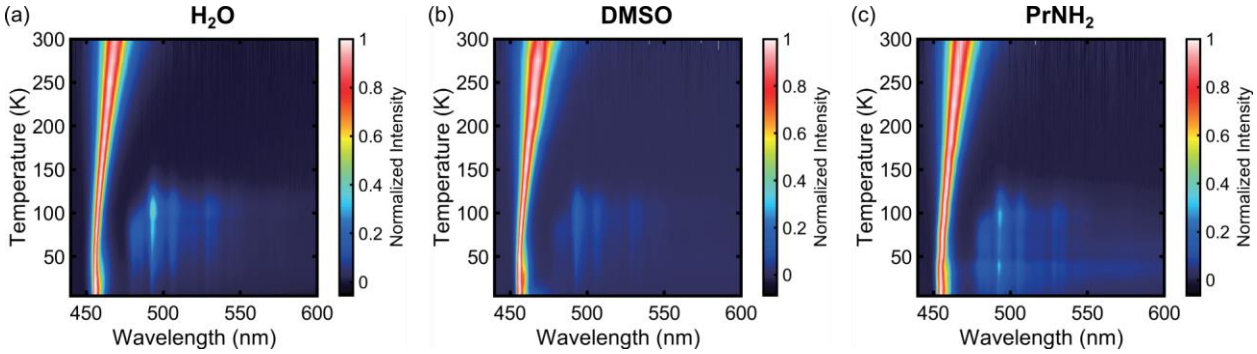

Figure 5-19. Maps of normalized photoluminescence spectra at temperatures ranging from 5 K to 300 K of AgSePh films prepared in the presence of (a) H_2O, (b) DMSO, and (c) $PrNH_2$ vapors.

temperatures due to reduced exciton-phonon coupling. When the temperature was reduced to below ~140 K, a new broad emission feature emerged at ~500 nm, suggesting the presence of optically-active mid-gap states. As the temperature decreased, these mid-gap states' integrated intensity increased sharply at 100-140 K before leveling off at lower temperatures. Assuming that there is only one thermally-activated nonradiative recombination channel, the integrated intensity can be well fitted by the Arrhenius equation:[223,224]

$$I(T) = \frac{I_0}{1 + A\exp(\frac{-E_a}{k_b T})} \tag{5-4}$$

where $I(T)$ is the integrated PL intensity at a temperature T, I_0 is the integrated PL intensity at a temperature approaching 0 K, A is a process rate parameter, E_a is the activation energy for nonradiative exciton decay, and k_B is the Boltzmann constant. Fitting to the Arrhenius equation gave E_a of AgSePh films prepared in the presence of H_2O, DMSO, and $PrNH_2$ vapors to be 125, 115, and 76 meV, respectively (Figure 5-20).

A similar analysis on integrated PL intensity can be performed on the excitonic PL transition. The plot of integrated excitonic PL intensity as a function of increasing temperature (Figure 5-21) showed two sharp decreases at ~5-40 K and ~200-300 K, suggesting the existence of two major

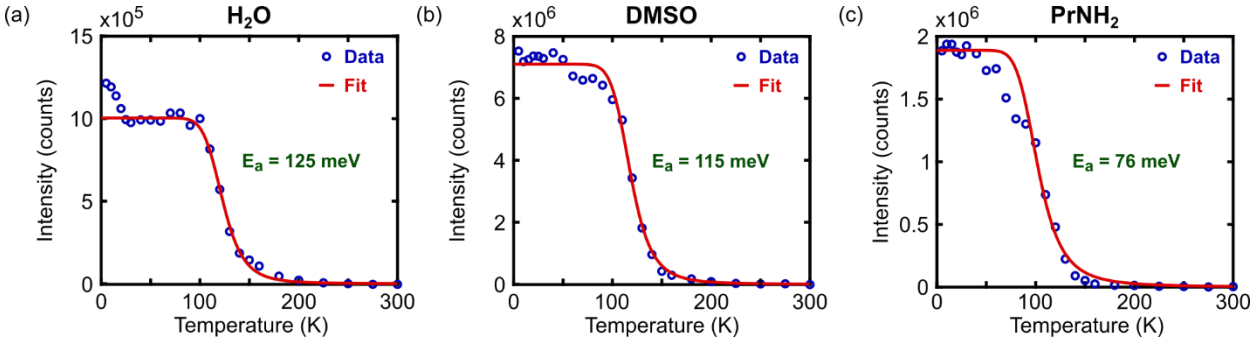

Figure 5-20. Integrated photoluminescence intensity of the mid-gap states as a function of temperature of AgSePh films prepared in the presence of (a) H_2O, (b) DMSO, and (c) $PrNH_2$ vapors along with the fit to the Arrhenius equation with one nonradiative recombination channel.

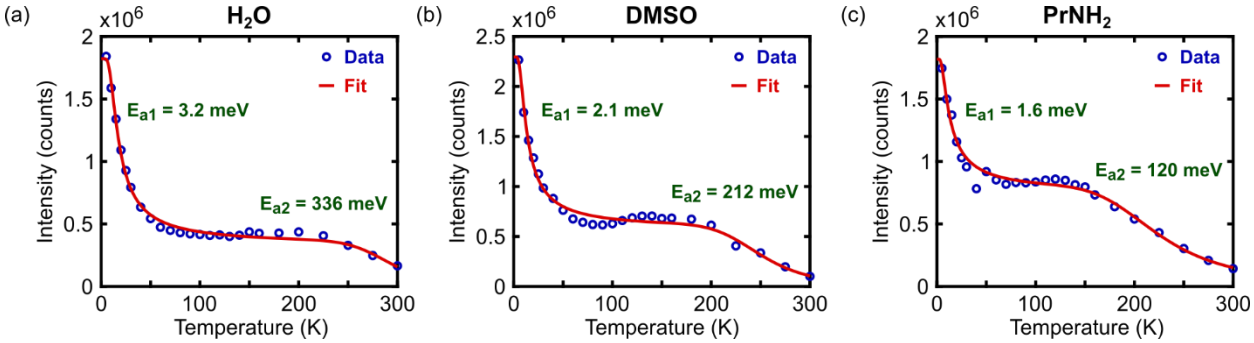

Figure 5-21. Integrated photoluminescence intensity of the excitonic emission as a function of temperature of AgSePh films prepared in the presence of (a) H_2O, (b) DMSO, and (c) $PrNH_2$ vapors along with the fit to the Arrhenius equation with two nonradiative recombination channels.

nonradiative processes dominating at low and high temperatures. The change in the integrated intensity was found to be well fitted by a modified Arrhenius formula:[223,224]

$$I(T) = \frac{I_0}{1 + A_1 \exp(\frac{-E_{a1}}{k_b T}) + A_2 \exp(\frac{-E_{a2}}{k_b T})} \quad (5\text{-}5)$$

where 1 and 2 denote the two nonradiative processes. For AgSePh films prepared in the presence of H_2O, DMSO, and $PrNH_2$ vapors, E_{a1} was found to be 3.2, 2.1, and 1.6 meV and E_{a2} was 336, 212, and 120 meV, respectively. The low magnitude of E_{a1} suggests the presence of a nonradiative electronic state whose energy is close to the excitonic state. This nonradiative state may be an energetically-higher dark excitonic state similar to what has been found in other 2D materials[225]

and hybrid organic-inorganic materials,[226,227] or may arise from shallow exciton trapping with low energy barrier commonly found in traditional semiconductors.[228] On the other hand, the large value of E_{a2} in quantum-confined materials is usually assigned to exciton binding energy.[229] Recent experiments using optical pump detuning of transient absorption spectroscopy and PL excitation spectroscopy have reported the exciton binding energy in AgSePh to be ~380 meV.[109,111] Compared to these previously reported numbers, our extracted values have the same order of magnitude but are slightly lower.

Overall, both wavelength-dependent photoconductivity and temperature-dependent PL spectroscopy support the presence of mid-gap states in AgSePh. While the physical origin of these mid-gap states is still unclear, it may be related to the localized electronic states above the valence band maximum as observed using ultra-violet photoemission spectroscopy by Maserati and co-workers.[112] The presence of these mid-gap states may contribute to the low PL QY values of ~0.05% on thin films reported in this work and of ~2% on microcrystals shown by Yao and co-workers.[109] Although the PL QY of AgSePh requires some improvement, these values are on the same level as those of TMDs and 2D LHPs in their early ages.[26,230,231] Recently, various chemical, electrical, and structural approaches have been used to improve the PL QYs of TMDs and 2D LHPs to almost unity.[83,217,232,233] Some of these methods may yield the same effect on AgSePh, opening up new application possibilities.

5.7 Conclusions

We have shown by testing 28 solvent vapors – with different polarities, boiling points and functional groups – that the introduction of solvent vapor during a chemical transformation reaction of metallic Ag to AgSePh can yield a wide range of crystal sizes from <200 nm to >1 μm, and more homogeneous orientation of crystals on the supporting substrate. Solvents known to form

complex with Ag^+ such as DMSO and $PrNH_2$ yielded the largest and flattest crystals. Furthermore, a higher photoconductivity by one order of magnitude, non-measurable dark conductivity, and no ionic migration in AgSePh prepared with DMSO suggest an improved crystalline quality with fewer defects. The existence of mid-gap states was confirmed by sub-gap excitation photo-responses in optoelectronic characterization and mid-gap emission in low-temperature photoluminescence spectroscopy, implying additional defect passivation may further improve the electrical and optical properties of AgSePh.

5.8 Methods

Chemicals. Silver pellets (Ag, 99.99% pure) were purchased from Kurt J Lesker. Diphenyl diselenide (Ph_2Se_2, 97.0+%) was purchased from TCI America. All organic solvents – hexane, heptane, octane, decane, diethyl ether, dichloromethane, chloroform, methyl acetate, acetone, methanol, ethanol, butanol, pentanol, hexanol, aqueous methylamine, aqueous ethylamine, propylamine, butylamine, dimethylformamide, diethylformamide, dimethyl sulfoxide, and acetonitrile – were purchased from Millipore Sigma. All chemicals were used as received.

Preparation of AgSePh films. AgSePh thin films were prepared by a chemical transformation reaction between silver films and diphenyl diselenide (Ph_2Se_2).[106] Silver films with thicknesses of 15 nm or 50 nm were deposited on glass substrates by thermal evaporation with a deposition rate of ~1.5 Å/s. After that, the prepared silver films and ~30 mg of Ph_2Se_2 powder, contained in an open culture tube, were sealed together inside a microwave reaction vial. After heating in an oven at 100 °C for 3 days or 6 days for 15 nm and 50 nm thick silver films, respectively, the silver films transformed into yellow AgSePh films. For solvent studies, 200 µL of solvent in an open culture tube was also added to the sealed microwave reaction vial alongside the Ph_2Se_2 culture tube and the prepared silver film.

Substrate preparation. Bare glass with dimensions of 12.2 x 12.2 x 1.1 mm was purchased from Luminescence Technology Corp. The glass substrates were cleaned by sonication for 8 mins in micro-90, water, acetone, and isopropanol, and dried by nitrogen gas before use.

Optical absorption. Optical absorption measurements were performed on films made from 15 nm thick silver films using Cary 5000 UV-Vis-NIR spectrometer.

Steady-state PL spectroscopy. Steady-state photoluminescence (PL) measurements were performed on an inverted microscope (Nikon, Ti-U Eclipse) in air. The samples were excited by focusing the output of a 405 nm laser diode (Picoquant, LDHDC-405M, continuous wave mode) by an objective lens (Nikon, CFI S Plan Fluor ELWD, 40x, 0.6 NA) to ~1 μm spot. The excitation light's polarization was controlled by a circular polarizer (Thorlabs, CP1R405). After the excitation, the photoluminescence was collected in the epi configuration and passed through a dichroic mirror and a long-pass filter. It was then directed into a spectrograph (Princeton Instruments, SP-2500) mounted with a cooled charge-coupled detector (Princeton Instruments, Pixis).

Time-resolved PL spectroscopy. Time-resolved PL measurements were performed using the same microscope setup as steady-state PL spectroscopy with some modifications. The excitation light source was replaced by a frequency-doubled light (405 nm) of the 810 nm output from a femtosecond laser (Coherent Mira HP) operating at 76 MHz. The detector used was a Si avalanche photodiode (Micro Photon Devices, PDM20) connected to a counting board for time-correlated single-photon counting (PicoQuant, PicoHarp 300). The instrument response function was obtained by detecting the Raman scattering from water appearing at ~470 nm close to the PL peak position of AgSePh. Extraction of PL lifetime was performed using a publicly available ChiSurf software developed by Thomas-Otavio Peulen and co-workers.[234]

Temperature-dependent PL spectroscopy. Temperature-dependent photoluminescence (PL) spectroscopy was performed by mounting samples in a microscopy cryostat (Janis Research, ST-500) and flowing liquid helium through a cold finger attached to the base of the cryostat. Single crystal quartz (MTI Corp.) was used as the sample substrate for these measurements to improve thermal conductivity at cryogenic temperatures.

Photoluminescent quantum yield. The measurement of PL quantum yield (QY) was performed using the absolute quantum yield method in an integrating sphere.[210] The excitation light from a 405 nm laser diode (Picoquant, LDHDC-405M, continuous wave mode) was directed into an integrating sphere (Labsphere) that housed a thin film of AgSePh. The output signal was collected by an optical fiber mounted on an exit port of the integrating sphere and was directed into a spectrograph (Princeton Instruments, SP-2500) mounted with a cooled charge-coupled detector (Princeton Instruments, Pixis). Neutral density and color glass filters were inserted in front of the spectrograph to avoid saturating the detector's pixels because of the large difference in the excitation and the emission signals' magnitudes.

Scanning electron microscopy (SEM). Scanning electron micrographs were collected using a Zeiss Merlin instrument operating at 1 kV and 100 pA.

Powder X-ray diffraction (PXRD). Powder X-ray diffraction data were collected using a PANalytical X'Pert Pro MPD X-ray diffractometer (Cu Kα radiation, $\lambda = 1.54184$ Å) with High-Speed Bragg-Brentano Optics. A 0.04 rad Soller slit, a 2° anti-scatter slit, a 10 mm mask, and a programmable divergence slit with an illuminated length of 6 mm were used in the incident beam path. The diffracted beam optics included a 0.04 rad Soller slit, a Ni Filter, and an automatic receiving slit. The detector was an ultrafast X'Celerator RTMS detector.

X-ray photoelectron spectroscopy (XPS). XPS was performed on Model PHI 5000 VersaProbe II manufactured by ULVAC-PHI, Inc. The source was a monochromatic Al Kα, the operating power was 50 V, and the beam size was 200 μm. Base pressure during analysis was kept at ~5e-9. The pass energy was set to 187.850 eV for survey scans and 93.900 V for individual energy scans. All XPS measurements were performed on samples made from 50 nm thick silver films. Because of the insulating glass substrates, a flood gun was used to prevent a charging effect. All recorded data were adjusted to shift the C1s peaks to 284.50 eV.

Photodetector fabrication. Photodetectors were fabricated on ~450 nm-thick AgSePh films (Figure S10 and S11) prepared from the original silver films with thickness of 50 nm. Subsequently, Au top contacts were deposited on AgSePh thin films by thermal evaporation. The channel width (W) and length (L) were 1.5 x 10^{-4} m and 2.25 x 10^{-3} m, respectively.

Optoelectronic characterization. A source meter (Model 2450, Keithley) and white light illuminator (MI-150, Edmund Optics, 4.17 mW/cm^2) were used for photoconductivity and transient optoelectronic characterizations. A semiconductor parameter analyzer (Model 4200A-SCS, Keithley) and several light-emitting diodes centered at 405 nm (Model S-SUV 3405, Skycares Corp., 1.66 mW/cm^2), 525 nm (Model S-VR 10525, Skycares Corp., 0.37 mW/cm^2) and 660 nm (Model S-VR 10660, Skycares Corp., 0.83 mW/cm^2) were used for high-resolution light on/off scan and wavelength-dependent photocurrent measurements.

Chapter 6 Size and Quality Enhancement of 2D Semiconducting Metal Organic Chalcogenolates by Amine Addition

The basis of this chapter has been prepared for a submission as:

W. Paritmongkol, T. Sakurada, W.S. Lee, R. Wan, P. Müller, W.A. Tisdale "Size and Quality Enhancement of 2D Semiconducting Metal Organic Chalcogenolate by Amine Addition"

6.1 Introduction

Two-dimensional (2D) hybrid organic-inorganic semiconductors exhibit a unique combination of excitonic behavior,[2,235,236] strong and tunable light-matter interactions,[2,3,5,235,236] and potential applications in optoelectronics.[3,5] An emerging family within this broader class of materials is 2D metal organic chalcogenolates (MOCs),[91,96,97,99–102] which are synthesized in the form of three-dimensional crystals consisting of 2D layers held together by van der Waals forces. Unlike the more studied ionic 2D lead halide perovskites, 2D MOCs are distinguished by the covalent interaction between inorganic and organic components. This covalent nature not only makes 2D MOCs stable against both polar and non-polar solvents,[91] but also allows for unique electronic bandgap tuning by organic modification[114] – a capability not easily achieved in other 2D semiconductors.

Of the 2D MOCs reported so far, silver phenylselenolate (AgSePh)[97,106–112] has received the most attention because of its blue luminescence[97] and in-plane anisotropy,[111] which are attractive features for light-emitting applications and light-matter coupling. AgSePh naturally adopts a multi-quantum-well structure consisting of slabs of silver selenide separated by layers of phenyl rings

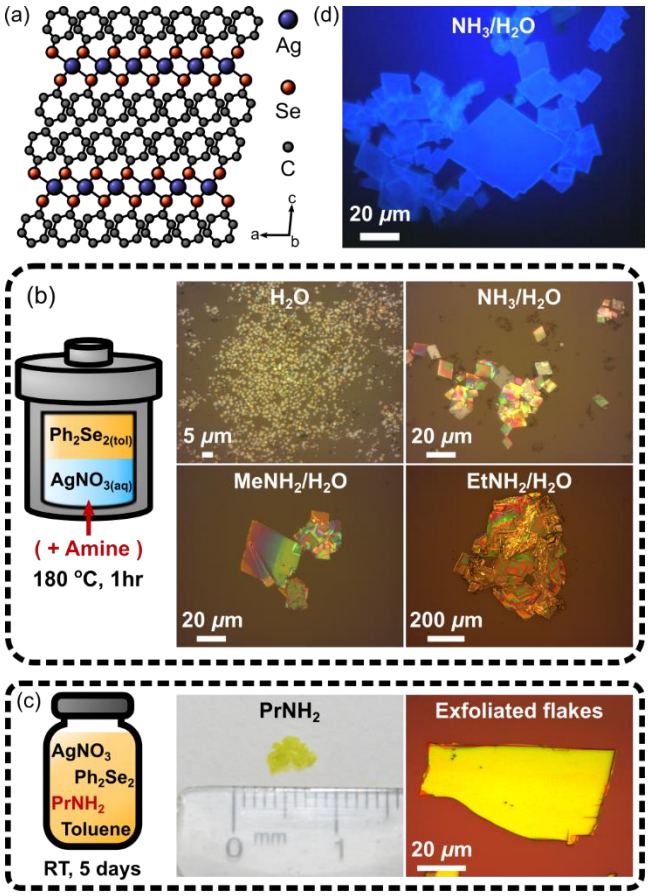

Figure 6-1. (a) Lamellar structure of 2D AgSePh. (b) Schematic illustration of a reaction mixture for a hydrothermal reaction and bright-field optical micrographs showing an increase in lateral size upon amine addition. (c) Schematic illustration of a reaction mixture for a single-phase reaction and images of a resulting crystal and its exfoliated flakes. (d) Photoluminescence micrograph of AgSePh microcrystals prepared according to the method reported in this work.

(Figure 6-1a), leading to a high exciton binding energy of ~400 meV[109,111] and a picosecond photoluminescence (PL) lifetime.[109,237] Furthermore, AgSePh can be prepared in different forms depending on the end use need. For example, AgSePh thin films can be prepared by a scalable vapor-phase chemical transformation[106,110] and microcrystals can be synthesized by a solution-phase hydrothermal synthesis.[107] However, these methods typically yield small AgSePh crystals with average lateral sizes of <5 μm, making fundamental studies and device integration

challenging. Additionally, AgSePh samples synthesized by these methods show optical and electrical signatures of mid-gap states that may limit AgSePh's optoelectronic performance.[109,112]

In this work, we show that the addition of amines during a solution-phase growth reaction can improve the size and quality of AgSePh crystals. Crystals with sizes ranging from <5 μm to >1 mm, as well as increased PL lifetime and suppression of mid-gap emission, could be synthesized by this simple chemical approach. Reaction kinetics and ^{77}Se NMR studies were conducted to understand the role of amines during AgSePh growth, and the knowledge gained through this work was used to develop a single-crystal growth method that is applicable to other 2D MOCs, as demonstrated by the synthesis of silver 4-methylphenylselenolate (AgSePhMe), a novel member of the 2D MOC family.

6.2 Size Enhancement by Amine-Assisted Syntheses

AgSePh crystals were synthesized by two different methods: a bi-phasic hydrothermal reaction (Figure 6-1b) and an organic single-phase reaction (Figure 6-1c). For the hydrothermal reaction, a bi-phasic mixture of diphenyl diselenide (Ph_2Se_2) in toluene and an aqueous solution of silver nitrate ($AgNO_3$) was heated at 180 °C for 1 hr to yield AgSePh crystals with average lateral size of ~2 μm (Figure 6-1b).[107] We found that the size of AgSePh crystals could be increased by the introduction of amines to the reaction mixture. By dissolving $AgNO_3$ in aqueous ammonia (NH_3/H_2O) instead of in pure water (H_2O), the hydrothermal reaction yielded microcrystals with larger sizes of ~20 μm (Figures 6-1b and 6-1d). This size improvement was not limited to NH_3/H_2O; larger microcrystals with sizes of ~30 μm and >200 μm could be obtained when aqueous methylamine ($MeNH_2/H_2O$) or aqueous ethylamine ($EtNH_2/H_2O$) were used, respectively (Figure

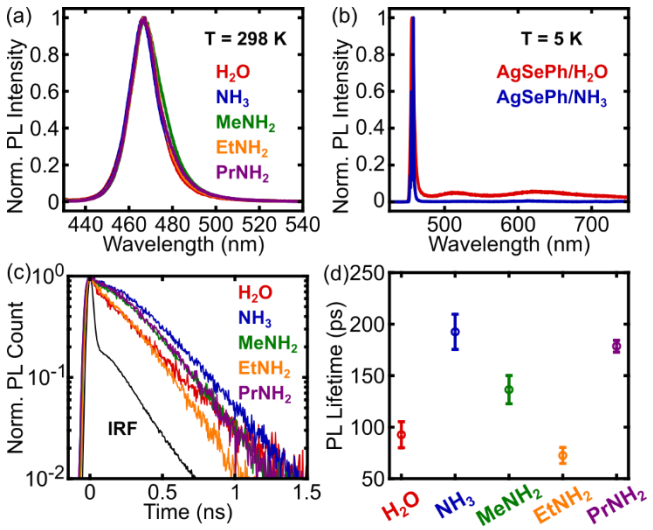

Figure 6-2. (a) Room-temperature photoluminescence (PL) spectra of AgSePh crystals prepared using water (H_2O), aqueous ammonia (NH_3/H_2O), aqueous methylamine ($MeNH_2/H_2O$), aqueous ethylamine ($EtNH_2/H_2O$), and propylamine ($PrNH_2$). (b) Comparison between PL spectra at 5 K of AgSePh crystals prepared in H_2O and in NH_3/H_2O showing the suppression of broad luminescent features at >500 nm in the latter. (c) Time-resolved photoluminescence decays of AgSePh crystals along with the decay due to instrument response function (IRF). (d) Extracted photoluminescence lifetimes.

6-1b). In all cases, the resulting microcrystals exhibited blue luminescence at 467 nm (Figures 6-1d and 6-2a), indicating that amines did not alter the product of the hydrothermal reaction.

An organic single-phase reaction (Figure 6-1c) was possible using longer-chain amines, which are liquid at room temperature. In this approach, the reaction was performed in a miscible solution of $AgNO_3$ and Ph_2Se_2 in a combined amine-toluene solution. For example, equal volumes of a 3 mM solution of $AgNO_3$ in propylamine ($PrNH_2$) and a 3 mM solution of Ph_2Se_2 in toluene were combined to form a 1.5 mM single-phase mixture with 50% v/v $PrNH_2$. When stored at room temperature for 3-5 days, this solution yielded millimeter-sized crystals that could be exfoliated to produce thin AgSePh flakes (Figure 6-1c) with PL emission centered at 467 nm (Figure 6-2a). Similar results were obtained using amines with longer hydrocarbon chains, such as butylamine, pentylamine, and hexylamine.

6.3 Quality Improvement by Amine-Assisted Syntheses

In almost all cases, the addition of amines led to an increase in AgSePh PL lifetime. In the presence of NH_3, the PL lifetime doubled from 93 ps to 193 ps (Figures 6-2c and 6-2d). However, the average PL lifetime decreased to 136 ps and 73 ps for crystals made in $MeNH_2/H_2O$ and $EtNH_2/H_2O$, respectively (Figures 6-2c and 6-2d). For these hydrothermally grown AgSePh crystals, the observed PL lifetime trend was correlated with AgSePh reaction kinetics: slower crystal formation at room temperature was observed in an increasing order of $EtNH_2/H_2O$, pure H_2O, $MeNH_2/H_2O$ and NH_3/H_2O, which is the same as the trend of increasing PL lifetime. Slower crystal growth may lead to an increase in PL lifetime by suppressing the formation of crystal defects, which can act as fast nonradiative recombination centers. Slower crystal growth in the presence of amines may be caused by reduced reaction activity of the readily formed silver-ammine complexes.[212] On the other hand, the faster kinetics in $EtNH_2/H_2O$ could be explained by the miscibility between $EtNH_2/H_2O$ and toluene, resulting in a single-phase reaction mixture with efficient diffusion of reactive chemical species to the growing crystallites.

An additional benefit of amine-assisted synthesis is the suppression of AgSePh mid-gap luminescence at low temperature. Figures 6-2b and 6-3 compare the PL spectra of hydrothermally

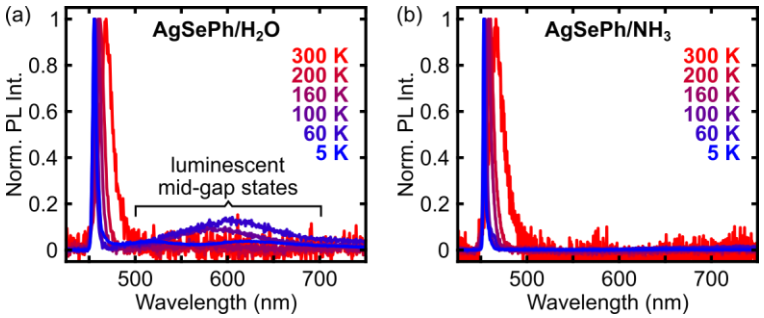

Figure 6-3. Selected temperature-dependent photoluminescence spectra between 5 K and 300 K of AgSePh crystals prepared in (a) H_2O and in (b) NH_3/H_2O.

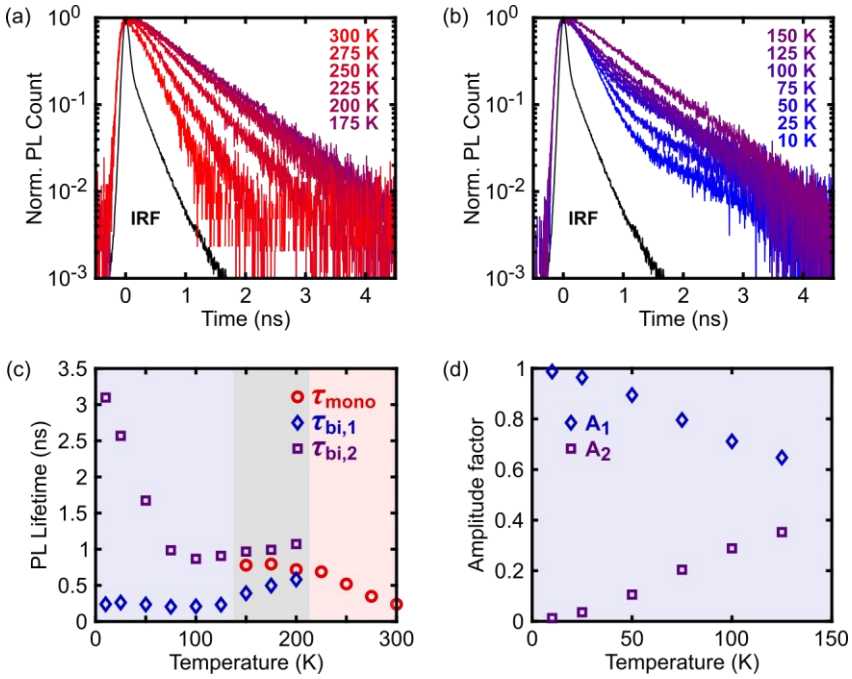

Figure 6-4. (a-b) Time-resolved photoluminescence decays at 10-300 K of AgSePh prepared in NH_3/H_2O along with the decay due to instrument response function (IRF). (c) Extracted temperature-dependent photoluminescence lifetimes between 10 K and 300 K when fitted with monoexponential (τ_{mono}) and biexponential (τ_{bi}) functions. (d) Amplitude factors of biexponential fitting between 10 K and 125 K.

grown AgSePh crystals with and without NH_3 present during the reaction. At low sample temperature (below ~150 K), AgSePh crystals prepared in the absence of NH_3 showed broad low-energy PL features spanning 500 – 700 nm in addition to narrow excitonic emission at ~460 nm. In contrast, only the narrow excitonic emission was observed for AgSePh crystals grown from NH_3/H_2O. The complete elimination of mid-gap luminescence explains the increased PL lifetime, and suggests that the broad low-energy luminescence band may relate to crystal defects formed during the synthesis and not solely to self-trapped excitons.[237,238] Temperature dependent transient PL data suggest a complicated exciton fine structure (Figure 6-4).

6.4 Reaction Kinetics and Mechanistic Studies

To understand the role of amines in AgSePh synthesis, reaction kinetics studies were conducted (Figure 6-5a). For simplicity, we focused our studies on the organic single-phase reaction in $PrNH_2$/toluene to eliminate any effects of the aqueous-organic interface. First, we found that chemical concentrations influenced the kinetics of crystal formation. While a 1.5 mM mixture of $AgNO_3$ and Ph_2Se_2 in 50% v/v $PrNH_2$/toluene did not form crystals until at least 3 days later,

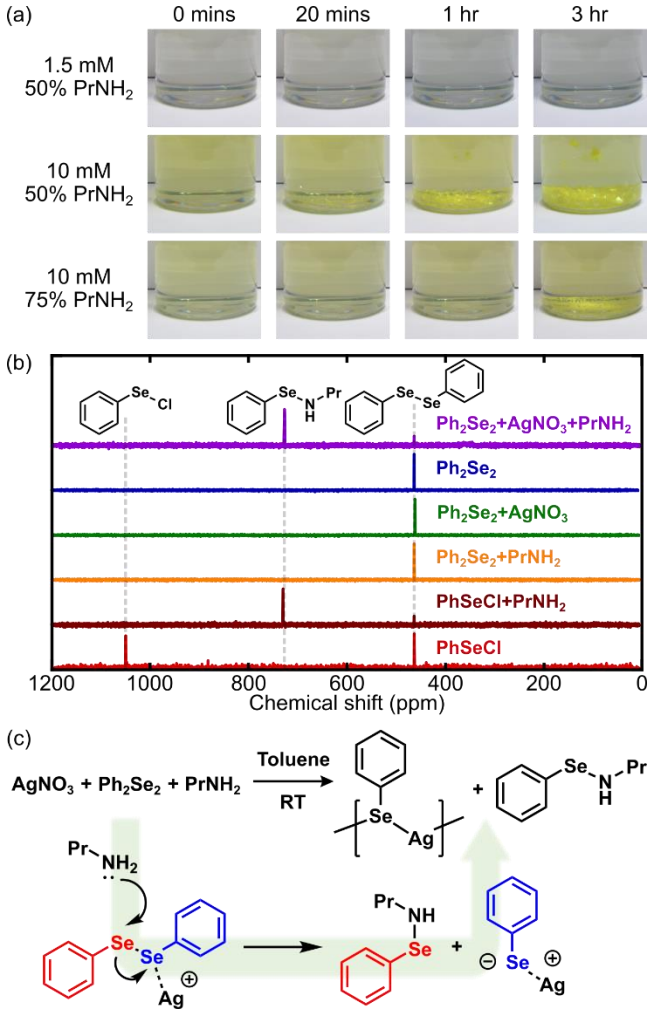

Figure 6-5. (a) Images of reaction mixtures showing the dependence of crystal formation rate on the solution concentration and the percentage by volume of $PrNH_2$ in the combined $PrNH_2$-toluene solution. (b) ^{77}Se nuclear magnetic resonance spectra of the reaction mixture and its individual components. (c) Proposed mechanism to form AgSePh from $AgNO_3$, Ph_2Se_2, and $PrNH_2$.

increasing the $AgNO_3$ and Ph_2Se_2 concentrations to 10 mM resulted in crystal formation within 20 minutes. Second, a slower crystal growth rate was observed in a solution mixture with a higher amine content. Compared to the 10 mM solution with 50% v/v $PrNH_2$ whose crystal formation was observed in 20 minutes, increasing the percentage of $PrNH_2$ to 75% lengthened the crystal formation time to 3 hr. These observations suggest that a key role of the amine is to form silver-ammine complexes in solution, which subsequently reduce the activity of reactive Ag^+ ions, thereby slowing down crystal growth and allowing for the formation of higher quality crystals.[212]

In addition to their role in the formation of silver-ammine coordination complexes, amines also react directly with Ph_2Se_2 to form a key reaction intermediate. Using ^{77}Se nuclear magnetic resonance (NMR) spectroscopy to study the single-phase reaction between $AgNO_3$ and Ph_2Se_2 in $PrNH_2$/toluene, we observed two peaks in the reaction mixture at 463.15 and 726.69 ppm (Figure 6-5b, violet). While the former could be assigned to Ph_2Se_2 (Figure 6-5b, blue), the presence of the latter implied a new Se-containing species in the solution mixture. This Se-containing species was observed only when Ph_2Se_2 was mixed with both $AgNO_3$ and $PrNH_2$ and not in the absence of one of the latter two (Figure 6-5b, green and orange). We hypothesized that this Se-containing species may be a selenenamide (RSe-NR'R'') as its sulfur analogues, sulfenamides (RS-NR'R''), are known to form when disulfides interact with amines in the presence of Ag^+ ions.[239–242] To confirm our hypothesis, we synthesized a N-propylphenylselenenamide (PhSeNHPr) by reacting phenylselenyl chloride (PhSeCl) with $PrNH_2$ (see Supporting Information).[243,244] The ^{77}Se NMR peak of PhSeNHPr appeared at 729.62 ppm (Figure 6-5b, brown), agreeing with the previously reported literature[245] and verifying the identity of the second Se-containing species in the reaction mixture.

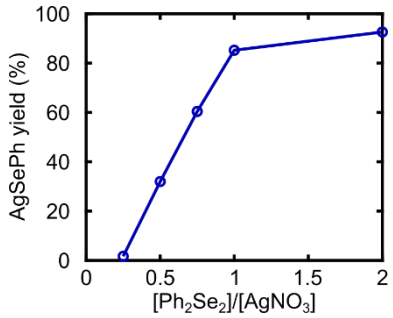

Figure 6-6. Determination of reaction stoichiometry of Ph_2Se_2 and $AgNO_3$.

Determination of the reaction stoichiometry further confirmed the production of selenenamide. We found that a 1:1 ratio of Ph_2Se_2:$AgNO_3$ was needed to obtain 100% formation yield of AgSePh (Figure 6-6), suggesting that half of the selenium atoms in Ph_2Se_2 were used to form AgSePh and the other half were converted into PhSeNHPr. Because Ag^+ ions were needed to see the ^{77}Se NMR peak of PhSeNHPr in the single-phase reaction, we propose that the reaction between Ph_2Se_2 and $PrNH_2$ is facilitated by Ag^+ ions acting as a Lewis acid to weaken the Se-Se bond (Figure 6-5c). The electrophilic Se-Se bond in Ph_2Se_2 then interacts with nucleophilic $PrNH_2$ to produce PhSeNHPr and a phenylselenolate ion ($PhSe^-$), which later interacts with Ag^+ ions to form AgSePh.

6.5 Generalizable Single-Crystal Growth

Understanding the role of amines in AgSePh synthesis enabled growth of even higher quality single crystals. Mixing a 20 mM solution of $AgNO_3$ in $PrNH_2$ with a 20 mM solution of Ph_2Se_2 in toluene at -20 °C for 4 weeks yielded AgSePh single crystals with sufficient quality for structural refinement by single-crystal X-ray diffraction. AgSePh crystallized in the monoclinic centrosymmetric space group $P2_1/c$ with a monolayer thickness of 1.4 nm (Figures 6-7 and 6-8, and Table 6-1). Compared to the previously reported multi-step method which involves the use of highly sensitive butyllithium and requires careful preparation,[113] our developed method reduces

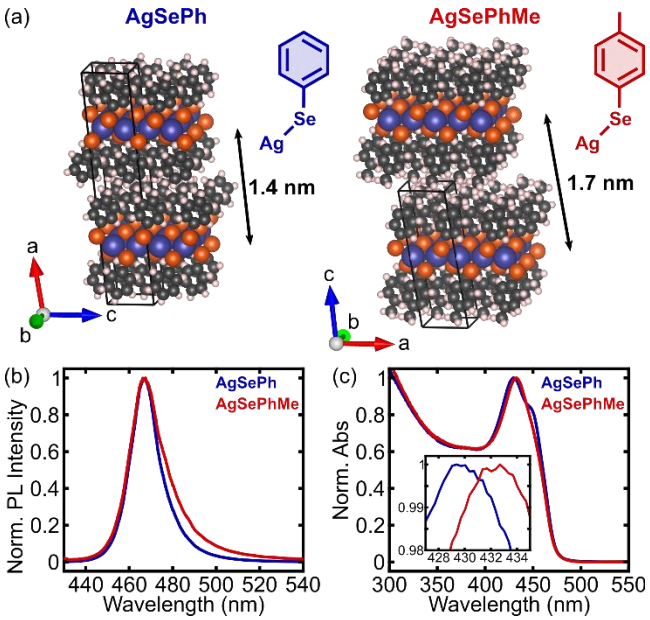

Figure 6-7. (a) Crystal structures of AgSePh and AgSePhMe. Ag, Se, C, H atoms are depicted by purple, orange, black, and cream spheres, respectively. (b) Photoluminescence spectra of AgSePh and AgSePhMe. (c) Absorption spectra obtained by diffuse reflectance spectroscopy of AgSePh and AgSePhMe with an inset showing the zoom-in view to excitonic absorption peaks.

the synthesis complexity to one step and allows the use of stable reagents.

The amine-assisted crystal growth method is also generalizable to other 2D MOCs. As an example, we grew single crystals of silver 4-methylphenylselenolate (AgSePhMe) – a new 2D MOC – which crystallized in the monoclinic centrosymmetric space group $P2_1/c$ with a monolayer thickness of 1.7 nm (Figures 6-7 and 6-8, and Table 6-1). Compared to AgSePh, AgSePhMe's PL peak appeared at the same wavelength but had a broader FWHM of 19 nm (Figure 6-7b). However, the excitonic absorption peak shifted from 429 nm in AgSePh to 433 nm in AgSePhMe (Figure 6-7c), indicating some ability to tune the band gap of 2D MOCs through organic functionalization.[114]

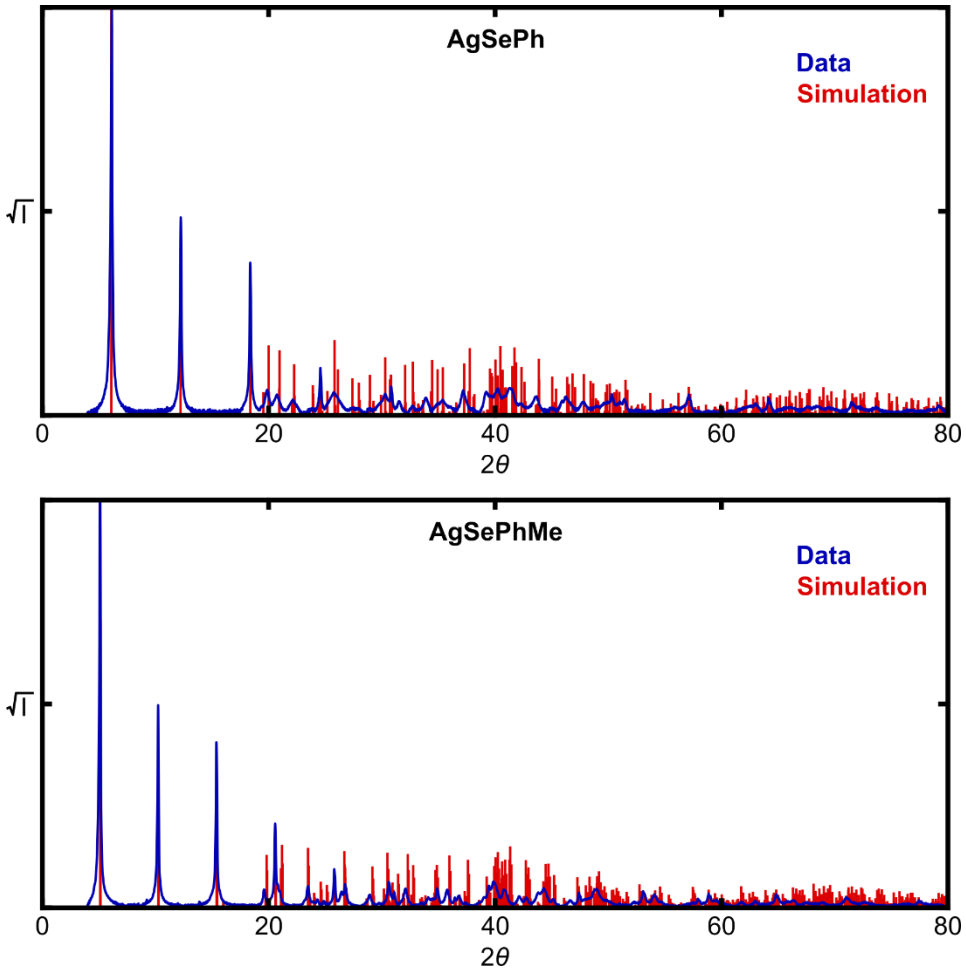

Figure 6-8. Powder X-ray diffraction patterns (blue) of AgSePh (top) and AgSePhMe (bottom) and the corresponding simulated patterns (red) from collected crystallographic information by single-crystal X-ray diffraction.

Table 6-1. Crystal data and structure refinement for AgSePh and AgSePhMe.

	AgSePh	AgSePhMe
Identification code	X21004	P21026
Empirical formula	$C_{12}H_{10}Ag_2Se_2$	$C_{14}H_{14}Ag_2Se_2$
M_r	527.86	555.91
Temperature (K)	100(2)	100(2)
Wavelength (Å)	0.71073	0.71073
Crystal system	Monoclinic	Monoclinic
Space group	$P2_1/c$	$P2_1/c$
a (Å)	5.8334(5)	17.2752(10)
b (Å)	7.2866(6)	7.2661(4)
c (Å)	29.079(3)	5.7676(3)
α (°)	90	90
β (°)	95.5819(16)	99.117
γ (°)	90	90
V (Å^3)	1230.16(18)	714.82(7)
Z	4	2
Calculated density (Mg/m^3)	2.850	2.583
Absorption coefficient (mm^{-1})	9.067	7.809
F(000)	976	520
Crystal size (mm)	0.230 x 0.220 x 0.020	0.230 x 0.215 x 0.010
Theta range for data collection (°)	2.815 to 31.540	2.803 to 30.994
Index ranges	-8<=h<=8, -10<=k<=10, -42<=l<=42	-25<=h<=25, -10<=k<=10, -8<=l<=8
Reflections collected	37922	31849
Independent reflections	4107 [R(int) = 0.0381]	2277 [R(int) = 0.0365]
Completeness to theta = 25.242°	99.5 %	99.5 %
Absorption correction	Semi-empirical from equivalents	Semi-empirical from equivalents
Refinement method	Full-matrix least-squares on F^2	Full-matrix least-squares on F^2
Data / restraints / parameters	4107 / 32 / 145	2277 / 0 / 84
Goodness-of-fit on F^2	1.155	1.147
Final R indices [I>2sigma(I)]	$R1$ = 0.0341, $wR2$ = 0.1051	$R1$ = 0.0214, $wR2$ = 0.0563
R indices (all data)	$R1$ = 0.0393, $wR2$ = 0.1090	$R1$ = 0.0239, $wR2$ = 0.0588
Largest diff. peak and hole (e.Å^{-3})	1.817 and -2.419	0.534 and -0.978

6.6 Conclusions

To summarize, we have shown that size and quality enhancement of AgSePh crystals can be achieved by promoting the formation of silver-ammine complexes. Detailed optical characterization by time-resolved and temperature-dependent PL spectroscopy showed that the addition of NH_3 led to a two-fold increase in PL lifetime and a complete suppression of luminescent mid-gap states. Reaction kinetics studies and mechanistic studies by ^{77}Se NMR spectroscopy suggest dual roles of amines as 1) a coordinating ligand to reduce the reaction activity of Ag^+ ions, and 2) a reactant to convert Ph_2Se_2 into an active intermediate. Based on this knowledge, a new growth method with single reaction step and stable reactants was developed to grow single crystals of AgSePh. The method was generalizable to other 2D MOCs such as AgSePhMe, a novel member of this family. The results of this work provide a general strategy for the growth of high-quality 2D MOC materials for further fundamental studies and device integration.

6.7 Methods

Preparation of silver phenylselenolate (AgSePh) microcrystals by a hydrothermal reaction. Microcrystals of AgSePh were prepared by a hydrothermal reaction.[107] A 3 mM solution of silver nitrate ($AgNO_3$; >=99.0%, Millipore Sigma) was prepared by dissolving 0.0102 g of $AgNO_3$ in 20 mL of either water (H_2O), ammonium hydroxide solution (NH_3/H_2O; ACS reagent, 28.0-30.0% NH_3 basis, Millipore Sigma), methylamine solution ($MeNH_2/H_2O$; 40 wt. % in H_2O, Millipore Sigma), or ethylamine solution ($EtNH_2/H_2O$; 68.0 wt. % solution in H_2O, Millipore Sigma). In a separate container, a 3 mM solution of diphenyl diselenide (Ph_2Se_2; 97.0+%, TCI America) was prepared by dissolving 0.0187 g of Ph_2Se_2 in 20 mL of toluene. Then, 3 mL of 3 mM $AgNO_3$

solution were transferred into a Teflon lined hydrothermal autoclave reactor (Homend) followed by 3 mL of 3 mM Ph_2Se_2 solution. The hydrothermal reactor was subsequently sealed and placed in an oven at 180 °C. After 1 hr, the hydrothermal reactor was removed from the oven and let to cool to room temperature for 1-3 hr. Resulting AgSePh microcrystals were then collected by inserting a clean coverslip into a tilted biphasic solution and slowly removing the substrate. The collected microcrystals were washed with isopropanol and dried by compressed nitrogen gas (N_2).

Preparation of AgSePh crystals by an organic single-phase reaction. Crystals of AgSePh were grown by mixing 10 mL of 3 mM solution of $AgNO_3$ in propylamine ($PrNH_2$) with 10 mL of 3 mM solution of Ph_2Se_2 in toluene at room temperature for 3-5 days. $PrNH_2$ can be substituted by other long-chain amines, such as butylamine, pentylamine, and hexylamine, to yield similar results.

Preparation of N-propylphenylselenenamide. N-propylphenylselenenamide (PhSeNHPr) was synthesized following the previously reported literature.[243,244] $PrNH_2$ (0.035 g, 0.6 mmol) was added to a solution of phenylselenyl chloride (PhSeCl; 0.057 g, 0.3 mmol) in toluene d8 (2 mL) in a glove box. A dark brown solution formed immediately after mixing and then turned into a yellow solution while forming a colorless solid. The resulting solution was filtered and nuclear magnetic resonance (NMR) measurements were carried out without further purification. Diphenyl diselenide (Ph_2Se_2) was added as an NMR standard.

Preparation of bis(4-methylphenyl) diselenide. Bis(4-methylphenyl) diselenide was synthesized following a previously reported procedure.[246,247] Firstly, a crystal of iodine was added to a dispersion of Mg (2.64 g, 110 mmol) in 100 mL of anhydrous tetrahydrofuran (THF) and the mixture was stirred under N_2 atmosphere for 20 min. After the solution became colorless, 4-bromotoluene (3.4 g, 20 mmol) was added at once and the reaction mixture was heated by a heat gun to initiate the reaction. After that, another portion of 4-bromotoluene (13.7 g, 80 mmol) in

THF (50 mL) was added dropwise to a vigorously stirred dispersion. The reaction mixture was further stirred at 50 °C for 1 hr before being cooled on ice. Next, elemental selenium (7.9 g, 100 mmol) was added in one portion, and the reaction mixture was allowed to warm to room temperature and stirred for 1 hr to yield a yellowish solution. This solution was filtered and poured into a 1 M hydrochloric acid (100 mL) to form a biphasic mixture. The organic phase was then extracted with dichloromethane (50 mL × 3) and washed with brine before being dried with sodium sulfate. Subsequently, solvents were evaporated under reduced pressure to obtain a crude product. Purification of this product was performed by column chromatography (hexane) followed by a reprecipitation in dichloromethane and hexane to afford bis(4-methylphenyl) diselenide as orange yellow powder (9.6 g, 56% yield). ^{1}H NMR ($CDCl_3$, 400 MHz) δ 7.50 (d, 4H, J = 8.1 Hz), 7.08 (d, 4H, J = 7.9 Hz), 2.35 (s, 6H).

Single-crystal growth of AgSePh and silver 4-methylphenylselenolate (AgSePhMe). Single crystals of AgSePh were obtained by mixing 5 mL of 20 mM solution of $AgNO_3$ in $PrNH_2$ and 5 mL of 20 mM solution of Ph_2Se_2 in toluene at -20 °C for 4 weeks. Single crystals of AgSePhMe were obtained by mixing 5 mL of 15 mM solution of $AgNO_3$ in $PrNH_2$ and 5 mL of 15 mM solution of bis(4-methylphenyl) diselenide in toluene at -20 °C for 4 weeks.

Nuclear Magnetic Resonance (NMR) spectroscopy. NMR spectra were recorded with a Bruker Advance 400 MHz spectrometer at 298 K. The spectral data are reported as chemical shift (in ppm). Chemical shifts for ^{77}Se NMR were calibrated against peak of Ph_2Se_2 (463.15 ppm).

Steady-state photoluminescence (PL) spectroscopy. Steady-state PL measurements were performed on an inverted microscope (Nikon, Ti-U Eclipse) in air. The samples were excited by focusing the output of a 405 nm laser diode (Picoquant, LDHDC-405M, continuous wave mode) by an objective lens (Nikon, CFI S Plan Fluor ELWD, 40x, 0.6 NA) to <1 μm spot. The

polarization of the excitation was controlled to be circularly polarized with a circular polarizer (Thorlabs, CP1R405). After the excitation, the photoluminescence was collected in the epi configuration, and passed through a dichroic mirror and a long-pass filter. Then, it was directed into a spectrograph (Princeton Instruments, SP-2500) mounted with a cooled charge-coupled detector (Princeton Instruments, Pixis).

Time-resolved PL spectroscopy. Time-resolved PL measurements were performed using the same microscope setup as steady-state PL spectroscopy with some modifications. The excitation light source was replaced by a frequency doubled light (405 nm) of the 810 nm output from a femtosecond laser (Coherent Mira HP) operating at 76 MHz. The detector used was a Si avalanche photodiode (Micro Photon Devices) connected to a counting board for time-correlated single photon counting (PicoQuant, PicoHarp 300). Instrument response function was obtained by detecting the Raman scattering from water appearing at ~470 nm close to the PL peak position of AgSePh. Extraction of PL lifetime was performed using a publicly available ChiSurf software package developed by Thomas-Otavio Peulen and co-workers.[234]

Temperature-dependent PL spectroscopy. Temperature-dependent experiments were performed by mounting samples on the cold finger of a microscopy cryostat (Janis Research, ST-500) and flowing liquid helium through the cold finger of the cryostat.

Diffuse reflectance spectroscopy. Measurements of diffuse reflectance were performed on Cary 5000 UV-Vis-NIR spectrometer equipped with a PIKE Technologies DiffusIR accessory. Solid samples were prepared by grinding with dry potassium bromide (KBr) to a ~1 wt% dilution and diffuse reflectance spectra were normalized to a 100% KBr baseline. The obtained diffuse reflectance spectra were converted into absorption spectra by Kubelka-Munk transform:[248]

$$F(R) = \frac{(1-R)^2}{2R},$$

where $F(R)$ is the Kubelka-Munk function with a value proportional to sample's absorption coefficient, and R is the relative reflectance of the sample with the 100% KBr baseline.

Single-crystal X-ray diffraction. Low-temperature diffraction data were collected on Bruker-AXS X8 Kappa Duo diffractometers with *IμS* micro-sources using Mo K_α radiation (λ = 0.71073 Å), using a Smart APEX2 CCD detector for the structure of AgSePh and a Photon 3 CPAD detector for the structure of AgSePhMe, performing ϕ-and ω-scans. The structures were solved by dual-space methods using SHELXT[152] and refined against F^2 on all data by full-matrix least squares with SHELXL-2017[153] following established refinement strategies.[249] All non-hydrogen atoms were refined anisotropically. All hydrogen atoms were included into the model at geometrically calculated positions and refined using a riding model. The isotropic displacement parameters of all hydrogen atoms were fixed to 1.2 times the *U*-value of the atoms they are linked to (1.5 times for the methyl group). Details of the data quality and a summary of the residual values of the refinements are listed in Table 6-1. Additional crystallographic information – atomic coordianates, isotropic and anisotropic displacement parameters, bond lengths, and bond angles – can be found in the summary of crystallographic information below in Appendix A. CCDC-2096771 and CCDC-2096772 contain the supplementary crystallographic data for this work. These data can be obtained free of charge via www.ccdc.cam.ac.uk/data_request/cif, or by emailing data_request@ccdc.cam.ac.uk, or by contacting The Cambridge Crystallographic Data Centre, 12 Union Road, Cambridge CB2 1EZ, UK; fax: +44 1223 336033

Powder X-ray diffraction (PXRD). Powder X-ray diffraction data were collected using a PANalytical Empyrean X-ray diffractometer (Cu Kα radiation, λ = 1.54184 Å). The incident beam

path optics included a 1/8° divergence slit, a 10 mm mask, Bragg-Brentano HD optics, a 0.02 rad soller slit, and a 1/4° anti-scatter slit with an illuminated length of 6 mm. The diffracted beam optics included a 0.02 rad soller slit and a PIXcel 1D detector. The angular step in 2θ was 0.013°.

6.8 Appendix A: Additional Crystallographic Information of AgSePh and AgSePhMe

The two crystal structures are similar (Figure 6-9). Both compounds crystallize in the monoclinic centrosymmetric space group $P2_1/c$: AgSePh with two monomeric subunits in the asymmetric unit (contents of asymmetric unit: $Ag_2Se_2Ar_2$; Ar = Ph = phenyl or C_6H_5) and AgSePhMe with one monomeric subunit in the asymmetric unit (contents of asymmetric unit: AgSeAr; Ar = 4-methyl-phenyl or C_7H_7). Both structures are 2D-polymers and application of crystallographic symmetry gives rise to infinite sheets with the phenyl rings displayed on both surfaces. Those sheets stack along the crystallographic *c*-direction for the structure of AgSePh and along the crystallographic *a*-direction for the structure of AgSePhMe in such a fashion that the

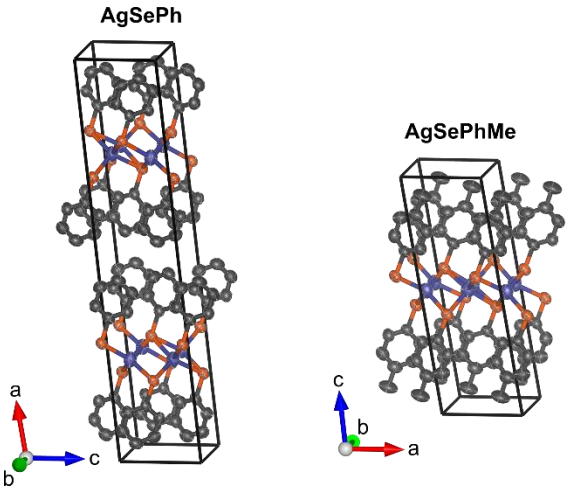

Figure 6-9. Crystallographic unit cells of AgSePh and AgSePhMe. Thermal ellipsoids of Ag, Se, and C are depicted in purple, orange, and black, respectively. H atoms are omitted for clarity.

phenyl rings from neighboring sheets meet in a hydrophobic layer that, in the crystallographic packing, alternates with a metallic layer of selenium and silver.

The crystal quality of AgSePh was comparatively low and there were signs of non-merohedral twinning. The twinning could not be resolved. It seems there are several minor domains that, individually, are too small to allow for stable data reduction but together they comprise an appreciable portion of the crystal so that some effects of the twinning are apparent in the structure. Most notably, there is unexplained positive and negative residual electron density located at seemingly random sites in the structure, which may well be an artefact of unresolved non-merohedral twinning. The highest residual density maximum corresponds to 1.82 electrons and is located 1.65 Å away from selenium atom Se2; the lowest negative peak corresponds to -2.42 electrons and is located 1.66 Å away from selenium atom Se1. The two phenyl rings were restrained to display similar geometry with respect to bonds and angles.

The structure of AgSePhMe was refined as a pseudo-merohedral twin (twin law -1 0 -1 0 -1 0 0 0 1). The twin ratio was refined freely and converged at 0.0258(3). In spite of the small size of the minor twin domain, introduction of the twin law improved the structure markedly. No restraints were applied.

Table 6-2. Atomic coordinates (x 10^4) and equivalent isotropic displacement parameters ($Å^2$ x 10^3) for AgSePh. U(eq) is defined as one third of the trace of the orthogonalized U^{ij} tensor.

	x	y	z	U(eq)
Ag(1)	2373(1)	11284(1)	2488(1)	18(1)
Se(1)	-469(1)	9292(1)	2964(1)	13(1)
C(1)	5866(5)	4350(4)	3581(1)	14(1)
C(2)	4574(5)	5121(5)	3912(1)	17(1)
C(3)	5447(6)	5105(5)	4376(1)	20(1)
C(4)	7583(6)	4323(5)	4507(1)	19(1)
C(5)	8875(6)	3571(5)	4175(1)	20(1)
C(6)	8027(5)	3596(4)	3710(1)	17(1)
Ag(2)	2594(1)	7313(1)	2540(1)	18(1)
Se(2)	4572(1)	4302(1)	2947(1)	13(1)
C(11)	810(5)	9284(4)	3602(1)	14(1)
C(12)	-514(5)	8585(5)	3933(1)	17(1)
C(13)	322(6)	8655(5)	4399(1)	20(1)
C(14)	2466(6)	9431(5)	4532(1)	20(1)
C(15)	3794(5)	10119(5)	4196(1)	19(1)
C(16)	2972(5)	10041(4)	3731(1)	17(1)

Table 6-3. Bond lengths [Å] and angles [°] for AgSePh.

Ag(1)-Se(1)	2.6878(4)	Se(1)-Ag(1)-Ag(2)	57.376(10)
Ag(1)-Se(2)#1	2.7013(4)	Se(2)#1-Ag(1)-Ag(2)	57.495(10)
Ag(1)-Se(1)#2	2.7353(4)	Se(1)#2-Ag(1)-Ag(2)	146.986(14)
Ag(1)-Se(2)#3	2.8155(4)	Se(2)#3-Ag(1)-Ag(2)	137.623(13)
Ag(1)-Ag(2)	2.8995(5)	Se(1)-Ag(1)-Ag(2)#2	60.250(10)
Ag(1)-Ag(2)#2	2.9866(4)	Se(2)#1-Ag(1)-Ag(2)#2	143.553(13)
Ag(1)-Ag(2)#1	3.0387(4)	Se(1)#2-Ag(1)-Ag(2)#2	55.842(10)
Se(1)-C(11)	1.930(3)	Se(2)#3-Ag(1)-Ag(2)#2	102.273(12)
Se(1)-Ag(2)	2.6885(4)	Ag(2)-Ag(1)-Ag(2)#2	106.864(10)
Se(1)-Ag(2)#2	2.8596(4)	Se(1)-Ag(1)-Ag(2)#1	142.448(13)
C(1)-C(6)	1.393(4)	Se(2)#1-Ag(1)-Ag(2)#1	55.710(10)
C(1)-C(2)	1.397(4)	Se(1)#2-Ag(1)-Ag(2)#1	97.920(12)
C(1)-Se(2)	1.924(3)	Se(2)#3-Ag(1)-Ag(2)#1	54.755(10)
C(2)-C(3)	1.394(4)	Ag(2)-Ag(1)-Ag(2)#1	102.087(10)
C(2)-H(2)	0.9500	Ag(2)#2-Ag(1)-Ag(2)#1	151.006(15)
C(3)-C(4)	1.390(5)	C(11)-Se(1)-Ag(1)	107.26(10)
C(3)-H(3)	0.9500	C(11)-Se(1)-Ag(2)	103.16(10)
C(4)-C(5)	1.393(5)	Ag(1)-Se(1)-Ag(2)	65.274(12)
C(4)-H(4)	0.9500	C(11)-Se(1)-Ag(1)#4	124.07(9)
C(5)-C(6)	1.393(4)	Ag(1)-Se(1)-Ag(1)#4	115.266(13)
C(5)-H(5)	0.9500	Ag(2)-Se(1)-Ag(1)#4	66.816(11)
C(6)-H(6)	0.9500	C(11)-Se(1)-Ag(2)#2	127.05(9)
Ag(2)-Se(2)	2.6984(4)	Ag(1)-Se(1)-Ag(2)#2	65.060(11)
Ag(2)-Se(2)#1	2.6993(4)	Ag(2)-Se(1)-Ag(2)#2	116.855(13)
C(11)-C(12)	1.389(4)	Ag(1)#4-Se(1)-Ag(2)#2	103.594(14)
C(11)-C(16)	1.394(4)	C(6)-C(1)-C(2)	120.4(3)
C(12)-C(13)	1.394(4)	C(6)-C(1)-Se(2)	120.9(2)
C(12)-H(12)	0.9500	C(2)-C(1)-Se(2)	118.7(2)
C(13)-C(14)	1.393(5)	C(3)-C(2)-C(1)	119.5(3)
C(13)-H(13)	0.9500	C(3)-C(2)-H(2)	120.2
C(14)-C(15)	1.395(5)	C(1)-C(2)-H(2)	120.2
C(14)-H(14)	0.9500	C(4)-C(3)-C(2)	120.1(3)
C(15)-C(16)	1.391(4)	C(4)-C(3)-H(3)	119.9
C(15)-H(15)	0.9500	C(2)-C(3)-H(3)	119.9
C(16)-H(16)	0.9500	C(3)-C(4)-C(5)	120.2(3)
		C(3)-C(4)-H(4)	119.9
Se(1)-Ag(1)-Se(2)#1	114.868(15)	C(5)-C(4)-H(4)	119.9
Se(1)-Ag(1)-Se(1)#2	116.018(11)	C(4)-C(5)-C(6)	120.1(3)
Se(2)#1-Ag(1)-Se(1)#2	117.339(14)	C(4)-C(5)-H(5)	120.0
Se(1)-Ag(1)-Se(2)#3	116.919(14)	C(6)-C(5)-H(5)	120.0
Se(2)#1-Ag(1)-Se(2)#3	110.387(11)	C(1)-C(6)-C(5)	119.7(3)
Se(1)#2-Ag(1)-Se(2)#3	75.343(13)	C(1)-C(6)-H(6)	120.2

C(5)-C(6)-H(6)	120.2
Se(1)-Ag(2)-Se(2)	120.631(15)
Se(1)-Ag(2)-Se(2)#1	114.908(15)
Se(2)-Ag(2)-Se(2)#1	114.127(11)
Se(1)-Ag(2)-Se(1)#4	111.963(11)
Se(2)-Ag(2)-Se(1)#4	75.180(13)
Se(2)#1-Ag(2)-Se(1)#4	113.692(14)
Se(1)-Ag(2)-Ag(1)	57.350(10)
Se(2)-Ag(2)-Ag(1)	148.134(14)
Se(2)#1-Ag(2)-Ag(1)	57.560(10)
Se(1)#4-Ag(2)-Ag(1)	136.609(14)
Se(1)-Ag(2)-Ag(1)#4	57.341(10)
Se(2)-Ag(2)-Ag(1)#4	100.352(13)
Se(2)#1-Ag(2)-Ag(1)#4	139.724(13)
Se(1)#4-Ag(2)-Ag(1)#4	54.691(9)
Ag(1)-Ag(2)-Ag(1)#4	102.182(10)
Se(1)-Ag(2)-Ag(1)#5	146.247(13)
Se(2)-Ag(2)-Ag(1)#5	55.797(10)
Se(2)#1-Ag(2)-Ag(1)#5	58.414(10)
Se(1)#4-Ag(2)-Ag(1)#5	99.693(12)
Ag(1)-Ag(2)-Ag(1)#5	106.448(10)
Ag(1)#4-Ag(2)-Ag(1)#5	151.007(15)
C(1)-Se(2)-Ag(2)	121.12(9)
C(1)-Se(2)-Ag(2)#5	107.97(10)
Ag(2)-Se(2)-Ag(2)#5	117.663(14)
C(1)-Se(2)-Ag(1)#5	102.89(9)
Ag(2)-Se(2)-Ag(1)#5	68.492(11)
Ag(2)#5-Se(2)-Ag(1)#5	64.947(12)
C(1)-Se(2)-Ag(1)#6	125.93(9)
Ag(2)-Se(2)-Ag(1)#6	105.762(14)
Ag(2)#5-Se(2)-Ag(1)#6	66.833(11)
Ag(1)#5-Se(2)-Ag(1)#6	119.139(13)
C(12)-C(11)-C(16)	120.5(3)
C(12)-C(11)-Se(1)	118.6(2)
C(16)-C(11)-Se(1)	120.9(2)
C(11)-C(12)-C(13)	119.6(3)
C(11)-C(12)-H(12)	120.2
C(13)-C(12)-H(12)	120.2
C(14)-C(13)-C(12)	120.2(3)
C(14)-C(13)-H(13)	119.9
C(12)-C(13)-H(13)	119.9
C(13)-C(14)-C(15)	119.8(3)
C(13)-C(14)-H(14)	120.1
C(15)-C(14)-H(14)	120.1
C(16)-C(15)-C(14)	120.1(3)
C(16)-C(15)-H(15)	119.9
C(14)-C(15)-H(15)	119.9
C(15)-C(16)-C(11)	119.7(3)
C(15)-C(16)-H(16)	120.2
C(11)-C(16)-H(16)	120.2

Symmetry transformations used to generate equivalent atoms: #1 -x+1,y+1/2,-z+1/2 #2 -x,y+1/2,-z+1/2 #3 x,y+1,z #4 -x,y-1/2,-z+1/2 #5 -x+1,y-1/2,-z+1/2 #6 x,y-1,z

Table 6-4. Anisotropic displacement parameters ($Å^2 x\ 10^3$) for AgSePh. The anisotropic displacement factor exponent takes the form: $-2p^2[\ h^2\ a^{*2}U^{11} + ...\ + 2\ h\ k\ a^*\ b^*\ U^{12}\ ]$

	U^{11}	U^{22}	U^{33}	U^{23}	U^{13}	U^{12}
Ag(1)	17(1)	12(1)	26(1)	1(1)	4(1)	1(1)
Se(1)	13(1)	11(1)	15(1)	0(1)	0(1)	0(1)
C(1)	13(1)	13(1)	16(1)	2(1)	0(1)	-2(1)
C(2)	16(1)	19(2)	18(1)	2(1)	3(1)	2(1)
C(3)	22(2)	21(2)	17(1)	1(1)	5(1)	1(1)
C(4)	20(2)	20(2)	17(2)	1(1)	-2(1)	-2(1)
C(5)	17(1)	20(2)	21(2)	1(1)	-2(1)	1(1)
C(6)	15(1)	16(1)	19(1)	0(1)	0(1)	2(1)
Ag(2)	18(1)	11(1)	26(1)	1(1)	3(1)	1(1)
Se(2)	13(1)	11(1)	15(1)	0(1)	0(1)	0(1)
C(11)	14(1)	13(1)	16(1)	0(1)	-2(1)	0(1)
C(12)	17(1)	17(1)	18(1)	0(1)	2(1)	-2(1)
C(13)	22(2)	20(2)	19(2)	2(1)	4(1)	0(1)
C(14)	22(2)	19(2)	17(2)	0(1)	-2(1)	2(1)
C(15)	17(1)	20(2)	20(2)	-1(1)	-1(1)	-1(1)
C(16)	16(1)	16(1)	19(1)	2(1)	1(1)	-1(1)

Table 6-5. Hydrogen coordinates (x 10^4) and isotropic displacement parameters ($Å^2$x 10^3) for AgSePh.

	x	y	z	U(eq)
H(2)	3112	5652	3822	21
H(3)	4579	5630	4602	24
H(4)	8164	4301	4823	23
H(5)	10337	3040	4266	23
H(6)	8917	3102	3483	20
H(12)	-1981	8062	3843	21
H(13)	-575	8172	4626	24
H(14)	3023	9493	4849	24
H(15)	5263	10640	4286	23
H(16)	3879	10503	3503	20

Table 6-6. Atomic coordinates (x 10^4) and equivalent isotropic displacement parameters ($Å^2$ x 10^3) for AgSePhMe. U(eq) is defined as one third of the trace of the orthogonalized U^{ij} tensor.

	x	y	z	U(eq)
Ag(1)	4942(1)	3035(1)	4816(1)	20(1)
Se(1)	5790(1)	5018(1)	2180(1)	14(1)
C(1)	6847(2)	5053(3)	3851(4)	15(1)
C(2)	7446(2)	5775(3)	2772(4)	18(1)
C(3)	8219(2)	5694(4)	3923(5)	22(1)
C(4)	8406(2)	4897(3)	6145(5)	20(1)
C(5)	7797(2)	4203(3)	7213(4)	19(1)
C(6)	7022(1)	4285(3)	6091(4)	17(1)
C(7)	9242(2)	4781(5)	7388(7)	31(1)

Table 6-7. Bond lengths [Å] and angles [°] for AgSePh.

Ag(1)-Se(1)	2.6909(3)	Se(1)#3-Ag(1)-Ag(1)#4	100.297(10)
Ag(1)-Se(1)#1	2.6961(3)	Ag(1)#3-Ag(1)-Ag(1)#4	149.825(15)
Ag(1)-Se(1)#2	2.7009(3)	C(1)-Se(1)-Ag(1)	106.41(8)
Ag(1)-Ag(1)#2	2.8682(4)	C(1)-Se(1)-Ag(1)#5	123.11(7)
Ag(1)-Se(1)#3	2.8797(3)	Ag(1)-Se(1)-Ag(1)#5	114.598(10)
Ag(1)-Ag(1)#3	2.98675(18)	C(1)-Se(1)-Ag(1)#2	100.08(8)
Ag(1)-Ag(1)#4	2.98676(18)	Ag(1)-Se(1)-Ag(1)#2	64.274(10)
Se(1)-C(1)	1.925(2)	Ag(1)#5-Se(1)-Ag(1)#2	67.202(7)
C(1)-C(2)	1.391(4)	C(1)-Se(1)-Ag(1)#4	128.21(7)
C(1)-C(6)	1.396(3)	Ag(1)-Se(1)-Ag(1)#4	64.742(7)
C(2)-C(3)	1.396(3)	Ag(1)#5-Se(1)-Ag(1)#4	104.786(10)
C(2)-H(2)	0.9500	Ag(1)#2-Se(1)-Ag(1)#4	116.897(10)
C(3)-C(4)	1.397(4)	C(2)-C(1)-C(6)	119.8(2)
C(3)-H(3)	0.9500	C(2)-C(1)-Se(1)	119.63(19)
C(4)-C(5)	1.395(4)	C(6)-C(1)-Se(1)	120.48(19)
C(4)-C(7)	1.510(4)	C(1)-C(2)-C(3)	119.6(2)
C(5)-C(6)	1.393(3)	C(1)-C(2)-H(2)	120.2
C(5)-H(5)	0.9500	C(3)-C(2)-H(2)	120.2
C(6)-H(6)	0.9500	C(2)-C(3)-C(4)	121.3(3)
C(7)-H(7A)	0.9800	C(2)-C(3)-H(3)	119.4
C(7)-H(7B)	0.9800	C(4)-C(3)-H(3)	119.4
C(7)-H(7C)	0.9800	C(5)-C(4)-C(3)	118.3(2)
		C(5)-C(4)-C(7)	120.1(3)
Se(1)-Ag(1)-Se(1)#1	117.032(9)	C(3)-C(4)-C(7)	121.6(3)
Se(1)-Ag(1)-Se(1)#2	115.726(10)	C(6)-C(5)-C(4)	121.1(2)
Se(1)#1-Ag(1)-Se(1)#2	117.676(13)	C(6)-C(5)-H(5)	119.5
Se(1)-Ag(1)-Ag(1)#2	58.034(9)	C(4)-C(5)-H(5)	119.5
Se(1)#1-Ag(1)-Ag(1)#2	149.744(13)	C(5)-C(6)-C(1)	119.9(2)
Se(1)#2-Ag(1)-Ag(1)#2	57.692(8)	C(5)-C(6)-H(6)	120.1
Se(1)-Ag(1)-Se(1)#3	113.464(12)	C(1)-C(6)-H(6)	120.1
Se(1)#1-Ag(1)-Se(1)#3	75.213(10)	C(4)-C(7)-H(7A)	109.5
Se(1)#2-Ag(1)-Se(1)#3	110.770(8)	C(4)-C(7)-H(7B)	109.5
Ag(1)#2-Ag(1)-Se(1)#3	135.031(12)	H(7A)-C(7)-H(7B)	109.5
Se(1)-Ag(1)-Ag(1)#3	140.200(8)	C(4)-C(7)-H(7C)	109.5
Se(1)#1-Ag(1)-Ag(1)#3	97.409(11)	H(7A)-C(7)-H(7C)	109.5
Se(1)#2-Ag(1)-Ag(1)#3	56.320(7)	H(7B)-C(7)-H(7C)	109.5
Ag(1)#2-Ag(1)-Ag(1)#3	101.453(10)		
Se(1)#3-Ag(1)-Ag(1)#3	54.568(8)		
Se(1)-Ag(1)-Ag(1)#4	60.690(7)		
Se(1)#1-Ag(1)-Ag(1)#4	56.476(8)		
Se(1)#2-Ag(1)-Ag(1)#4	145.817(9)		
Ag(1)#2-Ag(1)-Ag(1)#4	108.647(11)		

Symmetry transformations used to generate equivalent atoms: #1 -x+1,y-1/2,-z+1/2 #2 -x+1,-y+1,-z+1 #3 x,-y+1/2,z+1/2 #4 x,-y+1/2,z-1/2 #5 -x+1,y+1/2,-z+1/2

Table 6-8. Anisotropic displacement parameters ($Å^2 x\ 10^3$) for AgSePhMe. The anisotropic displacement factor exponent takes the form: $-2p^2[\ h^2\ a^{*2}U^{11} + ... + 2\ h\ k\ a^*\ b^*\ U^{12}\ ]$

	U^{11}	U^{22}	U^{33}	U^{23}	U^{13}	U^{12}
Ag(1)	26(1)	13(1)	20(1)	-2(1)	4(1)	-2(1)
Se(1)	16(1)	12(1)	15(1)	0(1)	-1(1)	0(1)
C(1)	15(1)	14(1)	14(1)	0(1)	-1(1)	1(1)
C(2)	22(1)	16(1)	17(1)	1(1)	3(1)	0(1)
C(3)	18(1)	22(1)	25(1)	0(1)	4(1)	-1(1)
C(4)	18(1)	19(1)	23(1)	-2(1)	0(1)	1(1)
C(5)	21(1)	18(1)	17(1)	0(1)	-2(1)	2(1)
C(6)	18(1)	16(1)	16(1)	1(1)	2(1)	-1(1)
C(7)	17(1)	37(2)	35(2)	0(1)	-5(1)	1(1)

Table 6-9. Hydrogen coordinates (x 10^4) and isotropic displacement parameters ($Å^2$x 10^3) for AgSePh.

	x	y	z	U(eq)
H(2)	7329	6319	1259	22
H(3)	8626	6190	3181	26
H(5)	7913	3666	8730	23
H(6)	6613	3818	6850	21
H(7A)	9464	3583	7067	46
H(7B)	9253	4918	9083	46
H(7C)	9553	5764	6821	46

Chapter 7 Summary and Outlook

In this thesis, we have shown advances in the syntheses and photophysical understanding of two families of 2D hybrid organic-inorganic semiconductors: 2D LHPs and 2D MOCs.

7.1 Summary and Outlook of 2D LHPs

For 2D LHPs, we have developed a cooling-induced crystallization method to produce phase-pure 2D LHPs with controllable chemical compositions and refined their crystal structures across temperature and phase transitions. The structural information was then used to understand the temperature-dependent optical properties and address the debate over the origin of broadband emission in 2D LHPs. We found that broadband emission could arise from defect-associated emission and emission from self-trapped excitons, but they appeared at different wavelengths and had different characteristics. Overall, my research on 2D LHPs highlights the importance of synthetic advance that enables better understanding of 2D LHPs' structures and optical properties.

While there has been a significant improvement in the understanding of 2D LHPs, more research is still needed to address the challenges of this materials family. These include issues on stability, performance, and lead toxicity. Some solutions to these problems may lie in compositional tuning and organic spacer engineering. For example, a result in this thesis suggests a connection of broadband emission by self-trapped excitons to exciton-phonon coupling and structural distortion, both of which are influenced by 2D LHPs chemical constituents.

7.2 Summary and Outlook of 2D MOCs

For 2D MOCs, we have presented two chemical strategies to produce AgSePh thin films with controllable grain size from <200 nm to >5 μm and AgSePh microcrystals with improved crystal size from ~2 μm to >1mm. Both of these methods rely on the complexation of Ag^+ ions and also give AgSePh with improved optical and electrical properties. These reported methods to produce high-quality 2D MOC materials will be important for further fundamental studies and device integration of this new class of 2D hybrid organic-inorganic semiconductors.

Although AgSePh and 2D MOCs possess many exciting properties, their research is still in its infancy. Many fundamental parameters such as dielectric constant and charge mobility have not been measured, and more applications in optoelectronic devices need to be elucidated. Moreover, the unique in-plane anisotropy of AgSePh requires further investigation and may lead to its application in polarized emitting and detecting applications. Additionally, discovering new MOC materials by organic functionalization is another interesting direction that may lead to new compounds with even more exciting properties.

Bibliography

(1) Novoselov, K. S.; Mishchenko, A.; Carvalho, A.; Castro Neto, A. H. 2D Materials and van Der Waals Heterostructures. *Science (80-.).* **2016**, *353* (6298), aac9439. https://doi.org/10.1126/science.aac9439.

(2) Mauck, C. M.; Tisdale, W. A. Excitons in 2D Organic–Inorganic Halide Perovskites. *Trends Chem.* **2019**, *1* (4), 380–393. https://doi.org/10.1016/j.trechm.2019.04.003.

(3) Zhang, F.; Lu, H.; Tong, J.; Berry, J. J.; Beard, M. C.; Zhu, K. Advances in Two-Dimensional Organic–Inorganic Hybrid Perovskites. *Energy Environ. Sci.* **2020**, *13* (4), 1154–1186. https://doi.org/10.1039/C9EE03757H.

(4) Liang, S. J.; Cheng, B.; Cui, X.; Miao, F. Van Der Waals Heterostructures for High-Performance Device Applications: Challenges and Opportunities. *Adv. Mater.* **2020**, *32* (27), 1–27. https://doi.org/10.1002/adma.201903800.

(5) Li, X.; Hoffman, J. M.; Kanatzidis, M. G. The 2D Halide Perovskite Rulebook: How the Spacer Influences Everything from the Structure to Optoelectronic Device Efficiency. *Chem. Rev.* **2021**, *121* (4), 2230–2291. https://doi.org/10.1021/acs.chemrev.0c01006.

(6) Chaves, A.; Azadani, J. G.; Alsalman, H.; da Costa, D. R.; Frisenda, R.; Chaves, A. J.; Song, S. H.; Kim, Y. D.; He, D.; Zhou, J.; et al. Bandgap Engineering of Two-Dimensional Semiconductor Materials. *npj 2D Mater. Appl.* **2020**, *4* (1), 29. https://doi.org/10.1038/s41699-020-00162-4.

(7) Mueller, T.; Malic, E. Exciton Physics and Device Application of Two-Dimensional Transition Metal Dichalcogenide Semiconductors. *npj 2D Mater. Appl.* **2018**, *2* (1), 1–12. https://doi.org/10.1038/s41699-018-0074-2.

(8) He, K.; Kumar, N.; Zhao, L.; Wang, Z.; Mak, K. F.; Zhao, H.; Shan, J. Tightly Bound Excitons in Monolayer WSe_2. *Phys. Rev. Lett.* **2014**, *113* (2), 026803. https://doi.org/10.1103/PhysRevLett.113.026803.

(9) Ugeda, M. M.; Bradley, A. J.; Shi, S. F.; Da Jornada, F. H.; Zhang, Y.; Qiu, D. Y.; Ruan, W.; Mo, S. K.; Hussain, Z.; Shen, Z. X.; et al. Giant Bandgap Renormalization and Excitonic Effects in a Monolayer Transition Metal Dichalcogenide Semiconductor. *Nat. Mater.* **2014**, *13* (12), 1091–1095. https://doi.org/10.1038/nmat4061.

(10) Chernikov, A.; Berkelbach, T. C.; Hill, H. M.; Rigosi, A.; Li, Y.; Aslan, O. B.; Reichman, D. R.; Hybertsen, M. S.; Heinz, T. F. Exciton Binding Energy and Nonhydrogenic Rydberg Series in Monolayer WS_2. *Phys. Rev. Lett.* **2014**, *113* (7), 1–5. https://doi.org/10.1103/PhysRevLett.113.076802.

(11) Qiu, D. Y.; da Jornada, F. H.; Louie, S. G. Optical Spectrum of MoS_2: Many-Body Effects and Diversity of Exciton States. *Phys. Rev. Lett.* **2013**, *111* (21), 216805. https://doi.org/10.1103/PhysRevLett.111.216805.

(12) Mak, K. F.; He, K.; Lee, C.; Lee, G. H.; Hone, J.; Heinz, T. F.; Shan, J. Tightly Bound Trions in Monolayer MoS_2. *Nat. Mater.* **2013**, *12* (3), 207–211. https://doi.org/10.1038/nmat3505.

(13) Fu, Y.; He, D.; He, J.; Bian, A.; Zhang, L.; Liu, S.; Wang, Y.; Zhao, H. Effect of

Dielectric Environment on Excitonic Dynamics in Monolayer WS_2. *Adv. Mater. Interfaces* **2019**, *6* (23), 1901307. https://doi.org/10.1002/admi.201901307.
(14) Goodman, A. J.; Lien, D.-H.; Ahn, G. H.; Spiegel, L. L.; Amani, M.; Willard, A. P.; Javey, A.; Tisdale, W. A. Substrate-Dependent Exciton Diffusion and Annihilation in Chemically Treated MoS_2 and WS_2. *J. Phys. Chem. C* **2020**, *124* (22), 12175–12184. https://doi.org/10.1021/acs.jpcc.0c04000.
(15) Jeong, H.; Oh, H. M.; Gokarna, A.; Kim, H.; Yun, S. J.; Han, G. H.; Jeong, M. S.; Lee, Y. H.; Lerondel, G. Integrated Freestanding Two-Dimensional Transition Metal Dichalcogenides. *Adv. Mater.* **2017**, *29* (18), 1700308. https://doi.org/10.1002/adma.201700308.
(16) Ahn, S.; Kim, G.; Nayak, P. K.; Yoon, S. I.; Lim, H.; Shin, H.-J.; Shin, H. S. Prevention of Transition Metal Dichalcogenide Photodegradation by Encapsulation with H-BN Layers. *ACS Nano* **2016**, *10* (9), 8973–8979. https://doi.org/10.1021/acsnano.6b05042.
(17) Iqbal, M. W.; Iqbal, M. Z.; Khan, M. F.; Shehzad, M. A.; Seo, Y.; Park, J. H.; Hwang, C.; Eom, J. High-Mobility and Air-Stable Single-Layer WS_2 Field-Effect Transistors Sandwiched between Chemical Vapor Deposition-Grown Hexagonal BN Films. *Sci. Rep.* **2015**, *5* (1), 10699. https://doi.org/10.1038/srep10699.
(18) Blancon, J.-C.; Stier, A. V.; Tsai, H.; Nie, W.; Stoumpos, C. C.; Traoré, B.; Pedesseau, L.; Kepenekian, M.; Katsutani, F.; Noe, G. T.; et al. Scaling Law for Excitons in 2D Perovskite Quantum Wells. *Nat. Commun.* **2018**, *9* (1), 2254. https://doi.org/10.1038/s41467-018-04659-x.
(19) Dyksik, M.; Duim, H.; Zhu, X.; Yang, Z.; Gen, M.; Kohama, Y.; Adjokatse, S.; Maude, D. K.; Loi, M. A.; Egger, D. A.; et al. Broad Tunability of Carrier Effective Masses in Two-Dimensional Halide Perovskites. *ACS Energy Lett.* **2020**, *5* (11), 3609–3616. https://doi.org/10.1021/acsenergylett.0c01758.
(20) Dyksik, M.; Wang, S.; Paritmongkol, W.; Maude, D. K.; Tisdale, W. A.; Baranowski, M.; Plochocka, P. Tuning the Excitonic Properties of the 2D $(PEA)_2(MA)_{n-1}Pb_nI_{3n+1}$ Perovskite Family via Quantum Confinement. *J. Phys. Chem. Lett.* **2021**, *12* (6), 1638–1643. https://doi.org/10.1021/acs.jpclett.0c03731.
(21) Paritmongkol, W.; Dahod, N. S.; Stollmann, A.; Mao, N.; Settens, C.; Zheng, S.-L.; Tisdale, W. A. Synthetic Variation and Structural Trends in Layered Two-Dimensional Alkylammonium Lead Halide Perovskites. *Chem. Mater.* **2019**, *31* (15), 5592–5607. https://doi.org/10.1021/acs.chemmater.9b01318.
(22) Smith, I. C.; Hoke, E. T.; Solis-Ibarra, D.; McGehee, M. D.; Karunadasa, H. I. A Layered Hybrid Perovskite Solar-Cell Absorber with Enhanced Moisture Stability. *Angew. Chemie Int. Ed.* **2014**, *53* (42), 11232–11235. https://doi.org/10.1002/anie.201406466.
(23) Tsai, H.; Nie, W.; Blancon, J.-C.; Stoumpos, C. C.; Asadpour, R.; Harutyunyan, B.; Neukirch, A. J.; Verduzco, R.; Crochet, J. J.; Tretiak, S.; et al. High-Efficiency Two-Dimensional Ruddlesden–Popper Perovskite Solar Cells. *Nature* **2016**, *536* (7616), 312–316. https://doi.org/10.1038/nature18306.
(24) Mao, L.; Stoumpos, C. C.; Kanatzidis, M. G. Two-Dimensional Hybrid Halide Perovskites: Principles and Promises. *J. Am. Chem. Soc.* **2019**, *141* (3), 1171–1190. https://doi.org/10.1021/jacs.8b10851.
(25) Cheng, Z.; Lin, J. Layered Organic–Inorganic Hybrid Perovskites: Structure, Optical Properties, Film Preparation, Patterning and Templating Engineering. *CrystEngComm*

2010, *12* (10), 2646. https://doi.org/10.1039/c001929a.
(26) Weidman, M. C.; Seitz, M.; Stranks, S. D.; Tisdale, W. A. Highly Tunable Colloidal Perovskite Nanoplatelets through Variable Cation, Metal, and Halide Composition. *ACS Nano* **2016**, *10* (8), 7830–7839. https://doi.org/10.1021/acsnano.6b03496.
(27) Zhou, N.; Shen, Y.; Li, L.; Tan, S.; Liu, N.; Zheng, G.; Chen, Q.; Zhou, H. Exploration of Crystallization Kinetics in Quasi Two-Dimensional Perovskite and High Performance Solar Cells. *J. Am. Chem. Soc.* **2018**, *140* (1), 459–465. https://doi.org/10.1021/jacs.7b11157.
(28) Proppe, A. H.; Quintero-Bermudez, R.; Tan, H.; Voznyy, O.; Kelley, S. O.; Sargent, E. H. Synthetic Control over Quantum Well Width Distribution and Carrier Migration in Low-Dimensional Perovskite Photovoltaics. *J. Am. Chem. Soc.* **2018**, *140* (8), 2890–2896. https://doi.org/10.1021/jacs.7b12551.
(29) Mao, L.; Ke, W.; Pedesseau, L.; Wu, Y.; Katan, C.; Even, J.; Wasielewski, M. R.; Stoumpos, C. C.; Kanatzidis, M. G. Hybrid Dion–Jacobson 2D Lead Iodide Perovskites. *J. Am. Chem. Soc.* **2018**, *140* (10), 3775–3783. https://doi.org/10.1021/jacs.8b00542.
(30) Mao, L.; Tsai, H.; Nie, W.; Ma, L.; Im, J.; Stoumpos, C. C.; Malliakas, C. D.; Hao, F.; Wasielewski, M. R.; Mohite, A. D.; et al. Role of Organic Counterion in Lead- and Tin-Based Two-Dimensional Semiconducting Iodide Perovskites and Application in Planar Solar Cells. *Chem. Mater.* **2016**, *28* (21), 7781–7792. https://doi.org/10.1021/acs.chemmater.6b03054.
(31) Cao, D. H.; Stoumpos, C. C.; Farha, O. K.; Hupp, J. T.; Kanatzidis, M. G. 2D Homologous Perovskites as Light-Absorbing Materials for Solar Cell Applications. *J. Am. Chem. Soc.* **2015**, *137* (24), 7843–7850. https://doi.org/10.1021/jacs.5b03796.
(32) Quan, L. N.; Zhao, Y.; García de Arquer, F. P.; Sabatini, R.; Walters, G.; Voznyy, O.; Comin, R.; Li, Y.; Fan, J. Z.; Tan, H.; et al. Tailoring the Energy Landscape in Quasi-2D Halide Perovskites Enables Efficient Green-Light Emission. *Nano Lett.* **2017**, *17* (6), 3701–3709. https://doi.org/10.1021/acs.nanolett.7b00976.
(33) Tsai, H.; Nie, W.; Blancon, J.-C.; Stoumpos, C. C.; Soe, C. M. M.; Yoo, J.; Crochet, J.; Tretiak, S.; Even, J.; Sadhanala, A.; et al. Stable Light-Emitting Diodes Using Phase-Pure Ruddlesden-Popper Layered Perovskites. *Adv. Mater.* **2018**, *30* (6), 1704217. https://doi.org/10.1002/adma.201704217.
(34) Wang, N.; Cheng, L.; Ge, R.; Zhang, S.; Miao, Y.; Zou, W.; Yi, C.; Sun, Y.; Cao, Y.; Yang, R.; et al. Perovskite Light-Emitting Diodes Based on Solution-Processed Self-Organized Multiple Quantum Wells. *Nat. Photonics* **2016**, *10* (11), 699–704. https://doi.org/10.1038/nphoton.2016.185.
(35) Congreve, D. N.; Weidman, M. C.; Seitz, M.; Paritmongkol, W.; Dahod, N. S.; Tisdale, W. A. Tunable Light-Emitting Diodes Utilizing Quantum-Confined Layered Perovskite Emitters. *ACS Photonics* **2017**, *4* (3), 476–481. https://doi.org/10.1021/acsphotonics.6b00963.
(36) Han, S.; Wang, P.; Zhang, J.; Liu, X.; Sun, Z.; Huang, X.; Li, L.; Ji, C.; Zhang, W.; Teng, B.; et al. Exploring a Polar Two-Dimensional Multi-Layered Hybrid Perovskite of (C 5 H 11 NH 3) 2 (CH 3 NH 3)Pb 2 I 7 for Ultrafast-Responding Photodetection. *Laser Photon. Rev.* **2018**, *12* (8), 1800060. https://doi.org/10.1002/lpor.201800060.
(37) Peng, W.; Yin, J.; Ho, K.-T.; Ouellette, O.; De Bastiani, M.; Murali, B.; El Tall, O.; Shen, C.; Miao, X.-H.; Pan, J.; et al. Ultralow Self-Doping in Two-Dimensional Hybrid

Perovskite Single Crystals. *Nano Lett.* **2017**, *17* (8), 4759–4767. https://doi.org/10.1021/acs.nanolett.7b01475.
(38) Sun, C.; Xu, G.; Jiang, X.-M.; Wang, G.-E.; Guo, P.-Y.; Wang, M.-S.; Guo, G.-C. Design Strategy for Improving Optical and Electrical Properties and Stability of Lead-Halide Semiconductors. *J. Am. Chem. Soc.* **2018**, *140* (8), 2805–2811. https://doi.org/10.1021/jacs.7b10101.
(39) Li, L.; Sun, Z.; Wang, P.; Hu, W.; Wang, S.; Ji, C.; Hong, M.; Luo, J. Tailored Engineering of an Unusual (C 4 H 9 NH 3) 2 (CH 3 NH 3) 2 Pb 3 Br 10 Two-Dimensional Multilayered Perovskite Ferroelectric for a High-Performance Photodetector. *Angew. Chemie Int. Ed.* **2017**, *56* (40), 12150–12154. https://doi.org/10.1002/anie.201705836.
(40) Saparov, B.; Mitzi, D. B. Organic–Inorganic Perovskites: Structural Versatility for Functional Materials Design. *Chem. Rev.* **2016**, *116* (7), 4558–4596. https://doi.org/10.1021/acs.chemrev.5b00715.
(41) Manser, J. S.; Christians, J. A.; Kamat, P. V. Intriguing Optoelectronic Properties of Metal Halide Perovskites. *Chem. Rev.* **2016**, *116* (21), 12956–13008. https://doi.org/10.1021/acs.chemrev.6b00136.
(42) Goldschmidt, V. M. Die Gesetze Der Krystallochemie. *Naturwissenschaften* **1926**, *14* (21), 477–485. https://doi.org/10.1007/BF01507527.
(43) Weber, D. CH3NH3SnBrxI3-x (x = 0-3), Ein Sn(II)-System Mit Kubischer Perowskitstruktur / CH3NH3SnBrxI3-x(x = 0-3), a Sn(II)-System with Cubic Perovskite Structure. *Zeitschrift für Naturforsch. B* **1978**, *33* (8), 3–6. https://doi.org/10.1515/znb-1978-0809.
(44) Kojima, A.; Teshima, K.; Shirai, Y.; Miyasaka, T. Organometal Halide Perovskites as Visible-Light Sensitizers for Photovoltaic Cells. *J. Am. Chem. Soc.* **2009**, *131* (17), 6050–6051. https://doi.org/10.1021/ja809598r.
(45) Green, M. A.; Ho-Baillie, A.; Snaith, H. J. The Emergence of Perovskite Solar Cells. *Nat. Photonics* **2014**, *8* (7), 506–514. https://doi.org/10.1038/nphoton.2014.134.
(46) Jeon, N. J.; Noh, J. H.; Kim, Y. C.; Yang, W. S.; Ryu, S.; Seok, S. Il. Solvent Engineering for High-Performance Inorganic–Organic Hybrid Perovskite Solar Cells. *Nat. Mater.* **2014**, *13* (9), 897–903. https://doi.org/10.1038/nmat4014.
(47) Kim, H.-S.; Lee, C.-R.; Im, J.-H.; Lee, K.-B.; Moehl, T.; Marchioro, A.; Moon, S.-J.; Humphry-Baker, R.; Yum, J.-H.; Moser, J. E.; et al. Lead Iodide Perovskite Sensitized All-Solid-State Submicron Thin Film Mesoscopic Solar Cell with Efficiency Exceeding 9%. *Sci. Rep.* **2012**, *2* (1), 591. https://doi.org/10.1038/srep00591.
(48) De Wolf, S.; Holovsky, J.; Moon, S.-J.; Löper, P.; Niesen, B.; Ledinsky, M.; Haug, F.-J.; Yum, J.-H.; Ballif, C. Organometallic Halide Perovskites: Sharp Optical Absorption Edge and Its Relation to Photovoltaic Performance. *J. Phys. Chem. Lett.* **2014**, *5* (6), 1035–1039. https://doi.org/10.1021/jz500279b.
(49) Kim, J.; Lee, S.-H.; Lee, J. H.; Hong, K.-H. The Role of Intrinsic Defects in Methylammonium Lead Iodide Perovskite. *J. Phys. Chem. Lett.* **2014**, *5* (8), 1312–1317. https://doi.org/10.1021/jz500370k.
(50) Yin, W.-J.; Shi, T.; Yan, Y. Unusual Defect Physics in CH 3 NH 3 PbI 3 Perovskite Solar Cell Absorber. *Appl. Phys. Lett.* **2014**, *104* (6), 063903. https://doi.org/10.1063/1.4864778.

(51) Ma, L.; Hao, F.; Stoumpos, C. C.; Phelan, B. T.; Wasielewski, M. R.; Kanatzidis, M. G. Carrier Diffusion Lengths of over 500 Nm in Lead-Free Perovskite CH 3 NH 3 SnI 3 Films. *J. Am. Chem. Soc.* **2016**, *138* (44), 14750–14755. https://doi.org/10.1021/jacs.6b09257.
(52) Shi, D.; Adinolfi, V.; Comin, R.; Yuan, M.; Alarousu, E.; Buin, A.; Chen, Y.; Hoogland, S.; Rothenberger, A.; Katsiev, K.; et al. Low Trap-State Density and Long Carrier Diffusion in Organolead Trihalide Perovskite Single Crystals. *Science (80-.).* **2015**, *347* (6221), 519–522. https://doi.org/10.1126/science.aaa2725.
(53) Stranks, S. D.; Eperon, G. E.; Grancini, G.; Menelaou, C.; Alcocer, M. J. P.; Leijtens, T.; Herz, L. M.; Petrozza, A.; Snaith, H. J. Electron-Hole Diffusion Lengths Exceeding 1 Micrometer in an Organometal Trihalide Perovskite Absorber. *Science (80-.).* **2013**, *342* (6156), 341–344. https://doi.org/10.1126/science.1243982.
(54) Wehrenfennig, C.; Eperon, G. E.; Johnston, M. B.; Snaith, H. J.; Herz, L. M. High Charge Carrier Mobilities and Lifetimes in Organolead Trihalide Perovskites. *Adv. Mater.* **2014**, *26* (10), 1584–1589. https://doi.org/10.1002/adma.201305172.
(55) Boyd, C. C.; Cheacharoen, R.; Leijtens, T.; McGehee, M. D. Understanding Degradation Mechanisms and Improving Stability of Perovskite Photovoltaics. *Chem. Rev.* **2019**, *119* (5), 3418–3451. https://doi.org/10.1021/acs.chemrev.8b00336.
(56) Sichert, J. A.; Tong, Y.; Mutz, N.; Vollmer, M.; Fischer, S.; Milowska, K. Z.; García Cortadella, R.; Nickel, B.; Cardenas-Daw, C.; Stolarczyk, J. K.; et al. Quantum Size Effect in Organometal Halide Perovskite Nanoplatelets. *Nano Lett.* **2015**, *15* (10), 6521–6527. https://doi.org/10.1021/acs.nanolett.5b02985.
(57) Ishihara, T.; Takahashi, J.; Goto, T. Optical Properties Due to Electronic Transitions in Two-Dimensional Semiconductors (<math Display="inline"> <mrow> <msub> <mrow> <mi Mathvariant="normal">C</Mi> </Mrow> <mrow> <mi Mathvariant="italic">n</Mi> </Mrow> </Msub> </Mrow> </Math> <math Display=. *Phys. Rev. B* **1990**, *42* (17), 11099–11107. https://doi.org/10.1103/PhysRevB.42.11099.
(58) Guo, P.; Huang, W.; Stoumpos, C. C.; Mao, L.; Gong, J.; Zeng, L.; Diroll, B. T.; Xia, Y.; Ma, X.; Gosztola, D. J.; et al. Hyperbolic Dispersion Arising from Anisotropic Excitons in Two-Dimensional Perovskites. *Phys. Rev. Lett.* **2018**, *121* (12), 127401. https://doi.org/10.1103/PhysRevLett.121.127401.
(59) Smith, M. D.; Connor, B. A.; Karunadasa, H. I. Tuning the Luminescence of Layered Halide Perovskites. *Chem. Rev.* **2019**, *119* (5), 3104–3139. https://doi.org/10.1021/acs.chemrev.8b00477.
(60) Yin, J.; Maity, P.; Xu, L.; El-Zohry, A. M.; Li, H.; Bakr, O. M.; Brédas, J.-L.; Mohammed, O. F. Layer-Dependent Rashba Band Splitting in 2D Hybrid Perovskites. *Chem. Mater.* **2018**, *30* (23), 8538–8545. https://doi.org/10.1021/acs.chemmater.8b03436.
(61) Park, I.-H.; Zhang, Q.; Kwon, K. C.; Zhu, Z.; Yu, W.; Leng, K.; Giovanni, D.; Choi, H. S.; Abdelwahab, I.; Xu, Q.-H.; et al. Ferroelectricity and Rashba Effect in a Two-Dimensional Dion-Jacobson Hybrid Organic–Inorganic Perovskite. *J. Am. Chem. Soc.* **2019**, *141* (40), 15972–15976. https://doi.org/10.1021/jacs.9b07776.
(62) Zhai, Y.; Baniya, S.; Zhang, C.; Li, J.; Haney, P.; Sheng, C.-X.; Ehrenfreund, E.; Vardeny, Z. V. Giant Rashba Splitting in 2D Organic-Inorganic Halide Perovskites Measured by Transient Spectroscopies. *Sci. Adv.* **2017**, *3* (7), e1700704. https://doi.org/10.1126/sciadv.1700704.

(63) Wang, S.; Liu, X.; Li, L.; Ji, C.; Sun, Z.; Wu, Z.; Hong, M.; Luo, J. An Unprecedented Biaxial Trilayered Hybrid Perovskite Ferroelectric with Directionally Tunable Photovoltaic Effects. *J. Am. Chem. Soc.* **2019**, *141* (19), 7693–7697. https://doi.org/10.1021/jacs.9b02558.
(64) Sun, B.; Liu, X.; Li, X.; Cao, Y.; Yan, Z.; Fu, L.; Tang, N.; Wang, Q.; Shao, X.; Yang, D.; et al. Reversible Thermochromism and Strong Ferromagnetism in Two-Dimensional Hybrid Perovskites. *Angew. Chemie Int. Ed.* **2020**, *59* (1), 203–208. https://doi.org/10.1002/anie.201910701.
(65) Sun, B.; Liu, X.-F.; Li, X.-Y.; Zhang, Y.; Shao, X.; Yang, D.; Zhang, H.-L. Two-Dimensional Perovskite Chiral Ferromagnets. *Chem. Mater.* **2020**, *32* (20), 8914–8920. https://doi.org/10.1021/acs.chemmater.0c02729.
(66) Wang, J.; Mi, Y.; Gao, X.; Li, J.; Li, J.; Lan, S.; Fang, C.; Shen, H.; Wen, X.; Chen, R.; et al. Giant Nonlinear Optical Response in 2D Perovskite Heterostructures. *Adv. Opt. Mater.* **2019**, *7* (15), 1900398. https://doi.org/10.1002/adom.201900398.
(67) Zhou, F.; Abdelwahab, I.; Leng, K.; Loh, K. P.; Ji, W. 2D Perovskites with Giant Excitonic Optical Nonlinearities for High-Performance Sub-Bandgap Photodetection. *Adv. Mater.* **2019**, *31* (48), 1904155. https://doi.org/10.1002/adma.201904155.
(68) Grinblat, G.; Abdelwahab, I.; Nielsen, M. P.; Dichtl, P.; Leng, K.; Oulton, R. F.; Loh, K. P.; Maier, S. A. Ultrafast All-Optical Modulation in 2D Hybrid Perovskites. *ACS Nano* **2019**, *13* (8), 9504–9510. https://doi.org/10.1021/acsnano.9b04483.
(69) Weidman, M. C.; Goodman, A. J.; Tisdale, W. A. Colloidal Halide Perovskite Nanoplatelets: An Exciting New Class of Semiconductor Nanomaterials. *Chem. Mater.* **2017**, *29* (12), 5019–5030. https://doi.org/10.1021/acs.chemmater.7b01384.
(70) Shi, E.; Gao, Y.; Finkenauer, B. P.; Akriti, A.; Coffey, A. H.; Dou, L. Two-Dimensional Halide Perovskite Nanomaterials and Heterostructures. *Chem. Soc. Rev.* **2018**, *47* (16), 6046–6072. https://doi.org/10.1039/C7CS00886D.
(71) Jagielski, J.; Kumar, S.; Yu, W.-Y.; Shih, C.-J. Layer-Controlled Two-Dimensional Perovskites: Synthesis and Optoelectronics. *J. Mater. Chem. C* **2017**, *5* (23), 5610–5627. https://doi.org/10.1039/C7TC00538E.
(72) Dou, L. Emerging Two-Dimensional Halide Perovskite Nanomaterials. *J. Mater. Chem. C* **2017**, *5* (43), 11165–11173. https://doi.org/10.1039/C7TC02863F.
(73) Huang, H.; Polavarapu, L.; Sichert, J. A.; Susha, A. S.; Urban, A. S.; Rogach, A. L. Colloidal Lead Halide Perovskite Nanocrystals: Synthesis, Optical Properties and Applications. *NPG Asia Mater.* **2016**, *8* (11), e328. https://doi.org/10.1038/am.2016.167.
(74) Sun, S.; Yuan, D.; Xu, Y.; Wang, A.; Deng, Z. Ligand-Mediated Synthesis of Shape-Controlled Cesium Lead Halide Perovskite Nanocrystals via Reprecipitation Process at Room Temperature. *ACS Nano* **2016**, *10* (3), 3648–3657. https://doi.org/10.1021/acsnano.5b08193.
(75) Bekenstein, Y.; Koscher, B. A.; Eaton, S. W.; Yang, P.; Alivisatos, A. P. Highly Luminescent Colloidal Nanoplates of Perovskite Cesium Lead Halide and Their Oriented Assemblies. *J. Am. Chem. Soc.* **2015**, *137* (51), 16008–16011. https://doi.org/10.1021/jacs.5b11199.
(76) Shamsi, J.; Dang, Z.; Bianchini, P.; Canale, C.; Stasio, F. Di; Brescia, R.; Prato, M.; Manna, L. Colloidal Synthesis of Quantum Confined Single Crystal CsPbBr3 Nanosheets with Lateral Size Control up to the Micrometer Range. *J. Am. Chem. Soc.* **2016**, *138* (23),

7240–7243. https://doi.org/10.1021/jacs.6b03166.
(77) Protesescu, L.; Yakunin, S.; Bodnarchuk, M. I.; Krieg, F.; Caputo, R.; Hendon, C. H.; Yang, R. X.; Walsh, A.; Kovalenko, M. V. Nanocrystals of Cesium Lead Halide Perovskites (CsPbX 3 , X = Cl, Br, and I): Novel Optoelectronic Materials Showing Bright Emission with Wide Color Gamut. *Nano Lett.* **2015**, *15* (6), 3692–3696. https://doi.org/10.1021/nl5048779.
(78) Dou, L.; Wong, A. B.; Yu, Y.; Lai, M.; Kornienko, N.; Eaton, S. W.; Fu, A.; Bischak, C. G.; Ma, J.; Ding, T.; et al. Atomically Thin Two-Dimensional Organic-Inorganic Hybrid Perovskites. *Science (80-.).* **2015**, *349* (6255), 1518–1521. https://doi.org/10.1126/science.aac7660.
(79) Liu, J.; Xue, Y.; Wang, Z.; Xu, Z.-Q.; Zheng, C.; Weber, B.; Song, J.; Wang, Y.; Lu, Y.; Zhang, Y.; et al. Two-Dimensional CH 3 NH 3 PbI 3 Perovskite: Synthesis and Optoelectronic Application. *ACS Nano* **2016**, *10* (3), 3536–3542. https://doi.org/10.1021/acsnano.5b07791.
(80) Niu, L.; Liu, X.; Cong, C.; Wu, C.; Wu, D.; Chang, T. R.; Wang, H.; Zeng, Q.; Zhou, J.; Wang, X.; et al. Controlled Synthesis of Organic/Inorganic van Der Waals Solid for Tunable Light-Matter Interactions. *Adv. Mater.* **2015**, *27* (47), 7800–7808. https://doi.org/10.1002/adma.201503367.
(81) Saidaminov, M. I.; Abdelhady, A. L.; Murali, B.; Alarousu, E.; Burlakov, V. M.; Peng, W.; Dursun, I.; Wang, L.; He, Y.; Maculan, G.; et al. High-Quality Bulk Hybrid Perovskite Single Crystals within Minutes by Inverse Temperature Crystallization. *Nat. Commun.* **2015**, *6* (1), 7586. https://doi.org/10.1038/ncomms8586.
(82) Raghavan, C. M.; Chen, T.-P.; Li, S.-S.; Chen, W.-L.; Lo, C.-Y.; Liao, Y.-M.; Haider, G.; Lin, C.-C.; Chen, C.-C.; Sankar, R.; et al. Low-Threshold Lasing from 2D Homologous Organic–Inorganic Hybrid Ruddlesden–Popper Perovskite Single Crystals. *Nano Lett.* **2018**, *18* (5), 3221–3228. https://doi.org/10.1021/acs.nanolett.8b00990.
(83) Gong, X.; Voznyy, O.; Jain, A.; Liu, W.; Sabatini, R.; Piontkowski, Z.; Walters, G.; Bappi, G.; Nokhrin, S.; Bushuyev, O.; et al. Electron–Phonon Interaction in Efficient Perovskite Blue Emitters. *Nat. Mater.* **2018**, *17* (6), 550–556. https://doi.org/10.1038/s41563-018-0081-x.
(84) Oswald, I. W. H.; Koegel, A. A.; Neilson, J. R. General Synthesis Principles for Ruddlesden–Popper Hybrid Perovskite Halides from a Dynamic Equilibrium. *Chem. Mater.* **2018**, *30* (23), 8606–8614. https://doi.org/10.1021/acs.chemmater.8b03817.
(85) Stoumpos, C. C.; Cao, D. H.; Clark, D. J.; Young, J.; Rondinelli, J. M.; Jang, J. I.; Hupp, J. T.; Kanatzidis, M. G. Ruddlesden-Popper Hybrid Lead Iodide Perovskite 2D Homologous Semiconductors. *Chem. Mater.* **2016**, *28* (8), 2852–2867. https://doi.org/10.1021/acs.chemmater.6b00847.
(86) Stoumpos, C. C.; Soe, C. M. M.; Tsai, H.; Nie, W.; Blancon, J.-C.; Cao, D. H.; Liu, F.; Traoré, B.; Katan, C.; Even, J.; et al. High Members of the 2D Ruddlesden-Popper Halide Perovskites: Synthesis, Optical Properties, and Solar Cells of (CH 3 (CH 2) 3 NH 3) 2 (CH 3 NH 3) 4 Pb 5 I 16. *Chem* **2017**, *2* (3), 427–440. https://doi.org/10.1016/j.chempr.2017.02.004.
(87) Mitzi, D. B.; Feild, C. A.; Harrison, W. T. A.; Guloy, A. M. Conducting Tin Halides with a Layered Organic-Based Perovskite Structure. *Nature* **1994**, *369* (6480), 467–469. https://doi.org/10.1038/369467a0.

(88) Soe, C. M. M.; Nagabhushana, G. P.; Shivaramaiah, R.; Tsai, H.; Nie, W.; Blancon, J.-C.; Melkonyan, F.; Cao, D. H.; Traoré, B.; Pedesseau, L.; et al. Structural and Thermodynamic Limits of Layer Thickness in 2D Halide Perovskites. *Proc. Natl. Acad. Sci.* **2019**, *116* (1), 58–66. https://doi.org/10.1073/pnas.1811006115.

(89) Li, X.; Hoffman, J.; Ke, W.; Chen, M.; Tsai, H.; Nie, W.; Mohite, A. D.; Kepenekian, M.; Katan, C.; Even, J.; et al. Two-Dimensional Halide Perovskites Incorporating Straight Chain Symmetric Diammonium Ions, (NH 3 C m H 2 m NH 3)(CH 3 NH 3) n −1 Pb n I 3 n +1 (m = 4–9; n = 1–4). *J. Am. Chem. Soc.* **2018**, *140* (38), 12226–12238. https://doi.org/10.1021/jacs.8b07712.

(90) Spanopoulos, I.; Hadar, I.; Ke, W.; Tu, Q.; Chen, M.; Tsai, H.; He, Y.; Shekhawat, G.; Dravid, V. P.; Wasielewski, M. R.; et al. Uniaxial Expansion of the 2D Ruddlesden–Popper Perovskite Family for Improved Environmental Stability. *J. Am. Chem. Soc.* **2019**, *141* (13), 5518–5534. https://doi.org/10.1021/jacs.9b01327.

(91) Veselska, O.; Demessence, A. D^{10} Coinage Metal Organic Chalcogenolates: From Oligomers to Coordination Polymers. *Coord. Chem. Rev.* **2018**, *355*, 240–270. https://doi.org/10.1016/j.ccr.2017.08.014.

(92) Brown, D. H.; Smith, W. E. The Chemistry of the Gold Drugs Used in the Treatment of Rheumatoid Arthritis. *Chem. Soc. Rev.* **1980**, *9* (2), 217. https://doi.org/10.1039/cs9800900217.

(93) Shaw, C. F. Gold-Based Therapeutic Agents. *Chem. Rev.* **1999**, *99* (9), 2589–2600. https://doi.org/10.1021/cr980431o.

(94) Nomiya, K.; Kondoh, Y.; Onoue, K.; Kasuga, N. C.; Nagano, H.; Oda, M.; Sudoh, T.; Sakuma, S. Synthesis and Characterization of Polymeric, Anionic Thiosalicylato-Ag(I) Complexes with Antimicrobial Activities. *J. Inorg. Biochem.* **1995**, *58* (4), 255–267. https://doi.org/10.1016/0162-0134(94)00059-J.

(95) Luo, Z.; Yuan, X.; Yu, Y.; Zhang, Q.; Leong, D. T.; Lee, J. Y.; Xie, J. From Aggregation-Induced Emission of Au(I)–Thiolate Complexes to Ultrabright Au(0)@Au(I)–Thiolate Core–Shell Nanoclusters. *J. Am. Chem. Soc.* **2012**, *134* (40), 16662–16670. https://doi.org/10.1021/ja306199p.

(96) Veselska, O.; Podbevšek, D.; Ledoux, G.; Fateeva, A.; Demessence, A. Intrinsic Triple-Emitting 2D Copper Thiolate Coordination Polymer as a Ratiometric Thermometer Working over 400 K Range. *Chem. Commun.* **2017**, *53* (90), 12225–12228. https://doi.org/10.1039/C7CC06815H.

(97) Schriber, E. A.; Popple, D. C.; Yeung, M.; Brady, M. A.; Corlett, S. A.; Hohman, J. N. Mithrene Is a Self-Assembling Robustly Blue Luminescent Metal–Organic Chalcogenolate Assembly for 2D Optoelectronic Applications. *ACS Appl. Nano Mater.* **2018**, *1* (7), 3498–3508. https://doi.org/10.1021/acsanm.8b00662.

(98) Lavenn, C.; Okhrimenko, L.; Guillou, N.; Monge, M.; Ledoux, G.; Dujardin, C.; Chiriac, R.; Fateeva, A.; Demessence, A. A Luminescent Double Helical Gold(I)–Thiophenolate Coordination Polymer Obtained by Hydrothermal Synthesis or by Thermal Solid-State Amorphous-to-Crystalline Isomerization. *J. Mater. Chem. C* **2015**, *3* (16), 4115–4125. https://doi.org/10.1039/C5TC00119F.

(99) Veselska, O.; Cai, L.; Podbevšek, D.; Ledoux, G.; Guillou, N.; Pilet, G.; Fateeva, A.; Demessence, A. Structural Diversity of Coordination Polymers Based on a Heterotopic Ligand: Cu(II)-Carboxylate vs Cu(I)-Thiolate. *Inorg. Chem.* **2018**, *57* (5), 2736–2743.

https://doi.org/10.1021/acs.inorgchem.7b03090.
(100) Veselska, O.; Dessal, C.; Melizi, S.; Guillou, N.; Podbevšek, D.; Ledoux, G.; Elkaim, E.; Fateeva, A.; Demessence, A. New Lamellar Silver Thiolate Coordination Polymers with Tunable Photoluminescence Energies by Metal Substitution. *Inorg. Chem.* **2019**, *58* (1), 99–105. https://doi.org/10.1021/acs.inorgchem.8b01257.
(101) Veselska, O.; Okhrimenko, L.; Guillou, N.; Podbevšek, D.; Ledoux, G.; Dujardin, C.; Monge, M.; Chevrier, D. M.; Yang, R.; Zhang, P.; et al. An Intrinsic Dual-Emitting Gold Thiolate Coordination Polymer, $[Au(+I)(p\text{-}SPhCO_2H)]_n$, for Ratiometric Temperature Sensing. *J. Mater. Chem. C* **2017**, *5* (38), 9843–9848. https://doi.org/10.1039/C7TC03605A.
(102) Lavenn, C.; Guillou, N.; Monge, M.; Podbevšek, D.; Ledoux, G.; Fateeva, A.; Demessence, A. Shedding Light on an Ultra-Bright Photoluminescent Lamellar Gold Thiolate Coordination Polymer $[Au(p\text{-}SPhCO_2Me)]_N$. *Chem. Commun.* **2016**, *52* (58), 9063–9066. https://doi.org/10.1039/C5CC10448C.
(103) Bonačić-Koutecký, V.; Kulesza, A.; Gell, L.; Mitrić, R.; Antoine, R.; Bertorelle, F.; Hamouda, R.; Rayane, D.; Broyer, M.; Tabarin, T.; et al. Silver Cluster–Biomolecule Hybrids: From Basics towards Sensors. *Phys. Chem. Chem. Phys.* **2012**, *14* (26), 9282. https://doi.org/10.1039/c2cp00050d.
(104) Singha, S.; Kim, D.; Seo, H.; Cho, S. W.; Ahn, K. H. Fluorescence Sensing Systems for Gold and Silver Species. *Chem. Soc. Rev.* **2015**, *44* (13), 4367–4399. https://doi.org/10.1039/C4CS00328D.
(105) Wang, Q.; Dong, S.-L.; Tao, D.-D.; Li, Z.; Jiang, Y.-B. Ag(I)-Thiolate Coordination Polymers: Synthesis, Structures and Applications as Emerging Sensory Ensembles. *Coord. Chem. Rev.* **2021**, *432*, 213717. https://doi.org/10.1016/j.ccr.2020.213717.
(106) Trang, B.; Yeung, M.; Popple, D. C.; Schriber, E. A.; Brady, M. A.; Kuykendall, T. R.; Hohman, J. N. Tarnishing Silver Metal into Mithrene. *J. Am. Chem. Soc.* **2018**, *140* (42), 13892–13903. https://doi.org/10.1021/jacs.8b08878.
(107) Popple, D. C.; Schriber, E. A.; Yeung, M.; Hohman, J. N. Competing Roles of Crystallization and Degradation of a Metal–Organic Chalcogenolate Assembly under Biphasic Solvothermal Conditions. *Langmuir* **2018**, *34* (47), 14265–14273. https://doi.org/10.1021/acs.langmuir.8b03282.
(108) Huang, Q.-Q.; Li, Y.-Z.; Zheng, Z.; Jiang, X.-M.; Sun, S.-S.; Jiang, H.-J.; Deng, W.-H.; Wang, G.-E.; Zhai, T.-Y.; Li, M.-D.; et al. Single-Component MLCT-Active Photodetecting Material Based on a Two-Dimensional Coordination Polymer. *CCS Chem.* **2020**, *2* (1), 655–662. https://doi.org/10.31635/ccschem.019.201900045.
(109) Yao, K.; Collins, M. S.; Nell, K. M.; Barnard, E. S.; Borys, N. J.; Kuykendall, T.; Hohman, J. N.; Schuck, P. J. Strongly Quantum-Confined Blue-Emitting Excitons in Chemically Configurable Multiquantum Wells. *ACS Nano* **2020**, acsnano.0c08096. https://doi.org/10.1021/acsnano.0c08096.
(110) Maserati, L.; Pecorario, S.; Prato, M.; Caironi, M. Understanding the Synthetic Pathway to Large-Area, High-Quality $[AgSePh]_\infty$ Nanocrystal Films. *J. Phys. Chem. C* **2020**, *124* (41), 22845–22852. https://doi.org/10.1021/acs.jpcc.0c07330.
(111) Maserati, L.; Refaely-Abramson, S.; Kastl, C.; Chen, C. T.; Borys, N. J.; Eisler, C. N.; Collins, M. S.; Smidt, T. E.; Barnard, E. S.; Strasbourg, M.; et al. Anisotropic 2D Excitons Unveiled in Organic–Inorganic Quantum Wells. *Mater. Horizons* **2021**, *8* (1), 197–208.

https://doi.org/10.1039/C9MH01917K.
(112) Maserati, L.; Prato, M.; Pecorario, S.; Passarella, B.; Perinot, A.; Thomas, A. A.; Melloni, F.; Natali, D.; Caironi, M. Photo-Electrical Properties of 2D Quantum Confined Metal–Organic Chalcogenide Nanocrystal Films. *Nanoscale* **2021**. https://doi.org/10.1039/D0NR07409H.
(113) Cuthbert, H. L.; Wallbank, A. I.; Taylor, N. J.; Corrigan, J. F. Synthesis and Structural Characterization of $[Cu_{20}Se_4(\mu_3\text{-}SePh)_{12}(PPh_3)_6]$ and $[Ag(SePh)]_\infty$. *Zeitschrift für Anorg. und Allg. Chemie* **2002**, *628* (11), 2483–2488. https://doi.org/10.1002/1521-3749(200211)628:11<2483::AID-ZAAC2483>3.0.CO;2-U.
(114) Li, Y.; Jiang, X.; Fu, Z.; Huang, Q.; Wang, G.-E.; Deng, W.-H.; Wang, C.; Li, Z.; Yin, W.; Chen, B.; et al. Coordination Assembly of 2D Ordered Organic Metal Chalcogenides with Widely Tunable Electronic Band Gaps. *Nat. Commun.* **2020**, *11* (1), 261. https://doi.org/10.1038/s41467-019-14136-8.
(115) Schriber, E. A.; Popple, D. C.; Yeung, M.; Brady, M. A.; Corlett, S. A.; Hohman, J. N. Mithrene Is a Self-Assembling Robustly Blue Luminescent Metal–Organic Chalcogenolate Assembly for 2D Optoelectronic Applications (SI). *ACS Appl. Nano Mater.* **2018**, *1* (7), 3498–3508. https://doi.org/10.1021/acsanm.8b00662.
(116) Chen, X.; Lu, H.; Li, Z.; Zhai, Y.; Ndione, P. F.; Berry, J. J.; Zhu, K.; Yang, Y.; Beard, M. C. Impact of Layer Thickness on the Charge Carrier and Spin Coherence Lifetime in Two-Dimensional Layered Perovskite Single Crystals. *ACS Energy Lett.* **2018**, *3* (9), 2273–2279. https://doi.org/10.1021/acsenergylett.8b01315.
(117) Whitfield, P. S.; Herron, N.; Guise, W. E.; Page, K.; Cheng, Y. Q.; Milas, I.; Crawford, M. K. Structures, Phase Transitions and Tricritical Behavior of the Hybrid Perovskite Methyl Ammonium Lead Iodide. *Sci. Rep.* **2016**, *6* (1), 35685. https://doi.org/10.1038/srep35685.
(118) Harwell, J. R.; Payne, J. L.; Sajjad, M. T.; Heutz, F. J. L.; Dawson, D. M.; Whitfield, P. S.; Irvine, J. T. S.; Samuel, I. D. W.; Carpenter, M. A. Role of Lattice Distortion and A Site Cation in the Phase Transitions of Methylammonium Lead Halide Perovskites. *Phys. Rev. Mater.* **2018**, *2* (6), 065404. https://doi.org/10.1103/PhysRevMaterials.2.065404.
(119) Stoumpos, C. C.; Malliakas, C. D.; Kanatzidis, M. G. Semiconducting Tin and Lead Iodide Perovskites with Organic Cations: Phase Transitions, High Mobilities, and Near-Infrared Photoluminescent Properties. *Inorg. Chem.* **2013**, *52* (15), 9019–9038. https://doi.org/10.1021/ic401215x.
(120) Billing, D. G.; Lemmerer, A. Synthesis, Characterization and Phase Transitions in the Inorganic–Organic Layered Perovskite-Type Hybrids [(C n H 2 n + 1 NH 3) 2 PbI 4], n = 4, 5 and 6. *Acta Crystallogr. Sect. B Struct. Sci.* **2007**, *63* (5), 735–747. https://doi.org/10.1107/S0108768107031758.
(121) Lemmerer, A.; Billing, D. G. Synthesis, Characterization and Phase Transitions of the Inorganic–Organic Layered Perovskite-Type Hybrids [(C n H 2n+1 NH 3) 2 PbI 4], n = 7, 8, 9 and 10. *Dalt. Trans.* **2012**, *41* (4), 1146–1157. https://doi.org/10.1039/C0DT01805H.
(122) Billing, D. G.; Lemmerer, A. Synthesis, Characterization and Phase Transitions of the Inorganic–Organic Layered Perovskite-Type Hybrids [(CnH2n+1NH3)2PbI4] (n = 12, 14, 16 and 18). *New J. Chem.* **2008**, *32* (10), 1736. https://doi.org/10.1039/b805417g.
(123) Hao, F.; Stoumpos, C. C.; Liu, Z.; Chang, R. P. H.; Kanatzidis, M. G. Controllable

Perovskite Crystallization at a Gas–Solid Interface for Hole Conductor-Free Solar Cells with Steady Power Conversion Efficiency over 10%. *J. Am. Chem. Soc.* **2014**, *136* (46), 16411–16419. https://doi.org/10.1021/ja509245x.

(124) Leguy, A. M. A.; Hu, Y.; Campoy-Quiles, M.; Alonso, M. I.; Weber, O. J.; Azarhoosh, P.; van Schilfgaarde, M.; Weller, M. T.; Bein, T.; Nelson, J.; et al. Reversible Hydration of CH 3 NH 3 PbI 3 in Films, Single Crystals, and Solar Cells. *Chem. Mater.* **2015**, *27* (9), 3397–3407. https://doi.org/10.1021/acs.chemmater.5b00660.

(125) Christians, J. A.; Miranda Herrera, P. A.; Kamat, P. V. Transformation of the Excited State and Photovoltaic Efficiency of CH 3 NH 3 PbI 3 Perovskite upon Controlled Exposure to Humidified Air. *J. Am. Chem. Soc.* **2015**, *137* (4), 1530–1538. https://doi.org/10.1021/ja511132a.

(126) Grancini, G.; D'Innocenzo, V.; Dohner, E. R.; Martino, N.; Srimath Kandada, A. R.; Mosconi, E.; De Angelis, F.; Karunadasa, H. I.; Hoke, E. T.; Petrozza, A. CH 3 NH 3 PbI 3 Perovskite Single Crystals: Surface Photophysics and Their Interaction with the Environment. *Chem. Sci.* **2015**, *6* (12), 7305–7310. https://doi.org/10.1039/C5SC02542G.

(127) Vincent, B. R.; Robertson, K. N.; Cameron, T. S.; Knop, O. Alkylammonium Lead Halides. Part 1. Isolated PbI 6 4− Ions in (CH 3 NH 3) 4 PbI 6 •2H 2 O. *Can. J. Chem.* **1987**, *65* (5), 1042–1046. https://doi.org/10.1139/v87-176.

(128) Mitzi, D. B. Templating and Structural Engineering in Organic–Inorganic Perovskites. *J. Chem. Soc. Dalt. Trans.* **2001**, No. 1, 1–12. https://doi.org/10.1039/b007070j.

(129) Li, Q.; Zhou, Q.; Shi, L.; Chen, Q.; Wang, J. Recent Advances in Oxidation and Degradation Mechanisms of Ultrathin 2D Materials under Ambient Conditions and Their Passivation Strategies. *J. Mater. Chem. A* **2019**, *7* (9), 4291–4312. https://doi.org/10.1039/C8TA10306B.

(130) Shi, E.; Deng, S.; Yuan, B.; Gao, Y.; Akriti; Yuan, L.; Davis, C. S.; Zemlyanov, D.; Yu, Y.; Huang, L.; et al. Extrinsic and Dynamic Edge States of Two-Dimensional Lead Halide Perovskites. *ACS Nano* **2019**, acsnano.8b07631. https://doi.org/10.1021/acsnano.8b07631.

(131) Lee, G.-H.; Cui, X.; Kim, Y. D.; Arefe, G.; Zhang, X.; Lee, C.-H.; Ye, F.; Watanabe, K.; Taniguchi, T.; Kim, P.; et al. Highly Stable, Dual-Gated MoS 2 Transistors Encapsulated by Hexagonal Boron Nitride with Gate-Controllable Contact, Resistance, and Threshold Voltage. *ACS Nano* **2015**, *9* (7), 7019–7026. https://doi.org/10.1021/acsnano.5b01341.

(132) Kim, K. K.; Lee, H. S.; Lee, Y. H. Synthesis of Hexagonal Boron Nitride Heterostructures for 2D van Der Waals Electronics. *Chem. Soc. Rev.* **2018**, *47* (16), 6342–6369. https://doi.org/10.1039/C8CS00450A.

(133) Leng, K.; Abdelwahab, I.; Verzhbitskiy, I.; Telychko, M.; Chu, L.; Fu, W.; Chi, X.; Guo, N.; Chen, Z.; Chen, Z.; et al. Molecularly Thin Two-Dimensional Hybrid Perovskites with Tunable Optoelectronic Properties Due to Reversible Surface Relaxation. *Nat. Mater.* **2018**, *17* (10), 908–914. https://doi.org/10.1038/s41563-018-0164-8.

(134) Blancon, J.-C.; Tsai, H.; Nie, W.; Stoumpos, C. C.; Pedesseau, L.; Katan, C.; Kepenekian, M.; Soe, C. M. M.; Appavoo, K.; Sfeir, M. Y.; et al. Extremely Efficient Internal Exciton Dissociation through Edge States in Layered 2D Perovskites. *Science (80-.).* **2017**, *355* (6331), 1288–1292. https://doi.org/10.1126/science.aal4211.

(135) Amat, A.; Mosconi, E.; Ronca, E.; Quarti, C.; Umari, P.; Nazeeruddin, M. K.; Grätzel, M.; De Angelis, F. Cation-Induced Band-Gap Tuning in Organohalide Perovskites: Interplay of Spin–Orbit Coupling and Octahedra Tilting. *Nano Lett.* **2014**, *14* (6), 3608–3616.

https://doi.org/10.1021/nl5012992.
(136) Dahod, N. S.; Paritmongkol, W.; Stollmann, A.; Settens, C.; Zheng, S.-L.; Tisdale, W. A. Melting Transitions of the Organic Subphase in Layered Two-Dimensional Halide Perovskites. *J. Phys. Chem. Lett.* **2019**, *10* (11), 2924–2930. https://doi.org/10.1021/acs.jpclett.9b00983.
(137) Barman, S.; Venkataraman, N. V; Vasudevan, S.; Seshadri, R. Phase Transitions in the Anchored Organic Bilayers of Long-Chain Alkylammonium Lead Iodides (C n H 2 n +1 NH 3) 2 PbI 4 ; n = 12, 16, 18. *J. Phys. Chem. B* **2003**, *107* (8), 1875–1883. https://doi.org/10.1021/jp026879h.
(138) Mao, L.; Guo, P.; Kepenekian, M.; Hadar, I.; Katan, C.; Even, J.; Schaller, R. D.; Stoumpos, C. C.; Kanatzidis, M. G. Structural Diversity in White-Light-Emitting Hybrid Lead Bromide Perovskites. *J. Am. Chem. Soc.* **2018**, *140* (40), 13078–13088. https://doi.org/10.1021/jacs.8b08691.
(139) Mao, L.; Wu, Y.; Stoumpos, C. C.; Traore, B.; Katan, C.; Even, J.; Wasielewski, M. R.; Kanatzidis, M. G. Tunable White-Light Emission in Single-Cation-Templated Three-Layered 2D Perovskites $(CH_3CH_2NH_3)_4Pb_3Br_{10-x}Cl_X$. *J. Am. Chem. Soc.* **2017**, *139* (34), 11956–11963. https://doi.org/10.1021/jacs.7b06143.
(140) Alonso, J. A.; Martínez-Lope, M. J.; Casais, M. T.; Fernández-Díaz, M. T. Evolution of the Jahn−Teller Distortion of MnO 6 Octahedra in RMnO 3 Perovskites (R = Pr, Nd, Dy, Tb, Ho, Er, Y): A Neutron Diffraction Study. *Inorg. Chem.* **2000**, *39* (5), 917–923. https://doi.org/10.1021/ic990921e.
(141) Lufaso, M. W.; Woodward, P. M. Jahn–Teller Distortions, Cation Ordering and Octahedral Tilting in Perovskites. *Acta Crystallogr. Sect. B Struct. Sci.* **2004**, *60* (1), 10–20. https://doi.org/10.1107/S0108768103026661.
(142) Robinson, K.; Gibbs, G. V.; Ribbe, P. H. Quadratic Elongation: A Quantitative Measure of Distortion in Coordination Polyhedra. *Science (80-.).* **1971**, *172* (3983), 567–570. https://doi.org/10.1126/science.172.3983.567.
(143) Coe, B. J.; Glenwright, S. J. Trans-Effects in Octahedral Transition Metal Complexes. *Coord. Chem. Rev.* **2000**, *203* (1), 5–80. https://doi.org/10.1016/S0010-8545(99)00184-8.
(144) Stoumpos, C. C.; Malliakas, C. D.; Kanatzidis, M. G. Semiconducting Tin and Lead Iodide Perovskites with Organic Cations: Phase Transitions, High Mobilities, and Near-Infrared Photoluminescent Properties. *Inorg. Chem.* **2013**, *52* (15), 9019–9038. https://doi.org/10.1021/ic401215x.
(145) Kawano, N.; Koshimizu, M.; Sun, Y.; Yahaba, N.; Fujimoto, Y.; Yanagida, T.; Asai, K. Effects of Organic Moieties on Luminescence Properties of Organic–Inorganic Layered Perovskite-Type Compounds. *J. Phys. Chem. C* **2014**, *118* (17), 9101–9106. https://doi.org/10.1021/jp4114305.
(146) Umebayashi, T.; Asai, K.; Kondo, T.; Nakao, A. Electronic Structures of Lead Iodide Based Low-Dimensional Crystals. *Phys. Rev. B* **2003**, *67* (15), 155405. https://doi.org/10.1103/PhysRevB.67.155405.
(147) Sourisseau, S.; Louvain, N.; Bi, W.; Mercier, N.; Rondeau, D.; Boucher, F.; Buzaré, J.-Y.; Legein, C. Reduced Band Gap Hybrid Perovskites Resulting from Combined Hydrogen and Halogen Bonding at the Organic−Inorganic Interface. *Chem. Mater.* **2007**, *19* (3), 600–607. https://doi.org/10.1021/cm062380e.
(148) Knutson, J. L.; Martin, J. D.; Mitzi, D. B. Tuning the Band Gap in Hybrid Tin Iodide

Perovskite Semiconductors Using Structural Templating. *Inorg. Chem.* **2005**, *44* (13), 4699–4705. https://doi.org/10.1021/ic050244q.
(149) Pradeesh, K.; Nageswara Rao, K.; Vijaya Prakash, G. Synthesis, Structural, Thermal and Optical Studies of Inorganic-Organic Hybrid Semiconductors, R-PbI 4. *J. Appl. Phys.* **2013**, *113* (8), 083523. https://doi.org/10.1063/1.4792667.
(150) Filip, M. R.; Eperon, G. E.; Snaith, H. J.; Giustino, F. Steric Engineering of Metal-Halide Perovskites with Tunable Optical Band Gaps. *Nat. Commun.* **2014**, *5* (1), 5757. https://doi.org/10.1038/ncomms6757.
(151) Smith, M. D.; Pedesseau, L.; Kepenekian, M.; Smith, I. C.; Katan, C.; Even, J.; Karunadasa, H. I. Decreasing the Electronic Confinement in Layered Perovskites through Intercalation. *Chem. Sci.* **2017**, *8* (3), 1960–1968. https://doi.org/10.1039/C6SC02848A.
(152) Sheldrick, G. M. SHELXT – Integrated Space-Group and Crystal-Structure Determination. *Acta Crystallogr. Sect. A Found. Adv.* **2015**, *71* (1), 3–8. https://doi.org/10.1107/S2053273314026370.
(153) Sheldrick, G. M. Crystal Structure Refinement with SHELXL. *Acta Crystallogr. Sect. C Struct. Chem.* **2015**, *71* (1), 3–8. https://doi.org/10.1107/S2053229614024218.
(154) Dolomanov, O. V; Bourhis, L. J.; Gildea, R. J.; Howard, J. A. K.; Puschmann, H. OLEX2 : A Complete Structure Solution, Refinement and Analysis Program. *J. Appl. Crystallogr.* **2009**, *42* (2), 339–341. https://doi.org/10.1107/S0021889808042726.
(155) Momma, K.; Izumi, F. VESTA 3 for Three-Dimensional Visualization of Crystal, Volumetric and Morphology Data. *J. Appl. Crystallogr.* **2011**, *44* (6), 1272–1276. https://doi.org/10.1107/S0021889811038970.
(156) Neogi, I.; Bruno, A.; Bahulayan, D.; Goh, T. W.; Ghosh, B.; Ganguly, R.; Cortecchia, D.; Sum, T. C.; Soci, C.; Mathews, N.; et al. Broadband-Emitting 2D Hybrid Organic-Inorganic Perovskite Based on Cyclohexane-Bis(Methylamonium) Cation. *ChemSusChem* **2017**, *10* (19), 3765–3772. https://doi.org/10.1002/cssc.201701227.
(157) Thirumal, K.; Chong, W. K.; Xie, W.; Ganguly, R.; Muduli, S. K.; Sherburne, M.; Asta, M.; Mhaisalkar, S.; Sum, T. C.; Soo, H. Sen; et al. Morphology-Independent Stable White-Light Emission from Self-Assembled Two-Dimensional Perovskites Driven by Strong Exciton–Phonon Coupling to the Organic Framework. *Chem. Mater.* **2017**, *29* (9), 3947–3953. https://doi.org/10.1021/acs.chemmater.7b00073.
(158) Dohner, E. R.; Jaffe, A.; Bradshaw, L. R.; Karunadasa, H. I. Intrinsic White-Light Emission from Layered Hybrid Perovskites. *J. Am. Chem. Soc.* **2014**, *136* (38), 13154–13157. https://doi.org/10.1021/ja507086b.
(159) Dohner, E. R.; Hoke, E. T.; Karunadasa, H. I. Self-Assembly of Broadband White-Light Emitters. *J. Am. Chem. Soc.* **2014**, *136* (5), 1718–1721. https://doi.org/10.1021/ja411045r.
(160) Smith, M. D.; Jaffe, A.; Dohner, E. R.; Lindenberg, A. M.; Karunadasa, H. I. Structural Origins of Broadband Emission from Layered Pb–Br Hybrid Perovskites. *Chem. Sci.* **2017**, *8* (6), 4497–4504. https://doi.org/10.1039/C7SC01590A.
(161) Zhou, C.; Lin, H.; Worku, M.; Neu, J.; Zhou, Y.; Tian, Y.; Lee, S.; Djurovich, P.; Siegrist, T.; Ma, B. Blue Emitting Single Crystalline Assembly of Metal Halide Clusters. *J. Am. Chem. Soc.* **2018**, *140* (41), 13181–13184. https://doi.org/10.1021/jacs.8b07731.
(162) Zhou, C.; Tian, Y.; Wang, M.; Rose, A.; Besara, T.; Doyle, N. K.; Yuan, Z.; Wang, J. C.; Clark, R.; Hu, Y.; et al. Low-Dimensional Organic Tin Bromide Perovskites and Their Photoinduced Structural Transformation. *Angew. Chemie Int. Ed.* **2017**, *56* (31), 9018–

9022. https://doi.org/10.1002/anie.201702825.
(163) Zhou, C.; Lin, H.; Tian, Y.; Yuan, Z.; Clark, R.; Chen, B.; van de Burgt, L. J.; Wang, J. C.; Zhou, Y.; Hanson, K.; et al. Luminescent Zero-Dimensional Organic Metal Halide Hybrids with near-Unity Quantum Efficiency. *Chem. Sci.* **2018**, *9* (3), 586–593. https://doi.org/10.1039/C7SC04539E.
(164) Fu, P.; Huang, M.; Shang, Y.; Yu, N.; Zhou, H.-L.; Zhang, Y.-B.; Chen, S.; Gong, J.; Ning, Z. Organic−Inorganic Layered and Hollow Tin Bromide Perovskite with Tunable Broadband Emission. *ACS Appl. Mater. Interfaces* **2018**, *10* (40), 34363–34369. https://doi.org/10.1021/acsami.8b07673.
(165) Benin, B. M.; Dirin, D. N.; Morad, V.; Wörle, M.; Yakunin, S.; Rainò, G.; Nazarenko, O.; Fischer, M.; Infante, I.; Kovalenko, M. V. Highly Emissive Self-Trapped Excitons in Fully Inorganic Zero-Dimensional Tin Halides. *Angew. Chemie Int. Ed.* **2018**, *57* (35), 11329–11333. https://doi.org/10.1002/anie.201806452.
(166) Zhou, C.; Worku, M.; Neu, J.; Lin, H.; Tian, Y.; Lee, S.; Zhou, Y.; Han, D.; Chen, S.; Hao, A.; et al. Facile Preparation of Light Emitting Organic Metal Halide Crystals with Near-Unity Quantum Efficiency. *Chem. Mater.* **2018**, *30* (7), 2374–2378. https://doi.org/10.1021/acs.chemmater.8b00129.
(167) Jun, T.; Sim, K.; Iimura, S.; Sasase, M.; Kamioka, H.; Kim, J.; Hosono, H. Lead-Free Highly Efficient Blue-Emitting $Cs_3Cu_2I_5$ with 0D Electronic Structure. *Adv. Mater.* **2018**, *30* (43), 1804547. https://doi.org/10.1002/adma.201804547.
(168) Luo, J.; Li, S.; Wu, H.; Zhou, Y.; Li, Y.; Liu, J.; Li, J.; Li, K.; Yi, F.; Niu, G.; et al. $Cs_2AgInCl_6$ Double Perovskite Single Crystals: Parity Forbidden Transitions and Their Application For Sensitive and Fast UV Photodetectors. *ACS Photonics* **2018**, *5* (2), 398–405. https://doi.org/10.1021/acsphotonics.7b00837.
(169) Luo, J.; Wang, X.; Li, S.; Liu, J.; Guo, Y.; Niu, G.; Yao, L.; Fu, Y.; Gao, L.; Dong, Q.; et al. Efficient and Stable Emission of Warm-White Light from Lead-Free Halide Double Perovskites. *Nature* **2018**, *563* (7732), 541–545. https://doi.org/10.1038/s41586-018-0691-0.
(170) Cortecchia, D.; Yin, J.; Petrozza, A.; Soci, C. White Light Emission in Low-Dimensional Perovskites. *J. Mater. Chem. C* **2019**, *7* (17), 4956–4969. https://doi.org/10.1039/C9TC01036J.
(171) Booker, E. P.; Thomas, T. H.; Quarti, C.; Stanton, M. R.; Dashwood, C. D.; Gillett, A. J.; Richter, J. M.; Pearson, A. J.; Davis, N. J. L. K.; Sirringhaus, H.; et al. Formation of Long-Lived Color Centers for Broadband Visible Light Emission in Low-Dimensional Layered Perovskites. *J. Am. Chem. Soc.* **2017**, *139* (51), 18632–18639. https://doi.org/10.1021/jacs.7b10223.
(172) Wu, X.; Trinh, M. T.; Niesner, D.; Zhu, H.; Norman, Z.; Owen, J. S.; Yaffe, O.; Kudisch, B. J.; Zhu, X. Y. Trap States in Lead Iodide Perovskites. *J. Am. Chem. Soc.* **2015**, *137* (5), 2089–2096. https://doi.org/10.1021/ja512833n.
(173) Zhang, Q.; Ji, Y.; Chen, Z.; Vella, D.; Wang, X.; Xu, Q.-H.; Li, Y.; Eda, G. Controlled Aqueous Synthesis of 2D Hybrid Perovskites with Bright Room-Temperature Long-Lived Luminescence. *J. Phys. Chem. Lett.* **2019**, *10* (11), 2869–2873. https://doi.org/10.1021/acs.jpclett.9b00934.
(174) Kahmann, S.; Tekelenburg, E. K.; Duim, H.; Kamminga, M. E.; Loi, M. A. Extrinsic Nature of the Broad Photoluminescence in Lead Iodide-Based Ruddlesden–Popper

Perovskites. *Nat. Commun.* **2020**, *11* (1), 2344–2351. https://doi.org/10.1038/s41467-020-15970-x.
(175) Cortecchia, D.; Yin, J.; Bruno, A.; Lo, S.-Z. A.; Gurzadyan, G. G.; Mhaisalkar, S.; Brédas, J.-L.; Soci, C. Polaron Self-Localization in White-Light Emitting Hybrid Perovskites. *J. Mater. Chem. C* **2017**, *5* (11), 2771–2780. https://doi.org/10.1039/C7TC00366H.
(176) Hu, T.; Smith, M. D.; Dohner, E. R.; Sher, M.-J.; Wu, X.; Trinh, M. T.; Fisher, A.; Corbett, J.; Zhu, X.-Y.; Karunadasa, H. I.; et al. Mechanism for Broadband White-Light Emission from Two-Dimensional (110) Hybrid Perovskites. *J. Phys. Chem. Lett.* **2016**, *7* (12), 2258–2263. https://doi.org/10.1021/acs.jpclett.6b00793.
(177) Wang, X.; Meng, W.; Liao, W.; Wang, J.; Xiong, R.-G.; Yan, Y. Atomistic Mechanism of Broadband Emission in Metal Halide Perovskites. *J. Phys. Chem. Lett.* **2019**, *10* (3), 501–506. https://doi.org/10.1021/acs.jpclett.8b03717.
(178) Yu, J.; Kong, J.; Hao, W.; Guo, X.; He, H.; Leow, W. R.; Liu, Z.; Cai, P.; Qian, G.; Li, S.; et al. Broadband Extrinsic Self-Trapped Exciton Emission in Sn-Doped 2D Lead-Halide Perovskites. *Adv. Mater.* **2018**, *31* (7), 1806385. https://doi.org/10.1002/adma.201806385.
(179) Li, S.; Luo, J.; Liu, J.; Tang, J. Self-Trapped Excitons in All-Inorganic Halide Perovskites: Fundamentals, Status, and Potential Applications. *J. Phys. Chem. Lett.* **2019**, *10* (8), 1999–2007. https://doi.org/10.1021/acs.jpclett.8b03604.
(180) Yin, J.; Li, H.; Cortecchia, D.; Soci, C.; Brédas, J.-L. Excitonic and Polaronic Properties of 2D Hybrid Organic–Inorganic Perovskites. *ACS Energy Lett.* **2017**, *2* (2), 417–423. https://doi.org/10.1021/acsenergylett.6b00659.
(181) Yangui, A.; Garrot, D.; Lauret, J. S.; Lusson, A.; Bouchez, G.; Deleporte, E.; Pillet, S.; Bendeif, E. E.; Castro, M.; Triki, S.; et al. Optical Investigation of Broadband White-Light Emission in Self-Assembled Organic–Inorganic Perovskite $(C_6H_{11}NH_3)_2PbBr_4$. *J. Phys. Chem. C* **2015**, *119* (41), 23638–23647. https://doi.org/10.1021/acs.jpcc.5b06211.
(182) Li, T.; Chen, X.; Wang, X.; Lu, H.; Yan, Y.; Beard, M. C.; Mitzi, D. B. Origin of Broad-Band Emission and Impact of Structural Dimensionality in Tin-Alloyed Ruddlesden–Popper Hybrid Lead Iodide Perovskites. *ACS Energy Lett.* **2020**, *5* (2), 347–352. https://doi.org/10.1021/acsenergylett.9b02490.
(183) Paritmongkol, W.; Dahod, N. S.; Stollmann, A.; Mao, N.; Settens, C.; Zheng, S.-L.; Tisdale, W. A. Synthetic Variation and Structural Trends in Layered Two-Dimensional Alkylammonium Lead Halide Perovskites. *Chem. Mater.* **2019**, *31* (15), 5592–5607. https://doi.org/10.1021/acs.chemmater.9b01318.
(184) Seitz, M.; Magdaleno, A. J.; Alcázar-Cano, N.; Meléndez, M.; Lubbers, T. J.; Walraven, S. W.; Pakdel, S.; Prada, E.; Delgado-Buscalioni, R.; Prins, F. Exciton Diffusion in Two-Dimensional Metal-Halide Perovskites. *Nat. Commun.* **2020**, *11* (1), 2035. https://doi.org/10.1038/s41467-020-15882-w.
(185) Ha, S. K.; Mauck, C. M.; Tisdale, W. A. Toward Stable Deep-Blue Luminescent Colloidal Lead Halide Perovskite Nanoplatelets: Systematic Photostability Investigation. *Chem. Mater.* **2019**, *31* (7), 2486–2496. https://doi.org/10.1021/acs.chemmater.8b05310.
(186) Guo, P.; Stoumpos, C. C.; Mao, L.; Sadasivam, S.; Ketterson, J. B.; Darancet, P.; Kanatzidis, M. G.; Schaller, R. D. Cross-Plane Coherent Acoustic Phonons in Two-Dimensional Organic-Inorganic Hybrid Perovskites. *Nat. Commun.* **2018**, *9* (1), 2019. https://doi.org/10.1038/s41467-018-04429-9.
(187) Kabanov, V. V; Mashtakov, O. Y. Electron Localization with and without Barrier

Formation. *Phys. Rev. B* **1993**, *47* (10), 6060–6064. https://doi.org/10.1103/PhysRevB.47.6060.
(188) Chen, Y.; Kothiyal, G. P.; Singh, J.; Bhattacharya, P. K. Absorption and Photoluminescence Studies of the Temperature Dependence of Exciton Life Time in Lattice-Matched and Strained Quantum Well Systems. *Superlattices Microstruct.* **1987**, *3* (6), 657–664. https://doi.org/10.1016/0749-6036(87)90195-9.
(189) Wright, A. D.; Verdi, C.; Milot, R. L.; Eperon, G. E.; Pérez-Osorio, M. A.; Snaith, H. J.; Giustino, F.; Johnston, M. B.; Herz, L. M. Electron–Phonon Coupling in Hybrid Lead Halide Perovskites. *Nat. Commun.* **2016**, *7* (1), 11755. https://doi.org/10.1038/ncomms11755.
(190) Lee, J.; Koteles, E. S.; Vassell, M. O. Luminescence Linewidths of Excitons in GaAs Quantum Wells below 150 K. *Phys. Rev. B* **1986**, *33* (8), 5512–5516. https://doi.org/10.1103/PhysRevB.33.5512.
(191) Rudin, S.; Reinecke, T. L. Temperature-Dependent Exciton Linewidths in Semiconductor Quantum Wells. *Phys. Rev. B* **1990**, *41* (5), 3017–3027. https://doi.org/10.1103/PhysRevB.41.3017.
(192) Ni, L.; Huynh, U.; Cheminal, A.; Thomas, T. H.; Shivanna, R.; Hinrichsen, T. F.; Ahmad, S.; Sadhanala, A.; Rao, A. Real-Time Observation of Exciton–Phonon Coupling Dynamics in Self-Assembled Hybrid Perovskite Quantum Wells. *ACS Nano* **2017**, *11* (11), 10834–10843. https://doi.org/10.1021/acsnano.7b03984.
(193) Bhosale, J.; Ramdas, A. K.; Burger, A.; Muñoz, A.; Romero, A. H.; Cardona, M.; Lauck, R.; Kremer, R. K. Temperature Dependence of Band Gaps in Semiconductors: Electron-Phonon Interaction. *Phys. Rev. B* **2012**, *86* (19), 195208. https://doi.org/10.1103/PhysRevB.86.195208.
(194) Yu, C.; Chen, Z.; J. Wang, J.; Pfenninger, W.; Vockic, N.; Kenney, J. T.; Shum, K. Temperature Dependence of the Band Gap of Perovskite Semiconductor Compound $CsSnI_3$. *J. Appl. Phys.* **2011**, *110* (6), 063526. https://doi.org/10.1063/1.3638699.
(195) Wei, K.; Xu, Z.; Chen, R.; Zheng, X.; Cheng, X.; Jiang, T. Temperature-Dependent Excitonic Photoluminescence Excited by Two-Photon Absorption in Perovskite $CsPbBr_3$ Quantum Dots. *Opt. Lett.* **2016**, *41* (16), 3821. https://doi.org/10.1364/OL.41.003821.
(196) Wang, S.; Ma, J.; Li, W.; Wang, J.; Wang, H.; Shen, H.; Li, J.; Wang, J.; Luo, H.; Li, D. Temperature-Dependent Band Gap in Two-Dimensional Perovskites: Thermal Expansion Interaction and Electron–Phonon Interaction. *J. Phys. Chem. Lett.* **2019**, *10* (10), 2546–2553. https://doi.org/10.1021/acs.jpclett.9b01011.
(197) Cortecchia, D.; Neutzner, S.; Srimath Kandada, A. R.; Mosconi, E.; Meggiolaro, D.; De Angelis, F.; Soci, C.; Petrozza, A. Broadband Emission in Two-Dimensional Hybrid Perovskites: The Role of Structural Deformation. *J. Am. Chem. Soc.* **2017**, *139* (1), 39–42. https://doi.org/10.1021/jacs.6b10390.
(198) Mao, L.; Wu, Y.; Stoumpos, C. C.; Wasielewski, M. R.; Kanatzidis, M. G. White-Light Emission and Structural Distortion in New Corrugated Two-Dimensional Lead Bromide Perovskites. *J. Am. Chem. Soc.* **2017**, *139* (14), 5210–5215. https://doi.org/10.1021/jacs.7b01312.
(199) Calabrese, J.; Jones, N. L.; Harlow, R. L.; Herron, N.; Thorn, D. L.; Wang, Y. Preparation and Characterization of Layered Lead Halide Compounds. *J. Am. Chem. Soc.* **1991**, *113* (6), 2328–2330. https://doi.org/10.1021/ja00006a076.

(200) Mooney, J.; Kambhampati, P. Get the Basics Right: Jacobian Conversion of Wavelength and Energy Scales for Quantitative Analysis of Emission Spectra. *J. Phys. Chem. Lett.* **2013**, *4* (19), 3316–3318. https://doi.org/10.1021/jz401508t.
(201) Li, J.; Yu, H.; Li, Y. Aligned Si Nanowire-Based Solar Cells. *Nanoscale* **2011**, *3* (12), 4888. https://doi.org/10.1039/c1nr10943j.
(202) Gao, Y.; Weidman, M. C.; Tisdale, W. A. CdSe Nanoplatelet Films with Controlled Orientation of Their Transition Dipole Moment. *Nano Lett.* **2017**, *17* (6), 3837–3843. https://doi.org/10.1021/acs.nanolett.7b01237.
(203) Liu, X.; Yu, D.; Cao, F.; Li, X.; Ji, J.; Chen, J.; Song, X.; Zeng, H. Low-Voltage Photodetectors with High Responsivity Based on Solution-Processed Micrometer-Scale All-Inorganic Perovskite Nanoplatelets. *Small* **2017**, *13* (25), 1700364. https://doi.org/10.1002/smll.201700364.
(204) Oh, S. J.; Uswachoke, C.; Zhao, T.; Choi, J.-H.; Diroll, B. T.; Murray, C. B.; Kagan, C. R. Selective P- and n-Doping of Colloidal PbSe Nanowires To Construct Electronic and Optoelectronic Devices. *ACS Nano* **2015**, *9* (7), 7536–7544. https://doi.org/10.1021/acsnano.5b02734.
(205) Li, D.; Wu, H.; Cheng, H.-C.; Wang, G.; Huang, Y.; Duan, X. Electronic and Ionic Transport Dynamics in Organolead Halide Perovskites. *ACS Nano* **2016**, *10* (7), 6933–6941. https://doi.org/10.1021/acsnano.6b02795.
(206) Liu, Y.; Gibbs, M.; Puthussery, J.; Gaik, S.; Ihly, R.; Hillhouse, H. W.; Law, M. Dependence of Carrier Mobility on Nanocrystal Size and Ligand Length in PbSe Nanocrystal Solids. *Nano Lett.* **2010**, *10* (5), 1960–1969. https://doi.org/10.1021/nl101284k.
(207) Kang, M. S.; Sahu, A.; Norris, D. J.; Frisbie, C. D. Size-Dependent Electrical Transport in CdSe Nanocrystal Thin Films. *Nano Lett.* **2010**, *10* (9), 3727–3732. https://doi.org/10.1021/nl102356x.
(208) Kang, M. S.; Sahu, A.; Norris, D. J.; Frisbie, C. D. Size- and Temperature-Dependent Charge Transport in PbSe Nanocrystal Thin Films. *Nano Lett.* **2011**, *11* (9), 3887–3892. https://doi.org/10.1021/nl2020153.
(209) Yu, D.; Cao, F.; Shen, Y.; Liu, X.; Zhu, Y.; Zeng, H. Dimensionality and Interface Engineering of 2D Homologous Perovskites for Boosted Charge-Carrier Transport and Photodetection Performances. *J. Phys. Chem. Lett.* **2017**, *8* (12), 2565–2572. https://doi.org/10.1021/acs.jpclett.7b00993.
(210) Valenta, J. Determination of Absolute Quantum Yields of Luminescing Nanomaterials over a Broad Spectral Range: From the Integrating Sphere Theory to the Correct Methodology. *Nanosci. Methods* **2014**, *3* (1), 11–27. https://doi.org/10.1080/21642311.2014.884288.
(211) Reichardt, C.; Welton, T. *Solvents and Solvent Effects in Organic Chemistry*, 4th ed.; Wiley-VCH Verlag GmbH & Co. KGaA: Weinheim, Germany, 2010. https://doi.org/10.1002/9783527632220.
(212) Schmidbaur, H.; Schier, A. Argentophilic Interactions. *Angew. Chemie Int. Ed.* **2015**, *54* (3), 746–784. https://doi.org/10.1002/anie.201405936.
(213) Luehrs, D. C. Dimethylformamide Complexes of Silver(I) in Solution. *J. Inorg. Nucl. Chem.* **1971**, *33* (8), 2701–2703. https://doi.org/10.1016/0022-1902(71)80256-7.
(214) Luehrs, D. C.; Nicholas, R. W.; Hamm, D. A. Dimethyl Sulfoxide Complexes of Silver(I)

in Solution. *J. Electroanal. Chem. Interfacial Electrochem.* **1971**, *29* (2), 417–420. https://doi.org/10.1016/S0022-0728(71)80103-1.
(215) Manahan, S. E.; Iwamoto, R. T. Complexes of Copper(I) and Silver(I) with Acetonitrile in Water, the Lower Alcohols, Acetone, and Nitroethane. *J. Electroanal. Chem. Interfacial Electrochem.* **1967**, *14* (2), 213–217. https://doi.org/10.1016/0022-0728(67)80073-1.
(216) Neaman, D. A. *Semiconductor Physics And Devices: Basic Principles*, 4th ed.; McGraw-Hill: New York, 2012.
(217) Lien, D.-H.; Uddin, S. Z.; Yeh, M.; Amani, M.; Kim, H.; Ager, J. W.; Yablonovitch, E.; Javey, A. Electrical Suppression of All Nonradiative Recombination Pathways in Monolayer Semiconductors. *Science (80-.).* **2019**, *364* (6439), 468–471. https://doi.org/10.1126/science.aaw8053.
(218) Zhou, W.; Zou, X.; Najmaei, S.; Liu, Z.; Shi, Y.; Kong, J.; Lou, J.; Ajayan, P. M.; Yakobson, B. I.; Idrobo, J.-C. Intrinsic Structural Defects in Monolayer Molybdenum Disulfide. *Nano Lett.* **2013**, *13* (6), 2615–2622. https://doi.org/10.1021/nl4007479.
(219) Senanayak, S. P.; Abdi-Jalebi, M.; Kamboj, V. S.; Carey, R.; Shivanna, R.; Tian, T.; Schweicher, G.; Wang, J.; Giesbrecht, N.; Di Nuzzo, D.; et al. A General Approach for Hysteresis-Free, Operationally Stable Metal Halide Perovskite Field-Effect Transistors. *Sci. Adv.* **2020**, *6* (15), eaaz4948. https://doi.org/10.1126/sciadv.aaz4948.
(220) Tress, W.; Marinova, N.; Moehl, T.; Zakeeruddin, S. M.; Nazeeruddin, M. K.; Grätzel, M. Understanding the Rate-Dependent J–V Hysteresis, Slow Time Component, and Aging in $CH_3NH_3PbI_3$ Perovskite Solar Cells: The Role of a Compensated Electric Field. *Energy Environ. Sci.* **2015**, *8* (3), 995–1004. https://doi.org/10.1039/C4EE03664F.
(221) Song, Y.; Katsman, A.; Butcher, A. L.; Paine, D. C.; Zaslavsky, A. Temporal and Voltage Stress Stability of High Performance Indium-Zinc-Oxide Thin Film Transistors. *Solid. State. Electron.* **2017**, *136*, 43–50. https://doi.org/10.1016/j.sse.2017.06.023.
(222) Song, J. H.; Mai, X. D.; Jeong, S.; Kim, Y.-H. Hysteresis and Photoinstability Caused by Mobile Ions in Colloidal Quantum Dot Photovoltaics. *J. Phys. Chem. Lett.* **2017**, *8* (21), 5259–5263. https://doi.org/10.1021/acs.jpclett.7b02350.
(223) Leroux, M.; Grandjean, N.; Beaumont, B.; Nataf, G.; Semond, F.; Massies, J.; Gibart, P. Temperature Quenching of Photoluminescence Intensities in Undoped and Doped GaN. *J. Appl. Phys.* **1999**, *86* (7), 3721–3728. https://doi.org/10.1063/1.371242.
(224) Lambkin, J. D.; Considine, L.; Walsh, S.; O'Connor, G. M.; McDonagh, C. J.; Glynn, T. J. Temperature Dependence of the Photoluminescence Intensity of Ordered and Disordered $In_{0.48}Ga_{0.52}P$. *Appl. Phys. Lett.* **1994**, *65* (1), 73–75. https://doi.org/10.1063/1.113078.
(225) Malic, E.; Selig, M.; Feierabend, M.; Brem, S.; Christiansen, D.; Wendler, F.; Knorr, A.; Berghäuser, G. Dark Excitons in Transition Metal Dichalcogenides. *Phys. Rev. Mater.* **2018**, *2* (1), 014002. https://doi.org/10.1103/PhysRevMaterials.2.014002.
(226) Becker, M. A.; Vaxenburg, R.; Nedelcu, G.; Sercel, P. C.; Shabaev, A.; Mehl, M. J.; Michopoulos, J. G.; Lambrakos, S. G.; Bernstein, N.; Lyons, J. L.; et al. Bright Triplet Excitons in Caesium Lead Halide Perovskites. *Nature* **2018**, *553* (7687), 189–193. https://doi.org/10.1038/nature25147.
(227) Sercel, P. C.; Lyons, J. L.; Wickramaratne, D.; Vaxenburg, R.; Bernstein, N.; Efros, A. L. Exciton Fine Structure in Perovskite Nanocrystals. *Nano Lett.* **2019**, *19* (6), 4068–4077. https://doi.org/10.1021/acs.nanolett.9b01467.

(228) Pelant, I.; Valenta, J. *Luminescence Spectroscopy of Semiconductors*; Oxford University Press, 2012. https://doi.org/10.1093/acprof:oso/9780199588336.001.0001.
(229) Woo, H. C.; Choi, J. W.; Shin, J.; Chin, S.-H.; Ann, M. H.; Lee, C.-L. Temperature-Dependent Photoluminescence of $CH_3NH_3PbBr_3$ Perovskite Quantum Dots and Bulk Counterparts. *J. Phys. Chem. Lett.* **2018**, *9* (14), 4066–4074. https://doi.org/10.1021/acs.jpclett.8b01593.
(230) Yuan, L.; Huang, L. Exciton Dynamics and Annihilation in WS_2 2D Semiconductors. *Nanoscale* **2015**, *7* (16), 7402–7408. https://doi.org/10.1039/C5NR00383K.
(231) Mak, K. F.; Lee, C.; Hone, J.; Shan, J.; Heinz, T. F. Atomically Thin MoS_2: A New Direct-Gap Semiconductor. *Phys. Rev. Lett.* **2010**, *105* (13), 136805. https://doi.org/10.1103/PhysRevLett.105.136805.
(232) Amani, M.; Lien, D. H.; Kiriya, D.; Xiao, J.; Azcatl, A.; Noh, J.; Madhvapathy, S. R.; Addou, R.; Santosh, K. C.; Dubey, M.; et al. Near-Unity Photoluminescence Quantum Yield in MoS2. *Science (80-.).* **2015**, *350* (6264), 1065–1068. https://doi.org/10.1126/science.aad2114.
(233) Tanoh, A. O. A.; Alexander-Webber, J.; Xiao, J.; Delport, G.; Williams, C. A.; Bretscher, H.; Gauriot, N.; Allardice, J.; Pandya, R.; Fan, Y.; et al. Enhancing Photoluminescence and Mobilities in WS_2 Monolayers with Oleic Acid Ligands. *Nano Lett.* **2019**, *19* (9), 6299–6307. https://doi.org/10.1021/acs.nanolett.9b02431.
(234) Peulen, T.-O.; Opanasyuk, O.; Seidel, C. A. M. Combining Graphical and Analytical Methods with Molecular Simulations To Analyze Time-Resolved FRET Measurements of Labeled Macromolecules Accurately. *J. Phys. Chem. B* **2017**, *121* (35), 8211–8241. https://doi.org/10.1021/acs.jpcb.7b03441.
(235) Blancon, J.-C.; Even, J.; Stoumpos, C. C.; Kanatzidis, M. G.; Mohite, A. D. Semiconductor Physics of Organic–Inorganic 2D Halide Perovskites. *Nat. Nanotechnol.* **2020**, *15* (12), 969–985. https://doi.org/10.1038/s41565-020-00811-1.
(236) Katan, C.; Mercier, N.; Even, J. Quantum and Dielectric Confinement Effects in Lower-Dimensional Hybrid Perovskite Semiconductors. *Chem. Rev.* **2019**, *119* (5), 3140–3192. https://doi.org/10.1021/acs.chemrev.8b00417.
(237) Kastl, C.; Schwartzberg, A. M.; Maserati, L. Exciton Self-Trapping Causes Picoseconds Recombination in Metal-Organic Chalcogenides Hybrid Quantum Wells. **2021**. https://doi.org/arXiv:2103.06390.
(238) Paritmongkol, W.; Powers, E. R.; Dahod, N. S.; Tisdale, W. A. Two Origins of Broadband Emission in Multilayered 2D Lead Iodide Perovskites. *J. Phys. Chem. Lett.* **2020**, *11* (20), 8565–8572. https://doi.org/10.1021/acs.jpclett.0c02214.
(239) Bentley, M. D.; Douglass, I. B.; Lacadie, J. A.; Weaver, D. C.; Davis, F. A.; Eitelman, S. J. A New One-Step Synthesis of Sulphenamides from Alkyl and Aryl Disulphides. *J. Chem. Soc. D Chem. Commun.* **1971**, No. 24, 1625–1626. https://doi.org/10.1039/C29710001625.
(240) Davis, F. A.; Friedman, A. J.; Kluger, E. W.; Skibo, E. B.; Fretz, E. R.; Milicia, A. P.; LeMasters, W. C.; Bentley, M. D.; Lacadie, J. A.; Douglass, I. B. Chemistry of the Sulfur-Nitrogen Bond. 12. Metal-Assisted Synthesis of Sulfenamide Derivatives from Aliphatic and Aromatic Disulfides. *J. Org. Chem.* **1977**, *42* (6), 967–972. https://doi.org/10.1021/jo00426a008.
(241) Craine, L.; Raban, M. The Chemistry of Sulfenamides. *Chem. Rev.* **1989**, *89* (4), 689–712.

https://doi.org/10.1021/cr00094a001.
(242) Illyés, T.-Z.; Molnár-Gábor, D.; Szilágyi, L. Novel Approaches to the Syntheses of N-Substituted S-Glycosyl-Sulfenamides. *Carbohydr. Res.* **2004**, *339* (8), 1561–1564. https://doi.org/10.1016/j.carres.2004.03.023.
(243) Paulmier, C. N , N -Diethylbenzeneselenenamide. In *Encyclopedia of Reagents for Organic Synthesis*; John Wiley & Sons, Ltd: Chichester, UK, 2001; Vol. 2, pp 2–4. https://doi.org/10.1002/047084289X.rd177.
(244) Hiroi, K.; Sato, S. Asymmetric Synthesis with Organo-Selenium Compounds: A Facile Entry to Optically Active 4-Substituted 2-Cyclohexenones by Asymmetric Selenenylation of Ketones with Chiral Selenenamides. *Synthesis (Stuttg).* **1985**, *1985* (6/7), 635–638. https://doi.org/10.1055/s-1985-34139.
(245) Paulmier, C.; Lerouge, P.; Outurquin, F.; Chapelle, S.; Granger, P. ^{1}H, ^{13}C, ^{15}N, ^{17}O and ^{77}Se NMR of Selenenamides. *Magn. Reson. Chem.* **1987**, *25* (11), 955–959. https://doi.org/10.1002/mrc.1260251106.
(246) Wang, X.; Zhong, Y.; Mo, Z.; Wu, S.; Xu, Y.; Tang, H.; Pan, Y. Synthesis of Seleno Oxindoles via Electrochemical Cyclization of N-arylacrylamides with Diorganyl Diselenides. *Adv. Synth. Catal.* **2021**, *363* (1), 208–214. https://doi.org/10.1002/adsc.202001192.
(247) Reich, H. J.; Renga, J. M.; Reich, I. L. Organoselenium Chemistry. Conversion of Ketones to Enones by Selenoxide Syn Elimination. *J. Am. Chem. Soc.* **1975**, *97* (19), 5434–5447. https://doi.org/10.1021/ja00852a019.
(248) Kubelka, P.; Munk, F. An Article on Optics of Paint Layers. *Z. Tech. Phys.* **1931**, *12* (1930), 593–601.
(249) Müller, P. Practical Suggestions for Better Crystal Structures. *Crystallogr. Rev.* **2009**, *15* (1), 57–83. https://doi.org/10.1080/08893110802547240.